Effect of Phosphorylation on the Structure and Dynamics of Cardiac Troponin Protein Complex: a molecular view of the regulation of heart muscle under stress conditions

Ehsan Kachooei

A thesis submitted in fulfilment of the requirements

for the degree of DOCTOR OF PHILOSOPHY

Supervisor: A/Prof. Louise Brown

MACQUARIE University
SYDNEY·AUSTRALIA

Department of Molecular Sciences

Macquarie University

Sydney, Australia

November, 2019

Abstract

The contraction of cardiac muscle is regulated by a large heterotrimeric complex, ~80 kDa, which is called 'Troponin' (Tn). Tn is located on the thin filament of striated muscle, playing a switch role in response to Ca^{2+} binding, to regulate the interaction of myosin with actin. The force of Ca^{2+} binding can initiate a series of conformational changes in the dynamic structure of the Tn complex which then propagate through the other components of the muscle filament, leading to contraction. Upon stress condition, and in response to β-adrenergic stimulations, Tn becomes phosphorylated in the heart which results in a faster relaxation and higher rate of contraction.

Despite the wealth of structural data on troponin, the molecular details of the conformational changes triggered by Ca^{2+} binding and phosphorylation within the intact Tn complex is still lacking and remains an experimental challenge. In this Thesis, site directed spin labeling (SDSL), using paramagnetic nitroxide, in conjugation with Nuclear Magnetic Resonance (NMR) and Electron Paramagnetic Resonance (EPR) was used to address fundamental questions about the structure and dynamics of the cardiac troponin complex upon phosphorylation. Long-range (10-25 Å) structural information was derived from Paramagnetic Relaxation Enhancement (PRE) effects of the NMR signal due to the presence of the nitroxide spin label. Interspin distances were also obtained from continuous wave (8 - 25 Å) and pulsed EPR (DEER, up to ~70 Å) techniques. Together, both magnetic resonance approaches provided us with a structural model that details the conformational interplay between key regions of the cardiac troponin complex in response to both Ca^{2+} binding and phosphorylation. Knowledge of the role of phosphorylation as a secondary regulatory mechanism in fine-tuning the cardiac Tn isoform is important for understanding why cardiac muscle is perturbed by mutations that lead to disease states such as cardiomyopathy.

Content

Declaration of Originality

I hereby declare that the research presented in this thesis herein contains original work conducted by the author. Where appropriate, work performed in collaboration with other groups and individuals has been recognised and acknowledged in their respective sections within the text. This thesis contains no material that has been submitted as part of the requirement of any other award, at any other institution and to the bet of my knowledge contains no material previously published or written except where reference is made.

Animal or Human ethics approvals were not required to perform the research presented in this Thesis. The research project was approved by the Macquarie University Institutional Biosafety Committee, as Exempt Dealings (IBC Reference Numbers 5201300898 and 5106), for the project titled “Expression of proteins that form the Troponin muscle protein complex”.

Ehsan Kachooei

November 2019

Acknowledgements

I wish to express my greatest gratitude for my supervisor, Dr. Louise Brown, for all her support and advice during my candidature. Being part of her group has been a wonderful opportunity, full of lots of scientific adventures; and I was always challenged to continue to learn many new skills.

I would also like to thank Dr. Nicole Cordina and Dr. Phani Potluri for their constant support and guidance.

Thanks everyone!

Publications forming part of this thesis

The following manuscripts form the basis of much of this Thesis. While it is acknowledged that scientific research is rarely an individual endeavour and thus multiple authorship is common, the author of this Thesis is the primary researcher and author of all manuscripts with the exception of Paper 3 (Appendix 1). The contribution of each author is described in the introduction to each paper. Manuscripts are listed here.

Chapter 1: Review Paper

Ehsan Kachooei, Nicole M. Cordina, and Louise J. Brown (2019) Constructing a structural model of troponin using site-directed spin labeling: EPR and PRE-NMR. *Biophysical Reviews*, **11 (4)**, 621-639

Chapter 4: Paper 1

Ehsan Kachooei, Nicole M. Cordina, Phani R. Potluri, Joanna A. Guse, Dane McCamey, and Louise J. Brown. Phosphorylation of Troponin I finely controls the positioning of Troponin for the optimal regulation of cardiac muscle contraction. Prepared for submission to *PNAS-USA*.

Chapter 5: Paper 2

Ehsan Kachooei, Nicole M. Cordina, and Louise J. Brown. The release of the cardiac Troponin switch region is coupled to both Ca^{2+} binding and phosphorylation. *In preparation*.

Appendix 1: Paper 3

Phani R. Potluri, Nicole M. Cordina, Ehsan Kachooei, and Louise J. Brown (2019) Characterization of the L29Q Hypertrophic Cardiomyopathy Mutation in Cardiac Troponin C by Paramagnetic Relaxation Enhancement Nuclear Magnetic Resonance. *Biochemistry*, **58 (7)**, 908-917

Additional Relevant Publications and Presentations

Presented Abstracts

1. Ehsan Kachooei, Phani R. Potluri, Joanna A. Guse, Dane R. McCamey, Louise J. Brown (2017) The Ca^{2+} and phosphorylated triggered movement of the cardiac muscle Troponin switch as tracked by conventional and pulsed (DEER) EPR. *11th Australian and New Zealand Society for Magnetic Resonance Conference*. Kingscliff, New South Wales, Australia. December 2-6. (*Short Talk*)
2. Ehsan Kachooei, Phani R. Potluri, Joanna A. Guse, Dane R. McCamey, Louise J. Brown (2018) Monitoring the effect of phosphorylation on the positioning of the cardiac specific troponin N-terminus with respect to regulatory N-domain by conventional and pulsed (DEER) EPR. *EUROMAR 2018 Conference*. Nantes, France. July 1-5. (*Poster*)
3. Ehsan Kachooei, Phani R. Potluri, Joanna A. Guse, Dane R. McCamey, Louise J. Brown (2018) Tracking of phosphorylation triggered structural changes in cardiac troponin by pulsed (DEER) EPR. *3rd joint conference of the Asia Pacific EPR Society (APES) and the international EPR Society (IES)*. Brisbane, Queensland, Australia. September 23-27. (*Poster*)
4. Ehsan Kachooei, Phani R. Potluri, Joanna A. Guse, Dane R. McCamey, Louise J. Brown (2018) Tracking phosphorylation induced conformational changes in cardiac Troponin: an EPR and PRE-NMR study. *Asian Biophysics Association Symposium and Annual Meeting of the Australian Society for Biophysics*. Melbourne, Australia. December 2-6 (*Poster*)

Upcoming presentations

1. Ehsan Kachooei, Nicole M. Cordina, Jeffrey, R Harmer, Louise J. Brown (2019) The Ca^{2+} and phosphorylated triggered movement of the cardiac muscle Troponin switch as tracked by site directed spin labeling. *Australian Physiology Society (AuPS) and the Australian Society for Biophysics (ASB) meeting*. Canberra, Australian Capital Territory, Australia. December 1-4. (*Young Biophysicist Talk*)

List of Figures

CHAPTER 1

CHAPTER 2

CHAPTER 3

CHAPTER 4. PAPER 1

CHAPTER 5. PAPER 2

CHAPTER 6

List of Tables

CHAPTER 1

CHAPTER 2

CHAPTER 3

CHAPTER 4. PAPER 1

CHAPTER 5. PAPER 2

Abbreviation and Symbols

Tn	Troponin
Tm	Tropomyosin
TnC	Troponin C
TnI	Troponin I
TnT	Troponin T
cTn	cardiac Troponin
skTn	skeletal Troponin
Ca^{2+}	Calcium
Mg^{2+}	Magnesium
PRE	Paramagnetic Relaxation Enhancement
NMR	Nuclear Magnetic Resonance
EPR	Electron Paramagnetic Resonance
FRET	Fluorescence resonance energy transfer
HSQC	Heteronuclear Single Quantum Coherence
TROSY	Transverse Relaxation Optimised Spectroscopy
PCS	Pseudo Contact Shift
FID	Free Induction decay
FT	Fourier Transform
HCM	Hypertrophic cardiomyopathy
DCM	Dilated cardiomyopathy
RCM	Restrictive cardiomyopathy
cAMP	cyclic adenosine monophosphate
ATP	adenosine triphosphate
BCA	bicinchoninic acid
BSA	bovine serum albumin
B_0	magnetic field
χ^2	goodness of fit
CM	carboxy methyl
CW	continuous wave

ddH_2O	distilled water
DNA	deoxyribonucleic acid
DMF	N, N-dimethyl formamide
DTT	Dithiothreitol
E. coli	*Escherichia coli*
EDTA	ethylenediaminetetraacetic acid
EGTA	ethylene glycol bis(2-aminoethyl ether)-N,N,N'N'-tetraacetic acid
F-actin	filamentous actin
G-actin	globular actin
IPTG	isopropyl-beta-D-thiogalactopyranoside
LB	Luria-Bertani media
MOPS	4-morpholinepropanesulfonic acid
MTSL	1-oxyl-2,2,5,5-tetra-methylpyrroline-3-methyl)-methanethiosulfonate spin label

1. Introduction

1.0 Aim & scope

The vitality of living systems is highly dependent on proteins. Proteins and protein complexes, play various roles in living systems; including building the structures of cells and tissues, facilitating biochemical reactions to occur on very fast timescales, and converting chemical energy to mechanical work. Many physiological processes are also controlled by large multi-protein complexes which can work together like a molecular motor. These motor-like complexes can transfer small forces, introduced by an effector molecule, into larger-scale structural changes via small conformational changes, subunit motions, or inter-macromolecular interactions. These large-scale macromolecular interactions then control a mechanical activity at the macroscopic level of the cell. However, sometimes these delicately controlled protein regulatory complexes can be disrupted by disease-producing mutations. Therefore, understanding the structure and dynamics of these important regulatory complexes is prerequisite for deciphering the molecular basis for disease causing mutations and the possibility of future rational therapeutic intervention.

Contraction of striated muscle is a prime example of a physiological process controlled by a protein complex. The protein complex that regulates the interaction between the thin and thick filaments in the muscle is Troponin (Tn) and is often referred to as the calcium (Ca^{2+})-switch. Troponin consists of three subunits: Troponin C (TnC), the Ca^{2+}-binding subunit; Troponin I (TnI), the inhibitory subunit; and, Troponin T (TnT), the thin filament anchoring subunit. The Tn complex is large and highly dynamic, and is located on the muscle thin filament where it interacts with Tropomyosin (Tm) and actin. In this position, Tn regulates the force generating actin-myosin interaction in response to the effector molecule - Ca^{2+}. TnC is the smallest of the three subunits and it undergoes a small conformational change in response to Ca^{2+} binding. This signal is then amplified into a larger-scale conformational change involving TnI and Tm. Together, this cascade of structural changes triggers the effective switching of the thin filament into a state where the acto-myosin interaction, and thus muscle contraction, can then occur.

There are two isoforms of striated muscle controlled by Tn: skeletal and cardiac. In cardiac muscle, force propagation by Tn is controlled by additional molecular regulatory processes compared to the skeletal isoform (which is primarily controlled by Ca^{2+} binding). Contraction of cardiac muscle is involuntary, rhythmic, and it increases in stress conditions. Increasing the rate of cardiac muscle contraction is understood to be controlled by the activation of protein kinase A (PKA) which phosphorylates target proteins in the muscle sarcomere, including Tn. Two of the target sites in Tn are located at the N-terminal end of TnI. This is a unique region in the cardiac isoform which is not present in the skeletal isoform and is approximately 32 amino acids in length. The current hypothesis is that, in cardiac muscle, phosphorylation is a secondary effector regulatory mechanism which further modulates the intricate Ca^{2+}-dependent interactions within the cardiac Tn complex. However, the manner through which phosphorylation regulates cardiac muscle contraction at a molecular level is still not well understood.

Our current knowledge of the role of the Tn complex in the regulation of striated muscle contraction is based mostly on the x-ray crystallographic structures of the core region of Tn. However, these high resolutions structures represent only a static snapshot of a highly dynamic system; and many mobile regions, including the cardiac specific TnI N-terminal region remains undefined. Further, while high resolution information from NMR studies has contributed to our understanding of the Tn structure and how it works, most of this structural information was obtained using isolated Tn subunits and/or small fragments of the complex in solution. While several structural models exist to describe the role of phosphorylation in muscle regulation, there is little direct structural information obtained in solution, using intact Tn systems, to support these models.

The Aim of this Thesis was therefore to investigate the structural interactions between the cardiac Tn subunits upon phosphorylation of the cardiac specific TnI N-terminal region. Specifically, magnetic resonance experiments were designed to examine the positioning of key functional regions of TnI with respect to TnC. The results presented in this Thesis provide us with information about the structure and dynamics of the Tn complex in response to phosphorylation but also Ca^{2+} binding. This structural information was then used to further

refine a model which describes the regulatory role of phosphorylation in cardiac muscle contraction.

To achieve this, Site-Directed Spin Labeling (SDSL) methods are described in this Thesis to introduce a paramagnetic moiety onto a desired site in Tn. Afterward, either ***Electron Paramagnetic Resonance*** (EPR) or ***Nuclear Magnetic Resonance*** (NMR) spectroscopy methods were used to obtain distance constrains between the many spin-labeled locations on Tn; and in response to the two different effectors: (i) Ca^{2+} binding and (ii) phosphorylation. To do this, the techniques of Continuous Wave (CW)-EPR, Double Electron-Electron Resonance (DEER)-EPR and Paramagnetic Relaxation Enhancement-NMR (PRE-NMR) were applied to measure the interspin distances within Tn. The distance between two strategically placed spin labels by CW-EPR is within the range of 8 to 20 Å; and for pulsed EPR methods (i.e. DEER), the range is up to ~80 Å. EPR is practically not limited by the size of a protein, and this advantage allows for the study of the individual subunits of Tn, the whole intact Tn complex, through to the thin filament, and even whole muscle fibres.

The method of PRE-NMR provides both protein structure and dynamic information by providing long-range distance restraints of up to 25 Å for a proton experiencing relaxation enhancement from a nearby paramagnetic moiety, such as a nitroxide spin label. Combining the structural information from both these spin-label based EPR and NMR approaches provides complementary information about the conformation and dynamics of Tn in solution.

In this Thesis, two main experimental studies were performed to understand the structural response of Tn to phosphorylation. These studies were (i) examination of the phosphorylation associated positioning of the cardiac specific TnI N-terminal region within Tn (**Chapter 4**: manuscript 1); and (ii) examination of phosphorylation associated changes in the position of the TnI regulatory region, known as the 'switch peptide' (**Chapter 5**: manuscript 2).

Following on in this Chapter is a brief description of the structure of striated muscle and its sarcomeric components. An overview of the current model of cardiac Troponin and its regulatory mechanism is also reviewed and the contribution of spin labeling methods to the

Tn muscle field is presented. This work is published in the manuscript titled '*Constructing a structural model of troponin using site-directed spin labeling: EPR and PRE-NMR*' (Paper 1).

1.1 Muscle Types

Vertebrate muscles, based on their histological appearances, are classified into two types; smooth or striated. Smooth muscle cells do not show regular patterns of organization under the microscope. Smooth muscle is specialized for slow and sustained contraction, including rhythmic and tonic contraction. Digestive tract and blood vessels are examples of smooth muscle. Striated muscle, on the other hand, appears as aligned stripes under the microscope. The repeated structural feature of the contractile units in striated muscle are called 'sarcomeres'. There are two types of striated muscle, skeletal and cardiac (**Figure 1.1**). The cardiac isoform is the focus of this Thesis.

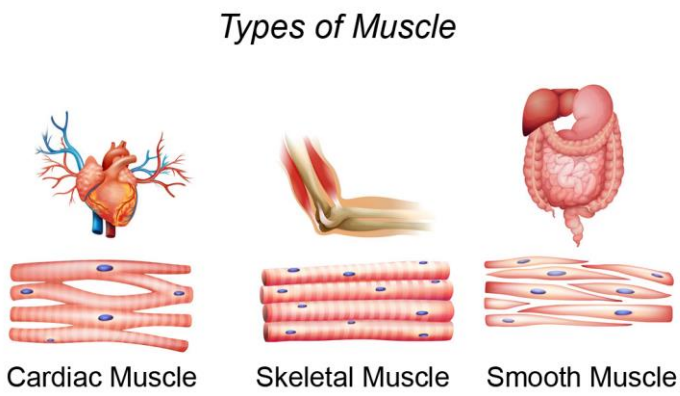

Figure 1.1 There are three types of muscle found in vertebrates - smooth muscle, skeletal muscle and cardiac muscle. Cardiac and skeletal muscle are the two isoforms of striated muscle which share a similar structural organisation. Image adapted from [1].

1.2 Striated muscle and the Sarcomere

The sarcomeres in striated muscle are highly structured units consist of thick and thin filaments arranged in an overlapping manner (**Figure 1.2**). The thick filaments consist mainly of myosin, an elongated protein with a coiled-coil tail and a globular head. The myosin molecules are organised in a staggered arrangement with their globular heads protruding out from the thick filament which is composed of their tail regions. The thin filament is

comprised largely of polymerised actin monomers which form a double helical structure with a periodicity of ~14 actin monomer units.

Muscle contraction occurs when the myosin heads of the thick filament interact with the actin thin filament to form a cross-bridge [2]. This cross-bridge formation is coupled to the simultaneous hydrolysis of ATP by myosin and results in the relative sliding of the thin filaments over the thick filaments. This shortens the length of the sarcomere, leading to muscle contraction. The sliding process is initiated upon the influx of calcium (Ca^{2+}) across the muscle fibre membrane which occurs upon nervous excitation [3]. As introduced earlier, in striated muscle, the 'calcium switch' that regulates muscle contraction is Troponin, a highly flexible, heterotrimeric protein of ~77 kDa.

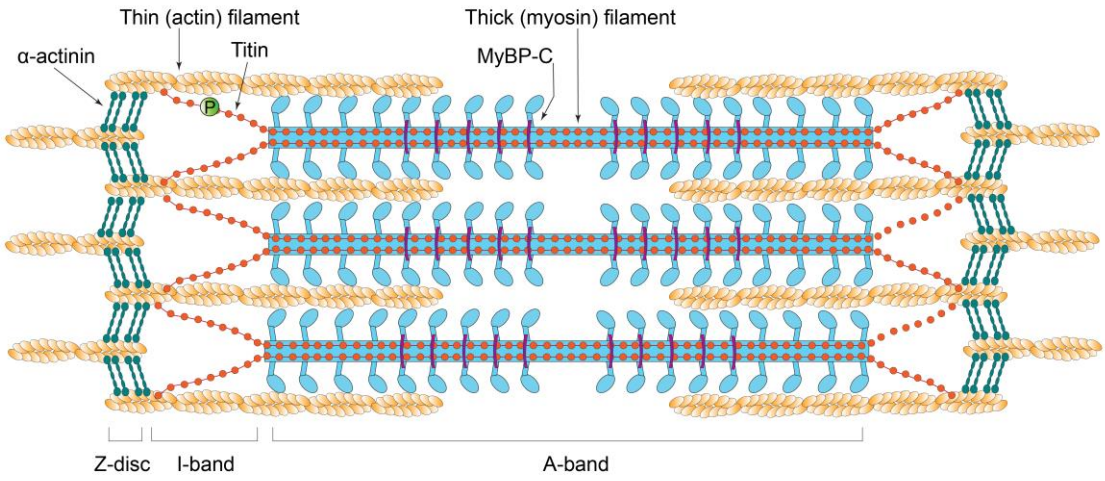

Figure 1.2 Sarcomere structure. The central bipolar thick filaments are composed primarily of myosin, with each thick filament surrounded by six parallel thin filaments originating from the Z-disc at both ends of the sarcomere. Thin filaments from adjacent sarcomeres are crosslinked by α-actinin at the Z-disc. Six giant titin proteins lie along the entire length of the thick filament and beyond, spanning the centre of the sarcomere to the Z-disc, where they interact with α-actinin [4]. As seen by microscopy, the dark A-band corresponds to the thick filament, and the light I-band is spanned by thin filaments and titin. Myosin binding protein C (MyBP-C) is distributed at 11 transverse stripes ~43 nm apart along the thick filament [5]. Image is adapted from [6].

1.3 Troponin complex

As introduced earlier, there are two distinct isoforms for Troponin, cardiac (cTn) and skeletal (skTn). Both Tn isoforms share a high degree of sequence homology. The regulatory mechanism of both isoforms is believed to involve similar conformational switching mechanisms between the high and low states of Ca^{2+}. Each of the three subunits comprising Tn has a unique role in the Ca^{2+} mediated regulation of muscle contraction, as discussed below. However, there are some important differences between these isoforms. For example, there is a unique N-terminal of 32 residues in cardiac TnI which is absent in skeletal isoform. Moreover, the linker between two lobes of skeletal TnC, in its Ca^{2+} saturated state, adopts a straight helical structure, while in cardiac isoform this linker is disordered [7, 8]. Notably, while there is a structure of the skeletal isoform in each saturated and free Ca^{2+} state, there is still no structure resolved in Ca^{2+} free state for the cardiac Tn complex.

1.3.1 Troponin C

The troponin C (TnC) molecule is the regulatory subunit in the Tn complex, and as the name suggests, it has binding sites for Ca^{2+}. TnC is a 161-residue long protein (~18 kDa) made up of two globular domains joined by a flexible hydrophobic linker. TnC contains nine short α-helices which form four structural motifs known as EF-hands. The EF-hand motif is capable of binding positive divalent cations. Each EF-hand consists of two α-helices interconnected by a loop with negatively charged residues that coordinate the positive ion (**Figure 1.3**). EF hand I (residues 16 to 51) and EF hand II (residues 52 to 87) have a low affinity for Ca^{2+} ($Ka \approx 10^5$ M^{-1}) but are highly selective to this metal over Mg^{2+}. These different behaviours between the metal sites in the N- and C-domains have resulted in the naming of the Ca^{2+} ions that bind to Site I and II as the 'catalytic' or 'regulatory' Ca^{2+} sites, while Sites III (residues 92 to 127) and IV (residues 128 to 161) are known as the 'structural' Ca^{2+}/Mg^{2+} sites. The structural sites are always occupied under physiological conditions ($Ka \approx 10^7$ M^{-1}); and other divalent cations such as Mg^{2+} and Cd^{2+} can also bind to these sites. In the cardiac isoform, the first EF-hand motif (Site I) is defunct and does not bind Ca^{2+} at any concentration. Thus Site II is the only site in the cardiac isoform which is solely responsible for Ca^{2+} sensing .

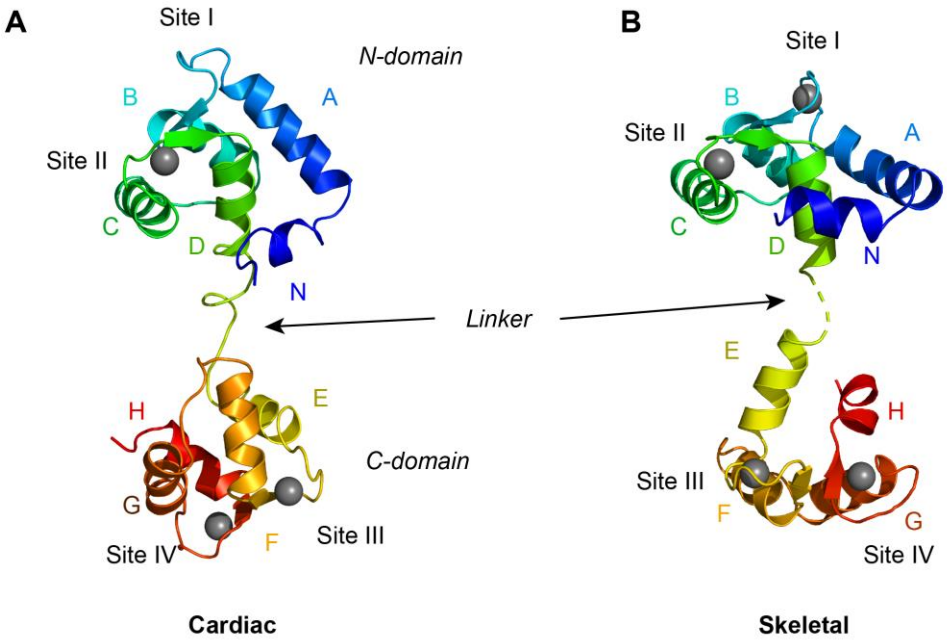

Figure 1.3 Solution structures of (A) Cardiac TnC (PDB 1AJ4 [9]) and (B) Skeletal TnC (PDB 1TNX [10]) in the Ca^{2+} saturated state. Both cTnC and skTnC consist of two domains which are connected by a flexible linker. The N-domain consists of five α-helices (N, A, B, C and D) and contains two Ca^{2+}-binding sites (Sites I and II). The C-domain consists of four helices (E, F, G and H) and contains two Ca^{2+} binding sites (Sites III and IV). While all Ca^{2+} sites are functional in skTnC, Site I in cTnC is incapable of binding Ca^{2+}.

1.3.2 Troponin I

Troponin I (TnI) is expressed in three different isoforms: cardiac, slow skeletal and fast skeletal. The mature form of human TnI consists of a 210-residue long protein (including the first Met residue) with a molecular mass of approximately 24 kDa. This protein is arranged as four α-helices intercalated by flexible disordered regions. Structurally, it can be classified into the following domains: the cardiac-exclusive N terminal domain (NH_2-TnI, or N-extension), the structurally rigid IT arm, the "inhibitory" peptide region, the "switch" peptide region, and the C-terminal mobile domain or second actin-binding domain (**Figure 1.4 A** and **Table 1.1**).

The cardiac specific NH_2-TnI extension region consists of an acidic region (residues 2 to 11) and a Xaa-Pro motif (residues 12 to 18) [11]. Within this region, two adjacent serine residues are located (Ser 22 and Ser 23). These two serines are the targets of PKA-mediated phosphorylation [12]. A structure has been proposed for this region based on experiments which used a peptide in isolation [13]. However, in the whole troponin molecule, this region is reported to be disordered [14, 15].

The 'IT arm' of Tn is a rigid coiled-coil of α helices of TnI and TnT. The function of the IT arm is structural, as it is the least mobile region of the Tn complex. It serves as an anchoring region for the C-terminal domain of troponin C. The inhibitory peptide of TnI (residues 137 to 148) is alone sufficient for achieving maximum inhibition of actomyosin ATPase activity at a substoichiometric ratio to actin [16]. The switch peptide of TnI incorporates helix H3 (residues 151 to 162). At high Ca^{2+} levels, this functionally important switch peptide region interacts with the hydrophobic pocket in the N-domain of TnC. This is a Ca^{2+} controlled interaction and is a key feature of muscle contraction.

1.3.3 Troponin T

The troponin T (TnT) subunit is the largest of the three subunits and has mainly a structural role. It is responsible for the fixation and positioning of the Tn complex with respect to the thin filament. In an adult human heart, TnT is a 288-residue long protein (including the first Met) with an approximate molecular weight of 36 kDa. Despite its structural role, the majority of the TnT molecule has not been resolved experimentally, and most of what is known about has been gathered from studies of partial structures. The Troponin T amino acid sequence can be divided into three structural domains: (i) the N terminal domain, (ii) the linking domain, and (iii) the C terminal domain (Table 1). The C terminal domain is part of the Tn complex core whilst the remainder of the protein is associated with tropomyosin. The N-terminal segment (residues 1 to 181), also named TnT1, has an extended structure that includes regions of single α-helix that bind to tropomyosin. Functionally, the presence of TnT1 in the thin filament independently enhances the cooperativity of the Ca^{2+} switch, presumably via its interactions with tropomyosin [17].

The TnT2 domain (residues 226 to 271) is upstream of the linker region and forms an integral part of the Tn complex core (**Figure 1.4 B**). The TnT Helix H2 is the central component of the IT arm where it forms an antiparallel coiled-coil with Helix H2 of TnI that spans the length of troponin. It also interacts with helix H1 of TnI. Lastly, there is a flexible linker between TnT1 and TnT2. This is essential for locating and anchoring the troponin complex onto the actin - tropomyosin filament.

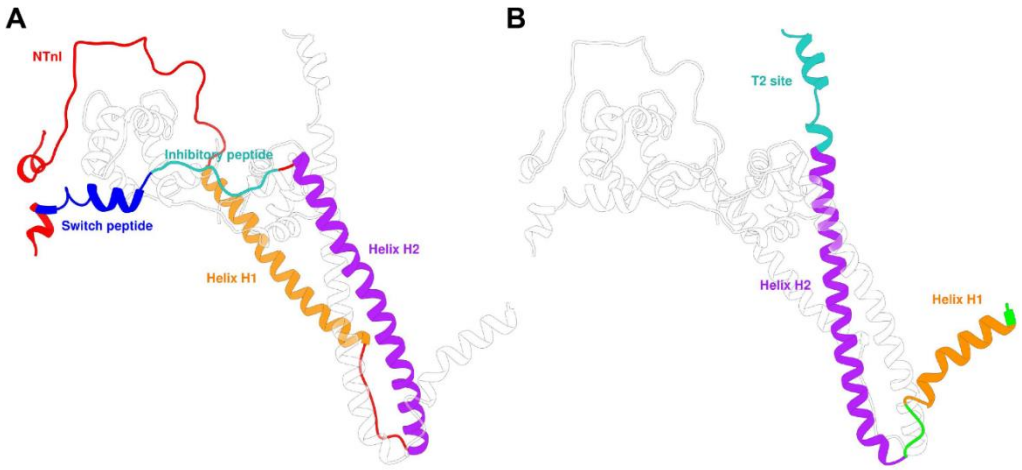

Figure 1.4 Structural components of TnI and TnT. A) The TnI molecule with its relevant structural regions are highlighted. Red colour represents the unique cardiac NH_2-TnI region. H1 (orange) and H2 (violet) are part of the IT arm. The inhibitory region (green) is a flexible peptide responsible for blocking actin. The switch peptide corresponds to Helix H3 (dark blue). Residues 172 to 210 of TnI are not present in this structure. B) The TnT2 domain, with its relevant structural regions, is highlighted. H1 (residues 202-220, orange) and H2 (residues 226-271, violet) are parts of IT-arm subdomain. T2 site (green) is the Tm interaction site. Residues 1 to 201 of TnT (TnT1) are not present in this structure. Image is from [11].

Table 1.1 The conformation of the key functional regions of each subunit within the cardiac troponin crystal structure [7]. The residue numbers for each region are according to the cardiac Tn core crystal structure (PDB 1J1D).

Subunit	Region	Residues	Function / structural information	Crystallised	Resolved
Troponin C	N-domain	1-84	Binds the switch peptide in the +Ca^{2+} state. Part of the regulatory head subdomain.	Yes	Yes
	Linker	85-93	Flexible hinge region, enables regulatory head to move independently of IT-arm.	Yes	Yes
	C-domain	94-161	Interacts with TnI & TnT in the structural IT-arm.	Yes	Yes
Troponin I	N-extension	1-30	Specific to cardiac TnI isoform. Contains phosphorylation sites. Unknown structure.	No	
	N-region	31-42	Residues 31-34 are not defined, and residues 35-42 are highly variable among crystal structures	Yes	No
	H1(I)	43-79	Part of the IT-arm, N-terminus interacts with TnC, and C-terminus interacts with TnT.	Yes	Yes
	Linker	80-89	Extended loop connecting H1 and H2 helices. Interacts with TnT in within the IT-arm.	Yes	Yes
	H2(I)	90-135	Forms a parallel coiled coil with TnT helix H2(T2). Part of the IT-arm.	Yes	Yes
	Inhibitory region .	137-148	Assumed extended, as the missing 13 residues span ~30Å. This region is likely to be flexible	Yes	No
	H3(I) .	150-159	The 'switch peptide' binds to TnC N-domain. Part of the regulatory head subdomain	Yes	Yes
	H4(I)	164-188	Protruded helix, no interactions with other subunits. Possibly a crystallisation artefact.	Yes	Yes
	C-terminus	189-210	Residues 181-191 in an extended conformation, residues 192-210 not defined.	Yes	Yes
Troponin T	N-terminus	1-76	T1 domain. Contains phosphorylation sites. No known interactions, unknown function.	No	No
	Central region (CR)	77-181	(CR) of T1 domain binds strongly to Tm, anchors the complex to the filament.	No	No
	Linker	182-200	The region linking the T1 and T2 domains of TnT is thought to be flexible.	Yes	No
	H1(T2) .	204-220	T2 domain. This α-helix is stabilised by H-bonds to TnI. Part of the IT-arm subdomain	Yes	Yes
	H2(T2)	226-271	T2 domain. This α-helix forms a coiled coil with TnI H2(I) in the IT-arm subdomain.	Yes	Yes
	C-terminus	272-288	Binds Tm (higher affinity in under low Ca^{2+} conditions (51). May stabilise OFF state (52).	Yes	No

1.4 Tropomyosin

Tropomyosin (Tm) is a two-chain α-helical coiled-coil rod-shaped protein (~35 kDa). The binding and flexibility of Tm on the actin filament can vary with the specific Tm isoform, with cardiac Tm found to be more flexible than skeletal Tm [18]. The Tm molecules interacts end-to-end to form two strands and lies in the grooves formed by the long pitch helices of F-actin. Each Tm dimer makes contact with seven actin monomers [19]. Attached to each Tm

dimer is one set of Troponin complex proteins. The arrangement of this complex is shown in Figure 3. Binding of Ca^{2+} to the N-domain lobe of TnC (N-TnC) induces a conformational change in Tm that, in turn, initiates a series of intra- and intermolecular structural changes in the thin filament proteins allowing myosin to bind to F-actin [19].

1.5 Actin thin filament

The thin filament is a multiprotein complex of approximately 9 nm in diameter. A thin filament segment can be considered as essentially a long repeating unit made of seven actin monomers (G-actin), and one regulatory protein complex comprised of a coiled coil dimer of α- tropomyosin (Tm), and one Troponin complex (Tn) (**Figure 1.5**). These proteins are found at precise stoichiometric intervals along the thin filament. The polymerization of the actin monomers forms the filamentous F-actin structure.

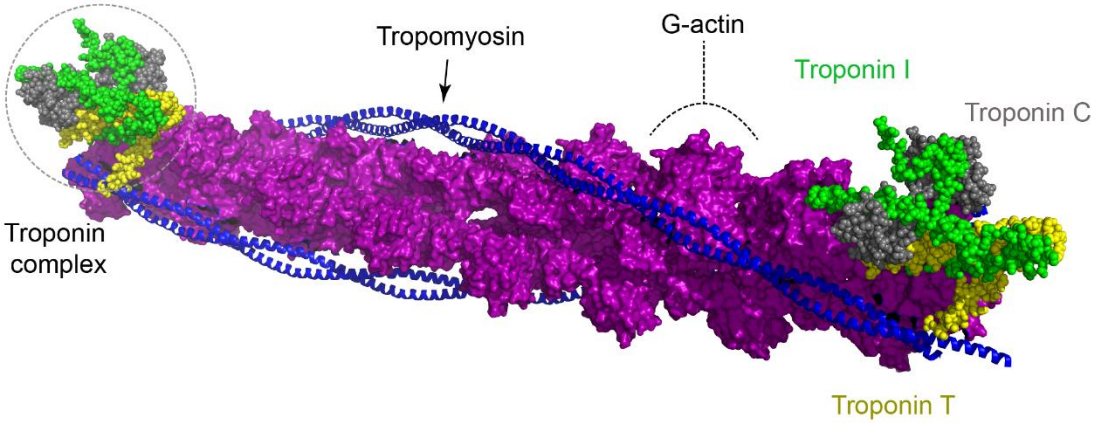

Figure 1.5 Structural organization of thin filaments. F-actin is comprised of polymerization of G-actin monomers (purple). Tropomyosin dimer and Tn complex is repeated at precise interval of 7 actin monomers. Image drawn with PyMol using (PDB 2W4U [20]).

1.6 Modulation of Ca^{2+} switch by phosphorylation

Heart muscle possesses a unique regulatory mechanism, via phosphorylation, that allows it to meet enhanced oxygen demand by increasing the rate of blood circulation. During periods of high stress or increased physical activity, catecholamines such as adrenaline and noradrenaline, are released into the bloodstream and subsequently bind to β-1 receptors in cardiac myocytes. This triggers an increase of the cytosolic cyclic adenosine monophosphate (cAMP) levels and activation of protein kinase A (PKA). PKA then phosphorylates TnI and other sarcomeric proteins.

There are several sites across TnI that are phosphorylated by different protein kinases (**Figure 1.6**). Within the cardiac specific TnI N-terminal region, there are two PKA's phosphorylation sites - residues Ser22 and Ser23 [21-23]. The faster relaxation rate (lusitropy) of the cardiac muscle, due to TnI phosphorylation, is essential for shortening the heart's contraction-relaxation cycle, thereby allowing for a faster heart rate. This post-translational modification of Tn alters the interactions between the TnC and TnI subunits. As a result, there is a decrease in the affinity of Ca^{2+} for TnC due to an increased rate of Ca^{2+} dissociation from TnC [24-26]. Although the physiological implications of the modulation of the Ca^{2+} switch by TnI phosphorylation are well understood, understanding the underlying structural mechanisms at the molecular level that are triggered by phosphorylation is still needed. A major reason why this information is still lacking is that the TnI cardiac NH_2-TnI (also known as N-extension) region is not present in the crystal structure of the cardiac Tn core complex [7]. In fact, no experimentally derived models of this region within the Tn complex are available.

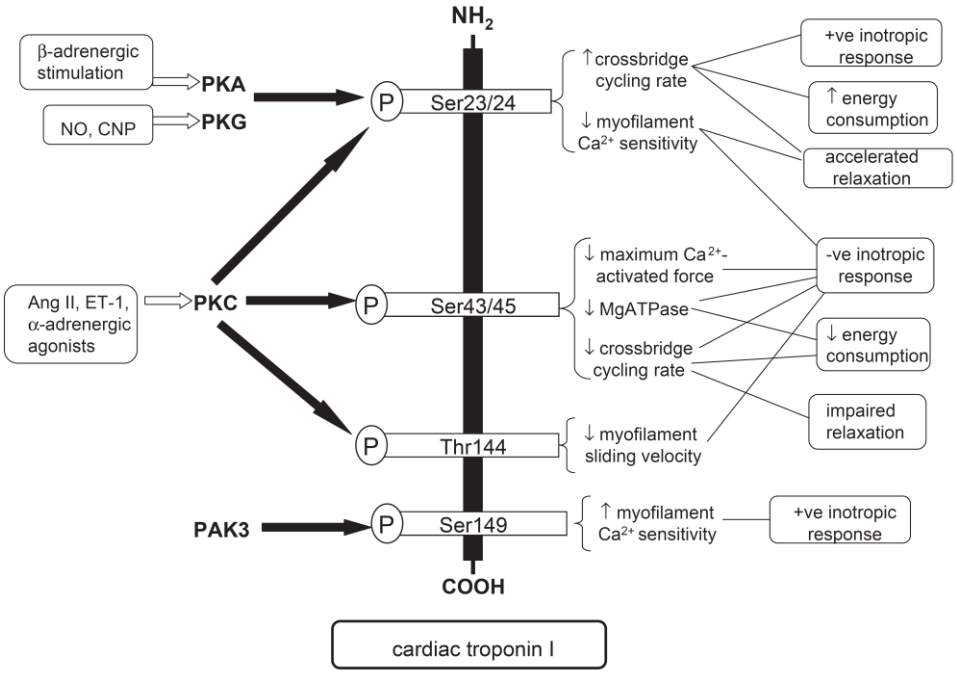

Figure 1.6 Schematic showing the major pathways involved in the physiological regulation of cardiac function through TnI phosphorylation. From the initial signal (*left*) received by the kinase (PKA, PKG, PKC or PAK3), this leads to phosphorylation of TnI at specific residues. Phosphorylation results in changes in myofilament properties, and alters the overall muscle or heart function as indicated on the *far right*. The contractile effects of TnI phosphorylation are determined by several factors: the combination of activated kinases; the specific sites phosphorylated; and the activities of protein phosphatases on the background of the other effects induced by the specific agonist in question e.g., the increase in Ca^{2+} transient amplitude and alteration in kinetics that occur with β-adrenergic stimulation. NH_2 and COOH indicate the amino and carboxy termini of TnI, respectively. Ang II=angiotensin II; ET-1=endothelin-1. Diagram from [27].

Tn is a large complex and dynamic protein with a considerable content of intrinsically disordered regions which together make it challenging for sample preparation and structural study. Hence, computational molecular modelling and molecular dynamics simulations have become the method of choice for understanding phosphorylation induced molecular changes. To date, only a few studies have investigated the impact of phosphorylation on the structural dynamics of Tn by proposing structural models. In the following section, the challenges and major findings of these studies have been summarized.

In 2007, Howarth *et al*. resolved the NMR structure of an isolated peptide representing the 32 residue TnI N-terminus, containing Ser22 and Ser23, in both the wild type (WT-unphosphorylated) and phosphorylated states [13]. Then, using docking methods, the interaction of each of the WT and phosphorylated NH_2-TnI with Tn was studied. In their study, the authors proposed that phosphorylation caused an extension of an helical motif at the end of the NH_2-TnI region which reduced the interactions between the N-domain of cTnC and NH_2-TnI of TnI. As a result, the first few acidic residues of the NH_2-TnI region were repositioned to interact with the positively-charged 'inhibitory' peptide region of TnI, defining a new and potentially significant interaction within troponin (**Figure 1.7**).

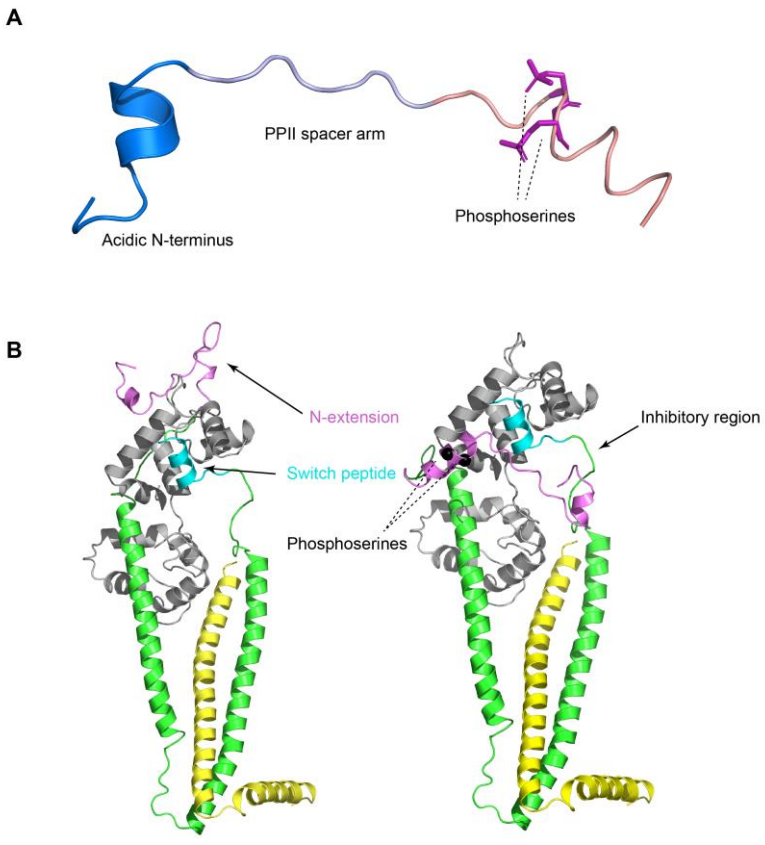

Figure 1.7 (A) The structure of the phosphorylated N-terminal extension peptide (drawn with Pymol using PDB 2JPW, [13]). The spacer arm region adopts a poly-proline type II helix (PPII). The two phosphorylated serine residues are colored purple. **(B)** Docking model for the effect of TnI S23/24 phosphorylation. TnC is coloured grey, TnI in green, and TnT in yellow. In the unphosphorylated state, it is proposed that the NH_2-TnI interacts with the N domain of TnC (*left*). In the phosphorylated

state, interactions between the NH_2-TnI and the N-domain of TnC are perturbed, and the acidic N terminus interacts with the basic residues of the inhibitory region of TnI.

In 2014, Hwang et al. studied the interaction of TnC with a 73 residue TnI fragment representing residues 1-73 [14]. In this study, the phosphorylation impact was not studied but significant interactions to explain the role of the TnI N-extension was proposed. First, TnI, via residues 39–60, interacted with the hydrophobic face of TnC C-domain, stabilizing an α-helix in TnI [residues 41-67]. Second, and in contrast to Howarth *et al*. (2007), they did not observe evidence for a helical structure for the N-extension of TnI. Rather, they reported that this region remains largely disordered while it interacts electrostatically with N-domain of TnC. The N-extension interaction with the TnC N-domain was proposed to indirectly increase Ca^{2+} sensitivity by optimizing the positioning of the N-domain of TnC to bind the TnI switch peptide (**Figure 1.8**). The authors suggested that phosphorylation at TnI Ser22 & 23 then disrupts this delicate arrangement. However, this hypothesis was not examined in this study.

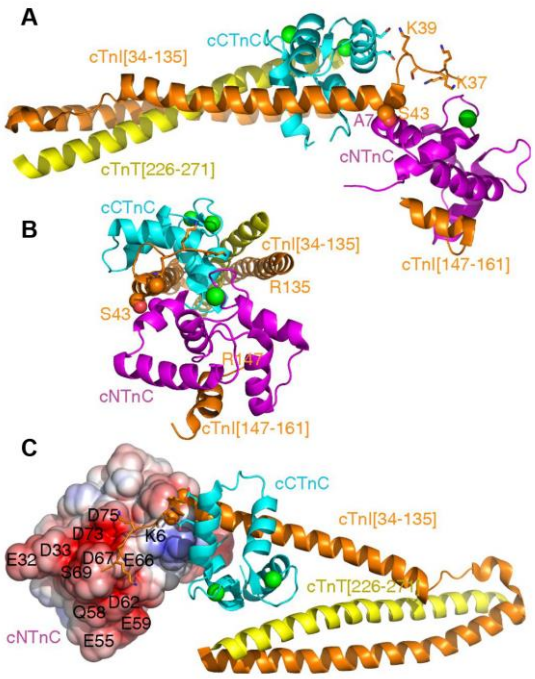

Figure 1.8 Ribbon structure of cardiac Tn (cTn) complex (PDB 1J1D [7]). N-domain of TnC is shown in magenta, and C-domain of TnC is shown in cyan. Ca^{2+} is shown as green spheres. Troponin T is shown in yellow. TnI, residues 34–135 and 147–161 (switch peptide), is shown in orange. (A & B) The key contact that fixes the position of TnC N-domain relative to TnC C-domain is between Ala7 of TnC N-domain and Ala42/Ser43 of TnI, as shown as space-filling spheres. The side chains of TnI residues 35 to 39 are also shown in sticks, with K39 of TnI contacting D131 and E135 of TnC C-domain (shown in sticks) and K35-S38 hovering over the TnC N-domain. (C) Electrostatic surface of TnC N-domain showing the negatively charged surface interacting with TnI residues 19–37. Image taken from [14].

In the same year, in a molecular dynamics (MD) study, Cheng *et al*. (2014) observed the formation of an intra-subunit interaction between the N-domain of TnI and the TnI inhibitory peptide due to phosphorylation [28]. In this study, missing residues in the previous model of Tn were built in, and so the final structure included residues TnC [1–161], TnI [1–172], and TnT [236–285]. This model was used as a starting structure in a MD simulation of 150 ns, where the Tn model was solvated in a rectangular box with at least 14 A distance between the molecule and its nearest periodic image. The NMR structure proposed by Howarth *et al*. was used for modeling of the missing residues of the TnI N-extension region. An increase in the Root Mean Square Fluctuation (RMSF) of residues in Site I and Site II of TnC, and in the

N-extension and switch peptide regions of TnI were observed (**Figure 1.9**). The three major findings of the study presented here are that phosphorylation: 1) did not affect the coordination of Ca^{2+} in site II; 2) significantly altered the TnC-TnI interactions, particularly for the inhibitory and switch peptide regions; and 3) led to the formation of an intra-subunit interaction between the N-extension and inhibitory regions of TnI. These results mostly supported the proposed model by Howarth *et al* (2007).

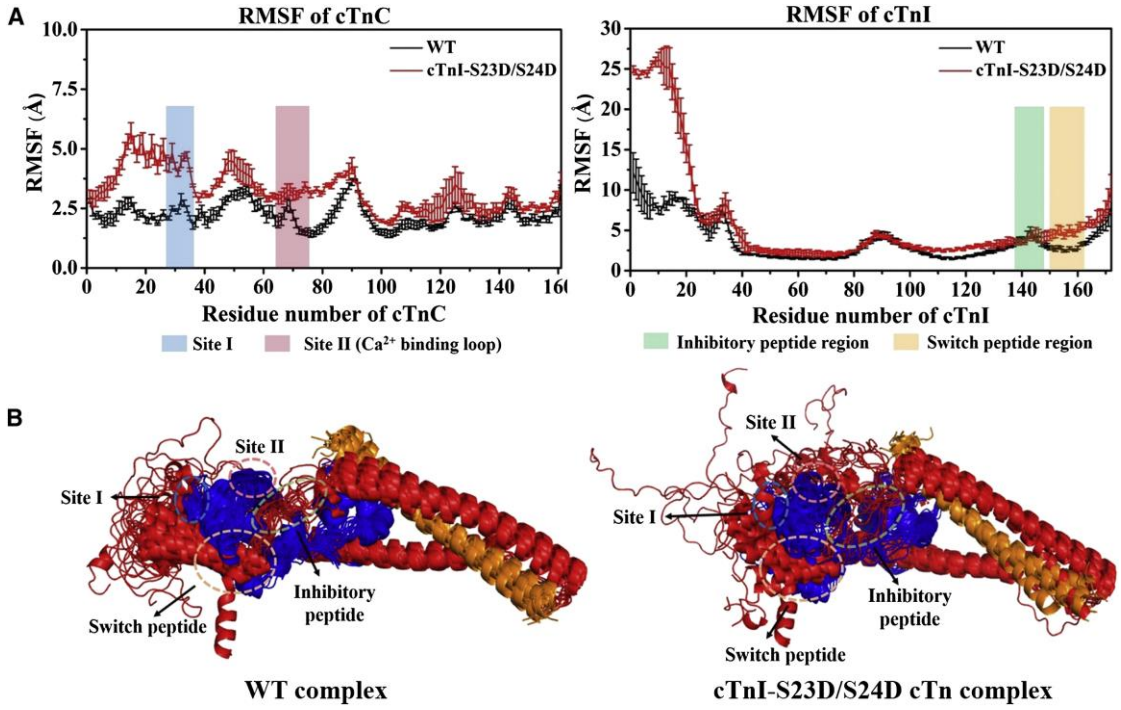

Figure 1.9 (A) Comparison of the Root Mean Square Fluctuation (RMSF) values of TnC and TnI for both the wild-type (WT, black) and phosphorylated Tn (S23D/S24D, red). Site I and Site II (the Ca^{2+} -binding loop) of TnC are highlighted in blue and pink, respectively. The inhibitory-peptide and switch peptide regions of TnI are highlighted in green and orange, respectively. **(B)** Superposition of snapshots extracted every 10 ns during 150 ns MD simulations for both WT and phosphorylated complexes. TnC is shown in blue, TnI is in red, TnT is in gold, and all key regions are highlighted with dashed circles Image from [28].

Two years later, Zamora *et al*. (2016) extended the previous MD model of Cheng *et al*. (2014) by improving the simulation parameters. In this new simulation, the authors used a 419

amino acid Tn model including residues TnC [1–161], TnI [1–171] and TnT [212–298] to perform the simulation for 750 ns in a 25 to 30 Å water box (**Figure 1.10**) [15]. In contrast to the previously published MD study, the RMSF analysis did not show any change in flexibility upon phosphorylation. In general, this study did not reproduce the earlier reported phosphorylation effects from Cheng et al. (2014) [28] of phosphorylation. In this new MD study, the intra-subunit interactions between the N-extension and inhibitory region of TnI were occasionally samples and are not phosphorylation dependent. Although some apparent phosphorylation-related changes were observed, they suggested that the structural and dynamic changes induced by phosphorylation could not be defined with any statistical significance using only a small number of independent MD trajectories of only a few hundred ns in length [15]. However, this study demonstrated a phosphorylation-induced loss of Ca^{2+} affinity due to the probability of out-of-coordination distances of residues in Site II. In addition, an interaction was observed between the C-domain of TnT and the inhibitory peptide and N-extension regions of TnI.

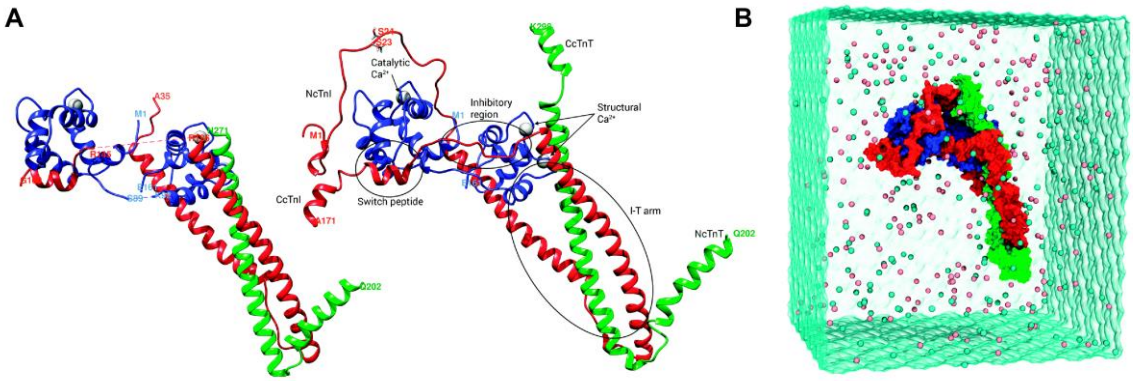

Figure 1.10 (A) Comparison of the X-ray structure of Tn core domain (PDB 1J1D, left) with the model used by Zamora *et al*. (2016) to perform the MD simulations (right). The most significant parts of the model are circled. TnC is coloured in blue, TnI in red, and TnT in green. **(B)** The WT system was solvated in a 25 Å water box. The three subunits are colored in the same way as in part A. Na^+ and Cl^- counter ions (shown as ice-blue/blue spheres) were added to mimic 150 mM ionic strength. Image from [29].

Although significant findings reported by these above NMR and MD studies, they all have their shortcomings. First, the experimental results were not obtained for the intact Tn complex. Also, computational methods are performed on a known structural model, and since the only available structure for cardiac Tn is in Ca^{2+} saturated state, these methods are not able to study phosphorylation effects in the Ca^{2+} free condition. **Chapter 4** of this Thesis therefore examines the effect of phosphorylation on the position of the N-extension region of TnI with respect to TnC. These experiments were performed in the intact Tn complex. Then, **Chapter 5** examines the position and dynamics of TnI switch peptide upon phosphorylation of Tn. Both these experiments provide structural information which has aided in the construction of a structural model describing the phosphorylation effects, for the first time, on the intact Tn complex.

1.7 Cardiomyopathy

Mutations in sarcomeric proteins are a leading cause for a wide variety of cardiac disease states. Cardiomyopathy is one prominent group of heart failure arising from mutations in all of the three subunits of Tn. Therefore, association of mutations in Tn with cardiac diseases, such as cardiomyopathy, is a driving force to better understand the structural nature of the Tn complex. The three main cardiomyopathies linked to mutations in Tn can be categorized as:

1. **Hypertrophic cardiomyopathy (HCM)** is a condition that causes morphological thickening of the ventricular walls of cardiac muscle. In HCM the thickening of the left ventricular wall causes left ventricular hypertrophy, which is also accompanied by cellular disarray within the myocardium [30]. Normal thickness of left ventricular hypertrophy is 12 mm or less, whereas in HCM patients, this thickness can be >15 mm and can reach up to 50 mm in extreme hypertrophy cases [31]. Cardiac hypertrophy leads to flow obstruction. The morbidity and premature death resulted from HCM has been estimated ~1 in 500 in the general population [32].

2. Dilated cardiomyopathy (DCM) is a condition where the heart becomes weakened and enlarged and cannot pump blood efficiently (systolic dysfunction). Approximately 25% to 35% of cases of DCM are familial, caused by mutations in genes encoding sarcomeric

proteins, including Tn subunits. DCM is most common in patients 40 to 59 years of age with an estimated prevalence of ~1 in 2500 [30].

3. Restrictive cardiomyopathy (RCM) is the least common type of cardiomyopathy with prevalence of 2% to 5% of cases. Although of unknown etiology, RCM causes myocardial stiffness, resulting in reduced blood flow due to restricted diastolic volume [30].

Table 1.2 Cardiac troponin subunits: genes, physiologic role and diseases caused by mutations (adapted from [6]). DCM, dilated cardiomyopathy; HCM, hypertrophic cardiomyopathy.

Protein	Gene	Physiological role / Features	Disease associations
Troponin T	*TNNT2*	Anchors troponin complex to tropomyosin	HCM, DCM, RCM
Troponin I	*TNNI3*	Inhibitory region maintains actin–tropomyosin in a blocked state preventing strong myosin binding	HCM, DCM, RCM
Troponin C	*TNNC1*	Binds the switch region of troponin I in a calcium-dependent manner to activate contraction	HCM and DCM

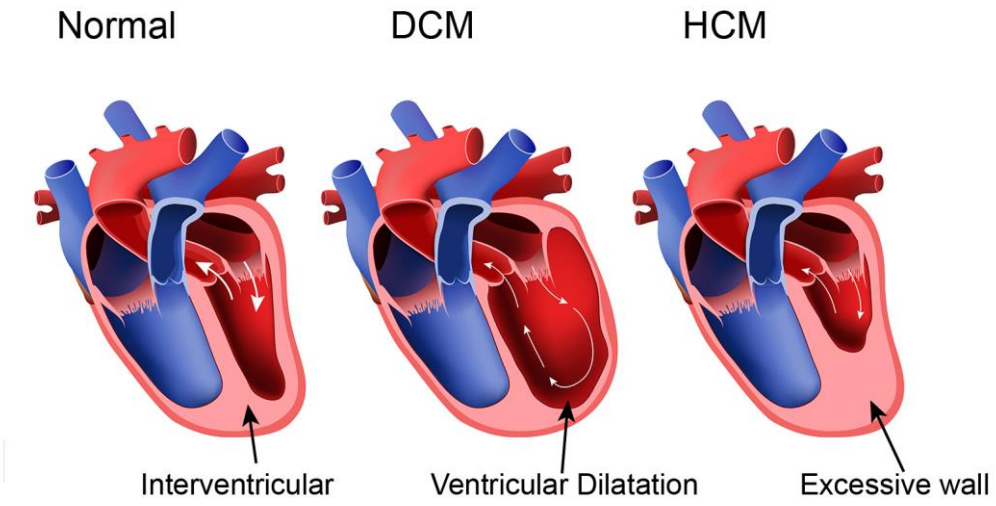

Figure 1.11 Schematic showing the types of cardiomyopathy phenotypes Figure taken from [33].

There are more than hundred identified mutations in the Troponin subunits which are associated with cardiomyopathy diseases. To date, six TnC mutations have been identified to be associated with HCM (A8V, L29Q, A31S, C84Y, E134D, D145E), and six other (Y5H, Q50R, E59D/D75Y, M103I, I148V, G159D) associated with DCM [34] (**Figure 1.12**). In general, mutations present on TnC could alter its function in two possible ways, either by altering its binding affinity for Ca^{2+} or by altering the interactions of TnC with its binding partners (Ca^{2+} sensitivity). During my PhD studies, I examined the structural effects arising from one of these HCM associated mutations - L29Q. L29Q is the first HCM associated mutation on TnC and the most extensively studied mutation amongst other mutations in TnC. L29Q is located the N-domain of TnC and at defunct site I. The functional impact of L29Q on the regulation of Tn complex is still controversial. There are similarities in structure, Ca^{2+} affinity, and Ca^{2+} sensitivity of force development or of ATPase activity between L29Q mutant and wild-type Tn. However, L29Q seems to abolish the effect of phosphorylation on Tn regulation. [34]. Therefore, conformational and interaction changes mediated by L29Q are of interest. The manuscript "*Characterization of the L29Q Hypertrophic Cardiomyopathy Mutation in Cardiac Troponin C by Paramagnetic Relaxation Enhancement Nuclear Magnetic Resonance*" was published and included in (***Appendix 1***).

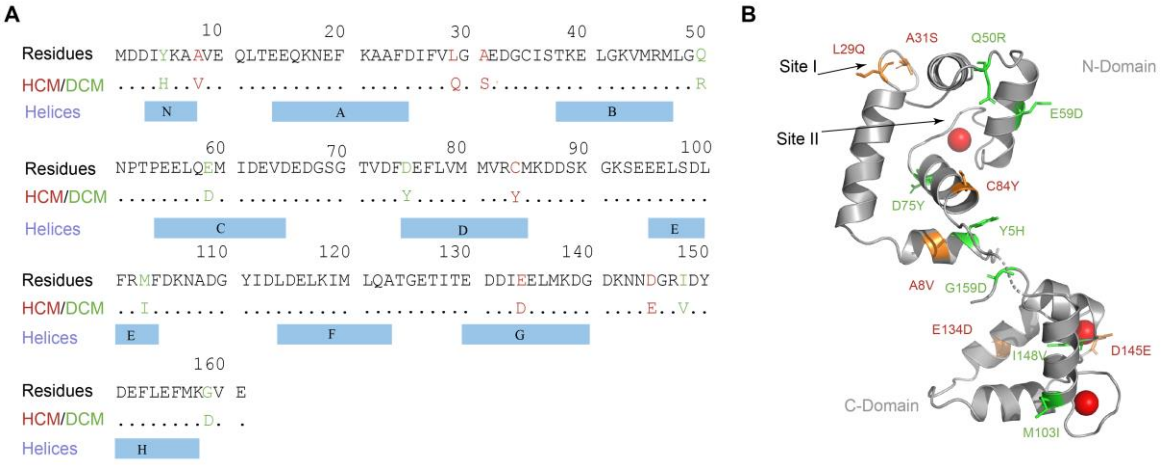

Figure 1.12 A) Amino acid sequence of human cardiac Troponin C. Below the sequence are shown the location of the HCM and DCM TnC mutations. The helices of TnC are indicated by blue boxes to show the location of the mutations with respect to the secondary structure of TnC. **B)** The location of

the HCM (orange) and DCM (green) mutations found in cardiac TnC are mapped onto the crystal structure (PDB 1J1D). Image adapted from [34].

1.8 Specific Aims

The overall aim is to obtain a structural picture of the dynamics of Tn complex upon phosphorylation. The specific aims are:

i. examination of the phosphorylation associated positioning of the cardiac specific TnI N-terminal region within Tn
ii. examination of phosphorylation associated changes in the position of the TnI regulatory region, known as the 'switch peptide'

But also, an aim of this project was to review the contributions of spin labeling to our understanding of muscle architecture, specifically troponin.

References

1. Vector, A.S. *Diagram showing types of muscle cells illustration* 2016; Available from: https://www.alamy.com/stock-photo-diagram-showing-types-of-muscle-cells-illustration-110524786.html.
2. Gordon, A.M., E. Homsher, and M. Regnier, *Regulation of contraction in striated muscle.* Physiol Rev, 2000. **80**(2): p. 853-924.
3. Knox, B., et al., *Biology: an Australian focus.* 2014 Australia: McGraw-Hill
4. Kontrogianni-Konstantopoulos, A., et al., *Muscle giants: molecular scaffolds in sarcomerogenesis.* Physiol Rev, 2009. **89**(4): p. 1217-67.
5. Flashman, E., et al., *Cardiac myosin binding protein C: its role in physiology and disease.* Circ Res, 2004. **94**(10): p. 1279-89.
6. Hwang, P.M. and B.D. Sykes, *Targeting the sarcomere to correct muscle function.* Nat Rev Drug Discov, 2015. **14**(5): p. 313-28.
7. Takeda, S., et al., *Structure of the core domain of human cardiac troponin in the Ca(2+)-saturated form.* Nature, 2003. **424**(6944): p. 35-41.
8. Vinogradova, M.V., et al., *Ca^{2+}-regulated structural changes in troponin.* Proc Natl Acad Sci U S A, 2005. **102**(14): p. 5038-43.
9. Sia, S.K., et al., *Structure of cardiac muscle troponin C unexpectedly reveals a closed regulatory domain.* J Biol Chem, 1997. **272**(29): p. 18216-21.
10. Slupsky, C.M. and B.D. Sykes, *NMR solution structure of calcium-saturated skeletal muscle troponin C.* Biochemistry, 1995. **34**(49): p. 15953-64.
11. Marston, S. and J.E. Zamora, *Troponin structure and function: a view of recent progress.* J Muscle Res Cell Motil, 2019.
12. Solaro, R.J., M. Henze, and T. Kobayashi, *Integration of troponin I phosphorylation with cardiac regulatory networks.* Circ Res, 2013. **112**(2): p. 355-66.
13. Howarth, J.W., et al., *Phosphorylation-dependent conformational transition of the cardiac specific N-extension of troponin I in cardiac troponin.* J Mol Biol, 2007. **373**(3): p. 706-22.
14. Hwang, P.M., et al., *The cardiac-specific N-terminal region of troponin I positions the regulatory domain of troponin C.* Proc Natl Acad Sci U S A, 2014. **111**(40): p. 14412-7.
15. Zamora, J.E., et al., *Troponin structure: its modulation by Ca^{2+} and phosphorylation studied by molecular dynamics simulations.* Phys Chem Chem Phys, 2016. **18**(30): p. 20691-707.
16. Van Eyk, J.E., et al., *Distinct regions of troponin I regulate Ca^{2+}-dependent activation and Ca^{2+} sensitivity of the acto-S1-TM ATPase activity of the thin filament.* J Biol Chem, 1997. **272**(16): p. 10529-37.
17. Schaertl, S., S.S. Lehrer, and M.A. Geeves, *Separation and characterization of the two functional regions of troponin involved in muscle thin filament regulation.* Biochemistry, 1995. **34**(49): p. 15890-4.
18. Chandy, I.K., J.C. Lo, and R.D. Ludescher, *Differential mobility of skeletal and cardiac tropomyosin on the surface of F-actin.* Biochemistry, 1999. **38**(29): p. 9286-94.
19. Leavis, P.C. and J. Gergely, *Thin filament proteins and thin filament-linked regulation of vertebrate muscle contraction.* CRC Crit Rev Biochem, 1984. **16**(3): p. 235-305.
20. Wu, S., et al., *Structural changes in isometrically contracting insect flight muscle trapped following a mechanical perturbation.* PLoS One, 2012. **7**(6): p. e39422.
21. Mittmann, K., K. Jaquet, and L.M. Heilmeyer, Jr., *A common motif of two adjacent phosphoserines in bovine, rabbit and human cardiac troponin I.* FEBS Lett, 1990. **273**(1-2): p. 41-5.
22. al-Hillawi, E., et al., *The effects of phosphorylation of cardiac troponin-I on its interactions with actin and cardiac troponin-C.* Eur J Biochem, 1995. **228**(3): p. 962-70.

23. Ayaz-Guner, S., et al., *In vivo phosphorylation site mapping in mouse cardiac troponin I by high resolution top-down electron capture dissociation mass spectrometry: Ser22/23 are the only sites basally phosphorylated.* Biochemistry, 2009. **48**(34): p. 8161-70.
24. Dong, W.J., et al., *Effects of PKA phosphorylation of cardiac troponin I and strong crossbridge on conformational transitions of the N-domain of cardiac troponin C in regulated thin filaments.* Biochemistry, 2007. **46**(34): p. 9752-61.
25. Robertson, S.P., et al., *The effect of troponin I phosphorylation on the Ca^{2+}-binding properties of the Ca^{2+}-regulatory site of bovine cardiac troponin.* J Biol Chem, 1982. **257**(1): p. 260-3.
26. Solaro, R.J., A.J. Moir, and S.V. Perry, *Phosphorylation of troponin I and the inotropic effect of adrenaline in the perfused rabbit heart.* Nature, 1976. **262**(5569): p. 615-7.
27. Layland, J., R.J. Solaro, and A.M. Shah, *Regulation of cardiac contractile function by troponin I phosphorylation.* Cardiovasc Res, 2005. **66**(1): p. 12-21.
28. Cheng, Y., et al., *Computational studies of the effect of the S23D/S24D troponin I mutation on cardiac troponin structural dynamics.* Biophys J, 2014. **107**(7): p. 1675-85.
29. Zamora, J.E., et al., *Troponin structure: its modulation by Ca^{2+} and phosphorylation studied by molecular dynamics simulations.* Phys Chem Chem Phys, 2016. **18**(30): p. 20691-20707.
30. Brieler, J., M.A. Breeden, and J. Tucker, *Cardiomyopathy: An Overview.* Am Fam Physician, 2017. **96**(10): p. 640-646.
31. Maron, B.J., B.W. Gross, and S.I. Stark, *Images in cardiovascular medicine. Extreme left ventricular hypertrophy.* Circulation, 1995. **92**(9): p. 2748.
32. Maron, B.J., *Hypertrophic cardiomyopathy: a systematic review.* JAMA, 2002. **287**(10): p. 1308-20.
33. Lopes, L.R. and P.M. Elliott, *A straightforward guide to the sarcomeric basis of cardiomyopathies.* Heart, 2014. **100**(24): p. 1916-23.
34. Kalyva, A., et al., *Biochemical characterisation of Troponin C mutations causing hypertrophic and dilated cardiomyopathies.* J Muscle Res Cell Motil, 2014. **35**(2): p. 161-78.

1.9 Review paper

This review paper '*Constructing a structural model of troponin using site-directed spin labeling: EPR and PRE-NMR'* was written by myself and published in 2019 in the '*Biophysical Reviews*' Journal. Images 1, 2, and 9 were drawn by the co-author Dr. Nicole Cordina. All other images were prepared by myself.

Pages 27-45 of this thesis have been removed as they contain published material. Please refer to the following citation for details of the article contained in these pages:

Kachooei, E., Cordina, N.M. and Brown, L.J., 2019. Constructing a structural model of troponin using site-directed spin labeling: EPR and PRE-NMR. *Biophysical reviews*, *11*(4), pp.621-639.

2. Materials and Methods

This Chapter covers the materials, basic molecular biology, cell biology, protein chemistry and spectroscopy techniques used to obtain all the required muscle protein components used in this Thesis. An overview of the experimental procedures performed to obtain the NMR and EPR distance constraints are presented in the flow diagram shown in **Figure 2.1**.

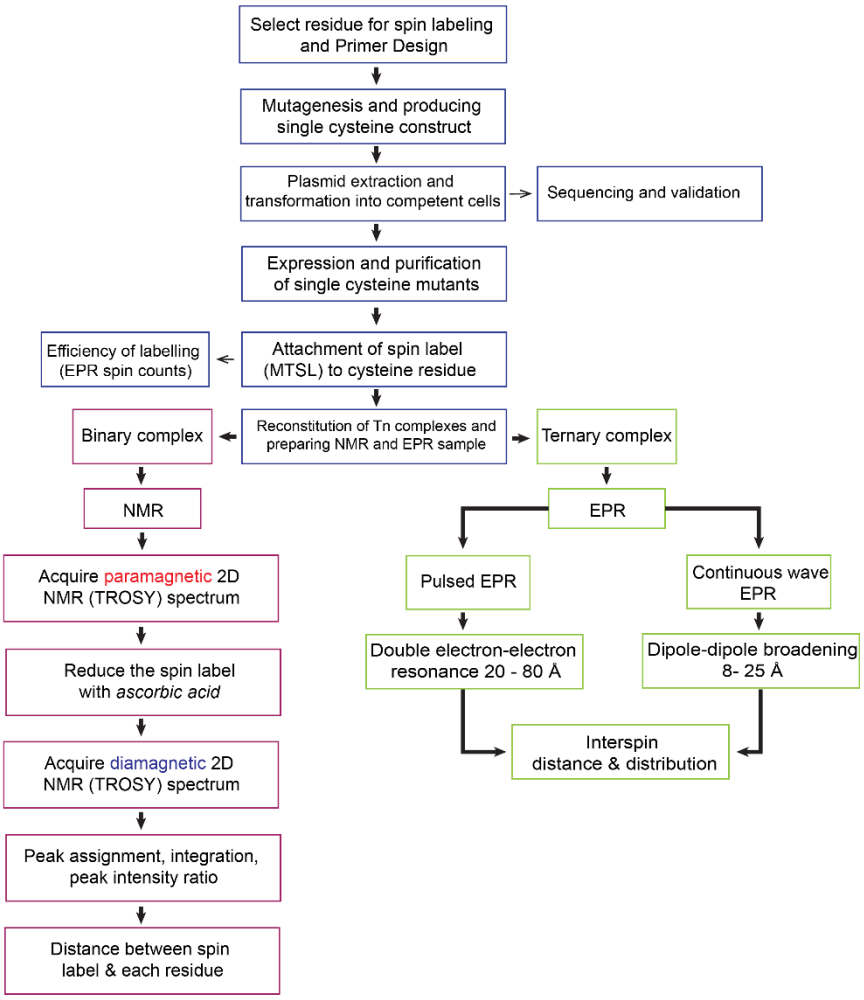

Figure 2.1 An overview of the steps and methods used in this Thesis.

2.1 Materials and General Methods

2.1.1 Chemicals

All chemicals used in this project were of analytical grade or higher, unless otherwise specified. All solutions were prepared using water, purified by reverse osmosis, followed by organic filtration (Milli-Q). Media and purified water used for cloning methods and bacterial growth were autoclaved at 1.5 kg f cm^{-2} for 20 minutes at 121°C. Heat liable solutions (including antibiotics and Isopropyl β-D^{-1}-thiogalactopyranoside (IPTG)), minerals, dithiothreitol (DTT), $^{15}NH_4Cl$, and glucose were all filter sterilised by passing the solution through a sterile 0.22 µM filter unit (Millex). Stock solutions were stored at -20°C.

2.1.2 Media Components

Terrific Broth (TB) (Sigma-Aldrich) was used for the expression all TnC and TnI recombinant protein constructs and was prepared with the addition of 2% glycerol, as per manufacturer's instructions. All other small-scale bacterial culture growths (< 5 mL) used for plasmid purification of all newly constructed mutants and for glycerol stock preparation of mutants created by mutagenesis were performed in Luria-Bertani (LB) media (10 g L^{-1} tryptone, 5 g L^{-1} yeast extract, 5 g L^{-1} NaCl and 50 µg mL^{-1} carbenicillin). LB media was also used for TnT recombinant protein expression.

LB agar plates required for colony selection during transformation were prepared by adding 15 g L^{-1} agar to the LB media. Filter-sterilised antibiotics (carbenicillin or ampicillin) were added to the LB-agar after it was autoclaved and left to cool to < 50°C. For plasmid transformation of site-directed mutants into *E.coli* cells, NZY+ broth (5 g L^{-1} NaCl, 2 g L^{-1} $MgSO_4$, 5 g L^{-1} yeast extract and 10 g L^{-1} NZ amine) or SOC medium (20 g L^{-1} tryptone, 5 g L^{-1} yeast extract, 0.4 mM NaCl, 2.5 mM KCl, 10 mM $MgCl_2$, 10 mM $MgSO_4$ and 2% (v/v) glucose) was used.

M9 Minimal Media was used for the recombinant expression of ^{15}N-labeled proteins required for NMR. The M9 recipe was that of Sambrook *et al* (1989) [1] and contained 2.5 g L^{-1} glucose and 1 g L^{-1} $^{15}NH_4Cl$. Minimal media used for starter cultures contained 5 g L^{-1} glucose and 1 g L^{-1} $^{15}NH_4Cl$.

2.1.3 DNA & Protein Quantification

2.1.3.1 Protein Assay

An accurate measure of protein concentrations was required in order to determine the percentage of spin labeling of the protein and to assess the reconstitution of the Tn complex. Protein concentrations were determined using the BCA (bicinchoninic acid) Protein Assay Kit (Quantum Scientific), following the manufacturer's instructions. Initially, a standard curve was prepared using known concentrations of bovine serum albumin (BSA). The BCA reagent solution was added to both the standards and protein samples of unknown concentrations. After 30 mins incubation at room temperature, a colour change induced by the BCA reagent in the presence of protein, enabled the absorbance at 562 nm to be measured using a Varian Cary 50 Bio UV-Vis spectrophotometer. A standard curve was constructed from the absorption at 562 nm for the BSA standards. Using the standard curve, the concentrations of the 'unknown' protein samples were then determined. Protein concentrations (*c*) were also determined by UV-Vis spectroscopy using a Nanodrop spectrometer (Thermo Scientific) when a known extinction coefficient (ε) was applied in conjunction with the Beer-Lambert law:

$$A = \varepsilon . c . l \qquad \text{Eqn 2.1}$$

where A = absorption; ε = extinction coefficient specific to the wavelength measured (L g^{-1} cm^{-1}); c = concentration (g L^{-1}); and l = path length (cm). The ε values for a protein can be estimated from its amino acid composition [2]. In this thesis, the ε values were calculated with help of *ProtParam tool*, ExPASy**.**

2.1.3.2 UV-VIS Spectroscopy & DNA Quantification

The quantity and quality of plasmid or amplified DNA required for sequencing and mutagenesis was determined by measuring the absorbance of DNA at 260 nm and 280 nm. The absorbance signal at 260 nm is mostly due to nucleotide bases, whereas a high absorbance at 280 nm is due predominately to protein contamination. A DNA sample with a 260 nm/280 nm ratio of ~1.8 was judged to be of high quality. For DNA quantitation, the Beer-Lambert law was also used, as follows:

$$c = A.\varepsilon/l \qquad \text{Eqn 2.2}$$

where c = nucleic acid concentration (ng μL^{-1}); ε = extinction coefficient for double stranded DNA (50 ng cm μL^{-1}); A = absorbance, and l = path length (cm).

2.1.3.3 Sodium dodecyl sulphate-polyacrylamide gel electrophoresis (SDS-PAGE)

Sodium dodecyl sulphate-polyacrylamide gel electrophoresis (SDS-PAGE) is an important technique used for confirming the protein expression and assessing the purity of all protein samples during purification processes. It also helps in judging the stoichiometry of the reconstituted Tn complexes required for this project. SDS is an anionic detergent that solubilises, partially denatures, and coats the protein with a negative charge. The concentration of acrylamide and its cross-linker, bis-acrylamide, determines the pore size of the gel matrix. Amresco 12.5% Acrylamide NEXT-gels, with a separation range of 3.5 kDa to 100 kDa, were utilized in this work; and prepared as per the manufacturer's instructions. Prior to loading, protein samples were prepared by boiling for two minutes in suspension buffer containing 5% (v/v) β-mercaptoethanol, 2.5% (w/v) SDS, 10% glycerol (v/v), 0.01% bromophenol blue (w/v) and 50 mM Tris-HCl pH 6.8 to reduce disulphide bonds. Gels were electrophoresed at 170V for ~60 mins (or until the bromophenol blue tracking dye reached the bottom of the gel). The Benchmark Protein Ladder (Invitrogen) was used as the marker for molecular weight estimation of proteins in all gels. On completion of electrophoresis, gels were stained with 0.1% Coomassie brilliant blue stain in 40% methanol and 10% acetic acid for approximately 1 h. Gels were then destained with a solution of 40% methanol and 10% acetic acid overnight with 1-2 changes.

2.2 Bacteria and Expression Vectors

The pET-3d expression vector (Novagen), containing rat cardiac TnC (99% identical to human cTnC) [3], and rat cardiac TnI construct (92% identical to human cTnI) [4, 5], were used. The 'cysteine-less' constructs of each clone were already available in the laboratory (originally constructed by the research group of Prof H Cheung, University of Birmingham, USA). For TnI, this required mutagenesis of the native cysteine residues at positions 81 and 98 to serine residues (C81S, C98S). It was also found that the original cTnI construct obtained from the Cheung group was found to inadvertently contain two point mutations (K178E, K183R).

These residues were corrected using the QuikChange II site-directed mutagenesis kit. All experiments performed in this Thesis were done using this corrected TnI construct [6]. For TnC, the native cysteine residues at positions 35 and 84 were mutated to serine residues (C35S, C84S). All TnC and TnI constructs were expressed recombinant *E coli* BL21(DE3) cells (Novagen, Merck).

The pET-28a expression vector (Novagen), containing the rat cardiac TnT clone (89% homology to human cardiac TnT), with a thrombin-cleavable N-terminal 6 x his-tag was already available in the laboratory [6]. In this construct, four rare arginine codons present in the TnT clone at amino acids 167/168 and 216/217 were mutated from AGG/AGG to CGT/CGT. *E. coli* Rosetta cell line (DE3) pLys (Novagen) was used to express the TnT protein to high levels.

2.2.1 Site-Directed Mutagenesis

Site-directed mutagenesis is a simple tool for introducing targeted changes into the plasmid constructs for subsequent protein expression. Mutagenesis using the Quikchange® II Site-Directed Mutagenesis Kit (Stratagene) was done to generate mono cysteine mutants or double cysteine mutants of TnC or TnI for subsequent modification with the sulfhydryl-specific spin labeling reagent 'MTSL'. In brief, following the primer design guidelines in the Quikchange instruction manual, the forward and reverse complementary primers containing the desired mutation were designed to anneal to the cysteine-less TnC or TnI plasmid templates. The primers were designed to be between 24 – 45 bases in length (*N*) with a melting temperature of ≥78°C; as calculated by the following formula:

$$Melting\ temperature = 81.5 + 0.41(\%GC) - 675/N - \%mismatch \quad \text{Eqn 2.4}$$

Table 2.1 Components for site-directed mutagenesis reaction

Component	Amount/Reaction
10X reaction buffer	5 µL
ds DNA template	~50 ng
Primer #1 (forward)	125 ng
Primer #2 (reverse)	125 ng
dNTP mix	1 µL
ddH2O	To final volume of 50 µL
Pfu Turbo	1 µL (2.5 U µL-1)

Mutations were introduced onto the templates of the cysteine-less TnC and TnI expression vectors. The mutation to be introduced was designed to be located towards the middle of the primer with 10 to 15 correct bases on either side. The primers were also terminated in at least one G or C base; and designed to contain a minimum GC content of 40%. PCR reactions were prepared, as per **Table 2.1**, and the PCR reaction performed using a Bio-Rad iCycler™, as per **Table 2.2**.

After 18 cycles of logarithmic amplification, 1 µL of the restriction enzyme Dpn I (10 U μL^{-1}) was then added to each amplification reaction. After gentle mixing of the solution, the reaction was incubated at 37°C for 1 h to digest the parent template. The newly synthesised TnC or TnI vector containing the introduced cysteine(s) at the desired location(s) remained intact and was transformed into cell lines, as detailed below in Section 2.2.2.

Table 2.2 PCR program for site-directed mutagenesis of TnC and TnI single and double cysteine mutants.

Cycles	Temperature	Time
1	95°C	30 sec
18	95°C	30 sec
	55°C	1 min
	68°C	10.5 mins

2.2.2 Vector Product Transformation

For transformation of the PCR generated vector into *E.Coli* XL1-Blue super competent cells, LB-ampicillin agar plates were prepared (Section 2.1.2). Super competent cells were gently thawed on ice from -80°C. To each amplification reaction, 50 µL of competent cells were transferred into a pre-chilled microtube. The undigested plasmid mutagenesis product was

transferred (1 – 2 µL) to the cells and gently mixed. A control reaction of 1 – 2 µL of ddH_2O, in place of the mutagenesis vector, was performed to confirm the selectivity of the antibiotics. After incubation on ice for 30 mins, the cells were heat shocked at exactly 42°C for 45 sec in a water bath. The cells were cooled on ice for 2 mins and 0.5 mL of pre-warmed (42°C) NZY+ broth was added to the cells and further incubated for 1 h with shaking (220 rpm, 37°C). The transformations were then plated as either 'high' or 'low' concentrations (250 µL or 150 µL transformation reaction, respectively) onto LB-ampicillin (50 µg mL^{-1}) agar plates. The LB-agar plates were incubated overnight at 37°C.

2.2.3 Plasmid Extraction

From the *E. coli* colony growths on the plasmid mutagenesis plates, the newly created cysteine mutant plasmids were extracted as per manufacturer's instructions using a QIAprep® Miniprep plasmid kit (QIAGEN Pty Ltd). In brief, 5 mL of LB-amp (50 µg mL^{-1}) media was inoculated with a single colony from the plasmid mutagenesis plates and incubated overnight with shaking (170 rpm, 37°C). Approximately 4 mL of the overnight culture was used for plasmid extraction. Elution of the plasmid from the QIAprep® Miniprep columns was achieved with ddH_20 (50 µL). Prior to sequencing, the concentrations of the purified plasmids were determined by UV-Vis spectrophotometry, as described before. A minimum of 2 colonies from each mutagenesis reaction were selected from the LB-plates for plasmid purification and subsequent DNA sequencing analysis.

2.2.4 DNA Sequencing of Plasmid Constructs

The quantified plasmid was submitted for sequencing to Macrogen Inc (South Korea). Sample preparation required the addition of 200 – 500 ng of double-stranded plasmid DNA and 3.2 pmol of a sequencing primer. The T7 promoter sequencing primer (5'-AAATTAATACGACTCACTATAGGG-3'), specific for the pET expression vector was used for sequencing in the 5' to 3' direction. The T7 pET terminator primer (5'-GCTAGTTATTGCTCAGCGG-3') was used to sequence in the reverse 3' to 5' direction. Using both sequencing primers allowed for 100% coverage of the DNA for both the TnI and TnC sequences.

2.2.4.1 TnI Monocysteine and Pseudo-phosphorylated Constructs (S22/23D)

Site-directed mutagenesis was performed, as per Section 2.2, to create the following TnI single cysteine mutants: S5C, S28C, S39C, A151C, and L159C onto the cardiac TnI cysless template. All the mono cysteine TnI constructs are referred to herein as I5, I28, I39, I151 and I159. Site directed mutagenesis was also performed to mimic the effects of phosphorylation of the cardiac specific N-extension region. These 'pseudo'-phosphorylated forms of the mono cysteine TnI constructs were generated by mutating the phosphorylated serine residues in the N-extension region to aspartic acid (S22D, S23D). Pseudo phosphorylated mutants were done for all TnI single cysteine constructs. These TnI mutant constructs are referred to as $TnI5_{S22/23D}$, $TnI28_{S22/23D}$,$TnI39_{S22/23D}$, $TnI151_{S22/23D}$, and $TnI159_{S22/23D}$ where the number refers to the location of the cysteine residue (***Chapters 4 & 5***).

2.2.4.2 TnC Monocysteine Constructs

Site-directed mutagenesis was performed on the TnC cys-less clone to generate the mono cysteine constructs used in this work (S35C, S84C) and here in referred to as TnC35 and TnC84 (***Chapter 4 & 5***). The other mono cysteine TnC constructs was hypertrophic cardiomyopathy mutation L29Q. The L29Q mutation was introduced onto the TnC84 template to create a single cys mutation (***Appendix 1***).

2.2.5 Transformation of TnC and TnI plasmids for Protein Expression

The verified sequences of all TnC and TnI constructs were transformed into *E.coli* competent BL21(DE3) cells (Novagen) for protein expression with the addition of 80 µL of pre-warmed SOC before incubation. The transformation product was plated onto LB agar plates containing 50 µg mL^{-1} carbenicillin and incubated overnight at 37°C. Single colonies were chosen to inoculate individual 5 mL cultures of LB broth (50 µg mL^{-1} carbenicillin), which were then incubated at 37°C for 4-5 h with 220 rpm shaking. Glycerol stocks were prepared by mixing 1 mL of the overnight culture with 1 mL of autoclaved glycerol before storing at -80°C.

2.3 Protein Purification

2.3.1 TnC Purification

2.3.1.1 Large Scale Expression & Purification of TnC for EPR

Large-scale expression (~1 L) and purification of wild-type TnC, single TnC cysteine mutants or the cys-less TnC construct was performed. In brief, 5 × 5 mL cultures of TnC (TB + 50 µg mL^{-1} carbenicillin) were inoculated either directly from transformation plates or glycerol stocks and incubated for 4 – 5 h at 170 rpm (37°C). 6 mL of the combined cultures were then distributed into 4 × 1 L conical flasks containing 250 mL TB + 50 µg mL^{-1} carbenicillin. The cells were then further grown overnight at 37°C with shaking at 120 rpm. Cells were then pelleted by centrifugation (9 820 x g, 12 mins, and 4°C) and the supernatant discarded. The pelleted cells from the large-scale expression were re-suspended in 5 to 10 mL/gram wet pellet weight of Buffer A (0.1 M NaCl, 1 mM DTT, 5 mM $CaCl_2$ and 50 mM Tris pH 7.5). The resuspended cells were sonicated for ~5 mins in a Branson 450 sonifier by using a tapered micro tip of ¼" at an amplitude setting of 50% and an instrument power output control value of 6. Sonicated cells were then centrifuged at 30 966 x g for 20 mins at 4°C; and the pellet waste discarded. $CaCl_2$ was then added to the supernatant, containing the soluble TnC, to a final concentration of 10 mM. The supernatant was further dialysed against 500 mL of Buffer A at 4°C for 2 h with a complete buffer change after 1 h.

The dialysed sample was loaded onto a 1.5 cm × 15 cm Phenyl Sepharose 6B column (Pharmacia, GE Healthcare) equilibrated with Buffer A and run at 3.5 mL min^{-1}. Nonspecific bound proteins were eluted with a high salt wash Buffer B (0.2 M NaCl, 1 mM DTT, and 50 mM Tris pH 7.5). Elution of TnC was achieved by the application of Buffer C (0.2 M NaCl, 1 mM DTT, 10 mM EDTA and 50 mM Tris pH 7.5) to the column. The application of EDTA results in the chelation of Ca^{2+} from TnC. Addition of EDTA 'closes' the hydrophobic binding pocket of TnC and, as a result, disrupts the hydrophobic interaction of TnC with the phenyl sepharose resin (**Figure 2.2 A**).

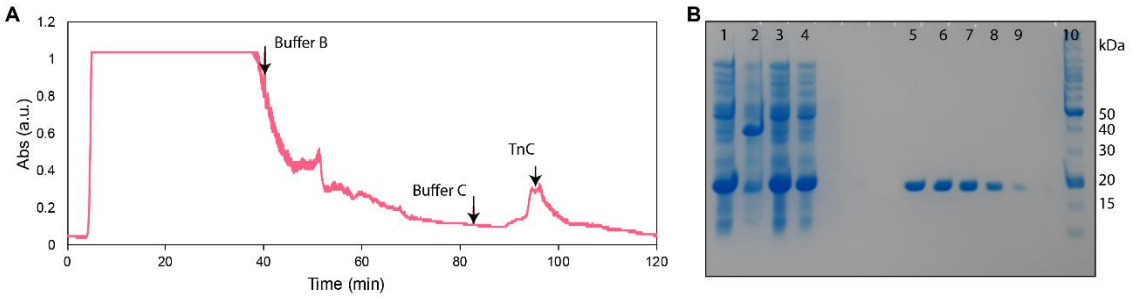

Figure 2.2 TnC Purification: **(A)** Elution profile of TnC from phenyl sepharose column (1.5 x 15cm, 3.5 mL min^{-1} flow rate). Weakly bound proteins were eluted with salt wash (Buffer B) and TnC was eluted with 10 mM EDTA salt wash (Buffer C). **(B)** SDS-PAGE of expression and purification of TnC. Lane 1, expression of TnC from overnight growth. Lane 2, insoluble fraction. Lane 3, soluble fraction. Lane 4, soluble fraction after dialysis. Lanes 5-9, purified TnC fractions (taken from peak eluting between 90 – 100 mins in panel A). Lane 10, Benchmark ladder. Time of application of Buffer B and Buffer C to the column is indicated by the arrows.

Column fractions were collected and the purity and content of each fraction assessed using SDS-PAGE (**Figure 2.2 B**). The fractions containing TnC were pooled. Pure TnC fractions were concentrated using an Amicon Ultra-15 centrifugal filtration device and protein concentrations determined using a BCA Assay Kit, as described in Section 2.1.3.1.

2.3.1.2 Large Scale Expression & Purification of TnC for NMR

For NMR, TnC mutants were expressed in M9 minimal media containing 2.5 g L^{-1} glucose and 1 g L^{-1} $^{15}NH_4Cl$, as described by Sambrook *et al* (1989) [1]; and using the IPTG (β-D-1-

Thiogalactopyranoside) induction protocol of Studier *et al* (1990) [7]. Four 10 mL starter cultures (M9 minimal media containing 5 g L^{-1} glucose and 50 µg mL^{-1} carbenicillin) were inoculated from transformation plates and incubated at 37°C with 170 rpm shaking overnight (~16 - 18 h). The starter cultures were then pooled for inoculation into 4 × 250 mL cultures of M9 minimal media containing 2.5 g L^{-1} glucose and 50 µg mL^{-1} carbenicillin. The cultures were incubated at 37°C with 170 rpm shaking until an optical density at 600 nm of 0.8. This typically took approximately 3 - 4 h of growth. At this optical density, TnC expression was induced by the addition of IPTG to 1 mM. After 3 h of expression, cells were harvested by centrifugation (9 820 x g, 12 mins, and 4°C), and then, resuspended in 20-30 mL

of Phenyl Sepharose Buffer A. The TnC protein was then purified using Phenyl Sepharose 6B column, as described above.

2.3.2 Large Scale Expression & Purification of TnI

Following transformation of the TnI cysteine constructs, the large-scale expression (~ 1 L) and purification of TnI constructs was performed. For TnI expression, 5 × 5 mL cultures (TB + 50 µg mL^{-1} carbenicillin) was inoculated either directly from transformation plates or glycerol stocks and incubated for 4 – 5 h at 37°C with shaking at 170 rpm. The cultures were then combined and distributed into 4 × 1 L conical flasks containing 250 mL TB + 50 µg mL^{-1} carbenicillin. The cells were grown overnight at 37°C with shaking at 120 rpm. Cells were pelleted by centrifugation (9 820 x g, 12 mins, and 4°C) and the supernatant discarded. Cell pellets from the large-scale expression of TnI were resuspended in ice-cold Lysis Buffer (1 mM DTT, 1 mM EDTA, Roche complete EDTA-free protease inhibitor cocktail and 40 mM Tris pH 8.0) at 10 mL/gram wet pellet weight. The cells were then sonicated for ~6 mins. The lysed cells were then centrifuged (30 966 × g, 20 mins, and 4°C) where the insoluble TnI inclusion bodies were separated from the soluble proteins in the cell lysate. The pellet containing insoluble TnI inclusion bodies was re-suspended in approximately 30 mL of Buffer A (6 M urea, 1 mM DTT, 1 mM EDTA and 20 mM Tris pH 8.0) and dialysed against ~500 mL of Buffer A overnight at 4°C with one complete buffer change. The dialysed sample was then clarified by centrifugation (30 966 x g, 20 mins, and 4°C) and the supernatant containing TnI was applied to a 1.5 cm × 15 cm Carboxy-Methyl (CM)- Sepharose column (Pharmacia, GE Healthcare). The CM-Sepharose column was equilibrated with Buffer A, at a flow rate of 2 mL min^{-1} and fractions were collected every 4 mins. Following sample loading onto the column, Buffer A was washed through the column until the absorbance (at 280 nm) returned to baseline (**Figure 2.3 A**). TnI was eluted with a linear NaCl gradient from 0 M NaCl to 0.3 M NaCl. Following the application of the salt gradient, 100% of high salt Buffer B was used to elute any remaining contaminating proteins from the column. Samples were run on an SDS-PAGE and fractions containing purified TnI were pooled (**Figure 2.3 B**) and stored at -20°C.

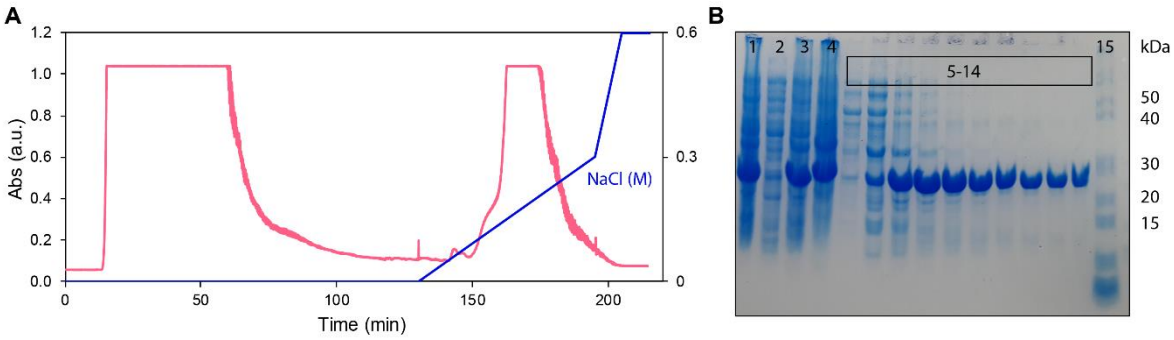

Figure 2.3 TnI Purification: (A) Elution profile of TnI from carboxymethyl (CM)-Sepharose column (1.5 x 15cm, 2 mL min-1 flow rate). TnI was eluted with a linear NaCl gradient and the fractions were collected at ~0.2 M NaCl and analysed by SDS-PAGE. (B) SDS-PAGE of expression and purification of TnI. Lane 1, sonicated cells. Lane 2, soluble fraction. Lane 3, insoluble fraction. Lane 4, insoluble fraction after overnight dialysis. Lanes 5 to 14 contain TnI fractions obtained from the peak eluted between 150-190 min in panel A.

2.3.3 Large scale Expression & Purification of TnT

The TnT clone was transformed into competent *E. coli* BL21(DE3)pLys cells as described in Section 2.2.5. Five 8 mL cultures (LB + 15 µg mL^{-1} kanamycin) were inoculated from transformation plates for overnight growth at 37°C at 190 rpm (~16 - 18 h). The overnight cultures were pooled and distributed into 6 × 500 mL flasks each containing 125 mL LB +15 µg mL^{-1} kanamycin. Cells were grown at 30°C, 220 rpm for ~2.5 h and then induced with 1 mM IPTG. After induction, the cells were further grown for another 4 – 5 h at 220 rpm, 30°C. Cells were harvested by centrifuging at 9 820 × g for 10 mins at 4°C and, were resuspended in 6 M urea, 100 mM NaH_2PO_4, and 10 mM Tris pH 8.0.

Table 2.3 Buffers prepared for TnT purification

Binding Buffer	Thrombin Buffer A	Thrombin Buffer B
10 mM Tris pH 8.0	20 mM Tris pH 8.4	20 mM Tris pH 8.4
100 mM NaH_2PO_4	150 mM NaCl	150 mM NaCl
6 M urea	2.5 mM $CaCl_2$	2.5 mM $CaCl_2$
	2 M urea	6 M urea

After sonication for 5-6 min, cell debris was removed by centrifuging at 30 966 × g for 20 mins at 4°C. The supernatant was batch bound to ~5 mL Ni-NTA beads equilibrated with Binding Buffer. The beads were then loaded into an Econo-Pac column (Bio-Rad) and rotated for ~30 mins at room temperature. After 30 mins the column was washed with several column volumes of Binding Buffer followed by equilibration with Thrombin Buffer A. Cleavage of the N-terminal 6 x His-tag was achieved using ~60 U of bovine thrombin (Sigma). The thrombin remains active at a urea concentration of 2 M for an overnight incubation but not in the presence of 6 M urea. Cleaved TnT was then eluted with Thrombin Buffer A. Application of Thrombin Buffer B to the column then solubilised the majority of the TnT which had precipitated after cleavage from the 6 x His-tag. The TnT fractions were analysed via SDS-PAGE and pooled (**Figure 2.4 A**). The cleaved 6 x His-tag was removed from the column by decreasing the column pH to 5.

Anion exchange chromatography was used to remove significant nucleic acid contamination from the eluted TnT. Purified TnT fractions collected from the Ni-NTA purification step were pooled and dialysed against Binding Buffer (6 M Urea, 2 mM EDTA, 0.5 mM DTT, 50 mM Tris pH 8.0) prior to loading onto a pre-equilibrated 20 mL DEAE Sephadex A-25 column (Pharmacia). TnT was eluted with 0.3 M KCl and nucleic acid contaminants were removed with a 1 M KCl wash (**Figure 2.4 B**). TnT fractions were analysed by SDS-PAGE (**Figure 2.4 C**) and pooled and stored at -20°C until required

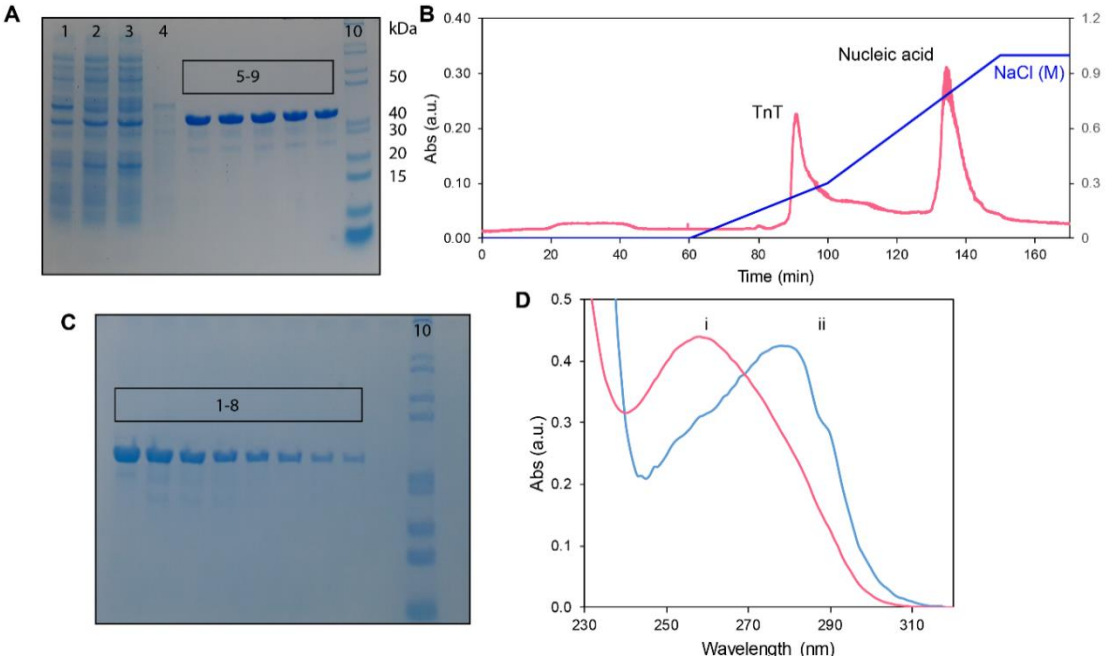

Figure 2.4 TnT Purification. **(A)** SDS-PAGE of Peak C from Ni-NTA column. Lane 1, expression of TnT from overnight growth. Lane 2, soluble fraction. Lane 3, unbound protein fraction. Lanes 4, TnT eluted with 2 M Urea. Lanes 5-9, TnT eluted with 6 M Urea. Lane 10, Benchmark ladder. **(B)** Elution profile with DEAE column for nucleic acid removal. Peaks 1, TnT elution with 0.3 M KCl. Peak 2, elution of nucleic acid contamination with 1 M KCl. **(C)** SDS-PAGE of DEAE column fractions. Lanes 1-8, purified TnT fractions. Lane 10, Benchmark Ladder. **(D)** Absorbance of TnT. *i,* TnT fraction with significant nucleic acid contamination following elution from the Ni-NTA column, as observed at 260 nm. *ii,* Purified TnT fraction from DEAE column at 280 nm with removal of nucleic acid contamination.

2.4 Site-Directed Spin Labeling - SDSL

2.4.1 Nitroxide Spin Labels

As the Troponin protein complex is an EPR silent system, the attachment of a spin label is required. This was achieved by covalently attaching a nitroxide spin label onto one or more cysteine residues for single and double labeled mutants, respectively. Cysteine residues are targeted as their unique 'sulphydryl' group can form a covalent disulphide bond with the spin label. The site-directed mutagenesis approach (as described in Section 2.2.1) was therefore used to introduce cysteine residues at specific and targeted locations on the protein backbone. The nitroxide spin label used in this study, 1-oxyl- 2,2,5,5-tetra-

methylpyrroline-3-methylmethanethiosulfonate spin label (MTSL, Toronto Research Chemicals, Toronto, Canada) contains the reactive sulphydryl group for attachment to the desired cysteine side chain (**Figure 2.5**). In general, the size of the nitroxide EPR spin label used in these studies is quite small, similar in size to that of a tryptophan residue. Attachment of a nitroxide spin label has been demonstrated by many studies in various protein systems to have minimal effect on the overall protein structure [8-10].

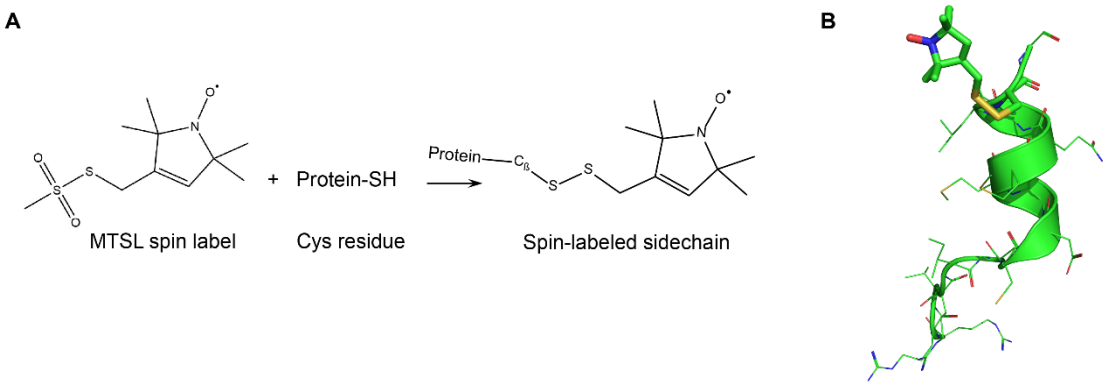

Figure 2.5 (A) MTSL is covalently attached to a protein via a disulphide bond to the cysteine sidechain of a single cysteine residue on a protein. The stable unpaired electron is localised almost entirely to the π-orbital of the nitroxide bond [11]. **(B)** The nitroxide group is tethered to the protein (switch peptide) backbone via a flexible linker arm. The size of the modified side chain is approximately equivalent to a tryptophan residue, thus structural perturbation by spin-labeling is minimal [12].

2.4.2 Spin Labeling Methods for EPR

Once cysteine residues were engineered at specific locations the unique sulphydryl side chain they were then targeted for labeling. Buffers used for the labeling of these subunits with MTSSL are provided in **Table 2.4**.

To ensure optimal reactivity of the cysteine side chain with the nitroxide label, the cysteine side-chain was first reduced with DTT. It was important to remove all traces of the reducing agent prior to adding MTSL so as to avoid reduction of the nitroxide group of the spin label.

The presence of remaining DTT may also inhibit conjugation of the disulphide bond between the cysteine and the spin label. A desalting column was a reliable strategy for this step, where the reduced protein was eluted into a suitable buffer (slightly alkaline, free of reducing agent) for the spin-labeling reaction. For the ternary Tn complexes, all subunits, except TnC, were initially required to be prepared at [6 M] urea. It was therefore most practical to spin label the TnC and TnI subunits in denaturing conditions, where the cysteine residues were also more likely to be in a solvent exposed state for efficient labeling. Following a series of buffer changes with labeling buffer (**Table 2.4**) over 24 h at 4°C, the protein samples were reduced by addition of DTT to a final concentration of 10 mM. Samples were incubated at 4°C for 2 h to ensure complete reduction of cysteine residues. DTT was then removed by gel filtration (HiTrap™ Desalting column, GE Healthcare) with elution into the labeling buffer. Immediately after DTT was removed, the nitroxide spin label (MTSL stock at 0.1 M in dimethyl formamide (DMF)) was slowly introduced drop-wise to the protein solution for covalent attachment (**Figure 2.5**), while gently vortexing. Adding greater than 1% (v/v) DMF to the protein solution was avoided. A 7.5-fold molar excess of the spin label over cysteine was added to ensure complete labeling. The labeling reaction was then incubated for ~4 h at room temperature with gentle rocking. An additional second aliquot of spin label stock of 2.5-fold molar excess was added prior to further incubation overnight at 4°C. The non-reacted spin label was removed at 4°C by extensive dialysis against Buffer 1. Buffer 2 (**Table 2.4**) was used as a final change of dialysis to store the sample as required for reconstitution. Protein concentration and thus cysteine concentration was determined. The extent of labeling (efficiency) was determined by EPR spectroscopy spin count measurements as described in the next section.

Table 2.4 Buffers required for MTSL labeling of TnC and TnI subunits

Labeling buffer	Buffer 1	Buffer 2
6 M urea	2 M urea	6 M urea
1 mM EDTA	1 mM EDTA	1 mM EDTA
0.1 M KCl	0.1 M KCl	0.5 M KCl
50 mM MOPS pH 7.5	50 mM MOPS pH 7.2	2 mM $CaCl_2$
		50 mM MOPS pH 7.2

2.4.3 Spin Labeling Methods for PRE-NMR

The nitroxide spin labeling process for preparing the TnC NMR samples was essentially the same as discussed for EPR samples, except the labeling buffer that was used for labeling a single TnC cysteine residue was 100 mM KCl, 20 mM potassium phosphate buffer (K_2HPO_4/KH_2PO_4) pH 8. For TnI, the labeling buffer used was 6 M urea, 100 mM KCl, 1 mM EDTA and 50 mM MOPS pH 8.0. As for TnC, the TnI eluted free of DTT into labeling buffer by the use of a HiTrap™ Desalting column, GE Healthcare. After labeling, excess MTSL was then removed by extensive dialysis against TnI Dialysis Buffer (2 M urea, 100 mM KCl, 1 mM EDTA and 50 mM MOPS pH 8.0), before dialysing into Reconstitution Buffer (6 M urea, 1 mM EDTA, 0.5 M KCl 2 mM $CaCl_2$, 3 mM $MgCl_2$ and 50 mM MOPS pH 7.2).

2.4.4 Spin counting by CW-EPR Spectra Collection

The theory of EPR spectroscopy is provided in next Chapter. However, here, the EPR method that was performed to assess the proportion of labeling of all Tn subunits by continuous wave (CW) EPR is briefly described. The EPR spin count provides an estimate of the proportion of cysteine residues modified by the MTSL spin label.

In a CW-EPR experiment, the applied magnetic field is swept while the frequency is held constant. The nitroxide spin label contains the unpaired electron in the *p*-π orbital of the N-O bond which interacts with the nitrogen (^{14}N) nucleus splitting the EPR signal. The EPR spectrum of the nitroxide label therefore shows three distinct peaks; a central peak resulting from the unpaired electron and two hyperfine peaks resulting from electron-nuclei interactions (**Figure 2.6 A**). By convention, EPR spectra are presented as the first derivative of the corresponding EPR absorption spectrum which provides the characteristic three peak EPR lineshape (**Figure 2.6 B**). This first derivative spectrum allows for more accurate measurements of line shape parameters, such as peak widths, and peak heights. These features of the EPR lineshape are important when determining spin label mobility and peak broadening from dipolar interactions. The later is used in this Thesis to measure interspin distances.

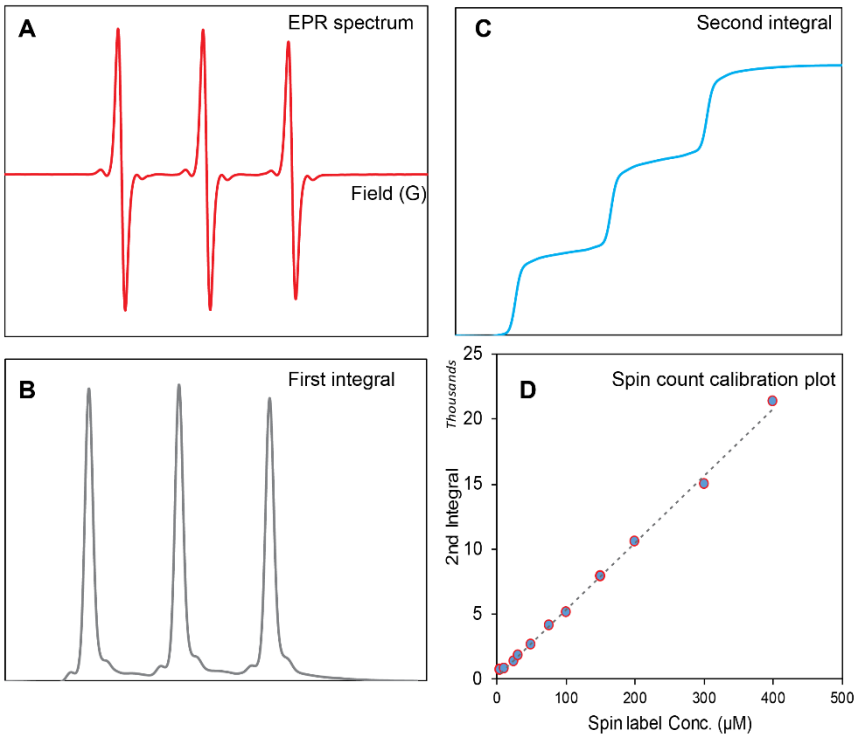

Figure 2.6 EPR Spin Count: **(A)** A free 'MTSL-label' CW EPR spectral signal recorded at room temperature. The central peak results from the unpaired electron while the two hyperfine peaks result from electron-nuclei interactions. **(B)** Corresponding first integral of the EPR spectrum. **(C)** Double integration of the EPR signal used for constructing a calibration curve. **(D)** Using the double integral values obtained from C a standard curve is used constructed to obtain the spin concentration of the protein sample. The ratio of spin concentration to protein concentration, determined via the BCA assay, gives the spin labeling yield.

All EPR spectroscopy was performed on a Bruker EMX X-Band (9.5 GHz) EPR spectrometer with a standard rectangular TE cavity. The EPR spectra were collected at room temperature with a microwave power of 5.0 mW, modulation amplitude of 1.0 G and sweep width of 140 G. The integrated area under the EPR absorbance spectrum, or the second integral of the EPR spectrum, is proportional to the concentration of the spin label in a sample and is referred to the 'spin count' of the sample (**Figure 2.6 C**). Thus, a calibration plot (**Figure 2.6 D**) was constructed from the spin counts of a series of MTSL standard to enable determination of the spin concentration for all spin-labeled protein samples used in this Thesis. The simple double integration of the EPR spectral lineshape was achieved using a LabView (National Instruments, Austin, TX) package of programs designed specifically for

EPR spectral analysis (courtesy of P. Fajer, Florida State University, Florida). The labeling efficiency was obtained by comparison of the protein concentration (determined by a BCA assay), to the concentration of MTSL (determined from the EPR spin count) (**Figure 2.6 D**). In all cases, complete modification of each single cysteine to levels of at least >95% was achieved.

2.5 Protein Reconstitution

2.5.1 Binary Tn Complex Reconstitution

The buffers used for reconstitution of the troponin complexes are given in **Table 2.5**. Binary troponin complex reconstitution (TnC-TnI) was achieved by the incubation of purified TnI with TnC in a 5.0:4.0 molar ratio in reconstitution buffer A containing 6 M urea and a high salt concentration of 0.5 M KCl. Reconstitution was then achieved via dialysis by slowly decreasing the urea concentration to 0 M and [KCl] to 0.15 M. After the initial mixing of the Tn subunits in Buffer A, this was achieved by replacing 50% of the current dialysis buffer with Buffer B to reduce the [urea] to 3 M. After a further 6 h of dialysis, 2/3 of the volume of the dialysis buffer was then discarded and replaced with fresh Buffer B to bring the [urea] to 1 M. Two further changes of fresh Buffer B were then used to remove remaining urea, followed by one change of Buffer C, and then two changes of Buffer D to bring [KCl] to 0.15 M. Excess TnI that did not bind to TnC to form the binary complex precipitated out of solution (0 M urea and 0.15 M KCl). Centrifugation (15 000 × g, 2 mins) was used to remove the precipitated TnI before dialysing the reconstituted Tn complex back into Buffer E. Each buffer exchange was allowed at least 6 h dialysis time at 4°C with stirring. Reconstitution of the binary complex was confirmed by SDS-PAGE (**Figure 2.7**). For spectral measurements, the 'high' and 'low' Ca^{2+} activation states were achieved by adding either $CaCl_2$ to a concentration of 5 mM or EGTA to a concentration of 8 mM, respectively, to the final reconstituted sample.

Table 2.5 Buffers required for Binary complex reconstitution

Buffer A	Buffer B	Buffer C	Buffer D	Buffer E
0.5 M KCl	0.5 M KCl	0.3 M KCl	0.15 M KCl	0.15 M KCl
2 mM $CaCl_2$	2 mM $CaCl_2$	2 mM $CaCl_2$	2 mM $CaCl_2$	
3 mM $MgCl_2$	3 mM $MgCl_2$	3 mM $MgCl_2$	3 mM $MgCl_2$	3 mM $MgCl_2$
6 M urea				
50 mM MOPS	50 mM MOPS	50 mM MOPS	50 mM MOPS	50 mM MOPS
pH 7.2	pH 7.2	pH 7.2	pH 7.2	pH 7.2

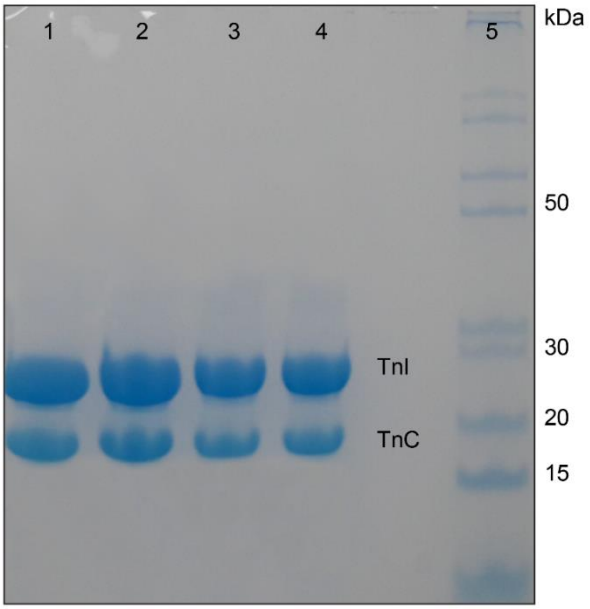

Figure 2.7 SDS-PAGE of reconstituted binary troponin complex. Lane 1-4, binary Tn complex reconstituted with TnI $151_{S22/23D}$ or TnI159 $_{S22/23D}$ (~24 kDa), TnC cys-less (~18kDa) in the presence and absence of calcium.

2.5.2 Ternary Tn Complex Reconstitution

Similar to the binary complex, reconstitution of the active ternary Tn complex was achieved using the three recombinant Tn subunits (TnI, TnT and TnC). Reconstitution also followed well-established methods (**Figure 2.8**) [4]. The buffers used for reconstitution are given in **Table 2.6**.

Table 2.6 Buffers required for Ternary complex reconstitution

Buffer A	Buffer B	Buffer C	Buffer D	Buffer E
0.5 M KCl	0.5 M KCl	0.3 M KCl	0.1 M KCl	0.2 M KCl
2 mM $CaCl_2$	2 mM $CaCl_2$	2 mM $CaCl_2$	2 mM $CaCl_2$	
3 mM $MgCl_2$	3 mM $MgCl_2$	3 mM $MgCl_2$	3 mM $MgCl_2$	3 mM $MgCl_2$
6 M urea				
50 mM MOPS	50 mM MOPS	50 mM MOPS	50 mM MOPS	50 mM MOPS
pH 7.2	pH 7.2	pH 7.2	pH 7.2	pH 7.2

The method for reconstituting the ternary complex is based on the properties that TnI and TnT are both insoluble polypeptides in isolation, while TnC and the final reconstituted Tn ternary complex are both soluble. Reconstitution was therefore achieved by combining the three polypeptide subunits in a 1.2:1.2:1 molar ratio of TnT:TnI:TnC. After mixing in the appropriate ratio, similar steps to reduce the urea and salt concentrations, as for the binary complex, were performed. Excess precipitated TnI and TnT that did not bind to TnC to form the ternary complex was removed by centrifugation (15 000 × g, 2 mins) before dialysing the reconstituted ternary Tn complex back into Buffer E for stability.

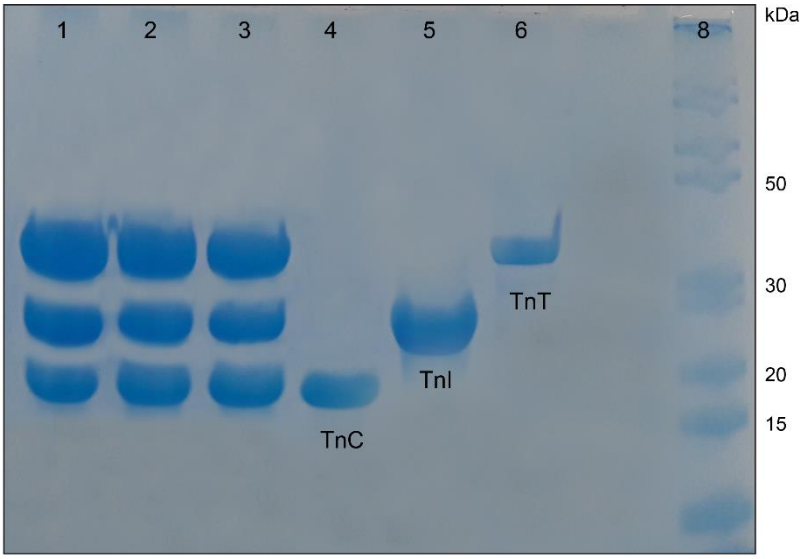

Figure 2.8 SDS-PAGE of reconstituted troponin complex. Lanes 1-3, Tn complex reconstituted with TnI 39 (~24 kDa), TnC35/TnC84/TnC Cys-less (~18 kDa; lane 1/lane 2/lane3) and TnT (~35 kDa). Lane4, TnC monomer. Lane 5, TnI monomer. Lane 6, TnT monomer. Lane 8, Benchmark ladder.

2.6 NMR Spectroscopy

The following section contains some general details of NMR methodology and other considerations undertaken in the development of NMR samples and data interpretation for this project. Further detailed NMR theory is provided in Chapter 3.

2.6.1 NMR Samples

All NMR samples (550 µL) were prepared at protein concentrations ranging from 130 µM to 300 µM to prevent unwanted intermolecular paramagnetic relaxation enhancement (PRE) effects [13]. The isolated TnC or binary TnC-TnI NMR samples were prepared in 200 mM KCl and 20 mM imidazole pH 6.9 supplemented with either 1 mM $CaCl_2$ or 3 mM $MgCl_2$ to mimic the high (+) or low (-) Ca^{2+} states, respectively. To do this, the MTSL-labeled sample was dialysed against 0.2 M EDTA for 2 h at 4°C to chelate all Ca^{2+}/Mg^{2+} ions [8], then exhaustively dialysed into NMR buffer (50 mM KCl and 20 mM KH_2PO_4/ K_2HPO_4 pH 6.7). All NMR buffers were first pre-treated with Chelex 100 resin (Bio-Rad) to remove any traces of Ca^{2+}, following the manufacturer's instructions. All glassware and plasticware was also acid washed with 10% hydrochloric acid and rinsed thoroughly with decalcified Milli-Q dH_2O. NMR samples in the high Ca^{2+} state were then supplemented with 1 mM $CaCl_2$ and low Ca^{2+} samples with 3 mM $MgCl_2$. Immediately prior to acquiring NMR spectra, 10% D_2O and 0.02 mM 2,2-dimethyl-2- silapentane-5-sulfonate (DSS) were added to each sample.

2.6.2 NMR Spectroscopy

All the TROSY spectra of ^{15}N TnCcysless-^{14}N TnI samples were acquired on a 600 MHz Bruker spectrometer equipped with a cryogenically cooled probe at Department of Molecular Sciences at Macquarie University. All NMR experiments were performed at 303 K (30°C) and acquired using Topspin 1.3 software (Bruker).

PRE NMR Experiments: For each paramagnetic spin-labeled sample, a HSQC or TROSY-HSQC (detailed description provided in Chapter 3) spectrum was acquired. After acquiring the paramagnetic spectrum, the nitroxyl radical of the MTSL label was reduced to its hydroxylamine equivalent by the addition of a 5-fold molar excess of ascorbic acid (from a 0.5 M stock) directly to the NMR sample. One hour at room temperature was sufficient time

to allow for the reduction reaction to go to completion. The reduction was confirmed by EPR; in complete reduction there was no EPR signal. After reduction of the spin label, the diamagnetic reference spectrum was then acquired, with identical parameters. The small volume of ascorbic acid (0.7 – 1.7 µL) did not cause any significant dilution of the sample (550 µL), thus enabling direct comparison of peak intensities between paramagnetic and diamagnetic spectra used in the calculation of the relaxation enhancement

References

1. Sambrook, J., E.F. Fritsch, and T. Maniatis, *Molecular cloning: a laboratory manual*. 1989: Cold spring harbor laboratory press.
2. Gill, S.C. and P.H. von Hippel, *Calculation of protein extinction coefficients from amino acid sequence data.* Anal Biochem, 1989. **182**(2): p. 319-26.
3. Dong, W.J., et al., *Conformation of the regulatory domain of cardiac muscle troponin C in its complex with cardiac troponin I.* J Biol Chem, 1999. **274**(44): p. 31382-90.
4. Dong, W.J., et al., *Conformation of the N-terminal segment of a monocysteine mutant of troponin I from cardiac muscle.* Biochemistry, 1997. **36**(22): p. 6745-53.
5. Guo, X., et al., *Mutagenesis of cardiac troponin I. Role of the unique NH2-terminal peptide in myofilament activation.* J Biol Chem, 1994. **269**(21): p. 15210-6.
6. Potluri, P.R., et al., *The concerted movement of the switch region of Troponin I in cardiac muscle thin filaments as tracked by conventional and pulsed (DEER) EPR.* J Struct Biol, 2017. **200**(3): p. 376-387.
7. Studier, F.W., et al., *Use of T7 RNA polymerase to direct expression of cloned genes.* Methods Enzymol, 1990. **185**: p. 60-89.
8. Brown, L.J., et al., *Structure of the inhibitory region of troponin by site directed spin labeling electron paramagnetic resonance.* Proc Natl Acad Sci U S A, 2002. **99**(20): p. 12765-70.
9. Langen, R., et al., *Crystal structures of spin labeled T4 lysozyme mutants: implications for the interpretation of EPR spectra in terms of structure.* Biochemistry, 2000. **39**(29): p. 8396-405.
10. Perozo, E., et al., *Open channel structure of MscL and the gating mechanism of mechanosensitive channels.* Nature, 2002. **418**(6901): p. 942-8.
11. Otting, G., *Protein NMR using paramagnetic ions.* Annu Rev Biophys, 2010. **39**: p. 387-405.
12. Kachooei, E., N.M. Cordina, and L.J. Brown, *Constructing a structural model of troponin using site-directed spin labeling: EPR and PRE-NMR.* Biophys Rev, 2019. **11**(4): p. 621-639.
13. Donaldson, L.W., et al., *Structural characterization of proteins with an attached ATCUN motif by paramagnetic relaxation enhancement NMR spectroscopy.* J Am Chem Soc, 2001. **123**(40): p. 9843-7.

3. Magnetic Resonance Spectroscopic Techniques for Studying Troponin Structure and Dynamics

As discussed earlier (**Section 1.9, Review Paper**), the limitations of conventional structural biology approaches such as x-ray crystallography or NMR requires the employment of other approaches to better investigate weaker physical protein-protein interactions which can expand our understanding of protein dynamics, especially for Tn. In this Chapter, the theoretical, as well as some practical considerations, of both Paramagnetic Relaxation Enhancement (PRE) and Electron Paramagnetic Resonance (EPR) are described. Paramagnetic NMR and EPR spectroscopy have different advantages and also disadvantages in structural biology, and their uses will often depend on the nature of the material under investigation and the biological question being asked. These advantages are also discussed in this Chapter.

3.1 The Paramagnetic Relaxation Effect

3.1.1 Nuclear Magnetic Resonance – Physical basics

In an external magnetic field, nuclei with a non-zero spin quantum number (such as ^{1}H, ^{15}N and ^{13}C) possess spin angular momentum. ^{1}H, ^{15}N and ^{13}C nuclei are spin ½ particles. In other words, the magnetic dipole moment of these nuclei particles are quantised and in an applied magnetic field (B_0) can adopt one of two orientations (**Figure 3.1 A**). The spin state orientation aligned parallel to the magnetic field (m_s = +½, α) has the lowest energy spin state and the spin state in antiparallel orientation (m_s = -½, β) has highest energy [1]. The magnetogyric ratio (γ) is unique for the particular type of nucleus and affects the magnetic moment of the spin. The nuclear magnetic moment precesses around the axis of the external field due to the torque produced by the interaction between the nuclear dipole and the magnetic field (**Figure 3.1 B**). The precession frequency of the spin (ν), known as Larmor frequency, is directly proportional to the magnetic field experienced by the spin [1],

$$\nu = \frac{\gamma}{2\pi} B_0 \qquad \text{Eqn. 3.1}$$

where γ is magnetogyric ratio, and B_0 is applied magnetic field. At equilibrium, individual nuclear spins within a population are randomly phased in their precession, and the majority

of the spins are in lower energy state, therefore the net magnetization (M_0) is aligned to the direction of magnetic field (**Figure 3.1 C**).

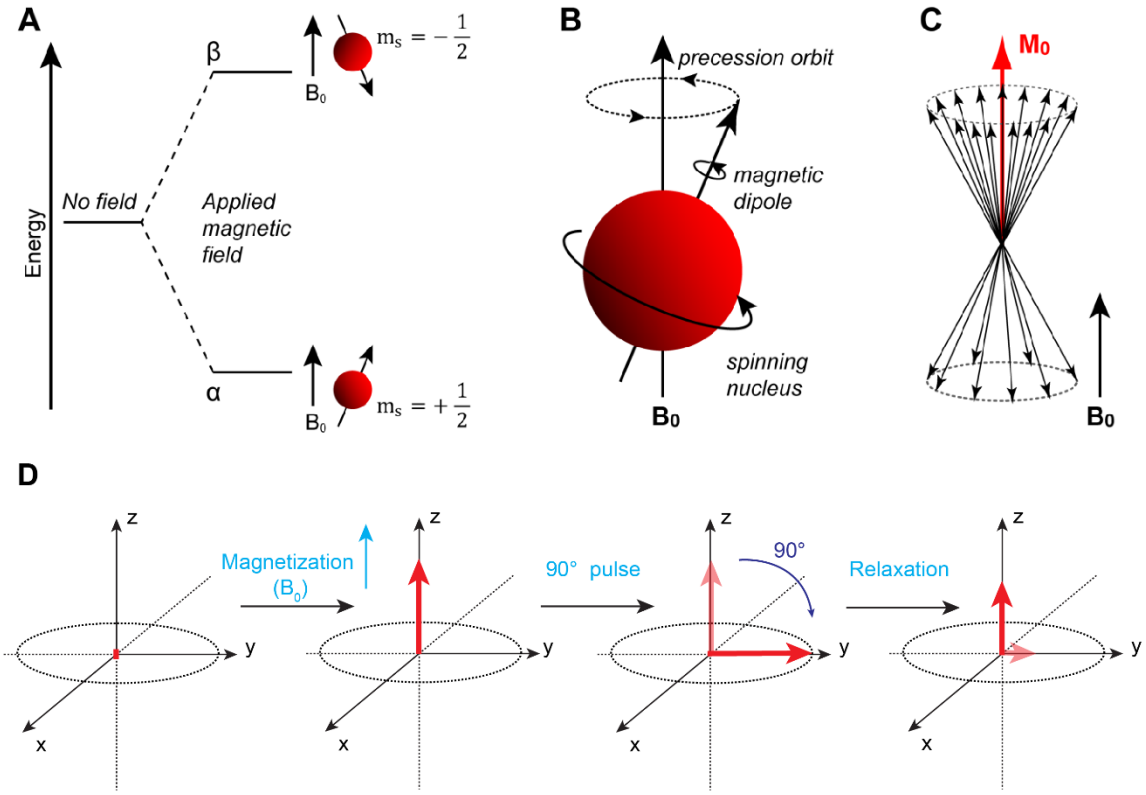

Figure 3.1 The principles of NMR. **(A)** In a magnetic field, spin ½ particles such as ^1H nuclei can exist in one of two spin states, the low energy state where the dipole moment is aligned with the field (m_s = + ½), or a higher energy state where the dipole opposes the external field (m_s = - ½). **(B)** The torque exerted on the spin dipole by the external field causes the spin to precess around the field axis. **(C)** At equilibrium, there is a majority of spins in the lower energy spin state, thus the net magnetisation is directed along the +z field axis (M_0) (images shown in panels A to C courtesy of Dr. Nicole Cordina). **(D)** NMR experiments involve the excitation of spins by applying a 90° pulse along the x-axis. This pulse tips the net magnetisation onto the y-axis. After the pulse is turned off, the precession axis returns to the B_0 field axis (relaxation).

The basic principles of NMR are shown in **Figure 3.1 D**. At equilibrium, there is no net magnetization in the transverse (xy) plane as the spins precess around B_0 at the Larmor frequency. When a strong electromagnetic field (B_1), oscillating at the Larmor resonance

frequency is applied perpendicular to B_0, the orientating effect of B_0 is cancelled and the axis of the precession changes temporarily to the B_1 axis (4). The B_1 field is applied as a short excitation pulse, which 'tips' the magnetisation into the transverse plane through a 90° angle. The pulse equalizes the spin state populations and generates phase coherence among the individual precessing magnetic moments. The net magnetisation is now along the y axis. The magnetisation precesses in the transverse plane toward the x-axis [2].

3.1.2 Spin Relaxation

The return of the spins to their thermal equilibrium is known as 'relaxation', and it involves the exchange of energy between spins (spin-spin or transverse relaxation) or between spins and the surrounding environment (spin-lattice or longitudinal relaxation). This energy transfer implies magnetic interactions with the magnetic dipoles associated with the spins. After excitation by a 90° pulse, relaxation processes return the perturbed system to thermal equilibrium, with the net magnetization along the z field axis [3].

3.1.2.1 Longitudinal Relaxation

As mentioned above, the excitation pulse tilts the macroscopic magnetization, M_0, of spins by an angle from its equilibrium position, M_z. Then the magnetization will precess in the xy plane (M_x or M_y). If the system is allowed to relax, the net magnetization will return to its equilibrium position (**Figure 3.2 A**). M_z will return to its equilibrium value M_0 according to a first order rate process characterized by the time constant T_1 in the equation:

$$\frac{dM_z}{dt} = \frac{-(M_z - M_0)}{T_1} \qquad \text{Eqn. 3.2}$$

where T_1 is the longitudinal (or spin-lattice) relaxation time.

3.1.2.2 Transverse Relaxation

The M_x and M_y components of magnetization also return to their equilibrium state, which is zero. This return corresponds to the dephasing of the spins, and arises from the exchange of energy between spins. The exchange of energy between neighbouring spins corresponds to gain or loss of energy, and it changes the precision frequency. As a result, the magnetization component in the xy-plane, which is the sum of all individual moments, will then decrease.

This magnetization decrease is a first-order process characterized by the time constant T_2 (**Figure 3.2 B**), and is called the spin-spin relaxation time or the transverse relaxation time:

$$\frac{dM_x}{dt} = -\frac{M_x}{T_2} \text{ or } \frac{dM_y}{dt} = -\frac{M_y}{T_2} \qquad \text{Eqn. 3.3}$$

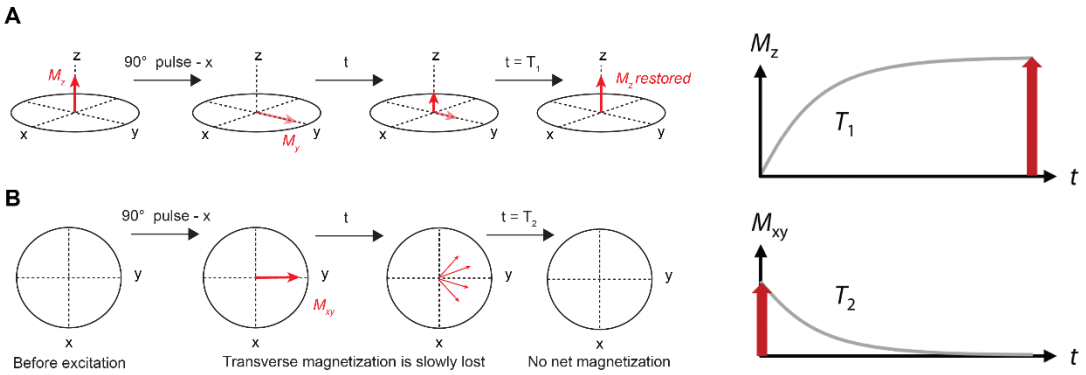

Figure 3.2 The recovery of a net magnetization. **(A)** Longitudinal relaxation time (T_1) is the time over which the equilibrium magnetisation along the z-axis (M_z) is restored. **(B)** Transverse relaxation (T_2) occurs as the coherence generated upon exciting is lost due to dephasing. This occurs due to slight variations in the precession frequency of individual spins which arise due to dipolar interactions between spins.

3.1.3 Spectrum Processing

A 'short pulse' of radiofrequency energy is used to excite nuclear resonances over a range of frequencies and is called as monochromatic radiation or pulse excitation. For signal detection, the energy emitted by the excited spins produces tiny analogue electrical signals that are then converted into a series of binary numbers for all the frequencies in the spectrum.

The NMR spectrum is then obtained by converting the time domain signal to a frequency domain signal by Fourier transformation (FT) of Free Induction Decay (FID) (**Figure 3.3 A**).

Improvement of the digital resolution for the processing of two-dimensional NMR spectra can be achieved by a process called zero filling. This process is where number of data points is increased by appending zeros to the end of the free induction decay before Fourier transformation. It can be performed multiple times and it is possible to improve the frequency resolution in the spectrum times by doubling the number of data points in the time domain by appending zeros (**Figure 3.3 B**).

In the NMR experiment, the repeated acquisition and summation of the FID leads to an overall increase in the signal-to-noise ratio as the NMR signals add coherently over the total number of scans. Hence, signal averaging is most necessary when noise levels are relatively high and it helps in the continuous improvement of the signal-to-noise ratio.

3.1.4 NMR and protein structure

NMR spectroscopy helps in solving protein structures by measuring a large number of angle and distance restraints. The NMR spectra is indeed the absorbance of radio frequency due to the nuclei spin resonance. These restraints are obtained from the spectra of multidimensional NMR experiments. NMR spectroscopy is the only biophysical technique capable of generating atomic resolution structural models of proteins in solution. The NMR experiments used in this Thesis are described in this following section.

3.1.4.1 HSQC experiment

The ^{1}H-^{15}N Heteronuclear Single-Quantum Coherence (HSQC) spectra provide a single peak for each backbone amide with high-resolution and high sensitivity in a two dimensional maps of ^{15}N–labeled samples. It can be achieved by relatively low cost and ease of ^{15}N enrichment of proteins [4]. The spectrum obtained from the HSQC experiment consists of two frequency axes, with a cross peak located at the coordinate corresponding to the resonance frequencies of the ^{1}H and ^{15}N nuclear spins. Each single peak obtained in the HSQC arises from a single amide group. Since every amino acid has typically one amid group, in protein HSQC a spectrum shows as many resonances as there are in the protein. Proline is an exception to this as it does not have an amide proton and thus is not seen in the HSQC spectrum. The HSQC experiment can be considered as a highly useful experiment because it provides a near complete map of the entire protein.

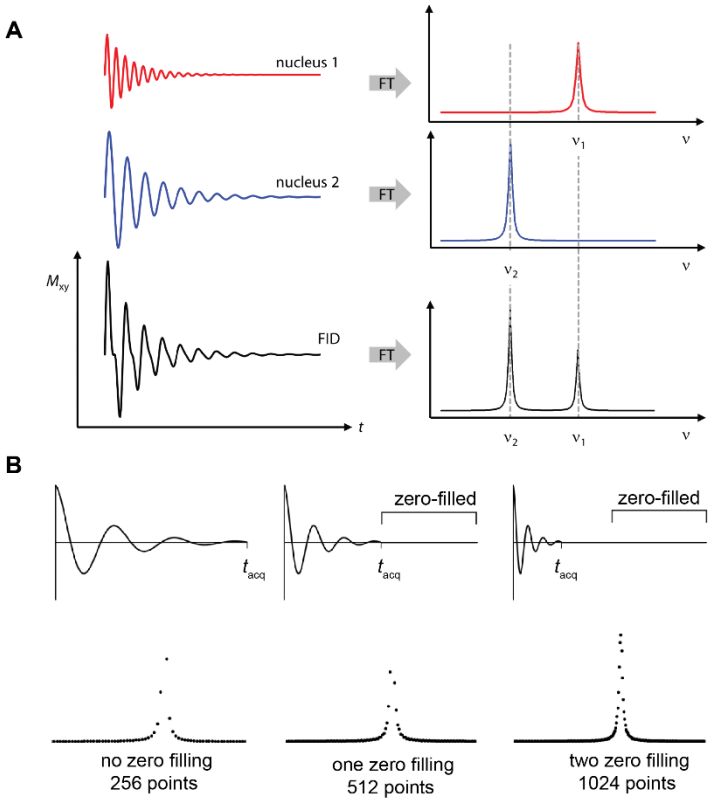

Figure 3.3 (A) The free induction decay (FID) is a time-domain signal. Fourier transformation of the FID converts the time-domain signal to frequency-domain (the spectrum). Line-broadening occurs when the decay rate of the FID is fast Image taken from [2]. **(B)** The free induction decay (FID) and the corresponding spectrum obtained after Fourier transformation (FT), are shown on the top and bottom, respectively. The FID consists of 256 points, however only a few points define the peak. After one zero-filling has been added to the end of the FID, the peak is defined by more points. Even more points define the peak after zero-filling a second time. Image adapted from [5].

3.1.4.2 TROSY experiment

The linewidth in the NMR spectrum is governed by the transverse relaxation time (T_2). Sharp peaks are obtained from slowly relaxing systems and broad peaks are obtained from rapidly relaxing systems. As shown in **Figure 3.4** (A-C), line-broadening due to fast relaxation is a problem for large proteins. The transverse relaxation rate is strongly dependent on the rotational correlation time (τ_c), which is defined as the time taken for a protein to tumble

around its own axis. There is a linear relationship between protein size and τ_c, assuming the protein behaves more or less spherically, with large proteins having long correlation times τ_c since they naturally take longer to tumble around their own axis. The effect of the correlation time (τ_c) on the transverse relaxation time (T_2) can be understood by considering the predominant mechanism through which transverse relaxation occurs, that is, dipolar interactions. Whether a dipolar interaction adds to or subtracts from the external B_0 field depends on the orientation of the interacting spins with respect to B_0, and therefore fluctuates as the protein tumbles in solution. If the protein rotational motion is very fast, then the fluctuation is also fast, and the dipolar field is averaged to zero. For large proteins rotating slowly, there is more time for the dipolar interaction to facilitate relaxation.

Because of the fast relaxation rate that occurs as a consequence of the slow correlation time of the protein, the HSQC experiments typically yield poor quality spectra. Transverse Relaxation Optimized Spectroscopy (TROSY) is utilised for improving the spectrum resolution and line widths for such large proteins. The TROSY principle is described in **Figure 3.4** (D & E). Briefly, each peak observed in the HSQC spectrum is actually the average of four peaks, corresponding to different states of the coupled ^{1}H and ^{15}N spins. The TROSY experiment selects only for the multiplet component with the narrowest linewidth.

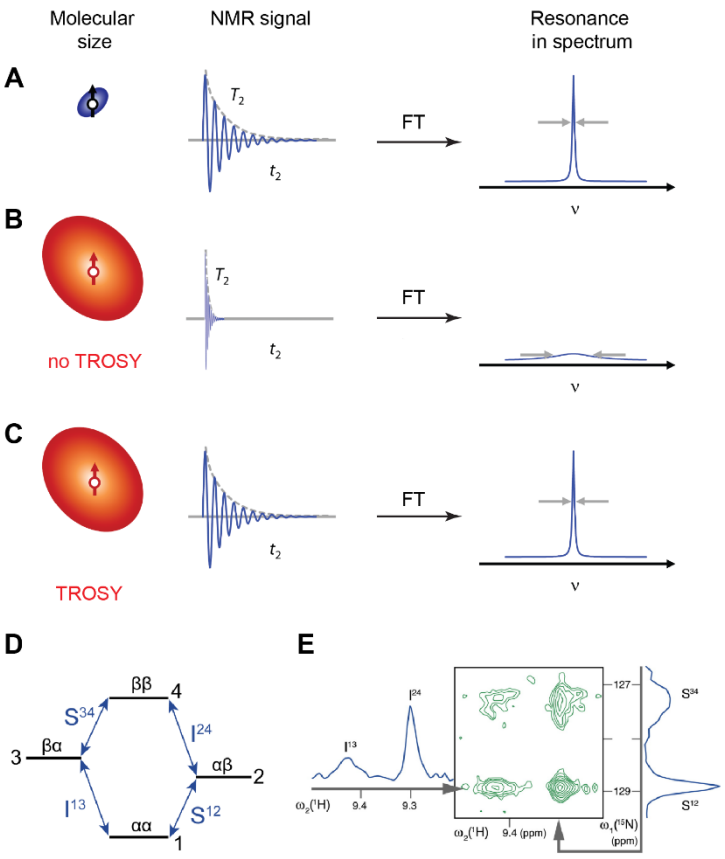

Figure 3.4 NMR spectroscopy of large molecules in solution. **(A)** The relaxation rate of NMR signal obtained from small molecules in solution is slow; i.e. it has a long transverse relaxation time (T_2). Larger T_2 value gives narrow line widths (Δν) in the NMR spectrum after Fourier transformation (FT) of the NMR signal. **(B)** For larger molecules, such as proteins, the relaxation rate of NMR signal is faster (T_2 is smaller). This small T_2 value translates into broad lines in the spectra. **(C)** TROSY results in improved spectral resolution and sensitivity for large protein molecules. Images shown in panels A to C adapted from [6]. **(D)** A physical picture of TROSY. There are four possible spin states for the ^{1}H (I) and ^{15}N (S) coupled spins, as shown in this energy level diagram. **(E)** The peaks corresponding to transitions in (D). In a HSQC experiment, the four peaks are averaged, resulting in a single, broadened peak. In the TROSY experiment, only the narrowest peak is selected for (bottom right corner). Images shown in panels D to E are adapted from [7].

3.1.5 Paramagnetic NMR

Paramagnetism assisted NMR is a valuable approach for obtaining information on both the structure and dynamics of the biological system of interest [64]. Paramagnetic NMR involves

introducing a paramagnetic species which contains an unpaired electron, such as the nitroxide spin label (as used in this Thesis) or a lanthanide, into a protein for NMR studies. The magnetic moment of the unpaired electron in the paramagnetic species is very large thus the resulting dipolar interactions between nuclear spins and the electron become the major relaxation pathway. This dipolar interaction is distance dependant and causes characteristic changes in NMR spectra which enables one to calculate the distance between an affected residue and the electron [8].

Various types of paramagnetic restraints can be measured and used for structural analysis, such as pseudo contact shifts (PCS), residual dipolar couplings (RDC) induced by the alignment caused by the paramagnetic centre, or paramagnetic relaxation enhancement (PRE). The two major paramagnetic effects observed in the HSQC experiment are PCS and PRE effects. These effects are detected by comparing the NMR spectra obtained in the presence and absence of the paramagnetic species. The magnitude of the peak-broadening can then be related to the distance between paramagnetic centre and the detected nuclear spin.

Of note, PCS are observed if the magnetic field generated by the paramagnetic species is anisotropic. The anisotropy in the magnetic susceptibility tensor causes the partial alignment of paramagnetic species with the external magnetic field. Thus, PCS depends not only on distance, but also on the orientation of residues relative to the paramagnetic species. As a result of PSCs, the peaks in the spectrum become shifted.

The spectrum most commonly used in paramagnetic NMR studies is the two-dimensional HSQC spectrum. The HSQC spectrum effectively provides a map of the entire protein, since each residue in the protein is represented by a single peak. For large proteins (> ~20 kDa), TROSY experiments, as described in the preceding section, are often utilized instead. TROSY spectra effectively yield the same information as the HSQC but with improved resolution. In this Thesis, both TROSY (***Chapter 4 and 5***) and HSQC (***Appendix 1***) were performed.

3.1.5.1 Paramagnetic Relaxation Enhancement - PRE

PRE effects arise from the dipolar interactions between unpaired electrons, of the paramagnetic species and protein nuclei resulting in increased nuclear relaxation rates in a

distance dependent manner. They can be used to provide information on both protein structure and dynamics or reveal the presence of a transient structure [9-12]. Once a paramagnetic species has been introduced, such as a nitroxide label via SDSL, hundreds of long-range distance measurements can be obtained at once in a single protein sample [13].

The increase in the relaxation rates due to the presence of the paramagnetic species is observed in the NMR spectra as peak broadening. This interaction is detectable at distances of up to ~25 Å from the paramagnetic centre [8]. In other words, signals far from the probe (> 25 Å) remain unaffected while those close to the paramagnetic probe appear broader or may disappear completely if within a 10 Å radius. The magnitude of the PRE-broadening is determined by comparing the NMR spectra initially in the presence of the paramagnetic species to the spectra acquired in its absence, also called the diamagnetic reference. In the case of the experiments performed in this Thesis, the paramagnetic species used throughout was the nitroxide spin label - MTSL.

Nitroxide spin labels cause strong paramagnetic relaxation. Further, PCS is eliminated due to the isotropic nature of the nitroxide magnetism. Therefore, the assignment of NMR spectra labeled with a nitroxide spin label is significantly simplified. The reduced diamagnetic reference sample for MTSL was easily obtained following the reduction of the label with ascorbic acid. The change in peak intensity between the paramagnetic and diamagnetic samples is distance dependent, thus enabling the distance between an affected residue and the electron to be derived. Spectral analysis of PRE-NMR is also further discussed in **Chapter 1, Review paper - see Fig. 9**.

3.1.6 Data Acquisition and Analysis

All NMR spectra were acquired on the Bruker DRX 600MHz spectrometer equipped with cryoprobe at the Department of Molecular Sciences, Macquarie University at 303K (30 °C) using Topspin 1.3 software (Bruker). ^{15}N-HSQC spectra were utilised for measuring the PRE for isolated TnC. For the TnC-TnI binary complex, the TROSY version of the HSQC experiment was utilised.

^{15}N-HSQC of isolated samples were collected with 256 x 2048 data points in the F_1 (^{15}N) and the F_2 (^{1}H) dimensions. The number of scans was adjusted based on the sample

concentrations (ranging from 4 to 16 scans), with a 1 s relaxation decay. Spectral widths of 30 ppm (centred at 117 ppm) and 16 ppm (centred at 4.69 ppm) were used for the ^{15}N and the ^{1}H dimension, respectively.

^{15}N-HSQC-TROSY spectra were collected with 256 x 1024 complex incremental data points in the F_1 (^{15}N) and the F_2 (^{1}H) dimensions and a 1 s relaxation decay. The number of scans varied depending on the protein sample concentration, ranging from 32 to 64 scans and even more if the sample signal was weak. Signals were then converted into a series of binary numbers for all the frequencies in the spectrum.

3.1.6.1 Peak Assignment

A complete assignment of all backbone and sidechain resonances is required to determine NMR structure for a protein. However, the HSQC spectrum used for PRE analyses maps only the amide resonances, therefore a 'backbone' assignment is sufficient to enable interpretation of PRE data from HSQC spectra. For the required backbone assignment, assistance is obtained by triple resonance heteronuclear NMR experiments. The sequential assignment strategy using HNCO experiment correlates the ^{13}C chemical shifts of carboxylic group of residue (*i-1*) with ^{15}N and ^{1}H chemical shifts of shifts of residue *i*. The crosspeaks are observed in the 3D spectra and represent the resonance of the amide group in backbone (**Figure 3.5**). Since spin labeling does not generally cause significant changes in chemical shift values [14], assignments can be transferred to the spectra of each monocysteine construct. The backbone assignment for TnC was performed by Dr. Nicole Cordina [14], and this assignment was used in this Thesis interpret PRE data.

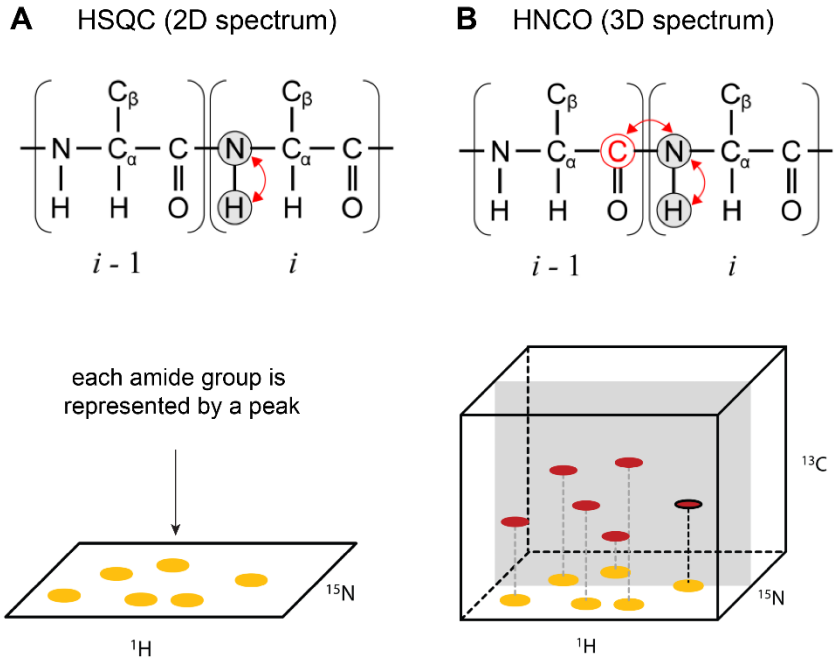

Figure 3.5 (A) The HSQC experiment correlates the amide ^{1}H and ^{15}N nuclei. Peaks in the two dimensional HSQC spectrum are located at the resonance frequency coordinates of these correlated nuclei. **(B)** Triple resonance experiments correlate amide ^{1}H and ^{15}N nuclei with ^{13}C nuclei. In the HNCO experiment shown here, the amide ^{1}H and ^{15}N nuclei of residue *i* are correlated to the carbonyl ^{13}C nucleus of the previous residue (*i-1*). If the 3D spectrum were viewed from above, the HSQC spectrum would be seen. Image is adapted from [2].

3.1.6.2 Analysis of the Spectra

The relaxation enhancement caused by the spin label can be obtained from the peak intensities in the paramagnetic state and diamagnetic state. Lorentzian peak models which are fit to both dimensions and intensity ratios (I_{para}/I_{dia}) are calculated for each assigned resonance [8]. Intensities in the paramagnetic state (I_{para}), and in the diamagnetic state after reduction of the spin label (I_{dia}), are obtained using:

$$\frac{I_{para}}{I_{dia}} = \frac{R_2 \exp(-\Gamma_2 t)}{R_2 + \Gamma_2} \qquad \text{Eqn. 3.4}$$

where, t is the evolution period of the NMR experiment where relaxation via electron-nuclear dipolar coupling occurs [15]. This is equal to 10 ms for the HSQC experiment [8, 16].

R_2 is the intrinsic relaxation rate for each amide and was estimated from the ^{1}H peak width at half height ($R_2 = \pi\Delta\nu_{½}$). The calculated PRE rates (Γ_2) were then converted to distances (r) using a modified form of the Solomon-Bloembergen equation [8, 16, 17].

$$\Gamma_2 = \frac{K}{r^6}\left[4\tau_c + \frac{3\tau_c}{1+\omega_H^2\tau_c^2}\right] \qquad \text{Eqn 3.5}$$

Where ω_H is the lamor frequency of the proton, K is a constant (1.23 x 10^{-32} cm^6s^{-2}) that describes the spin properties of this nitroxide spin label and τ_c is the correlation time of electron-proton interaction defined as $\tau_c = \tau_r^{-1} + \tau_s^{-1}$, where, τ_r is the overall rotational correlation of the protein, and τ_s is the electron relaxation time [18]. Since the electron relaxation time of nitroxide spin labels (in the order of 10^{-7} s) is very long compared to the correlation time of proteins (in the order of 10^{-9} s), the correlation time of the electron-proton vector is effectively equal to overall correlation time of the protein [18].

3.2 Electron Paramagnetic Resonance Spectroscopy

3.2.1 Physical Basis of the EPR signal

The principles of EPR spectroscopy are similar to NMR. Instead of nuclear spins, in EPR we are probing the energy levels of *unpaired electron spins* and their transitions between different energy states. In the absence of an external field, all electron states have the same energy and any spatial orientation is possible for free electrons with spin ½. In an external magnetic field (B_0), unpaired electrons are only distributed in two orientations; (i) aligned parallel with the magnetic field in a low energy state with spin orientation m_s = -½, or (ii) antiparallel in a high energy state with spin orientation of m_s = +½ (Figure 3.6A). The energy difference (ΔE) between these two states is directly proportional to the strength of the applied magnetic field. The splitting in energy level induced by external magnetic field in called 'Zeeman effect' (**Figure 3.6 A**). Transitions between the two energy states are induced by irradiation with electromagnetic radiation of the same quantum energy, i.e. wavelengths in the centimetre range (microwave radiation).

The interaction of an electron spin *S* with the spin *I* of a neighbouring nucleus results in the hyperfine coupling. Both the electron and the nuclear spin experience the Zeeman effect in the presence of an external magnetic field. The spin-spin interaction leads to mutual effects

on the local magnetic field experienced by nucleus and electron. That is, the orientation of one spin can either increase or decrease the total magnetic field sensed by the other spin (**Figure 3.6 B**). The important implication for EPR spectroscopy is the splitting of an EPR signal into (*2I + 1*) signals by a nucleus of spin I. A nucleus with I = ½ such as ^{1}H splits the EPR resonance into two lines, a nucleus with I = 1 such as ^{14}N splits it into three lines. Nitroxide spin labels show a characteristic three-line resonance because of hyperfine coupling of the electron spin with the nuclear spin of the nitrogen (**Figure 3.6 C**).

Since the energy difference between the two states is small, their population is almost equal, with just a tiny excess in the lower energy parallel spin orientation. The absorption signal in EPR experiments is therefore small, and EPR is rather insensitive. To achieve higher sensitivity (signal-to-noise), instruments typically measure the change in signal upon modulation of the sweeping the *B*-field instead of the signal itself. The result of this field modulation is that the signal that is obtained is not the value of the absorbance, rather the difference in the absorbance between the ends of the modulation amplitude, i.e. ~d(absorption)/dB. As a result, continuous wave (CW) EPR spectra are recorded as the first derivative of the absorption (**Figure 3.6 C**). This derivative signal is detected at an external magnetic field B_0 where the energy difference between the spin states equals the energy of the constant microwave radiation that is applied. It is the 'lineshape' of the derivative EPR spectrum that is then used to obtain all the magnetic information of the sample (**Figure 3.6 D**). The relative orientations between the unpaired electron in the sample, and the applied magnetic field, is reflected in the lineshape. Together the EPR sensitivity to the orientation and rotational motion of the spin label attached to the protein is defined with 'Zeeman effect' and hyperfine interactions.

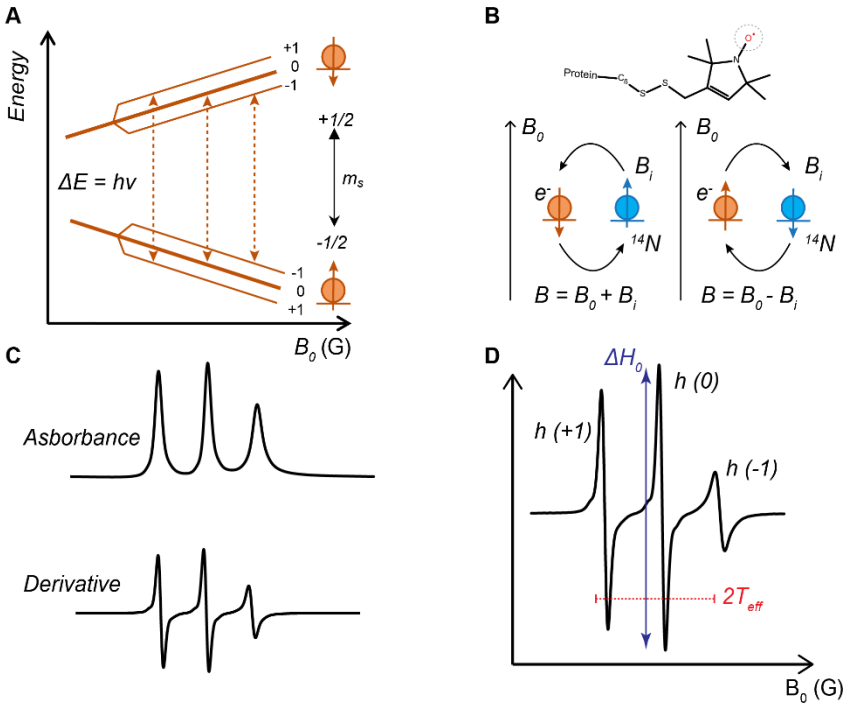

Figure 3.6 (A) The EPR experiment. The magnetic field is scanned and a constant microwave radiation is applied to a sample. When the *ΔE* spacing is tuned into resonance with the applied MW radiation, the electron is excited from m_s=-½ to m_s=+½ due to absorption of a microwave photon. **(B)** Hyperfine interactions between the unpaired electron and the nitrogen nuclear spin moment (which is true in the case of nitroxide spin labels) cause splitting of the electron spin energy levels by adding to, or subtracting from, the external field. **(C)** Due to the hyperfine interaction, there are three possible transitions. These transitions give rise to the three peaks observed in the absorbance spectrum of the nitroxide spin label. **(D)** EPR spectra are presented as the first derivative of the absorbance spectrum. Lineshape analysis provides information of the mobility and orientation of spin labeled residue in protein. ΔH_0 is the peak-to-peak line width of the central line and $2T_{eff}$ is the width between the low- and high-field absorption peaks. Image adapted from [19].

3.2.2 EPR Instrumentation

EPR spectra can be measured at a constant magnetic field while scanning the frequency of the microwave radiation. Measurements can also be done in the opposite way by keeping the microwave radiation at a constant frequency and varying the strength of the magnetic field B_0, which is the typical configuration in modern EPR spectrometers. Spectrometers are named according to the wavelength used (**Table 3.1**).

Table 3.1 Frequency bands of EPR spectrometers [2].

Band *	Typical frequency (range) (GHz)	Typical wavelength (cm)	Typical B-field (T)
L	1.5 (1–2)	20	0.0054
S	3.0 (2–4)	10	0.11
X	9.5 (8–12)	3	0.34
Ku	17 (12–18)	1.7	0.6
Q	36 (30–50)	0.8	1.28
V	70 (50–75)	0.4	2.5
W	95 (75–110)	0.3	3.39
D	149 (110–170)	0.2	5

* According to the Radio Society of Great Britain.

An EPR spectrometer is designed to optimize the weak magnetic resonance signal. Commercial EPR spectrometers are commonly available at several microwave frequencies, however the majority of research groups having access to an X-band spectrometer operating in the range of ~9.5 GHz.

Three basic components in a typical EPR spectrometer are: (i) a microwave bridge and resonator; (ii) a variable field magnet; and (iii) a signal amplification (**Figure 3.7**). The microwave bridge contains the detector and the electromagnetic radiation source which helps in generating the microwaves from either a klystron or gunn diode. The bridge also contains the resonator which has the sample cell that stores microwave energy in the form of a standing wave and converts the sample response into a detectable microwave signal. The resonators are in different varieties including standard rectangular or cylindrical cavity, split ring or dielectric resonator. A circulator separates the incident and reflected microwaves, and directs the incident microwaves and the microwaves reflected back from the cavity to the resonator and the detector diode, respectively. The reference arm works as an additional pathway to enable balanced detection, enhancing overall sensitivity of the system, and the magnet tunes the electronic energy levels. A small magnetic field generated by the modulation coils helps in encoding the resonance signal by modulating the static field, to reduce the microwave noise. The lock-in amplifier helps in selecting and amplifying the signal in phase and in frequency with the modulation field, and thereby rejects all other fluctuations as noise.

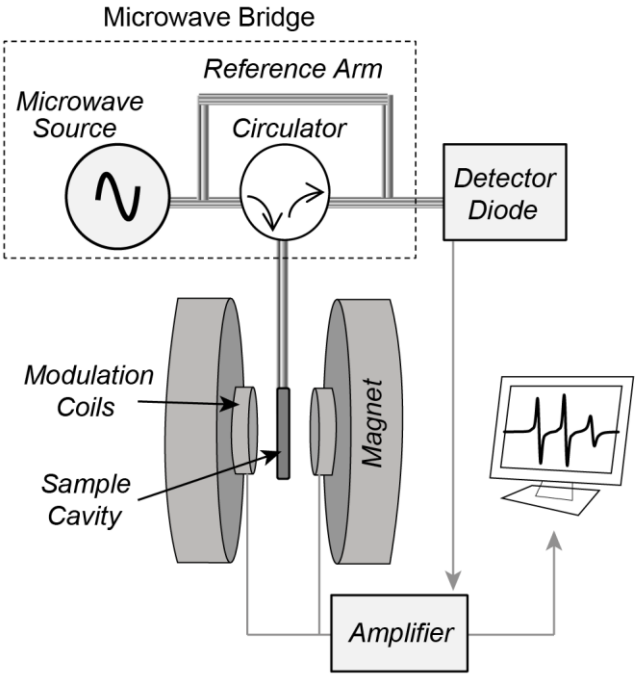

Figure 3.7 Typical block diagram of an EPR Spectrometer. Image from [20].

3.2.3 Spin label mobility – protein structure and dynamics

Proteins are highly dynamic structures. This includes dynamics associated with backbone and side-chain mobilities which are also essential contributors to protein function [21]. The SDSL-EPR method enables one to correlate structure and dynamics at local molecular, backbone, domain or protein level to the function of the protein. The simple analysis of the mobility of a spin label attached to a protein can reveal information about the protein structure and dynamics at these levels. Accessibility of paramagnetic species to different solvents can be measured by adding relaxing agents with different solubility properties. These agents include metal ion complexes such as NiEDDA or molecular oxygen. Collision of relaxing agents to a paramagnetic quencher species causes shortening of the longitudinal relaxation time (T_1) which translates to broadening of the EPR signal. Accessibility measurement is particularly useful in the case of proteins embedded in membrane bilayers. Mobility measurements are also often used to complement EPR accessibility measurements to nitroxide quenching agents to reveal local structure through cysteine scanning

approaches [22]. Analysis of EPR accessibility is not discussed further here as this experimental approach was not used in this Thesis.

The lineshape of the EPR spectrum, arising from an attached spin label in the protein, is highly sensitive to the local structural conformation and environment of the spin label [23]. The lineshape reflects the motional rate, anisotropy, amplitude and re-orientational motion of the spin label attached to a side chain. As such, a detailed analysis of the EPR lineshape can provide information regarding various motions, conformational changes, or even protein-protein interactions.

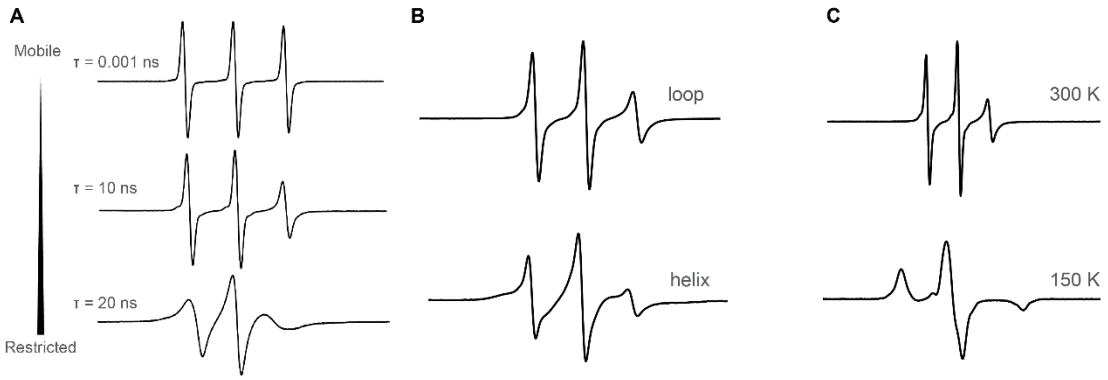

Figure 3.8 Reflection of the effect of the rotational correlation time on the EPR spectral lineshape. **(A)** For isotropic rotational motion, increasing peak broadness correlates with decreasing mobility; a restricted label gives rise to a broadened linewidth. Image adapted from [24]. **(B)** Different mobility of spin label located as different secondary environment. **(C)** At lower temperatures, the rotational motion of nitroxide label is lower.

In general, the mobility of a nitroxide spin label on a side chain can be characterised by three types of correlation times: (i) the rotational correlation time as a result of the tumbling of the entire protein, τ_R; (ii) the correlation time arose from the rotational isomerization about the bonds linking the nitroxide to the backbone of the protein, τ_B; and (iii) the correlation time due to the segmental motion of the backbone with respect to the protein i.e. backbone fluctuation, τ_S [25]. In the case of a membrane protein, or a large filamentous protein

system, such as a reconstituted muscle filament, τ_R can typically be ignored because the correlation time typically would exceed ~60 ns. Such a large τ_R time is beyond the sensitivity of the EPR timescale and is generally then a constant value for all side chains in the folded protein. The correlation time τ_B is a complex function of the structure of the label and is also expected to depend on the primary, secondary, tertiary and quaternary structure of the protein. Lastly, τ_S is determined by the backbone flexibility that arises from the local secondary structural nature of the attached site [25]. On average, broadening of the linewidths of an EPR spectrum is observed when there is a decrease in the motional freedom of the attached spin label (**Figure 3.8 A**).

The appearance of the nitroxide spectrum is influenced by the rotational correlation time. In a conventional X-band CW EPR the lineshape and appearance of the positive and negative peaks, respectively in the low and high field region, as well as central line of the CW spectrum represents the mobility of the nitroxide spin label. The narrower the line shape, the faster the motion of nitroxide spin, and vice versa. As such, the nitroxide spin label on a loop represents narrower lineshape, while the lineshape of a spin label on helical secondary structure is broader (**Figure 3.8 B**). The spectrum in fact is the sum of the spectra over all possible molecular orientations and blocking the molecular motion, e.g. by freezing the sample or in the case of bifunctional labels, remarkably changes the spectrum appearance to broader lineshape (**Figure 3.8 C**). MTSL, when attached to a protein, has a specific spectral shape arising by the reorientational freedom of the linker and five rotatable bonds. This spectral shape is affected by the intrinsic dynamic of the backbone as well as protein secondary, tertiary, and quaternary interactions. Thus, the lineshape analysis reports the dynamic of a specific labeled site in a protein which provides information of protein-protein interaction, and also protein translocation into the membrane.

In summary, the mobility of the side chain, reflected in EPR spectral lineshape provides a finger print of the protein fold and its dynamics. Also, the changes in mobility upon a ligand binding event can provide clues as to structural changes that occur within a protein (as done in ***Appendix 1***, Figure 4; where the impact of L29Q mutation on the conformation of TnC was shown).

3.2.4 EPR interspin distance measurements

3.2.4.1 Introduction

In addition to the mobility measurements described above, EPR spectroscopy can also be used to measure distances. The insertion of two cysteine residues and subsequent attachment of the spin label to the protein backbone enables spin-spin interactions to be obtained. Distances can be intra- or inter-subunit, if in a protein complex. While still a low resolution approach for revealing protein structure, together with mobility information or a static x-ray crystal structure, interspin distances can be a powerful means for 'building' a structure [26], verifying a structure or model [27], or distinguishing between two competing structural models [28].

In general, there are three categories over which EPR techniques can be used to detect interspin interactions. Firstly, distances can be analysed between 4 to 8 Å where the exchange interaction is most dominant [29]. For these very short distances, the effects on the double-labeled CW-EPR spectrum are that the classical three-line nitroxide spectrum becomes reduced to a single broadened feature [30]. The second category is for distances between 8 to 25 Å [31]. Dipole-dipole interactions over these distances manifest themselves as lineshape changes in CW-EPR, typically obtained under frozen conditions [32]. The final and more advanced technique used for detecting interspin interactions are pulsed EPR techniques. Pulsed EPR allows for measuring larger interspin distances greater than 18 Å and up to as long as 160 Å [33]. Two widely used pulsed EPR methods are the DEER (Double Electron-Electron Resonance) and DQC (Double Quantum Coherence) experiments [34]. Both these approaches extract weaker dipolar couplings. For some experimental studies, as the one in this Thesis, it is necessary to use both CW-EPR and pulsed EPR methods in parallel to measure all the possible distances within the detection ranges of both techniques (between 15-25 Å).

Measuring EPR interspin distance is important for monitoring conformational changes in proteins in response to their activation by a physiological relevant trigger, such as ligand binding, membrane insertion, pH change or, and in the case of this Thesis, phosphorylation (***Chapters 4 & 5***).

3.2.4.2 CW-EPR distances

Dipolar coupling of two nitroxide spin label causes line broadening of the continuous wave EPR spectrum. The strength of line broadening is related to the distance between two nitroxide probes. In fact, line broadening is a distances detection technique limited to short range distances (< 2 nm). A variety of approaches, such as convolution of low temperature un-broadened CW spectra (single spin) with the corresponding dipolar spectrum (double labeled), can be used to extract the mean distance and distribution between two spins [35]. CW line broadening has been used to measure short range intra-and inter-subunit interspin distance in Tn, respectively, to validate secondary structure and to determine the possible interaction between specific regions of different subunits [28].

The magnetic dipoles of two spin labels can interact through space. The dipolar coupling ω_{dd} between the two electron spins depends on their distance, r_{AB}, and their relative orientation, described by the angle θ of the distance vector between spins A and B with the external magnetic field B_0 , according to:

$$\omega_{dd} \propto \frac{1}{r_{AB}^3} (1 - 3cos^2 \theta) \qquad \text{Eqn. 3.6}$$

If the two spins are close enough (below 2 nm), the dipolar coupling is large and leads to CW line-broadening. Secondary structure analysis [28], tertiary structure analysis [36], spatial mapping of quaternary structure [30], and conformational changes [37, 38] can all be measured with the CW-EPR technique. However, due to the distance limit of this approach of ~25 Å, CW-EPR distance measurements are most suited for determining local protein folds.

Extraction of a distance from the lineshape broadening observed in the CW spectrum can be obtained through a number of ways. These include: (i) simulation of the full spectral lineshape [39]; (ii) simple qualitative analysis of the spectral lineshape at room temperature such as the relative intensity of the half-field transition or ratios of peak heights [40, 41]; or (iii) Fourier deconvolution of the spectra under cryogenic conditions [28, 32]. Method (i) is considered as the best for obtaining accurate distances. However, this requires the fitting of all parameters of the EPR spectrum to define both the interspin distance and the orientation

of the interspin vector relative to the magnetic axes of both spin labels, as well as separating the dipolar and exchange interactions. Accurately achieving such spectral simulations to account for the conformation, mobility and tether length of the spin labels requires a large amount of computational time [42, 43].

The Fourier deconvolution approach was the main approach used in this Thesis to obtain distances from the CW-EPR lineshape. The broadening function is obtained by deconvolution of the broadened spectrum of the double-labeled sample with the spectrum of a corresponding single labeled sample. A Gaussian curve is then fitted to the broadening function, and that fit function is reverse- Fourier transformed to provide the function from which the interspin distance is calculated [32]. In next section, the experimental consideration and Fourier deconvolution method is described in further detail.

3.2.4.2.1 Frozen state CW distances – Fourier Deconvolution

The Fourier deconvolution method can be used to obtain interspin distances from the CW lineshape up to ~25 Å [32]. It is based on the assumption that double labeled EPR spectrum is the convolution of the dipolar broadening function and the single labeled spectrum. According to this method, two unpaired electrons separated by the distance '*r*' are coupled by electron-electron dipolar and other short-range interactions such as *J* coupling. However, when $r \geq 8$ Å, dipolar interactions dominate. The broadening function of EPR absorption lines, *B*, in the magnetic field, is then:

$$B = \frac{3g\beta(3\cos 2\theta - 1)}{4r^3} \qquad \text{Eqn. 3.7}$$

where *g* is the isotropic value of the electrons, β is the electron Bohr magneton and θ is the angle between the interspin vector and the applied magnetic field. An advantage of this approach is that the broadening function can identify and subtract the amount of any singly-labeled protein that may be present in the sample. This is important if 100% labeling at both label sites cannot be achieved. However, deconvolution measurements assume that the motion of spin label is restricted. This is achieved by snap-freezing and cooling of the sample to 150 K. The Fourier deconvolution approach is then valid as it is based on the assumption that there is a random distribution of relative orientations of the spin label axis relative to the interspin vector. In most cases this appears to be a sound assumption to make, as

confirmed by crystal structures of several spin labeled constructs [44]. However, freezing of the EPR samples may induce undesired conformational changes to the proteins. If this is suspected, then alternative approaches can be used to measure the interspin distance under physiological conditions in solution and at ambient temperatures [45].

3.2.4.2.2 Experimental considerations for CW distances – Fourier Deconvolution

For Fourier deconvolution analysis of CW-EPR, the EPR spectral lineshape must be collected for both the 'single' spin labeled components and the double labeled sample. In this Thesis, a Bruker E680 X/Q-band pulsed EPR instrument operating at 9 GHz was used for CW-EPR distance measurements under cryogenic conditions. Typical EPR instrument parameters included: a center field of ~3480 G, a sweep width of 300 G, modulation amplitude of 1 G, a microwave power of 0.02 mW and 4 scan repetitions. EPR samples of ≥ 50 µL with ≥ 10 µM of MTSSL signal, were loaded into a clean 4 mm OD quartz tube (Wilmad Labglass) and positioned in the middle of an MD5 standard rectangular EPR resonator which was held perpendicular to the static field. The cavity was tuned and the CW-EPR spectra were collected under cryogenic conditions (150 K). For isolated Tn samples, a cryo protectant (glycerol) was added to a final concentration of 40% to minimise ice crystals forming molecular clusters.

The two single non-interacting spectra were averaged (using a Matlab suite of programs, P Fajer, Florida State University) to generate an EPR lineshape for the non-interacting spectrum (*S*) for comparison to the double-labeled interacting spectrum (*D*). This was performed by normalising each of the two single non-interacting EPR spectra for unit area by dividing by the double integral so that each of the single non-interacting spectrum generated represented the same number of spins. It was important that the EPR spectra were processed to remove baseline artefacts (offset and/or slope errors) prior to analysis. Increasing the scan-width up to 300 G was also done to avoid the errors associated with baseline distortions of spectra. Additionally, labeling was optimized to ensure the labeling ratio of the cysteine residues was close to unity for optimal analysis of the interspin distance, and to avoid bias of the spectrum to the non-interacting spins. In practice, the limit for analysis by the CW method is ~20 Å. The dipolar interaction was often very difficult to detect when measuring longer distances in the range of 20 – 25 Å as there was a gradual loss in

detectable line-broadening. For distances that appeared to fall between 20 – 25 Å, DEER was also performed to confirm the magnitude of the interspin interaction.

3.2.4.3 Pulsed EPR Distances

Pulsed techniques are used to measure the weaker dipolar interactions that could not be observed in the CW lineshape. Pulsed techniques can therefore extend the measurable range for interspin interactions up to ~60 to 80 Å, and as large as 160 Å [46]. There are several available pulse methods that can be used to measure interspin distances with the most common one being the DEER technique. DEER is also known as the pulsed Double Electron-Electron resonance or PELDOR (Pulse Electron Electron Double Resonance).

In this study, DEER was used because of its simple instrumentation requirements and adaptable pulse sequences. DEER has the additional advantage over CW-EPR in that the analysis can also provide a description of the distribution of the measured distance (width, Δ*r*) and reveal if multiple distance populations are present [47]. The 4-pulse DEER is the vast used method to extract interspin distances on protein. This technique was introduced in 2000 after developing dead-time free pulses [48], and later development of software for data analysis [49], made it possible to measure distances longer than 1.5 nm with higher precise distributions. The principle of DEER is to excite one of the spins using a sequence of three pluses usually with length orders of 16, 32, and 32 ns to *observe* the spin echo (**Figure 3.9 A**). However, the position of pulses can vary to achieve the highest echo. The second spin (known as pump) is excited after second pulse in observe sequence to induce coupling with first spin (**Figure 3.9 B**). This coupling reduces the observe echo intensity along the sweep time of pump pulse. The echo modulations can be transformed to dipolar coupling (ν_{dd}) to extract interspin distances (for a comprehensive review of principles of DEER see [47]). The faster the echo decay, the shorter the distance between spins. DEER makes the distance constrains experimentally available to describe transmembrane regions of proteins (3–4 nm), or large protein complexes (5–10 nm) [46]. The upper distance limit sensitivity depends on the relaxation properties of the spin probes and by spin concentration. The longest distance detected by DEER is 16 nm and measured in an 80 μs DEER trace [33].

The rotation of the dihedral angles in the linker result in different spatial possibilities and lead to a rotameric distribution of the spin label (σ = ~3 Å in the absence of protein backbone motion; σ is the width of distance distribution as a result of spin rotation)[50]. The interspin distance measurements provide direct information on the nature and the extent of the conformational changes. However, to use the distance distribution for structural modelling, extrapolation of distances to the backbone is needed, so the rotameric states of the spin label need to be described. The rotameric states for a number of spin labels, especially for MTSL, have been rather well established [51], which enables the comparison of experimental data with an available structure, as well as modeling of a new functional or an oligomeric state from an existing structure [46].

3.2.4.3.1 Double Electron-Electron Resonance-theoretical rational

In DEER experiment a refocused Hahn echo is generated with the four pulse sequence $\pi/2–\tau_1–\pi–\tau_1—echo_1 –\tau_2–\pi– \tau_2—echo_2$ applied at the observer frequency (ν_o) on the first population of spins (A spins) (**Figure 3.10 A**). The spin A is excited with a π/2 pulse which tips the spins into the xy plane. Some spins will have different angular rates and will dephase in the xy plane due to the field inhomogeneities and different resonance fields. Applying a π pulse changes the direction of xy plane which generates a spin echo. Once spin echo start dephasing again, another π pulse is applied to refocus the echo. This second pulse is irradiated at the pump frequency ν_p is applied on the *B* spin at a variable time *t* with respect to the observer echo. The magnitude of the refocused echo is then recorded as a function of the pump pulse time t where the time of the first Hahn echo is set as $t = 0$ (**Figure 3.9 B**). The two frequencies of observe and pump are separated enough that the width of the pumping pulse does not excite the observed spins directly (**Figure 3.9 C**).

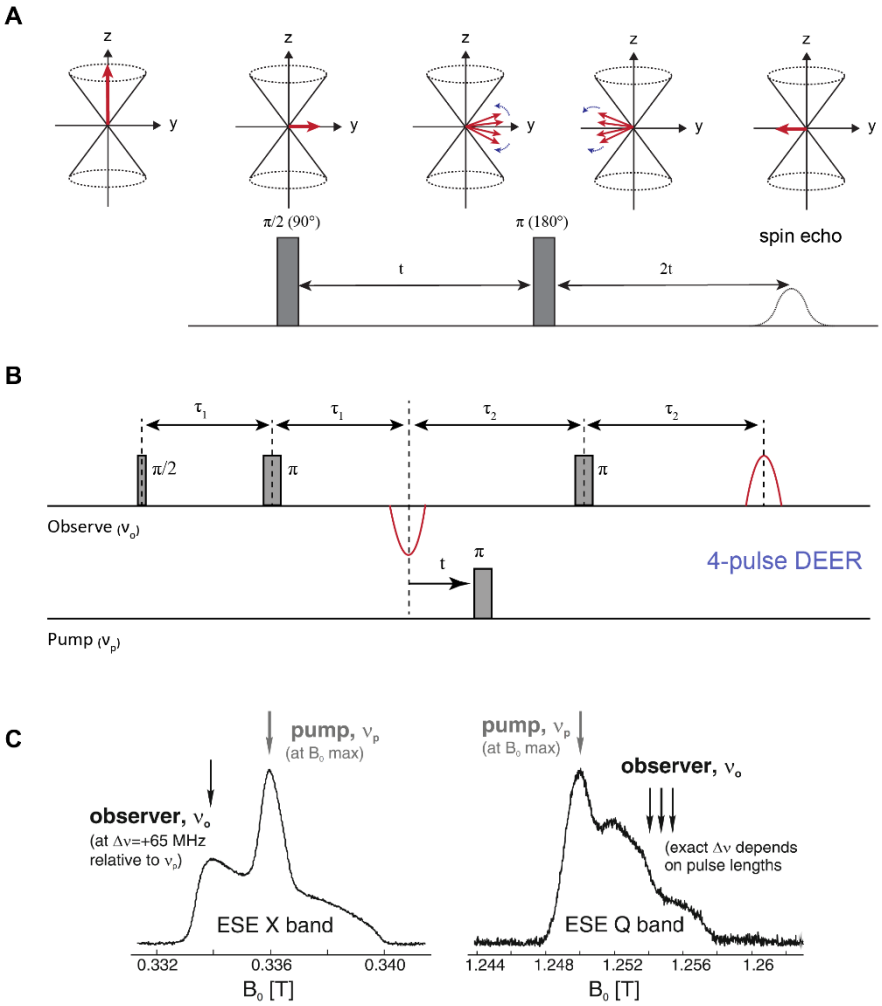

Figure 3.9 (A) Hahn echo for refocussing. The net magnetization in the z-direction is rotated to the y-direction by a 90° pulse (π/2). After the time t, a 180° pulse (π) inverts the magnetization to -y, leading to a refocusing of the magnetization vector at the time 2*t*, which generates the spin echo (adapted from [2]) **(B)** The four-pulse sequence for DEER includes an observer pulse (ν_o) which generates a spin echo and sweeping a pumping pulse (ν_p). **(C)** The field swept electron spin echo (ESE) detected spectra from a pair of coupled nitroxides at X and Q bands. The position of the observer and the pump has been indicated with arrows. Image is from [52].

When the pump pulse is applied, the spin packet (designated as Spin B) with the resonance frequency of ν_p will be excited and the spin state is inverted. This result in the inversion of the local magnetic field generated by Spin B at the location of Spin A (**Figure 3.10 B**). Inversion of Spin B causes the electron–electron coupling, ω_{ee}, and as a result change in the frequency, or more precisely the angular velocity of Spin A by (**Figure 3.10 C**) [47, 53].

Varying the timing of the pump pulse result in a phase gain of the A spin by $\phi = \omega_{ee}\, t$ and oscillation of the echo amplitude *V*. The resulting spectrum is a product of two contributions[54]:

$$V(t) = F(t) \times B(t) \qquad \text{Eqn. 3.8}$$

B(t), the intermolecular contribution, commonly known as the background function, arises from the interaction between spins in the neighbouring biomolecules. *F(t)*, also known as the form factor which is the desired intramolecular interaction, is the result of the interaction of the spins within the same biomolecular unit being observed. As a result of spin coupling, the echo amplitude of spin A is reduced in proportion to the excited fraction Δ (<1) of spin B; and the resulting amplitude as a function of time is given by:

$$F(t) = 1 - \Delta[1 - \cos \omega_{ee}\, t] \qquad \text{Eqn. 3.9}$$

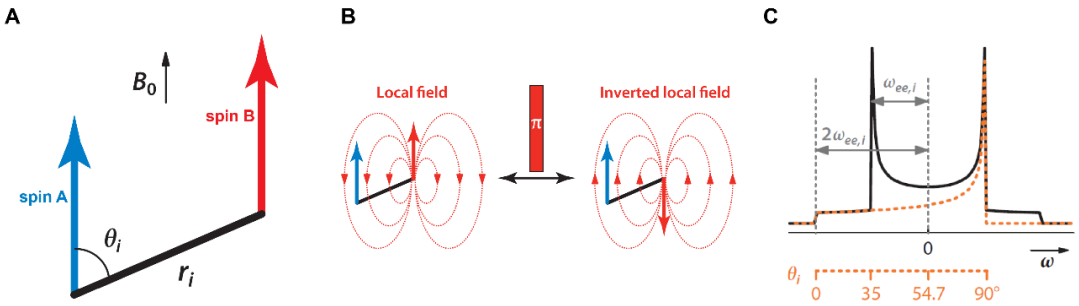

Figure 3.10 (A) Distance vector between spin A (blue) and B (red) with length of r_i at an angle θ_i in a magnetic field with B_0 vector. **(B)** The picture of local field at spin A. The π pump pulse at frequency ω_B inverts the state of spin B (red), and as a result inverts the local field imposed by spin B at the site of spin A (blue). **(C)** Dipolar spectrum, or Pake pattern (solid line), as detected by DEER and frequency $\omega_{ee,i}$ correlation with angle θ_i (orange dotted line and scale). Image from [47].

3.2.4.3.2 DEER at Q-band frequency

The principles of performing DEER measurements with Q-band frequency (34 GHz) is similar to X-band. The only difference is the resonator and microwave bridge. As the frequency increases, the magnetic field required for splitting the spins energy level is increased. As a result, the appearance of electron spin echo (ESE)-detected spectra is different compare to X-band (**Figure 3.9 C**).

In this Thesis, Q-band frequency was used to measure interspin distances presented in **Chapter 5**. Therefore, some advantages of Q-band will briefly be summarised here. The first use of Q-band DEER was reported in 2009 by Ghimire *et al*. [55]. The increased Boltzmann population difference between the spin states at the higher Zeeman energy and an increased sensitivity of the instrument/resonator at higher frequency both contribute to the improvement of the signal-to-noise ratio, resulting in significant boost in sensitivity [55, 56]. Together, this also makes the data acquisition by Q-band DEER experiments possible within minutes to hours in contrast to the lengthy time required by the X-band DEER experiments (hours to days, requiring hundreds of scans) [55]. The spectra and distance distributions are compared between X- and Q-band in **Figure 3.11**. Below are listed a few additional advantages of Q-band measurement.

Sensitivity: In X-band measurement, about 100-200 µM of the sample, in a volume of 100 µL (in 4mm o.d. tube) is required. In contrast, only 20–30 µM in 40 µl of sample volume is sufficient for Q-band resonators accepting 3 mm tubes. The resolution of DEER measurement by Q-band (signal to noise ratio) is therefore 20 fold higher and detection time is 400 fold smaller with respect to X-band.

Orientation selection: in DEER experiment, pulses excite only a small part of the spectrum, and therefore, only a subsection of all the molecular orientations in the magnetic field. Data analysis, to achieve distance distributions, neglects the correlation between B spin inversion efficiency Δ and electron-electron coupling $\omega_{ee,i}$ by assuming that values of angle θ_i (**Figure 3.10 A**) are selected with probability $\sin \theta_i$, corresponding to an isotropic powder average. As both pump and observer pulses are selective, this assumption does not apply. At Q-band

frequency, when coupled with the amplifier, non-selective pulses are used which minimize orientation section artefacts in the DEER traces that occur with X-band [51].

Nuclear modulation artefacts: Under optimum sensitivity conditions, there is still a slight overlap in excitation bands of the pump and observer pulses. Therefore, there is a slight probability for excitation of forbidden electron-nuclear transitions of A spins by the pump pulse, which causes nuclear modulation in the DEER signal [57]. The majority of modulation arises from protons or deuterons in matrix. Proton modulation is less prominent at Q-band frequencies and the deuterium modulation at approximately 8 MHz causes artefacts at approximately 2 nm (lower detection limit). The latter can be suppressed with systematic variation of the interpulse delay τ_1 ($\Delta\tau_1$ = 16 ns).

3.2.4.3.3 Distance Information

Generally, distances between two spin labels are distributed according to the conformational distribution of the spin label and protein backbone. So, this distribution, when close to a Gaussian distribution, can be characterized by its mean distance (*r*) and width (*Δr*).

3.2.4.3.3.1 Mean distances, r

At standard X-band conditions, the modulation depth decreases markedly below 2.0 nm. Modulation depth is the extent to which the echo amplitude is reduced in proportion with the fraction of spins excited with pump pulse (*Δ*) This often means that measurement of distances shorter than 1.7 nm is not reliable, unless the distribution is very narrow [35]. The upper limit for measuring an accurate mean distance can be approximated by $r_{max} \approx 5\sqrt[3]{t_{max}/(2\mu s)}$ nm. Deuteration of the same protein is a practical consideration that can be used to extend the transverse relaxation time, and therefore evolution time t_{max}, to approximately 24 µs which corresponds to a limit of approximately 11.5 nm [58]. The presence of spin pairs at longer distances can be recognized, but quantitative interpretation of such longer distances should be avoided.

3.2.4.3.3.2 Width of distance distributions, Δr

The width of the distance distribution is encoded in the decay rate of the dipolar oscillations in the form factor, *F*(*t*). Accordingly, several oscillations must be observed for an accurate determination of the width. The upper limit for such determination is $\Delta r_{max} \approx 4\sqrt[3]{t_{max}/(2\mu s)}$ nm. The detection limits for the width of distribution for soluble proteins in deuterated buffer and for deuterated soluble proteins are 6 and 9 nm, respectively.

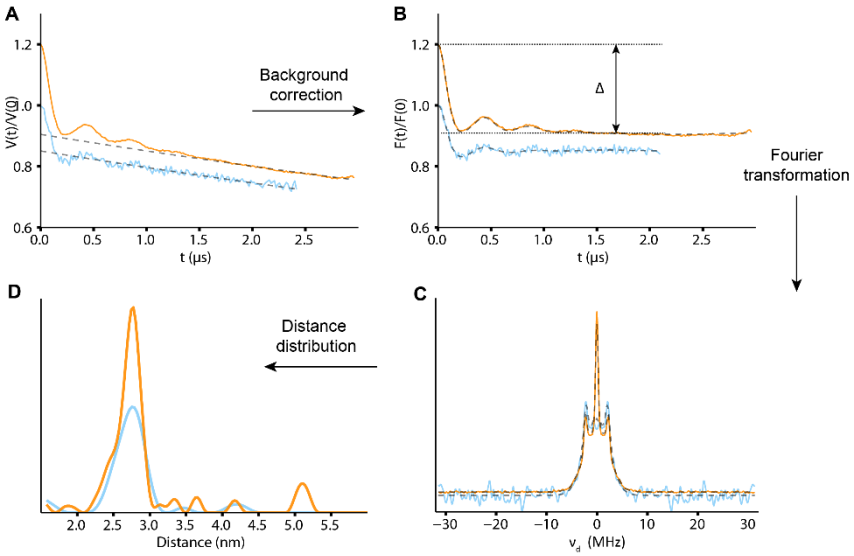

Figure 3.11 DEER measurements at X (light blue) and Q bands (orange) of the same Tn sample labeled at residues TnC35 and TnI159. **(A)** The normalized and phase-corrected initial experimental trace *V(t)/V(0)*. **(B)** DEER form-factor *F(t)* obtained after background correction. **(C)** Dipolar domain spectrum (Pake pattern). It is also called frequency domain; and **(D)** distance-distribution profile. The DeerAnalysis package (**Section 3.2.5.3**) was used for data processing; fits based on Tikhonov regularization are shown as black dashes. Δ is the modulation depth.

3.2.5 Data collection and analysis of DEER spectra

3.2.5.1 EPR Measurements

In this study, measurements were done for samples by both CW and DEER (X-band or Q-band). Samples were prepared in 40% glycerol and inserted into the appropriate tubes. For Q-band measurements, samples were prepared in deuterated glycerol to prolong the spin relaxation time. CW and DEER measurements were performed at 150 and 65 K, respectively. Both DEER (X-band or Q-band) experiments were performed with a shot repetition time of ≥ 2 ms, using a 16 ns π/2 pulse and a 32 ns π pulse in an over coupled dielectric resonator. Both the length of the pump pulse and microwave power were optimized to achieve the highest echo intensity. The pump and observer pulses were separated by 70-80 and 80-100 MHz for X- and Q-band frequencies, respectively. Data acquisition for X-band measurements were ~12 h to achieve a sufficient signal to noise ratio for reliable analysis. The acquisition time for the longest distance measurement in Q-band was ~4 h. In contrast, the shortest acquisition time for Q-band DEER measurements was 1 hours.

3.2.5.2 Rotamer Prediction

Depending on the labeling site, spin labels can adopt different rotamers. Each rotamer represents a unique conformation of the spin-label side chain arose from the variation in dihedral angels [47]. In this Thesis, the software package MMM [51] was used to simulate the conformations adopted by the spin probe with respect to the protein backbone (**Figure 3.12**). MMM applies Molecular Dynamics (MD) approaches to calculate the possible rotamers of the spin label. Simulation of the spin label rotamers can help to select the labeling site appropriately. Selection of spin labeling sites is restricted by the requirements for sufficient accessibility and avoidance of structural distortion. Spin-labeling site scans using a rotamer library approach can provide information on tight sites, where labeling may fail or distort structure, and on very loose sites, where broad conformational distributions are expected [47]. In addition, MMM was used to predict the interspin distances and distributions. Therefore, having an idea of the expected distance can be helpful to setup parameters for DEER experiment. However, for proteins with a high degree of inherent dynamics, the difference between predicted and experimental distances can be significant.

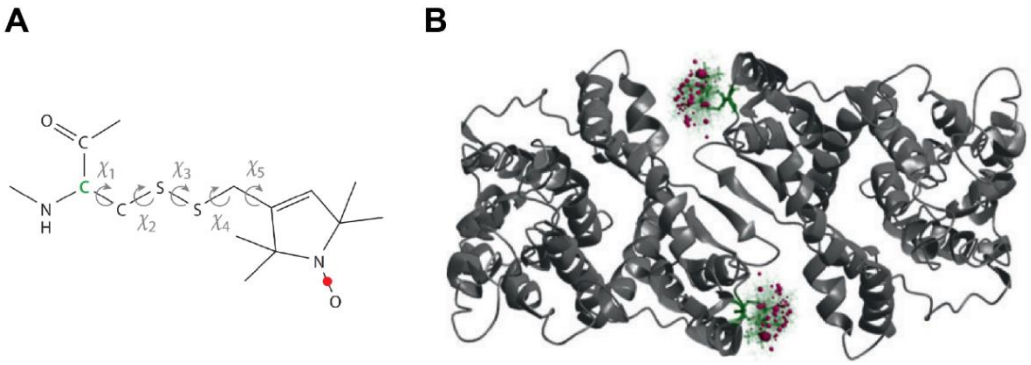

Figure 3.12 The conformational distribution of spin-label. **(A)** The rotatable bonds (dihedrals χ_1 . . . χ_5) result in distribution of the electron spin position (red dot) with respect to the C_α atom (green). **(B)** Example of predicted conformational distribution of spin label MTSL as represented by green stick models. Red spheres represent the location of the electron spin, with their radii corresponding to rotamer populations. Image from[47].

3.2.5.3 Distance and Distribution Analysis

DeFit is a DEER data analysis program in which a Gaussian fitting approach is used describe mean distances and distributions [53]. In this Thesis, DeFit was predominantly used for the analysis of all the DEER spectra. DeFit uses Gaussian distance distribution function to simulate DEER spectra and tests them against the experimental data. DeFit uses several random parameter sets as the starting conditions and then finds the best solution by minimising the sum-of-squares deviation using the Simplex algorithm. In DeFit, one can determine the number of distances by applying *F-test* as a function of the number of Gaussians, and as a result, determine how many distances are justified by the experimental data. The uniqueness of the resolved distances is determined from the Monte Carlo sampling of the full parameter space. The contours of the least square fit (reduced χ^2), as a function of Gaussian parameters, is used to determine the confidence interval for the best solution. Since DEER analysis can be viewed as an ill-defined problem, the uniqueness of fitting is a significant issue [59]. DeFit is able to check the uniqueness of fitting and estimate the errors of fitted parameters by using statistical analysis and a simple Gaussian model with a limited number of parameters [53]. The signal-to-noise ratio limits the number of

parameters that can be extracted from an experimental spectrum. As the number of components is increased, a good guide to how many components are justified by the experimental spectra is the change in “goodness of fit” parameter. This program is available from the Fajer lab website (http://biophysics.fsu.edu/fajer/software/defit-2/).

Of note, an alternative approach to extract the distance information from the DEER data is ‘DeerAnalysis’. The DeerAnalysis package applies Tikhonov requlariza tion approach to extract mean distance and distributions from DEER spectra [60]. This approach assumes that the dipolar spectrum (Pake pattern) from the DEER data represents all orientations of the sample, i.e., there is no orientation selection in sample excitation, therefore the spectrum corresponding to a known distance distribution *P(r)* for a pair of spin can be computed exactly by superposition of Pake patterns. Likewise, the theoretical form factor, i.e., the theoretical DEER modulation curve without background signal, can be computed for a probability distribution function *P(r)*. By comparing the experimental and theoretical curves, the Tikhonov regularization approach can find optimum distance distribution *P(r)* by minimizing the objective function. The major advantage of this fitting approach is the ability to estimate the errors and to check for the uniqueness of fit for the determined distance distribution(s). The disadvantage of fitting methods is therefore an assumption of a model. DeerAnalysis program can be downloaded from (https://epr.ethz.ch/software.html).

References

1. Pavia, D.L., et al., *Introduction to Spectroscopy*. 5th ed. 2014, Sramford, USA: Cengage Learning.
2. Klostermeier, D. and M.G. Rudolph, *Biophysical Chemistry*. 2017: CRC Press, Taylor & Francis Group.
3. Atkins, P. and J. de Paula, *Physical Chemistry for the Life Sciences*. 2nd ed. 2011, New York: Oxford University Press.
4. Rasia, R.M., et al., *Parallel screening and optimization of protein constructs for structural studies.* Protein Sci, 2009. **18**(2): p. 434-9.
5. Keeler, J., *Understanding NMR Spectroscopy*. 2011, Cambridge: Wiley.
6. Fernandez, C. and G. Wider, *TROSY in NMR studies of the structure and function of large biological macromolecules.* Curr Opin Struct Biol, 2003. **13**(5): p. 570-80.
7. Tzakos, A.G., et al., *NMR techniques for very large proteins and rnas in solution.* Annu Rev Biophys Biomol Struct, 2006. **35**: p. 319-42.
8. Battiste, J.L. and G. Wagner, *Utilization of site-directed spin labeling and high-resolution heteronuclear nuclear magnetic resonance for global fold determination of large proteins with limited nuclear overhauser effect data.* Biochemistry, 2000. **39**(18): p. 5355-65.
9. Yu, D., A.N. Volkov, and C. Tang, *Characterizing dynamic protein-protein interactions using differentially scaled paramagnetic relaxation enhancement.* J Am Chem Soc, 2009. **131**(47): p. 17291-7.
10. Tang, C., et al., *Visualizing transient events in amino-terminal autoprocessing of HIV-1 protease.* Nature, 2008. **455**(7213): p. 693-6.
11. Tang, C., J. Iwahara, and G.M. Clore, *Visualization of transient encounter complexes in protein-protein association.* Nature, 2006. **444**(7117): p. 383-6.
12. Iwahara, J. and G.M. Clore, *Detecting transient intermediates in macromolecular binding by paramagnetic NMR.* Nature, 2006. **440**(7088): p. 1227-30.
13. Clore, G.M. and J. Iwahara, *Theory, practice, and applications of paramagnetic relaxation enhancement for the characterization of transient low-population states of biological macromolecules and their complexes.* Chem Rev, 2009. **109**(9): p. 4108-39.
14. Cordina, N.M., et al., *Interdomain orientation of cardiac troponin C characterized by paramagnetic relaxation enhancement NMR reveals a compact state.* Protein Sci, 2012. **21**(9): p. 1376-87.
15. Johnson, P.E., et al., *The cellulose-binding domains from Cellulomonas fimi beta-1, 4-glucanase CenC bind nitroxide spin-labeled cellooligosaccharides in multiple orientations.* J Mol Biol, 1999. **287**(3): p. 609-25.
16. Volkov, A.N., et al., *Solution structure and dynamics of the complex between cytochrome c and cytochrome c peroxidase determined by paramagnetic NMR.* Proc Natl Acad Sci U S A, 2006. **103**(50): p. 18945-50.
17. Solomon, I., *Relaxation processes in a system of two spins.* J Physical Review, 1955. **99**(2): p. 559.
18. Iwahara, J., C.D. Schwieters, and G.M. Clore, *Ensemble approach for NMR structure refinement against (1)H paramagnetic relaxation enhancement data arising from a flexible paramagnetic group attached to a macromolecule.* J Am Chem Soc, 2004. **126**(18): p. 5879-96.
19. Fajer, P.G., *Electron spin resonance spectroscopy labeling in peptide and protein analysis.* Encyclopedia of Analytical Chemistry: Applications, Theory and Instrumentation, 2006.

20. Brown, L.J. and J.E. Hare, *Electron Paramagnetic Resonance: Site-Directed Spin Labeling*, in *Pumps, Channels Transporters: Methods of Functional Analysis*, R.J. Clarke and M.A.A. Khalid, Editors. 2015, John Wiley & Sons: New Jersey. p. 327.
21. McCammon, J.A. and M. Karplus, *The dynamic picture of protein structure.* Accounts of Chemical Research, 1983. **16**(6): p. 187-193.
22. Hubbell, W.L., et al., *Technological advances in site-directed spin labeling of proteins.* Curr Opin Struct Biol, 2013. **23**(5): p. 725-33.
23. Fanucci, G.E. and D.S. Cafiso, *Recent advances and applications of site-directed spin labeling.* Curr Opin Struct Biol, 2006. **16**(5): p. 644-53.
24. Klug, C.S. and J.B. Feix, *Methods and applications of site-directed spin labeling EPR spectroscopy.* Methods Cell Biol, 2008. **84**: p. 617-58.
25. McHaourab, H.S., et al., *Motion of spin-labeled side chains in T4 lysozyme. Correlation with protein structure and dynamics.* Biochemistry, 1996. **35**(24): p. 7692-704.
26. Perozo, E., *New structural perspectives on K(+) channel gating.* Structure, 2002. **10**(8): p. 1027-9.
27. Celia, H., et al., *Structural insight into the role of the Ton complex in energy transduction.* Nature, 2016. **538**(7623): p. 60-65.
28. Brown, L.J., et al., *Structure of the inhibitory region of troponin by site directed spin labeling electron paramagnetic resonance.* Proc Natl Acad Sci U S A, 2002. **99**(20): p. 12765-70.
29. Miick, S.M., et al., *Short alanine-based peptides may form 310-helices and not α-helices in aqueous solution.* Nature, 1992. **359**(6396): p. 653.
30. Chen, M., et al., *Investigation of alpha-synuclein fibril structure by site-directed spin labeling.* J Biol Chem, 2007. **282**(34): p. 24970-9.
31. McHaourab, H.S., et al., *Conformation of T4 lysozyme in solution. Hinge-bending motion and the substrate-induced conformational transition studied by site-directed spin labeling.* Biochemistry, 1997. **36**(2): p. 307-16.
32. Rabenstein, M.D. and Y.K. Shin, *Determination of the distance between two spin labels attached to a macromolecule.* Proc Natl Acad Sci U S A, 1995. **92**(18): p. 8239-43.
33. Schmidt, T., et al., *Long Distance Measurements up to 160 A in the GroEL Tetradecamer Using Q-Band DEER EPR Spectroscopy.* Angew Chem Int Ed Engl, 2016. **55**(51): p. 15905-15909.
34. Borbat, P.P., H.S. McHaourab, and J.H. Freed, *Protein structure determination using long-distance constraints from double-quantum coherence ESR: study of T4 lysozyme.* J Am Chem Soc, 2002. **124**(19): p. 5304-14.
35. Banham, J.E., et al., *Distance measurements in the borderline region of applicability of CW EPR and DEER: a model study on a homologous series of spin-labelled peptides.* J Magn Reson, 2008. **191**(2): p. 202-18.
36. Xiao, W., et al., *The neuronal t-SNARE complex is a parallel four-helix bundle.* Nat Struct Biol, 2001. **8**(4): p. 308-11.
37. Hanson, S.M., et al., *Visual arrestin binding to microtubules involves a distinct conformational change.* J Biol Chem, 2006. **281**(14): p. 9765-72.
38. Xiao, W., et al., *Light-induced rotation of a transmembrane alpha-helix in bacteriorhodopsin.* J Mol Biol, 2000. **304**(5): p. 715-21.
39. Hustedt, E.J., et al., *Molecular distances from dipolar coupled spin-labels: the global analysis of multifrequency continuous wave electron paramagnetic resonance data.* Biophys J, 1997. **72**(4): p. 1861-77.
40. Eaton, S.S., et al., *Use of the ESR half-field transition to determine the interspin distance and the orientation of the interspin vector in systems with two unpaired electrons.* J Am Chem Soc, 1983. **105**(22): p. 6560-6567.
41. Sun, J., et al., *Proximity between periplasmic loops in the lactose permease of Escherichia coli as determined by site-directed spin labeling.* Biochemistry, 1999. **38**(10): p. 3100-5.

42. Hustedt, E.J., et al., *Dipolar coupling between nitroxide spin labels: the development and application of a tether-in-a-cone model.* Biophys J, 2006. **90**(1): p. 340-56.
43. Hustedt, E.J. and A.H. Beth, *Nitroxide spin-spin interactions: applications to protein structure and dynamics.* Annu Rev Biophys Biomol Struct, 1999. **28**: p. 129-53.
44. Langen, R., et al., *Crystal structures of spin labeled T4 lysozyme mutants: implications for the interpretation of EPR spectra in terms of structure.* Biochemistry, 2000. **39**(29): p. 8396-405.
45. Altenbach, C., et al., *Estimation of inter-residue distances in spin labeled proteins at physiological temperatures: experimental strategies and practical limitations.* Biochemistry, 2001. **40**(51): p. 15471-82.
46. Bordignon, E. and S. Bleicken, *New limits of sensitivity of site-directed spin labeling electron paramagnetic resonance for membrane proteins.* Biochim Biophys Acta Biomembr, 2018. **1860**(4): p. 841-853.
47. Jeschke, G., *DEER distance measurements on proteins.* Annu Rev Phys Chem, 2012. **63**: p. 419-46.
48. Spiess, H.W., *Addendum to the paper "Dead-time free measurement of dipole-dipole interactions between electron spins" by M. Pannier, S. Veit, A. Godt, G. Jeschke, and H.W. Spiess [J. Magn. Reson. 142 (2000) 331-340].* J Magn Reson, 2011. **213**(2): p. 326-8.
49. Jeschke, G., et al., *DeerAnalysis2006—a comprehensive software package for analyzing pulsed ELDOR data.* Applied Magnetic Resonance, 2006. **30**(3): p. 473-498.
50. McHaourab, H.S., P.R. Steed, and K. Kazmier, *Toward the fourth dimension of membrane protein structure: insight into dynamics from spin-labeling EPR spectroscopy.* Structure, 2011. **19**(11): p. 1549-61.
51. Polyhach, Y., E. Bordignon, and G. Jeschke, *Rotamer libraries of spin labelled cysteines for protein studies.* Phys Chem Chem Phys, 2011. **13**(6): p. 2356-66.
52. Bordignon, E. and Y. Polyhach, *EPR techniques to probe insertion and conformation of spin-labeled proteins in lipid bilayers.* Methods Mol Biol, 2013. **974**: p. 329-55.
53. Fajer, P.G., L. Brown, and L. Song, *Practical pulsed dipolar ESR (DEER)*, in *ESR spectroscopy in membrane biophysics, Biological magnetic resonance*, M.A. Hemminga and L.J. Berliner, Editors. 2007, Springer: New York. p. 95–128
54. Milov, A.D., A.B. Ponomarev, and Y.D. Tsvetkov, *Electron-electron double resonance in electron spin echo: Model biradical systems and the sensitized photolysis of decalin.* J Chem phys lett, 1984. **110**(1): p. 67-72.
55. Ghimire, H., et al., *Significantly improved sensitivity of Q-band PELDOR/DEER experiments relative to X-band is observed in measuring the intercoil distance of a leucine zipper motif peptide (GCN4-LZ).* Biochemistry, 2009. **48**(25): p. 5782-4.
56. Zou, P. and H.S. McHaourab, *Increased sensitivity and extended range of distance measurements in spin-labeled membrane proteins: Q-band double electron-electron resonance and nanoscale bilayers.* Biophys J, 2010. **98**(6): p. L18-20.
57. Pannier, M., et al., *Dead-time free measurement of dipole-dipole interactions between electron spins.* J Magn Reson, 2000. **142**(2): p. 331-40.
58. Ward, R., et al., *EPR distance measurements in deuterated proteins.* J Magn Reson, 2010. **207**(1): p. 164-7.
59. Jeschke, G., et al., *Direct conversion of EPR dipolar time evolution data to distance distributions.* J Magn Reson, 2002. **155**(1): p. 72-82.
60. Jeschke, G., et al., *DeerAnalysis2006—a comprehensive software package for analyzing pulsed ELDOR data.* J Appl Magn Res, 2006. **30**(3-4): p. 473-498.

4. Paper 1 – Phosphorylation effect on interaction of the TnI N-extension region with TnC.

4.1 Introduction

The focus of this project was to investigate the effect of phosphorylation on the dynamics of cardiac specific N-terminal of Troponin I and its possible interaction with other components in intact Tn, especially with N-domain of Troponin C. The structure of Troponin I N-terminal region is not revealed in the sole crystal structure of Troponin. This region has two phosphorylation sites and has been proved to play a significant physiological role. There have been a few NMR and MD studies which have proposed a structural model for the dynamics and interaction of the TnI N-terminal region with TnC in response to phosphorylation. These models are all reviewed in **Section 1.6**.

The experiments described in this manuscript were designed to not only test the validity of the previous models, but to also obtain additional experimental evidence which could further contribute to an understanding of the dynamics of Troponin I N-terminal region as a result of phosphorylation and how this may contribute to control of muscle regulation in the cardiac isoform. In this manuscript, a combination of PRE-NMR (as described in **Section 3.1.5**) and EPR methods (as described in **Section 3.2.4**) were performed. Together, these approaches provide both mid-range (12 to 25 Å) and long-range (20 to 60 Å) distance constraints which can help test the structural model or further build a more comprehensive model of the dynamics of Tn complex protein systems.

The results presented in this manuscript provide distance constraints between the TnI N-extension (referred to as NH_2-TnI in this manuscript) and TnC using PRE-NMR and EPR. For PRE-NMR, three spin labels were introduced across the N-terminal region of TnI (Ser5, Ala28, Ser39) to ensure comprehensive coverage across this important domain. For EPR, the two interspin distances TnC35/TnI39 and TnC84/TnI39 were obtained in the different states of phosphorylation and Ca^{2+} binding. The results of this study demonstrated that phosphorylation abolishes the interaction of the TnI N-extension with TnC N-domain close to the Ca^{2+} binding site (Site II) and the hydrophobic switch pocket. Surprisingly,

phosphorylation also appears to induce a rotational movement in the N-domain of TnC which may be optimal to position the TnC N-domain for interaction with the TnI regulatory switch peptide.

4.2 Authors' contributions

This research was conducted under the supervision of A/Prof. Louise Brown. The design of the experiments and the writing of the manuscript was guided by Dr Brown across all preparation stages. Dr Brown also organised this project as a collaboration with A/Prof. Dane McCamey's group at the University of New South Wales. Dr McCamey's research group have the only pulsed EPR spectrometer in the Sydney region capable of performing pulsed DEER experiments. Dr. Phani Potluri and Dr. Nicole Cordina, both previous students in Dr Brown's laboratory, trained me on the preparation of the Troponin samples for EPR and NMR measurements. Dr. Cordina, in her role as the NMR facility manager at the Department of Molecular Sciences, Macquarie University, also trained me on NMR spectra collection and data analysis. Dr. Potluri advised me on EPR spectra collection and data analysis using the DeFit software programs (**Section 3.2.5.3**). Initial assistance with acquisition of EPR spectra was obtained from Dr. Joanna Guss who was a PhD student within A/Prof Dane McCamey at the University of New South Wales when I commenced this project. The NMR sample preparation and data collection were performed by Dr. Nicole Cordina and Dr. Phani Potluri. All sample preparation for EPR was performed by myself; and spectra were collected with the help of Dr Guse. All the EPR analysis and interpretation of data was performed by myself. The manuscript was written by myself under the guidance of Dr Brown. When the manuscript was nearly completed, it was sent to all collaborators, and their comments and suggestions were incorporated into the final submitted manuscript. The manuscript has been prepared for submission to PNAS-USA

Phosphorylation of Troponin I finely controls the positioning of Troponin for the optimal regulation of cardiac muscle contraction

Ehsan Kachooei[1], Nicole M. Cordina[1], Phani R. Potluri[1], Joanna A. Guse[2], Dane McCamey[2] and Louise J. Brown[1]

[1]Department of Molecular Sciences, Macquarie University, Sydney, New South Wales 2109, Australia

[2]School of Physics, The University of New South Wales, Sydney, New South Wales 2052, Australia

KEYWORDS: Cardiac Troponin, phosphorylation, spin labeling, paramagnetic NMR spectroscopy, pulsed EPR

Abstract

Troponin is the Ca^{2+} molecular switch that regulates striated muscle contraction. In the heart, troponin Ca^{2+} sensitivity is further modulated by the PKA-dependent phosphorylation of a unique 31 reside N-terminal extension region of the Troponin I subunit (NH_2-TnI). However, the detailed mechanism for the propagation of the phosphorylation induced structural changes within Tn, which leads to enhancement of the relaxation rate, is difficult to investigate within whole Tn. While several models exist for how phosphorylation modulates the troponin response in cardiac cells, these are mostly built from peptide-NMR studies and molecular dynamics simulations. Here we use a paramagnetic spin label approach, with both NMR and EPR, to position and track the movement of the NH_2-TnI region within whole Tn. Through paramagnetic relaxation enhancement (PRE)-NMR experiments, we show that the NH_2-TnI region interacts with a broad surface area on the N-domain of the Troponin C subunit which includes the Ca^{2+} regulatory Site II and the TnI switch binding site. Phosphorylation of the NH_2-TnI region both weakens and shifts this region to an adjacent site on TnC. Pulsed EPR interspin distances between NH_2-TnI and TnC reveal a phosphorylation induced re-orientation of the TnC N-domain under saturating Ca^{2+}

conditions. We propose an allosteric model where phosphorylation triggered cooperative changes in both the interaction of the NH_2-TnI region with TnC, and re-orientation of the TnC interdomain orientation, together promote the release of the TnI switch. Enhanced relaxation then occurs. Understanding the phosphorylation modulation of the cardiac Tn isoform is important for beginning to unravel pathological processes which result in disease in the human heart.

Introduction

In healthy individuals, β-adrenergic stimulation speeds up the sarcomeric controlled calcium (Ca^{2+}) release and relaxation of cardiac muscle, significantly increasing the heart rate (to over 220 bpm) and cardiac output (up to 30 L/min) [1]. At the molecular level, the release of β-adrenaline leads to the activation of protein kinase A (PKA) which then specifically phosphorylates a number of proteins in cardiac cells. This includes Troponin I (TnI). TnI is one of three subunits of the large (~78 kDa) cardiac Troponin (Tn) protein complex, positioned on the muscle thin filament [2]. Tn is a highly dynamic protein responsible for controlling the interaction between myosin and actin. Referred to as the Ca^{2+} 'switch' complex, Tn switches on muscle contraction under conditions of high Ca^{2+}. However, in cardiac muscle, phosphorylation of TnI plays an additional modulatory role.

In human cardiac TnI, there are two residues (Ser22 and Ser23) that are phosphorylated by PKA and other kinases [3]. These two serine residues are located within a 32 residue N-terminal extension region of Troponin I which is unique to the cardiac isoform and will be referred to herein as the NH_2-TnI region (**Figure 1A**) [3-5]. Phosphorylation of the NH_2-TnI region leads to a decrease in Ca^{2+} sensitivity and a reduction in the actomyosin ATPase activity [6, 7]. This results in an increase in crossbridge cycling and the muscle relaxation rate [8, 9]. High levels of phosphorylation of the NH_2-TnI region are often observed in healthy individuals. In contrast, decreased levels of phosphorylation are associated with a number of disease states including heart failure, dilated cardiomyopathy, and hypertrophic cardiomyopathy [10, 11]. Despite the clear physiological response and links to disease states, the role of phosphorylation in regulating cardiac muscle contraction is nonetheless considered to be secondary to Ca^{2+} binding.

The structural nature and the extent of the modulatory capacity that phosphorylation of TnI has in regulating the cardiac isoform can be revealed by examining the interaction of the NH_2-TnI region with the other Tn subunits: Troponin C (TnC) and Troponin T (TnT). TnC is the smallest of the three Tn subunits. TnC is a dumbbell shaped 18 kDa molecule comprised of two EF hand metal-binding domains (N- and C-domains) connected by a linker which is highly flexible in the cardiac isoform [12]. EF-hand proteins function as intracellular Ca^{2+} messengers by undergoing a domain opening transition upon binding micromolar

concentrations of Ca^{2+}. While there are four EF hand Ca^{2+} binding helix-loop-helix structural motifs across the N- and C-domains of TnC, only the two lower affinity N-domain motifs (residues 16-51 and 52-87) are directly involved in the regulatory function of TnC. The two 12 residue Ca^{2+}-binding loops in N-domain are Site I (residues 28-40) and Site II (residues 65-76). However, in the cardiac isoform, Site I is non-functional. Lastly, TnT is the largest of the three subunits and anchors the whole complex to the muscle thin filament.

Force generation in the cardiac Tn isoform is triggered by binding of Ca^{2+} to the N-domain of TnC, specifically metal Site II. This leads to the exposure of a hydrophobic pocket in the TnC N-domain for the TnI 'switch' region to then bind, relieving inhibition. The NH_2-TnI region is proposed to interact with TnC to position its regulatory N-domain for optimal interaction with the TnI switch region [13]. However, because of its disordered nature, the NH_2-TnI region is absent from the X-ray crystal structures of the Tn core [14].

The Ca^{2+} triggered interaction of the N-domain of TnC with TnI is the critical step in contractile activation. In the cardiac isoform, this mechanism is proposed to be further modulated by phosphorylation of the NH_2-TnI region. While several models exist in the literature for how the NH_2-TnI region can achieve this, they all differ quite significantly in the way this region interacts with TnC in both the phosphorylated and unphosphorylated states [13, 15, 16]. There is limited structural data, particularly for the phosphorylated state, available to support these models. One of the earliest models to explain phosphorylation induced conformational changes within Tn is a docking model constructed from NMR peptide studies of a 32 residue fragment representative of the NH_2-TnI region [15]. This NMR peptide structure was subsequently docked onto the cardiac Tn core X-ray structure. In the unphosphorylated state, the model shows the NH_2-TnI region as an extended, rod-like structure, wrapping around the N-lobe of TnC. Phosphorylation then results in compaction and bending of the acidic NH_2-TnI region to interact with residues near the basic inhibitory region of TnI (residues 137-148). This early model also suggested that interactions of the NH_2-TnI region with the N-lobe of cTnC occurs upon phosphorylation [15].

Another more recent NMR based model used a structure of a longer peptide fragment which incorporated the NH_2-TnI region (TnI residues 1-73). The NMR structure of this peptide was solved in complex with full-length cTnC in an unphosphorylated state only [13]. This structure showed that the NH_2-TnI region is intrinsically disordered but electrostatically tethered to the N-domain of TnC in the unphosphorylated form. The interaction between the NH_2-TnI peptide and TnC was suggested to not affect the closed-to-open equilibrium of the N-domain of TnC. Rather it was hypothesized that the interaction positions the N-domain of TnC, relative to the structural core of Tn called the 'IT arm', for its optimal interaction with the TnI switch region. This arrangement could account for the observed increase in Ca^{2+} affinity. From this model, the authors further postulated that phosphorylation of the NH_2-TnI region would disrupt this positioning. However, the manner through which phosphorylation can lead to such a structural rearrangement has not yet been determined; and is particularly challenging in the intact Tn system because of the large size of the complex and the dynamic nature of many of the key functional regions of the Tn complex. This is particular true for the NH_2-TnI region which is observed to be largely disordered in solution [13, 15].

In our present study, we have used a combination of Paramagnetic Relaxation Enhancement (PRE)-NMR and Electron Paramagnetic Resonance spectroscopy (EPR) to assess, for the first time, the influence of phosphorylation on the positioning of the NH_2-TnI with respect to TnC. Using full-length constructs, nitroxide spin probes were first introduced onto the NH_2-TnI region (residues 5, 28, or 39) to map PRE-derived distances to TnC in the Tn binary complex (**Figure 1B**). Troponin inter-subunit pairs (TnC35 and TnI39, or TnC84 and TnI39) were then labeled and both pulsed DEER (Double Electron-Electron Resonance) and Continuous Wave (CW) EPR interspin distances revealed the relative positioning between these paired sites within the Tn ternary complex (**Figure 1C**). Together, the complementary spin-labeling based approaches of NMR and EPR provide a detailed analysis of the position and dynamics of the NH_2-TnI region within the Tn complex in response to phosphorylation. Our structural model extends our understanding of the role that phosphorylation of this unique cardiac specific segment has in modulating cardiac muscle contraction.

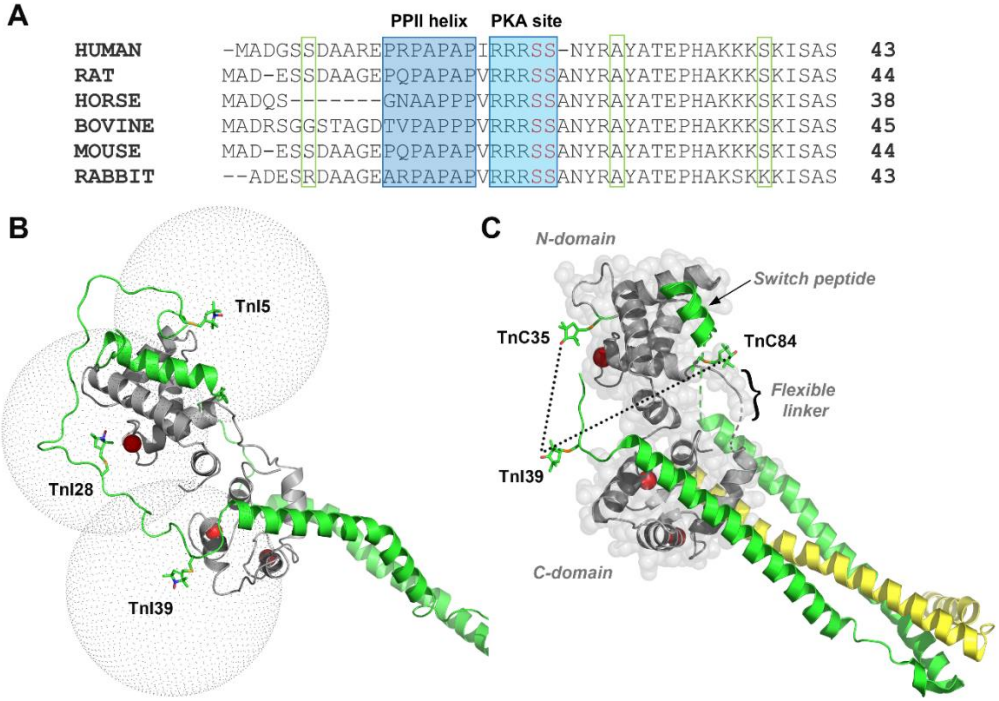

Figure 1 (A) Sequence alignment of cardiac isoforms of NH_2-TnI region. The highly conserved acidic N-terminus region [residues 1-11] is followed by a proline-rich poly-proline type II (PPII) spacer arm. The conserved PKA motif site is phosphorylated at Ser22 and Ser23. The residues spin-labeled in this study are boxed in green. Ribbon diagrams of the Tn complex showing residues on TnC (grey) and TnI (green) spin labeled with MTSL for **(B)** PRE-NMR and **(C)** EPR interspin distance measurements. Red spheres represent bound Ca^{2+}. For PRE-NMR, 3 single TnI cysteine mutants (TnI5, TnI28, TnI39) were individually labeled in the Tn binary complex. These sites are mapped onto a MD computational model of Tn [16] which includes the NH_2-TnI region. Dotted spheres indicate a 20 A° radius around each spin label site where the model predicts that PRE distances can most accurately be measured. For EPR, the interspin nitroxide pairs TnC35/TnI39 and TnC84/TnI39 are mapped onto the cardiac X-ray structure of the Tn core (PDB:1J1D, TnT is in yellow) [14]. TnI regions, missing from the X-ray structure, are shown as dashed lines.

Materials and Methods

Cardiac Troponin Protein Production and Purification

The cysteine-less constructs of rat cardiac TnC (cTnC) and rat cardiac TnI (cTnI) were expressed in the pET-3d expression vector (Novagen), as previously described [17]. Two

mono-cysteine cTnC constructs (C35, C84) and three mono-cysteine cTnI constructs (I5, I28, and I39) were generated from the cysteine-less TnC and TnI constructs, respectively. TnI constructs in the unphosphorylated state are referred to as wildtype (WT).

Site directed mutagenesis was performed to replace serine residues 22 and 23 with aspartic acid residues (TnI S22/23D) in the cysteine-less TnI to generate the pseudo-phosphorylated construct ($TnI_{S22/23D}$) [18]. This $TnI_{S222/23D}$ construct has been shown to change the contractile properties of myofibrils and Tn in a manner consistent with PKA treatment of cardiac Tn [18-22]. Each phosphorylated mono-cysteine construct is referred to according to the introduced cysteine, as follows: $TnI5_{S22/23D}$, $TnI28_{S22/23D}$ and $TnI39_{S22/23D}$. Constructs were verified by DNA sequencing and transformed into Escherichia coli BL21 (DE3) cells for expression in Terrific Broth media.

TnC and TnI was purified according to previously published protocols [23]. In brief, for TnC, this involved hydrophobic chromatography using a Phenyl Sepharose 6B column where bound TnC was eluted upon application of 10 mM EDTA following an initial high-salt wash (0.2 M NaCl) to elute nonspecific bound proteins. Following elution of the ^{15}N-TnC by hydrophobic interaction chromatography, this construct was further purified by ion exchange chromatography on a DEAE-Sephadex column, as previously described [24]. For PRE-NMR, the cysteine-less TnC construct was ^{15}N-labeled in M9 minimal media, containing 2.5 g/L glucose and 1 g/L $^{15}NH_4Cl$, using IPTG induction.

cTnI constructs were expressed as inclusion bodies and solubilised in 6 M urea before applying to a weak cation exchange chromatography column (carboxymethyl Sepharose). Bound TnI was eluted by the application of a linear NaCl gradient (0 M to 0.3 M) [23, 24].

Full length rat cardiac TnT with an N-terminal 6 histidine tag and a thrombin cleavage site was expressed in the pET-28a expression vector (Novagen), as previously described [23]. The insoluble TnT fraction was loaded onto a Ni-NTA column in 6M urea. Cleavage of the 6-His tag was achieved by overnight incubation with bovine thrombin (60 NIH units) in 2 M urea. Nucleic acid contamination was removed by weak anion exchange chromatography using a DEAE Sephadex A-25 column.

Paramagnetic labeling of cTnC & cTnI

The paramagnetic nitroxide moiety MTSL (1-oxyl-2,2,5,5-tetra-methylpyrroline-3-methyl-16 methanethiosulfonate) (Toronto Research Chemicals) was covalently attached to 2 single cysteine TnC constructs (TnC35, TnC84); and 6 single cysteine TnI constructs (TnI5 WT, $TnI5_{S22/23D}$, TnI28 WT, $TnI28_{S22/23D}$, TnI39 WT, and $TnI39_{S22/23D}$) in either the unphosphorylated (WT) or phosphorylated (S22/23D) state. As per established protocols, protein samples were first reduced with 20 mM dithiothreitol (DTT) in labeling buffer (6 M urea, 1 mM EDTA, 100 mM KCl, 50 mM MOPS pH 7.8) for 2–3 h at 4 °C. DTT was removed using a HiTrap desalting column before incubation with 2.5 molar excess of MTSL at 4 °C for 16 h. Excess MTSL was removed by exhaustive dialysis into reconstitution buffer (6 M urea, 1 mM EDTA, 0.5 M KCl, 2 mM $CaCl_2$, 3 mM $MgCl_2$, 50 mM MOPS pH 7.2). Spin labeling efficiency was calculated from the double integration of the EPR spectrum collected using a Bruker EMX X-Band (9.6 GHz) spectrometer. Continuous wave (CW)-EPR spectra were obtained at room temperature in a standard rectangular TE102 cavity, with a microwave power of 5.0 mW, modulation amplitude of 1.0 G and sweep width of 140 G.

Reconstitution of binary and ternary Tn samples for EPR and NMR

For PRE-NMR, binary samples were prepared by incubating ^{15}N-TnC with the MTSL-labeled (^{14}N)-TnI construct at a 4:5 molar ratio (TnC:TnI). For distance measurements by EPR, ternary complexes were assembled by reconstitution of MTSL-labeled TnC and TnI constructs with TnT at a 1.0:1.2:1.2 molar ratio (TnC:TnI:TnT). Binary and ternary complexes were incubated in reconstitution buffer containing 6 M urea and 0.5 M KCl. Renaturation was achieved through the gradual removal of urea by dialysis against respective NMR or EPR reconstitution buffers (for NMR: 1 mM EDTA, 2 mM $CaCl_2$, 3 mM $MgCl_2$, 50 mM MOPS pH 7.2; and for EPR: 2 mM $CaCl_2$, 3 mM $MgCl_2$, 50 mM MOPS pH 7.2). A final concentration of 0.1 M KCl was used to precipitate uncomplexed protein subunits which were then removed by centrifugation before stabilising the binary or ternary Tn complexes at 0.2 M KCl.

For NMR, the Ca^{2+} binary samples were dialysed into NMR buffer (0.2 M KCl, 3 mM $CaCl_2$, 3mM $MgCl_2$, 20 mM imidazole pH 6.9). The Ca^{2+}-free binary samples were prepared by exhaustive dialysis against 0.1 M EGTA into decalcified NMR buffer (treated with Chelex-100 resin, Bio-Rad) [25]. Binary complex formation was confirmed by SDS-PAGE and analytical

size exclusion chromatography, as previously described [24]. For EPR distance measurements, the +Ca^{2+} and Ca^{2+}-free ternary complexes were stabilised by the addition of 5 mM $CaCl_2$ and 8 mM EGTA, respectively, in EPR reconstitution buffer [26].

In total, six ^{15}N-TnC/MTSL-TnI constructs binary samples for PRE-NMR were prepared under conditions of saturating Ca^{2+} (TnI5 WT, TnI28 WT, TnI39 WT, $TnI5_{S22/23D}$, $TnI28_{S22/23D}$, and $TnI39_{S22/23D}$). The TnI28 WT and $TnI28_{S22/23D}$ binary samples were also prepared in the Ca^{2+}-free state. For EPR distance measurements, a total of eight ternary Tn double MTSL labeled samples for EPR (TnC35/TnI39 WT, TnC84/TnI39 WT, $TnC35/TnI39_{S22/23D}$ and $TnC84/TnI39_{S22/23D}$) in both +Ca^{2+} and Ca^{2+}-free states, and a 'single' MTSL-labeled ternary Tn construct with cysless TnI (TnC84 WT) were prepared.

PRE-NMR of binary (^{15}N-TnC/MTSL-TnI) complexes

NMR data on the paramagnetic spin-labeled binary ^{15}N-TnC/MTSL-TnI complexes were collected on a Bruker Avance 600 MHz spectrometer equipped with a cryoprobe. Data was collected at 303 K and spectra processed using Topspin 1.3 (Bruker, Inc). All samples were 550 µL with TnC-TnI concentrations of 150 - 250 mM. The *paramagnetic* ^{1}H-^{15}N-TROSY spectra was first collected before reduction of the nitroxyl radical of the spin label to its hydroxylamine equivalent by the addition of 5x molar excess of ascorbic acid (~1/250 volume). As confirmed by EPR, complete reduction of the spin label was achieved after 1h [24]. The *diamagnetic* ^{1}H-^{15}N-TROSY spectra were then collected for comparison.

PRE-NMR Data Analysis

Spectral assignment and analysis was performed with the program Sparky [27]. Peak assignments for TnC constructs were made using the assignments reported for the cardiac binary complex (TnC-TnI) [22, 28]; and using the chemical shifts of isolated TnC in the Ca^{2+}-free state [25]. Calculation of the intermolecular transverse $^{1}H_N$-Γ_2 PRE rates measured on the backbone amide protons of TnC in the presence of MTSL labeled TnI were obtained from the ratio of paramagnetic (I_{para}) and diamagnetic (I_{dia}) peak intensities (Eqn. 1):

$$\frac{I_{para}}{I_{dia}} = \frac{R_2 exp(-\Gamma_2 t)}{R_2+\Gamma_2} \qquad \text{Eqn. 1}$$

The intrinsic transverse relaxation rate (R_2) was estimated from the peak width at half-height ($R_2=\pi\Delta\nu_{1/2}$) [29, 30]. A single evolution time point (t) of 10 ms was used. PRE rates (Γ_2) were then converted to distances (r) using a modified form of the Solomon-Bloembergen equation [29-31] (Eqn. 2):

$$\Gamma_2 = \frac{K}{r^6}\left[4\tau_c + \frac{3\tau_c}{1+\omega_H^2\tau_c^2}\right] \qquad \text{Eqn. 2}$$

where ω_H is the Larmor frequency of the proton; K is a constant (1.23 x 10^{-32} cm^6 s^{-2}) describing the spin properties of the nitroxide spin label [30]; and τ_c is the correlation time of the electron-proton interaction $\tau_c = (\tau_r^{-1} + \tau_s^{-1})^{-1}$. τ_c is effectively equal to the overall correlation time of the protein [32] and was taken as 16 ns for the Tn binary complex [24].

Comparison of PRE distances was made with the cardiac Tn core crystal structure (PDB:1J1D) [14] and also two available Tn structural models with the TnI N-terminal region: (i) a docking structural models [15]; and (ii) a molecular dynamics (MD) structural model [16]. Both models were constructed using the NMR structure of a peptide of the NH_2-TnI region (PDB 2JPW) [16].

EPR Sample Preparation and Data Acquisition

For both CW EPR and DEER experiments, 40% glycerol was added to the spin labeled Tn ternary samples and spectra collected using an ELEXSYS E580 spectrometer (Bruker) with a X-band (9.6 GHz) resonator (ER 4118 X-MD5), as previously described [23]. The protein (100-120 µL of 80-120 µM) was inserted into 4 mm outer diameter quartz capillaries and snap frozen in liquid nitrogen before inserting into the pre-cooled resonator.

The X-band CW experiments were recorded at 150 K with a field sweep of 300 G, 0.2 mW microwave power, and modulation amplitude of 1 G. DEER experiments were recorded at 80 K using a four-pulse sequence with a 2 ms shot repetition time with a 16 ns 90° pulse. A 32 ns 180° ELDOR pulse was applied at a frequency detuned from the pulse frequency by 73 MHz to minimize the orientation selection and maximize the fraction of coupled spins.

EPR Data Analysis

The analysis of spectral broadening for double labeled Tn samples was performed using a Monte-Carlo/Simplex Gaussian convolution method using the CWdipFit software for CW spectra and DeFit software for DEER [33]. Monte Carlo sampling of the full parameter space determined the uniqueness of the solutions. Gaussian populations used to describe the experimental data are in terms of distance(s) (*r*) and distance distribution(s) (*Δr*); and are based on a statistical F-test. The MMM software package was used to model the rotameric distributions of the MTSL-labeled cysteine residues using a library approach [34].

Results

Mapping of interaction of spin labeled NH_2-TnI with ^{15}N-TnC by PRE-NMR

To measure phosphorylation and Ca^{2+} induced conformational changes in the positioning of the TnI N-terminal extension region (NH_2-TnI) with respect to TnC, we first performed PRE-NMR measurements in the binary TnC-TnI complex. Three sites on TnI were individually labeled with MTSL; two residues within the NH_2-TnI (TnI5 and TnI28) and TnI39 (**Figure 1B**). As determined by EPR, complete modification with MTSL (> 95%) was achieved for all six ^{15}N-TnC/MTSL-TnI constructs (TnI5 WT, TnI28 WT, TnI39 WT, $TnI5_{S22/23D}$, $TnI28_{S22/23D}$, and $TnI39_{S22/23D}$). The NMR data was collected under high (+Ca^{2+}) and low (Ca^{2+}-free) calcium concentrations.

PRE distance dependent effects are obtained by the direct comparison of the paramagnetic and diamagnetic spectra of each sample. For each sample, a ^{1}H-^{15}N-TROSY spectrum was initially acquired in the presence of the MTSL spin label (paramagnetic state) before reduction to the hydroxylamine equivalent of the nitroxide and collection of a further ^{1}H-^{15}N-TROSY spectrum (diamagnetic state). The full ^{1}H-^{15}N-TROSY spectra of all six binary troponin complexes obtained under conditions of saturating Ca^{2+} are shown in Supplementary Figure S1. NMR spectra were also obtained under Ca^{2+}-free conditions. However, notable PRE effects were only observed for TnI28 spin labeled construct (Supplementary Figure S2).

Comparison of the diamagnetic and paramagnetic spectra revealed varying levels of peak broadening effects (I_{para}/I_{dia} < 1) across the whole of TnC for all three spin labeled TnI constructs (Figure 2, *left panels*). Strongest broadening effects were observed for both the

TnI28 and TnI39 labeled constructs. The peak intensity ratios were then translated into distances (r) using the well-known distant dependent PRE effect ($\Gamma_2 \alpha 1/r^6$) for each assignable residue in TnC (Figure 2, *right panels*, Supplementary Table S1). Residues of TnC broadened beyond detection in the paramagnetic spectrum are in very close proximity ($r <$ ~10 Å) to the spin label. For residues beyond ~25 Å, the peak intensity for these residues remained unchanged ($I_{para}/I_{dia} \approx 1$). Due to the signal-to-noise ratio in our binary Tn complex (~42.6 kDa) ^{1}H-^{15}N-TROSY spectra, an estimated uncertainty of 10% in peak intensity ratios was applied and resonances with peak intensity ratios greater than 0.98 were all assigned to the upper limit. Residues to which no ratio could be assigned were excluded. The most effective range over which PREs can be detected with confidence from our ^{1}H-^{15}N-TROSY spectra is ~12-25 Å. This range agrees with our previous PRE studies for mapping interactions within TnC-TnI [24].

Changes in PRE-mapping effects upon phosphorylation

TnI5 WT & TnI5$_{S22/23D}$: Overall, the peak intensity ratio profile for the phosphorylated TnI5 labeled binary complexes (TnI5$_{WT}$ and TnI5$_{S22/23D}$) showed weak PRE broadening effects. In total, 114 resonance peaks of TnC showed some broadening although the I_{para}/I_{dia} ratio for most of these residues was close to unity (**Figure 2A**). The broad mapping of the PRE effects for this spin-labeled site indicate that, while the NH_2-TnI region can bind weakly to TnC, its positioning is not localised to a well-defined region for either domain of TnC. Diminished PRE effects were then detected in the TnI5$_{S22/23D}$ phosphorylation construct, particularly for residues in the B-C loop and helix D.

While most PRE broadening effects for the TnI5 labeled construct were weak, a few significant phosphorylation triggered changes were observed for several residues in the C and D helices of the N-domain of TnC. This included residues 51, 77 and 84 which all showed increases in PRE-derived distances of ~4-5 Å upon phosphorylation (Supplementary Table S1). Interestingly, residues 77 and 74 on helix D are involved in the binding of the TnI switch region to the hydrophobic pocket of the N-domain of TnC.

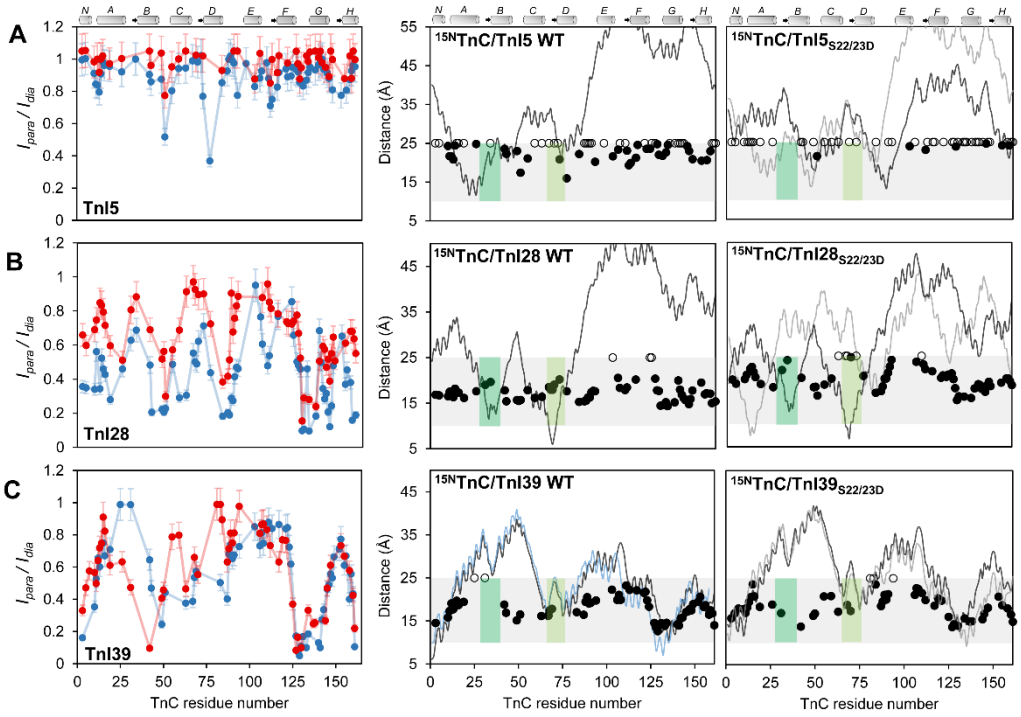

Figure 2 PRE-NMR peak intensity ratio (I_{para}/I_{dia}) profiles (*left*) and distance plots (*right*, black filled circles) for assigned TnC residues of the MTSL labeled Tn binary complex (^{15}N-TnC/MTSL-TnI) **(A)** TnI5, **(B)** TnI28, and **(C)** TnI39. Spectra were obtained under conditions of saturating Ca^{2+}. Peak intensity ratios obtained for the WT and phosphorylated constructs are shown in *blue* and *red*, respectively. Peaks broadened beyond detection are assigned an intensity ratio of 0.05. Error bars indicate a 10% uncertainty in the peak intensity ratios due to background noise in the TROSY spectra. The PRE distance profiles include distances calculated from two available structural models of the NH_2-TnI region in complex with Tn (*black line*, [15]; and *grey line*, [16]). For the TnI39 construct, the calculated distances from the cardiac crystal structure 1J1D (*blue line* [14]) are also included. Open circles indicate residues where peak intensity ratios were > 0.98 (distances > 25 Å). The grey shading across the distance plots is representative of the sensitivity of the PRE approach. Site I and Site II residues of TnC are boxed by dark and bright green shading, respectively.

TnI28 WT & TnI28$_{S22/23D}$: In comparison to the TnI5 construct, a greater number of strong PRE effects were observed for the TnI28 spin labeled construct. These suggested a tighter interaction of this region with TnC, particularly in the WT unphosphorylated sample (**Figure 2B**). In total, 57 TnC residues could be assigned in both the WT and phosphorylated states for this spin-labeled construct. TnC residues across both the N- and C-domains were broadened with several well-defined regions exhibiting particularly strong PREs (I_{para}/I_{dia} <

0.4). While the whole PRE profile across the full-length of TnC was similar in both states, the PRE effects were overall weaker for the phosphorylated construct. In the phosphorylated state, the average PRE-derived spin label to residue distance increased by 3.7 Å for the N-domain but only 1.8 Å for the C-domain (Supplementary Table S1). The correlation of PRE-derived distances to available structural models was poor, apart from a short cluster of residues which map to the central linker of TnC (residues 84-93).

The largest phosphorylation induced changes in PRE-derived distances across the N-domain of TnC for the TnI28 spin labeled construct were found clustered near the Ca^{2+} binding Site II (C-D loop), and also the TnI switch binding region (Ile26). While the increase in distance for these residues upon phosphorylation was calculated at ~5 Å, the magnitude of change may be significantly larger as the PRE-effects for the residues near Site II were all at the upper limit (25 Å) of the PRE technique in the phosphorylated construct.

Figure 3 shows the PRE derived distances mapped onto the Ca^{2+} saturated cardiac Tn core crystal structure (1J1D). A broad area is highlighted as the binding interface of the NH_2-TnI region with TnC. This comparative mapping of the PRE derived distances for the WT and phosphorylated states visually supports a phosphorylation triggered movement in the positioning of the NH_2-TnI region with respect to key regions of cTnC. The changes in the mapping patterns support the phosphorylation-controlled interaction of the NH_2-TnI region with residues surrounding the switch binding pocket on the N-lobe of TnC (**Figure 3A**) and the regulatory Ca^{2+} binding Site II (**Figure 3B**).

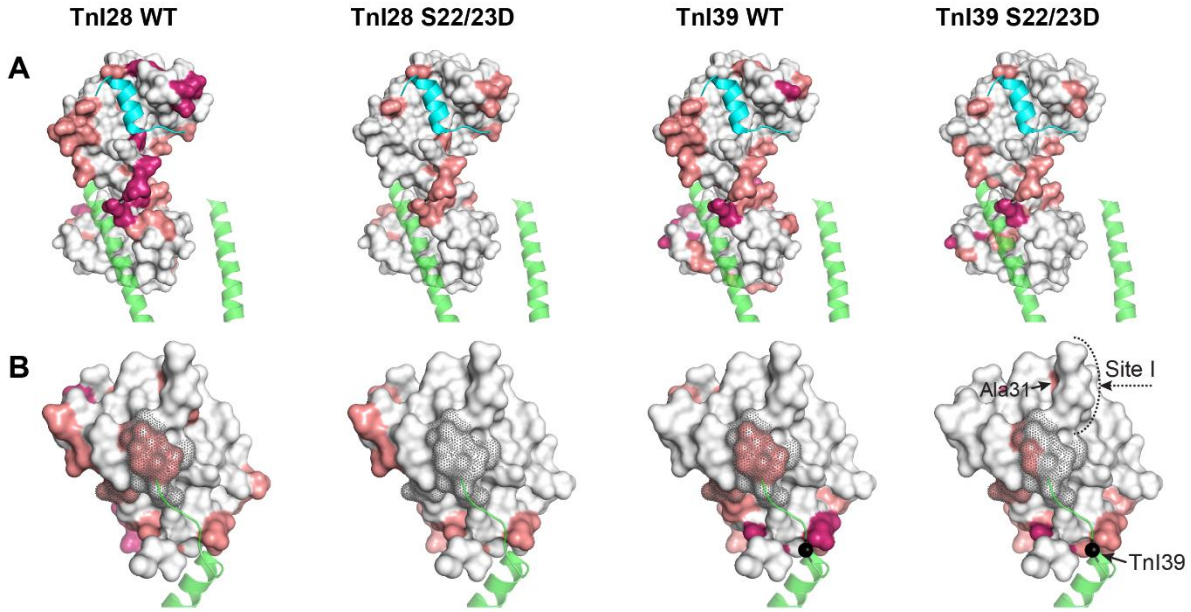

Figure 3 PRE distances obtained under conditions of saturating Ca^{2+} are mapped onto the cardiac core Tn complex (1J1D [14]) for spin labeled constructs TnI28 WT, $TnI28_{S22/23D}$, TnI39 WT, and $TnI39_{S22/23D}$. **(A)** Orientation shows residues in vicinity of the TnI switch peptide (*cyan*) binding site. **(B)** N-domain of TnC showing residues within vicinity of Ca^{2+} binding Site II (*dotted area in dark grey*). PRE distances of <16 Å are shaded dark pink, and distances between 16-20 Å are shaded *light pink*. TnC is *white surface*, TnI is in *green*. Dotted surface represents Site II. The TnI39 spin label position is indicated by a *black* sphere. Shown on the $TnI39_{S22/23D}$ map is the Ala31 (located on Site I). A decrease of 8 Å in the PRE-distance was observed for this residue upon phosphorylation. Additional views of these PRE-derived distance mapping profiles are shown in Supplementary Figure S3.

TnI39 WT & $TnI39_{S22/23D}$: The TnC-TnI complex labeled at residue TnI39 showed a similar pattern of strong PRE effects as the TnI28 labeled construct for both the WT state (60 constraints) and phosphorylated state (53 constraints) (**Figure 2C**). Overall, the mapping of the PRE-derived distance changes also showed that phosphorylation diminished the interactions of the NH_2-TnI region with TnC (**Figure 3**). Again, the changes were most noticeable for residues across the N-domain of TnC. There were some further features from the interaction of the spin label with TnC that were not observed by the spin label at the other two sites. Several short stretches of residues across the A and B helices were closer to the spin label in the phosphorylated state compared to the WT state. This phosphorylation induced movement may be interpreted as a shift of the spin label to a region on the N-

domain closer to the defunct Site I (*see* **Figure 3B**, Ala31). A similar phosphorylation triggered movement of the spin label away from residues near Site II (residues 65-76) was again a key feature of the mapping profiles for the spin label on residue 39 (**Figure 3B**). Large phosphorylation changes in PRE-distances were also observed for residues across the D-helix. This included TnC residue 83, a key residue involved in the binding of the TnI switch region, which increased by 8 Å upon phosphorylation. As discussed later, a similar phosphorylation associated increase in the EPR interspin distance between TnC84 and TnI39 was observed.

In general, for the TnI39 spin labeled construct, there was good agreement of the PRE derived distances with distance constraints calculated from Tn crystal structures and other Tn models, but only for C-domain residues. There was no significant change in the PRE interactions with C-domain residues upon phosphorylation. This lack of change in distance profiles across the TnC C-domain for the TnI39 spin labeled construct is consistent with a stable and structural role for the region of TnI upstream of the cardiac NH_2-TnI region.

Phosphorylation triggered changes in the interaction of NH_2-TnI with ^{15}N-TnC in Ca^{2+}-free conditions

To complete our understanding of Ca^{2+} effects on the interaction of the NH_2-TnI region with TnC, PRE distance measurements were also performed under Ca^{2+}-free conditions for the TnI28 and TnI39 constructs. NMR data was collected for these two sites as these were the two constructs where, if present, PRE effects would most likely be observed. However, we did not observe any strong PRE effects with either construct in the Ca^{2+}-state, nor any significant change in their PRE profiles upon phosphorylation (Supplementary **Figure S2**). While there were some small changes in the interaction of the NH_2-TnI region upon phosphorylation for the TnI28 construct with residues near TnC metal Site I, these movements are difficult to interpret as the majority of the PRE effects across these residues were close to the upper limit of detection (**Figure S2C**).

A comparison of the PRE mapping effects on TnC observed in the presence (**Figure 3A**) and absence (**Figure S2**) of Ca^{2+} did show a similar pattern of change in the PRE effects for

residues near the central linker region of TnC. This mapping pattern suggest a model where the TnC subunit is most likely in a collapsed conformation irrespective of its Ca^{2+} state. That is, these results imply that Ca^{2+} binding does not significantly alter the conformational ensemble between the N- and C-domains of TnC. However further experiments would be required to confirm this.

EPR interspin distances (DEER and CW) track the movement of the NH_2-TnI region

To further position and track the movement of the NH_2-TnI region with respect to TnC upon phosphorylation and Ca^{2+}, we next performed CW-EPR and pulsed DEER experiments. While the PRE-NMR approach was limited to the TnC-TnI binary complex, the EPR experiments were performed using the whole Tn ternary complex. Cysteine pairs (TnC35/TnI39 and TnC84/TnI39) were modified with MTSL before reconstitution with full-length TnT to form the Tn ternary complex. Pulsed DEER methods provided interspin distance information between 20 to ~60 Å [33] (**Figure 4**), whereas, CW measurements were sensitive to short interspin distances of ≤ 25 Å (**Figure S4**).

A four-pulse DEER experiment was employed to measure the interspin separations of the TnC35/TnI39 and TnC84/TnI39 ternary samples for all 8 combinations (±Ca^{2+}/±phosphorylation; Figure S4 A-D). DEER profiles show the decay of the spin echo intensity, where the rate of the initial decay is proportional to the interspin distance. As such, a fast decay implies a short interspin distance. The best model for the evolution decay is overlayed on the spectral data and corresponding Gaussian distributions shown. A two Gaussian model, showing a 'short' and a 'long' distance population, was found as the best fit for all samples (**Figure 4A**). Table 1 lists a summary of all DEER distances and populations.

Under conditions of saturating Ca^{2+}, the TnC35/TnI39 interspin pair showed both a short and long-distance population for both the WT and phosphorylated states (**Figure 4A**). In the phosphorylated state, the short distance was narrow (Δr = 8 Å) and centred at 26 ± 2 Å. The average distance for the short population did not change upon phosphorylation (27 ± 1 Å, Δr = 8 Å). For the long-distance population, the average distance decreased by ~7 Å upon phosphorylation. An accompanying decrease in Δr from 40 to 27 Å occurred. There was an increase in the proportion of interacting spins representing the short/narrow population from 30 to 53% upon introduction of the charge onto the NH_2-TnI region (and corresponding

decrease for the longer/broad distance population). Thus, phosphorylation of this construct led to an overall increase in the proportion of interactions of the NH_2-TnI region with the TnC N-domain and on average, this region moved closer to Cys35 near the defunct metal Site I.

In the Ca^{2+}-free state, a similar two distance distribution profile was observed for the TnC35/TnI39 interspin pair: a short/narrow distance 28 ± 2 Å (*Δr* = 10 Å) and a longer/broad distance population of 52 ± 2 Å (*Δr* = 32 Å) (**Figure 4B**). Phosphorylation resulted in a modest increase in the average distances for both populations of approximately 3-4 Å but did not significantly change the distribution width of either distance. However, phosphorylation again increased the population of interacting spins representing the short/narrow population from 22 to 42%.

Converse population changes were observed for the TnC84/TnI39 interspin pair under $+Ca^{2+}$ conditions (**Figure 4C**) where phosphorylation decreased the population of the short/narrow distance component. Phosphorylation however increased the average distance of both the short and longer distance populations. In the WT (unphosphorylated) state, the short distance was centred at 26 ± 1 Å (*Δr* = 8 Å) and the long distance at 46 ± 1 Å (*Δr* = 26 Å) in the presence of Ca^{2+}. Phosphorylation increased these average distances by approximately 3 Å and 12 Å, respectively. An accompanying increase in disorder also occurred. For the short distance, this increase in distance and disorder suggests a shift of the NH_2-TnI region away from Cys84. TnC84 is positioned close to the regulatory Site II.

However, under conditions of low Ca^{2+}, little change in the average distance or populations were observed for the TnC84/TnI39 interspin pair upon phosphorylation (**Figure 4D**). The average distances for the short and longer distance populations were similar to the Ca^{2+} saturated WT construct. Phosphorylation resulted in only a modest increase in the population of the short distance, with a small increase of 33 to 41%. Overall, the greatest phosphorylation associated changes, for both interspin distance pairs, were observed only in the presence of Ca^{2+}. This direction of the phosphorylation triggered movement observed in presence of Ca^{2+} is indicated by the arrows in Figure 4E where the NH_2-TnI region moves closer to Cys35 and further away from Cys84. When considered with the PRE data, these

distance changes support a model where the N-domain of TnC rotates with respect to the C-domain upon phosphorylation (**Figure 4F**).

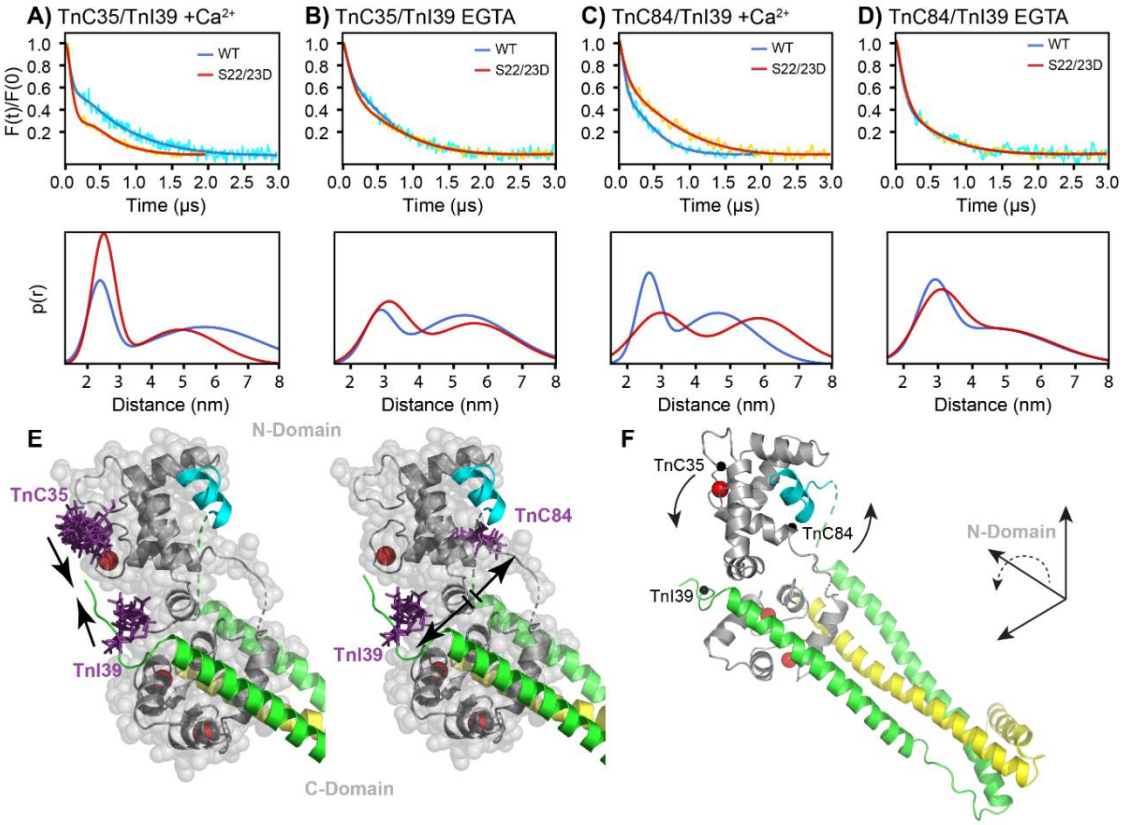

Figure 4 DEER spectra and distance analysis in the ternary Tn complex for the positioning of the NH_2-TnI region (via TnI39) with respect to two spin labeled sites on TnC (TnC35 and TnC84). Raw and fitted DEER time traces (*top row*) for TnC35/TnI39 under conditions of **(A)** $+Ca^{2+}$, and **(B)** Ca^{2+}-free (EGTA); and TnC84/TnI39 at **(C)** $+Ca^{2+}$, and **(D)** Ca^{2+}-free (EGTA). The corresponding 2 Gaussian distance-distribution fits to the experimental data are shown below with WT and phosphorylated (S22/23D) states in blue and red, respectively. **(E)** The representative DEER distance changes upon phosphorylation in the $+Ca^{2+}$ state is indicated by the arrows. The modelled rotameric distributions of the spin label (purple), obtained using MMM software, are also shown [35]. **(F)** Phosphorylation modulates the position of the N-domain for its interaction with the TnI switch region. An inter-domain rotation of TnC model indicating movement of the N-domain with respect to the C-domain upon phosphorylation.

To check for the presence of interspin populations of less than 20 Å, CW-EPR was also performed. Distances were derived from the CW-EPR spectra by comparison of the broadening of the double-labeled spectrum with the sum of the single non-interacting spin label sample (Supplementary **Figure S4**). Overall, limited broadening was observed for all double labeled samples with distances close to, or beyond the upper limit of CW sensitivity (> 20 Å). The CW derived distances close to the upper limit of the technique, as presented in Table S2, are likely to be representative of the short distance populations we observed by DEER. The CW distances agreed well with those modeled from the crystal structure of the cardiac Tn core [14] and also the two available NMR-peptide structural models of the NH_2-TnI region within the Tn complex in the Ca^{2+} saturated state only [15, 16].

Discussion

Phosphorylation of myofibril proteins by PKA, in response to β-adrenergic stimulation, is recognised as an important contributor for the regulation of cardiac contractility in humans. It does this by increasing the circulatory demand in the body under situations of increased physical activity or stress through increasing the myofilament relaxation kinetics. The cardiac specific NH_2-TnI region, via phosphorylation of residues Ser22 and Ser23, is a critical pathway for transferring the phosphorylation signal within the heart [36]. While the physiologic response to PKA phosphorylation of these TnI residues is notable, the structural changes in this Tn subunit are assumed to only be subtle as inferred by the modest 2-3 fold change in Ca^{2+} sensitivity of Tn upon phosphorylation [37, 38]. It is frequently reported in the literature that physiological signals arising from phosphorylation of specific residues on target proteins trigger only small conformational changes in a protein's structure to result in the observed functional change. Additionally, it has been observed that many of these regulatory proteins have phosphorylation target sites within intrinsically disordered domains, and as such, the response from phosphorylation is often a shift in the dynamic nature or equilibrium state of these disordered regions [39]. How cardiac Tn transmits such a small and subtle structural signal from the PKA phosphorylation of the two serine residues within the dynamic NH_2-TnI region of TnI in whole Tn has been, until now, difficult to investigate.

Using a spin labeling strategy, the small-scale movements and changes in protein dynamics can be tracked to obtain a better mechanistic view of the regulatory process in cardiac Tn [40]. When performed in parallel with NMR and EPR, the targeted spin labeling of Tn revealed the phosphorylation-controlled positioning and shift in dynamics of the NH_2-TnI region within whole Tn. In the unphosphorylated state, the NH_2-TnI region was observed to primarily interact with the TnC N-domain in an area close to, and including, the Ca^{2+} binding Site II. The changes in the PRE-mapping of the NH_2-TnI region with TnC upon phosphorylation mimic then represented a weakening of the electrostatic interaction between the two Tn subunits. EPR interspin distance experiments revealed that phosphorylation induced a change in the equilibrium positioning of the NH_2-TnI region with respect to TnC. Effectively, phosphorylation of the NH_2-TnI region triggered a shift in the equilibrium positioning of the NH_2-TnI region away from Site II to an alternate area on the N-domain closer to Site I. We propose that this is via a re-orientation of the N-domain with respect to the Troponin IT arm. Both the EPR and NMR detected phosphorylation induced changes were most significant under Ca^{2+} saturated conditions and not in the Ca^{2+}-free state.

While there are several models for the phosphorylation controlled interaction of the NH_2-TnI region with the subunits of Tn, these have mostly been constructed from peptide NMR studies [13, 15]. In one model built from the unphosphorylated NMR structure [13], the NH_2-TnI region is represented as a highly disordered peptide segment that interacts electrostatically with the negatively charged residues on the N-domain of TnC. This interaction of the NH_2-TnI region with TnC is proposed to orient the N-domain of TnC for its optimal binding to the TnI switch peptide, and thus result in the indirect increase in Ca^{2+} sensitivity. Phosphorylation is hypothesized by the authors to then disrupt this domain positioning via the introduction of additional negative charge [41]. This order-to-disorder model is in contrast with another earlier NMR peptide model where the role of the NH_2-TnI region is believed to stabilise an open state of the N-domain of TnC to directly increase its Ca^{2+} affinity [15]. However, conflicting with both these earlier NMR-peptide models are recent molecular dynamics (MD) simulation studies which show that both the phosphorylated and unphosphorylated forms of the NH_2-TnI region are disordered [16, 41]. Our results presented here extend further on these NMR-derived models but also provide support for some other key structural and dynamic features suggested from these MD

models. Importantly, our broad DEER distance distribution profiles support the MD models where the NH_2-TnI region exists in a highly disordered structural state under both phosphorylated and unphosphorylated forms.

Our PRE-NMR mapping and EPR distance data suggests a further unique feature of the phosphorylation modulated interaction of the NH_2-TnI region with TnC which may also be responsible for, or contribute in parallel with other proposed mechanisms, in enhancing relaxation. Specifically, the PRE-distance mapping showed that the NH_2-TnI region interacts with TnC close to, and with the regulatory Ca^{2+} binding Site II, but also with TnC N-domain residues involved in binding the TnI switch region. From these mapped interactions, one simplest interpretation of a possible mechanism is that, in the unphosphorylated state, the NH_2-TnI region of TnI acts as a physical block that sterically prevents the release of the TnI switch peptide from its hydrophobic pocket on the N-domain. Alternatively, the NH_2-TnI region, through its interactions with Site II, may effectively stabilise the Ca^{2+} bound open form of the N-domain in the unphosphorylated state, priming it for an optimal and thus sustained interaction with the TnI switch region. Either mechanism would be consistent with the observation of the slow relaxation state. Then, upon phosphorylation, the steric hindrance which prevented the release of the TnI switch region weakens, or again alternatively, the affinity of Ca^{2+} binding for Site II decreases which promotes the release of the TnI switch region. Or, a combination of both mechanisms occurs upon phosphorylation for the fast relaxation state to be observed.

However, although it may be intuitive, a note of caution should be made when interpreting the interspin TnC-TnI interspin distances and the PRE mapping changes into a mechanistic model of phosphorylation modulated regulation. While both the EPR and NMR derived distances can be interpreted as a simplistic shift in the positioning of the NH_2-TnI region relative to TnC; it is important to remember that the cardiac isoform of TnC is not a static entity. Cardiac TnC, via its flexible central linker can adopt multiple, although well-defined, inter-domain conformational states in solution [12]. The spin label on TnI used for the EPR distances in this study is residue 39. This residue is located at the N-terminus of a helical region adjacent to the C-domain fragments of TnT and TnC in the ‘structural core’ IT-arm of

Tn [14]. On the other hand, the two TnC sites (residues 35 and 84), are within the dynamic 'regulatory core' domain of Tn; although on near-opposite faces of the N-domain. The phosphorylation triggered DEER detected movement between the NH_2-TnI region and the TnC N-domain is more likely due to a rotation or twisting movement of the TnC molecule around its central linker. Notably, we did not detect any significant phosphorylation triggered re-orientation of the TnC N-domain when Ca^{2+} is not bound to Site II. This suggests that the NH_2-TnI region, through its interactions with TnC, is important for the re-orientation of the positioning of the Ca^{2+} 'primed' TnC N-domain to interact with the TnI switch region. Parallels between our interpretation and the NMR-peptide model of Hwang et al (2014) can be made. In the NMR-peptide model, the authors suggested that the NH_2-TnI region indirectly increases the Ca^{2+} affinity through the optimal positioning of the N-domain of TnC for its interaction with the TnI switch region [13]. Phosphorylation was proposed to disrupt this arrangement and we see evidence for this occurring.

While it is well known that the mechanical force-generating capability of a myofilament is directly associated with Ca^{2+} sensitivity, a major unanswered question is, how does phosphorylation achieve this? One proposed mechanism is that phosphorylation modulates Ca^{2+} sensitivity by decreasing the affinity of TnC for Ca^{2+} due to altered TnC-TnI interactions. These structural alterations cause a higher rate of Ca^{2+} dissociation from Site II and thus a decrease in the contraction-relaxation cycle in the heart. Other studies suggest that phosphorylation affects Ca^{2+} sensitivity by altering the opening and closing of the TnC N-domain [42]. However, others have reported that there is no direct effect of phosphorylation on the Ca^{2+} binding affinity to Site II, nor the 'closed-to-open' conformation of the N-domain [13]. On the other hand, an MD report by Zamora (2019), as reported in a recent review [43], suggested that phosphorylation does indeed enhance the probability of the open state under Ca^{2+} saturating conditions. Interestingly, in this recent reported MD study, a key backbone hydrogen bond interaction is observed in the open state conformation between TnC residues Val72 and Ile136, located in the loops connecting helices AB and CD, respectively. This interaction is modulated by phosphorylation. While our experiments cannot directly monitor the interaction between these two specific residues, we did observe significant increases (~5 Å) in our PRE distances from the spin label on TnI28 with other residues within the vicinity of this hydrogen bond (residues 34 and 73). This may provide

support for a phosphorylation modulated shift towards an open conformation of the N-domain. Another pulsed EPR study, which mapped changes in intra-domain interspin distances, also report small phosphomimetic induced modification effects on the Ca^{2+} induced changes across the N-domain of TnC [44]. These small structural changes detected within the TnC N-domain by us and others may further contribute to the modulatory role that phosphorylation plays in modifying the Ca^{2+} affinity by promoting the release of the TnI switch region as a result of small structural perturbations in the N-domain. Verification of this model requires a more detailed investigation of the switch release mechanism and also examination of other intrinsically disordered regions of Tn that play an essential role in the Ca^{2+} switch mechanism, such as the TnI inhibitory region.

In summary, we show that the phosphorylation of the NH_2-TnI region of the cardiac isoform results in several subtle but important changes in the interaction of this region with TnC and the dynamic nature of these interactions. We propose a model where phosphorylation shifts the interaction of the NH_2-TnI region away from Site II and the switch binding pocket and this results in release of the switch region, enhanced dissociation of Ca^{2+} from binding Site II, possibly via small structural perturbations to the N-domain, and re-orientation of the N-domain of TnC with respect to the IT-arm. As a result, the relaxation rate is enhanced. The dynamic allostery that we observe from phosphorylation of the NH_2-TnI region is primarily dominated by a population shift of the interaction of the NH_2-TnI region with the surface of the N-domain near Site II to a region on the N-domain closer to Site I. Electrostatics must be a key player in this process, with the introduction of additional charges leading to the weakening of the interactions between the TnC-TnI subunits.

Our site directed spin-labeling approach, performed in parallel with EPR and NMR, is therefore a viable tool which can provide a more complete description of the Ca^{2+} and phosphorylation triggered changes in the dynamics of the intact Tn complex. This is necessary to not only provide a better understanding of the physiological modulation of the cardiac Tn isoform but to also understand pathological processes which cause disease in the heart.

References

1. Mogensen, J., et al., *Severe disease expression of cardiac troponin C and T mutations in patients with idiopathic dilated cardiomyopathy.* J Am Coll Cardiol, 2004. **44**(10): p. 2033-40.
2. Noland, T.A., Jr., et al., *Cardiac troponin I mutants. Phosphorylation by protein kinases C and A and regulation of Ca^{2+}-stimulated MgATPase of reconstituted actomyosin S-1.* J Biol Chem, 1995. **270**(43): p. 25445-54.
3. Solaro, R.J., M. Henze, and T. Kobayashi, *Integration of troponin I phosphorylation with cardiac regulatory networks.* Circ Res, 2013. **112**(2): p. 355-66.
4. Solaro, R.J. and J. van der Velden, *Why does troponin I have so many phosphorylation sites? Fact and fancy.* J Mol Cell Cardiol, 2010. **48**(5): p. 810-6.
5. Zhang, J., et al., *Top-down quantitative proteomics identified phosphorylation of cardiac troponin I as a candidate biomarker for chronic heart failure.* J Proteome Res, 2011. **10**(9): p. 4054-65.
6. Holroyde, M.J., et al., *Isolation of cardiac myofibrils and myosin light chains with in vivo levels of light chain phosphorylation.* Biochim Biophys Acta, 1979. **587**(4): p. 628-37.
7. Ray, K.P. and P.J. England, *Phosphorylation of the inhibitory subunit of troponin and its effect on the calcium dependence of cardiac myofibril adenosine triphosphatase.* FEBS Lett, 1976. **70**(1): p. 11-6.
8. Herron, T.J., F.S. Korte, and K.S. McDonald, *Power output is increased after phosphorylation of myofibrillar proteins in rat skinned cardiac myocytes.* Circ Res, 2001. **89**(12): p. 1184-90.
9. Kentish, J.C., et al., *Phosphorylation of troponin I by protein kinase A accelerates relaxation and crossbridge cycle kinetics in mouse ventricular muscle.* Circ Res, 2001. **88**(10): p. 1059-65.
10. Zhang, J., et al., *Top-down quantitative proteomics identified phosphorylation of cardiac troponin I as a candidate biomarker for chronic heart failure.* J Proteome Res, 2011. **10**(9): p. 4054-4065.
11. Hamdani, N., et al., *Distinct myocardial effects of beta-blocker therapy in heart failure with normal and reduced left ventricular ejection fraction.* Eur Heart J, 2009. **30**(15): p. 1863-1872.
12. Cordina, N.M., et al., *Interdomain orientation of cardiac troponin C characterized by paramagnetic relaxation enhancement NMR reveals a compact state.* Protein Sci, 2012. **21**(9): p. 1376-87.
13. Hwang, P.M., et al., *The cardiac-specific N-terminal region of troponin I positions the regulatory domain of troponin C.* Proc Natl Acad Sci U S A, 2014. **111**(40): p. 14412-7.
14. Takeda, S., et al., *Structure of the core domain of human cardiac troponin in the Ca^{2+}-saturated form.* Nature, 2003. **424**(6944): p. 35-41.
15. Howarth, J.W., et al., *Phosphorylation-dependent conformational transition of the cardiac specific N-extension of troponin I in cardiac troponin.* J Mol Biol, 2007. **373**(3): p. 706-22.
16. Zamora, J.E., et al., *Troponin structure: its modulation by Ca^{2+} and phosphorylation studied by molecular dynamics simulations.* Phys Chem Chem Phys, 2016. **18**(30): p. 20691-20707.
17. Brown, L.J., et al., *Structure of the inhibitory region of troponin by site directed spin labeling electron paramagnetic resonance.* Proceedings of the National Academy of Sciences, 2002. **99**(20): p. 12765-12770.
18. Wijnker, P.J., et al., *Impact of site-specific phosphorylation of protein kinase A sites Ser23 and Ser24 of cardiac troponin I in human cardiomyocytes.* Am J Physiol Heart Circ Physiol, 2013. **304**(2): p. H260-8.

19. Hanft, L.M., B.J. Biesiadecki, and K.S. McDonald, *Length dependence of striated muscle force generation is controlled by phosphorylation of cTnI at serines 23/24.* J Physiol, 2013. **591**(18): p. 4535-47.
20. Rao, V.S., et al., *N-terminal phosphorylation of cardiac troponin-I reduces length-dependent calcium sensitivity of contraction in cardiac muscle.* J Physiol, 2013. **591**(2): p. 475-90.
21. Sakthivel, S., et al., *In vivo and in vitro analysis of cardiac troponin I phosphorylation.* J Biol Chem, 2005. **280**(1): p. 703-14.
22. Finley, N., et al., *NMR analysis of cardiac troponin C-troponin I complexes: effects of phosphorylation.* FEBS Lett, 1999. **453**(1-2): p. 107-12.
23. Potluri, P.R., et al., *The concerted movement of the switch region of Troponin I in cardiac muscle thin filaments as tracked by conventional and pulsed (DEER) EPR.* J Struct Biol, 2017. **200**(3): p. 376-387.
24. Cordina, N.M., et al., *Ca^{2+}-induced PRE-NMR changes in the troponin complex reveal the possessive nature of the cardiac isoform for its regulatory switch.* PLoS One, 2014. **9**(11): p. e112976.
25. Cordina, N.M., et al., *Effects of calcium binding and the hypertrophic cardiomyopathy A8V mutation on the dynamic equilibrium between closed and open conformations of the regulatory N-domain of isolated cardiac troponin C.* Biochemistry, 2013. **52**(11): p. 1950-62.
26. Dong, W.J., et al., *Conformation of the N-terminal segment of a monocysteine mutant of troponin I from cardiac muscle.* Biochemistry, 1997. **36**(22): p. 6745-53.
27. Goddard, T.D. and D.G. Kneller, *SPARKY 3*. 2008, University of California: San Francisco.
28. Abbott, M.B., et al., *Regulatory domain conformational exchange and linker region flexibility in cardiac troponin C bound to cardiac troponin I.* J Biol Chem, 2000. **275**(27): p. 20610-7.
29. Volkov, A.N., et al., *Solution structure and dynamics of the complex between cytochrome c and cytochrome c peroxidase determined by paramagnetic NMR.* Proc Natl Acad Sci U S A, 2006. **103**(50): p. 18945-50.
30. Battiste, J.L. and G. Wagner, *Utilization of site-directed spin labeling and high-resolution heteronuclear nuclear magnetic resonance for global fold determination of large proteins with limited nuclear overhauser effect data.* Biochemistry, 2000. **39**(18): p. 5355-65.
31. Liang, B., J.H. Bushweller, and L.K. Tamm, *Site-directed parallel spin-labeling and paramagnetic relaxation enhancement in structure determination of membrane proteins by solution NMR spectroscopy.* J Am Chem Soc, 2006. **128**(13): p. 4389-97.
32. Iwahara, J., C.D. Schwieters, and G.M. Clore, *Ensemble approach for NMR structure refinement against ^{1}H paramagnetic relaxation enhancement data arising from a flexible paramagnetic group attached to a macromolecule.* J Am Chem Soc, 2004. **126**(18): p. 5879-96.
33. Fajer, P.G., L. Brown, and L. Song, *Practical pulsed dipolar ESR (DEER)*, in *ESR spectroscopy in membrane biophysics, Biological magnetic resonance*, M.A. Hemminga and L.J. Berliner, Editors. 2007, Springer: New York. p. 95–128
34. Polyhach, Y., E. Bordignon, and G. Jeschke, *Rotamer libraries of spin labelled cysteines for protein studies.* Phys Chem Chem Phys, 2011. **13**(6): p. 2356-66.
35. Jeschke, G., *MMM: A toolbox for integrative structure modeling.* Protein Sci, 2018. **27**(1): p. 76-85.
36. Layland, J., R.J. Solaro, and A.M. Shah, *Regulation of cardiac contractile function by troponin I phosphorylation.* Cardiovasc Res, 2005. **66**(1): p. 12-21.
37. Ward, D.G., M.P. Cornes, and I.P. Trayer, *Structural consequences of cardiac troponin I phosphorylation.* J Biol Chem, 2002. **277**(44): p. 41795-801.
38. Ward, D.G., et al., *NMR and mutagenesis studies on the phosphorylation region of human cardiac troponin I.* Biochemistry, 2004. **43**(19): p. 5772-5781.

39. Iakoucheva, L.M., et al., *The importance of intrinsic disorder for protein phosphorylation.* Nucleic Acids Res, 2004. **32**(3): p. 1037-49.
40. Kachooei, E., N.M. Cordina, and L.J. Brown, *Constructing a structural model of troponin using site-directed spin labeling: EPR and PRE-NMR.* Biophys Rev, 2019. **11**(4): p. 621-639.
41. Papadaki, M. and S.B. Marston, *The Importance of Intrinsically Disordered Segments of Cardiac Troponin in Modulating Function by Phosphorylation and Disease-Causing Mutations.* Front Physiol, 2016. **7**: p. 508.
42. Dong, W.J., et al., *Effects of PKA phosphorylation of cardiac troponin I and strong crossbridge on conformational transitions of the N-domain of cardiac troponin C in regulated thin filaments.* Biochemistry, 2007. **46**(34): p. 9752-61.
43. Marston, S. and J.E. Zamora, *Troponin structure and function: a view of recent progress.* J Muscle Res Cell Motil, 2019.
44. Abe, J., et al., *Double Quantum Coherence EPR Reveals the Structure–Function Relationships of the Cardiac Troponin C–Troponin I Complex Regulated by Ca^{2+} Ions and a Phosphomimetic.* Appl Magn Reson, 2018. **49**(8): p. 893-910.

Tables

Table 1 Summary of 'short/narrow' and 'longer/broad' interspin distances in the ternary Tn complex by DEER. Distances were extracted using the DeFit program, where the numbers of Gaussians used to fit the distribution was increased from 1 to 3. r is the central distance, Δr is the width of the distance distribution. The error is calculated from the χ^2 surface of the Monte Carlo search within the arbitrary limits that encompass all possible ($\chi^2 > 10*\chi^2_{min}$) solutions. The percentage contribution was determined with 10% accuracy. $\chi^2_{1\rightarrow2}$ is the ratio of χ^2 values for the 1 Gaussians model to the 2 Gaussian model fit

Interspin distance	State		*r* (Å)	*Δr* (Å)	Population (%)	Mod Amp (%)	$\chi^2_{2\text{-}1}$
TnC35/TnI39	+Ca^{2+}	WT	26 ± 2	8 ± 5	30	10	1.6
			57 ± 2	40 ± 4	70		
		S22/23D	27 ± 1	8 ± 2	53	9	3.5
			50 ± 1	27 ± 3	47		
	EGTA	WT	28 ± 2	10 ± 5	22	8	1.1
			52 ± 2	32 ± 4	78		
		S22/23D	31 ± 2	15 ± 5	42	21	1.8
			56 ± 2	29 ± 5	58		
TnC84/TnI39	+Ca^{2+}	WT	26 ± 1	8 ± 3	34	7	1.5
			46 ± 1	26 ± 2	66		
		S22/23D	29 ± 2	17 ± 4	29	13	1.3
			58 ± 1	27 ± 3	71		
	EGTA	WT	29 ± 2	10 ± 5	33	10	1.2
			46 ± 2	38 ± 4	67		
		S22/23D	30 ± 1	15 ± 3	41	11	1.7
			49 ± 1	35 ± 4	59		

Supplementary Information

Table S1 Summary of distances (in Angstrom) derived from PRE-NMR effect. Distances were measured from the TnI spin labels to TnC residues. WT and S22/23D represent unphosphorylated and phosphorylated samples, respectively. Δ represents the distance change for residues which were measurable in both unphosphorylated and phosphorylated states (Δ = [S22/23D] – [WT]).

Location	Residue	TnI5, +Ca^{2+}			TnI28, +Ca^{2+}			TnI39, +Ca^{2+}		
		WT	S22/23D	Δ	WT	S22/23D	Δ	WT	S22/23D	Δ
	1	-	-	-	-	-	-	-	-	-
	2	-	-	-	-	-	-	-	-	-
Helix N	3	25.0	25.0	-	16.8	19.8	3.0	14.5	15.7	1.2
	4	-	-	-	-	-	-	-	-	-
	5	25.0	25.0	-	16.7	18.9	2.2	-	16.9	-
	6	-	-	-	-	-	-	-	-	-
	7	-	-	-	-	-	-	-	18.0	-
	8	-	-	-	-	-	-	-	-	-
	9	-	-	-	-	-	-	-	-	-
	10	24.3	25.0	0.7	16.5	19.9	3.4	15.8	17.9	2.1
	11	21.7	-	-	17.5	20.8	3.3	17.3	17.0	-0.3
	12	21.6	25.0	3.4	-	-	-	19.1	18.3	-0.8
	13	20.8	25.0	4.2	16.3	22.2	5.9	17.7	19.5	1.8
Helix A	14	24.4	25.0	0.6	18.2	22.6	4.4	-	20.6	-
	15	25.0	25.0	-	17.4	21.5	4.1	19.7	23.6	4.0
	16	25.0	-	-	17.3	20.3	3.1	18.7	20.8	2.2
	17	-	-	-	-	-	-	-	-	-
	18	-	-	-	-	-	-	-	-	-
	19	25.0	25.0	-	16.1	18.8	2.7	19.4	18.4	-1.0
	20	-	-	-	-	-	-	-	-	-
	21	-	-	-	-	-	-	-	-	-
	22	-	-	-	-	-	-	-	-	-
	23	-	-	-	-	-	-	-	-	-
	24	-	-	-	-	-	-	-	-	-
	25	-	-	-	-	-	-	25.0	-	-
	26	24.8	25.0	0.2	17.6	18.1	0.5	-	18.9	-
	27	-	-	-	-	-	-	-	-	-
Site I	28	-	-	-	-	-	-	-	-	-
	29	-	-	-	-	-	-	-	-	-
	30	-	-	-	-	-	-	-	-	-
	31	-	-	-	19.0	21.9	2.9	25.0	17.0	-8.0
	32	-	-	-	-	-	-	-	-	-
	33	-	-	-	-	-	-	-	-	-
	34	25.0	-	-	19.6	24.1	4.5	-	-	-
	35	-	-	-	-	-	-	-	-	-
	36	-	-	-	-	-	-	-	-	-
	37	-	-	-	-	-	-	-	-	-
Helix B	38	-	-	-	-	-	-	-	-	-
	39	-	-	-	-	-	-	-	-	-
	40	-	-	-	-	-	-	-	-	-
	41	-	-	-	-	-	-	-	-	-
	42	23.6	25.0	1.4	17.8	20.2	2.4	18.8	13.8	-5.0
	43	22.3	25.0	2.7	15.4	-	-	16.9	-	-
	44	-	-	-	-	-	-	-	-	-
	45	-	-	-	-	-	-	-	-	-
	46	-	-	-	-	-	-	-	-	-

	47	-	-	-	-	-	-	-	-	-
	48	-	-	-	-	-	-	-	-	-
	49	23.0	25.0	2.0	15.7	18.1	2.4	15.1	16.3	1.2
	50	-	-	-	15.5	18.2	2.8	-	16.8	-
	51	17.4	21.4	3.9	15.7	16.3	0.6	16.5	-	-
	52	-	-	-	-	-	-	-	-	-
	53	-	-	-	-	-	-	-	-	-
	54	-	-	-	-	-	-	-	-	-
	55	21.1	25.0	3.9	17.8	18.7	0.9	-	20.8	-
	56	-	-	-	-	-	-	-	-	-
	57	-	-	-	-	-	-	-	-	-
	58	-	-	-	-	-	-	-	-	-
Helix C	59	25.0	25.0	-	16.1	20.0	3.9	-	20.9	-
	60	-	-	-	-	-	-	-	-	-
	61	-	-	-	-	-	-	-	-	-
	62	-	-	-	-	-	-	-	-	-
	63	25.0	25.0	-	16.4	25.0	8.6	16.1	17.3	1.1
	64	-	-	-	-	-	-	-	-	-
	65	-	-	-	-	-	-	-	-	-
	66	-	-	-	-	-	-	-	-	-
	67	25.0	-	-	18.5	25.0	6.5	16.2	-	-
	68	-	-	-	17.9	25.0	7.1	17.5	18.9	1.3
Site II	69	-	25.0	-	17.9	-	-	17.8	-	-
	70	25.0	-	-	19.1	24.7	5.7	-	17.4	-
	71	-	-	-	-	-	-	-	-	-
	72	25.0	-	-	-	-	-	-	-	-
	73	20.9	25.0	4.1	20.2	25.0	4.8	-	-	-
	74	-	-	-	-	-	-	-	-	-
	75	-	-	-	-	-	-	-	-	-
	76	-	-	-	-	-	-	-	-	-
	77	16.0	-	-	17.6	20.6	3.0	-	-	-
	78	-	-	-	-	-	-	-	-	-
	79	-	-	-	-	-	-	-	-	-
Helix D	80	-	-	-	-	-	-	-	-	-
	81	-	-	-	-	-	-	-	25.0	-
	82	-	-	-	-	-	-	-	-	-
	83	-	-	-	-	-	-	17.0	25.0	8.0
	84	22.2	25.0	2.8	15.3	16.9	1.6	-	23.6	-
	85	-	-	-	-	-	-	-	-	-
	86	-	-	-	-	-	-	-	-	-
	87	25.0	-	-	15.4	17.3	1.9	16.4	18.6	2.2
	88	25.0	-	-	15.5	18.3	2.8	19.4	19.7	0.3
	89	25.0	-	-	16.3	20.0	3.8	20.5	21.2	0.7
	90	25.0	-	-	16.2	20.1	3.8	19.1	20.1	1.0
	91	25.0	25.0	-	17.4	21.3	3.9	19.2	21.3	2.1
	92	-	-	-	17.7	22.7	5.0	-	-	-
	93	20.2	25.0	4.8	17.6	24.1	6.5	-	-	-
	94	-	-	-	-	-	-	19.8	25.0	5.2
	95	-	-	-	-	-	-	-	-	-
	96	-	-	-	-	-	-	-	-	-
Helix E	97	-	-	-	-	-	-	-	-	-
	98	25.0	-	-	-	-	-	-	-	-
	99	-	-	-	-	-	-	-	-	-
	100	-	-	-	-	-	-	-	-	-

	101	-	-	-	-	-	-	-	-	-
	102	-	-	-	-	-	-	-	-	-
	103	21.6	23.9	2.3	25.0	-	-	22.2	-	-
	104	-	-	-	-	-	-	-	-	-
	105	-	-	-	-	-	-	-	-	-
	106	23.4	25.0	1.6	20.5	-	-	19.9	21.2	1.3
	107	25.0	-	-	18.3	23.7	5.4	21.0	22.7	1.7
	108	-	-	-	-	-	-	19.9	22.5	2.6
Site III	109	-	-	-	-	-	-	-	-	-
	110	25.0	-	-	17.9	25.0	7.1	-	21.6	-
	111	23.1	-	-	18.4	23.2	4.8	23.2	-	-
	112	19.4	23.0	3.6	-	22.1	-	-	20.0	-
	113	19.9	25.0	5.1	-	-	-	22.2	-	-
	114	-	-	-	-	-	-	-	-	-
	115	-	-	-	-	-	-	-	-	-
	116	21.2	25.0	3.8	20.2	21.6	1.5	-	-	-
	117	24.6	25.0	0.4	-	-	-	22.1	18.7	-3.5
	118	-	-	-	-	-	-	-	-	-
Helix F	119	-	-	-	-	-	-	-	20.4	-
	120	-	-	-	-	-	-	-	-	-
	121	25.0	-	-	-	20.2	-	21.5	19.8	-1.7
	122	23.6	25.0	1.4	-	20.8	-	21.8	-	-
	123	-	-	-	-	-	-	19.8	-	-
	124	23.6	-	-	25.0	20.4	-4.6	18.3	-	-
	125	25.0	-	-	25.0	20.9	-4.1	-	16.1	-
	126	-	-	-	-	-	-	-	-	-
	127	25.0	25.0	-	20.4	21.2	0.8	14.5	13.7	-0.8
	128	24.8	25.0	0.2	17.8	19.9	2.1	13.5	14.4	0.9
	129	22.0	23.9	1.8	17.7	17.9	0.2	12.6	-	-
	130	-	25.0	-	14.4	15.3	0.9	14.0	14.0	0.0
	131	21.8	-	-	14.5	16.1	1.6	14.5	-	-
	132	-	-	-	-	-	-	-	-	-
	133	22.7	25.0	2.3	15.2	-	-	13.9	-	-
	134	24.6	25.0	0.4	14.3	16.1	1.7	14.6	15.7	1.2
Helix G	135	25.0	25.0	-	-	-	-	-	-	-
	136	-	-	-	-	-	-	-	-	-
	137	-	-	-	-	-	-	-	15.0	-
	138	25.0	25.0	-	15.2	15.7	0.6	-	15.0	-
	139	-	-	-	-	-	-	-	-	-
	140	25.0	25.0	-	20.0	17.9	-2.1	14.2	-	-
	141	25.0	25.0	-	18.0	-	-	13.9	-	-
	142	25.0	25.0	-	16.8	18.8	1.9	15.6	-	-
	143	25.0	-	-	16.1	18.6	2.5	15.8	-	-
	144	-	25.0	-	15.7	17.8	2.1	-	15.5	-
Site IV	145	24.3	-	-	15.5	18.2	2.7	17.1	16.8	-0.2
	146	23.0	24.6	1.6	14.8	17.1	2.4	17.2	-	-
	147	-	25.0	-	15.9	18.6	2.7	17.7	18.2	0.4
	148	20.9	25.0	4.1	17.8	19.3	1.6	17.4	-	-
	149	-	-	-	-	18.4	-	18.9	-	-
	150	-	-	-	-	-	-	-	-	-
Helix H	151	-	-	-	-	-	-	-	-	-
	152	-	-	-	-	-	-	19.5	-	-

	153	20.5	-	-	19.5	-	-	20.6	20.8	0.1
	154	-	-	-	-	-	-	-	-	-
	155	-	24.2	-	16.9	19.1	2.2	18.3	18.8	0.5
	156	20.7	-	-	17.2	-	-	18.7	-	-
	157	-	-	-	-	-	-	-	-	-
	158	23.0	25.0	2.0	17.1	20.1	3.0	16.5	18.0	1.6
	159	25.0	24.1	-0.9	15.0	20.0	5.0	17.5	-	-
	160	25.0	25.0	-	-	19.5	-	16.8	16.6	-0.2
	161	25.0	25.0	-	15.4	18.6	3.2	14.0	15.0	1.0

Table S2 Summary of CW-EPR interspin distances (<20 Å) in the soluble ternary Tn complex. *r* is the central distance, *Δr* is the width of the distance distribution, and *f* is the percentage contribution of the Gaussian population. $\chi^2_{1\to2}$ is the ratio of χ^2 values for the 1 Gaussians model to the 2 Gaussian model fit. Student test applied to all fits resulted in p-value > 5% and only 1 Gaussian fits were selected. C.S. is the adopted Cα distances between corresponding residues from crystal structure of Tn core (PDB: 1J1E) [1]. Model A is a docking model from the NMR structure of the NH_2-TnI region to the Tn core [2]. Model B is a computational model based on a MD simulation in the presence of the missing disordered segments in the crystal structure [3].

Interspin distance	state		r (Å)	Δr (Å)	f (%)	$\chi^2_{1\to2}$	C.S and model distances (Cα)		
							C.S. [1]	Model A [2]	Model B [3]
TnC35/TnI39	+Ca^{2+}	WT	24 ± 2	10 ± 3	73 ± 1	1.0	23.0	25.6	29.3
		S22/23D	21 ± 1	2 ± 1	83 ± 1	1.0	-	27.8	23.7
	EGTA	WT	> 25	-	69 ± 1	1.0	-	-	-
		S22/23D	> 25	-	81 ± 1	1.0	-	-	-
TnC84/TnI39	+Ca^{2+}	WT	21 ± 2	6 ± 4	88 ± 1	1.1	22.6	23.2	22.6
		S22/23D	>25	-	100 ± 1	1.0	-	26.4	25.6
	EGTA	WT	23 ± 2	9 ± 3	80 ± 1	1.0	-	-	-
		S22/23D	>25	-	93 ± 1	1.0	-	-	-

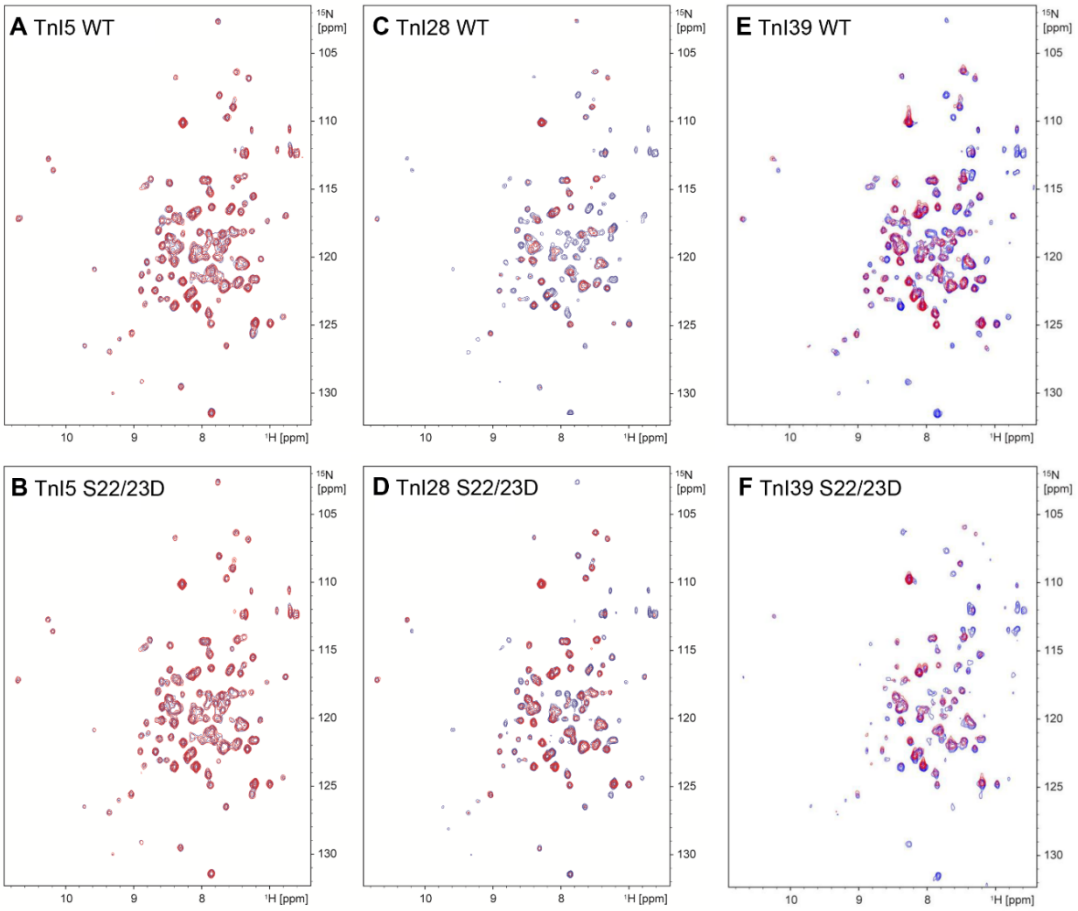

Figure S1 Two dimensional ^{1}H-^{15}N-TROSY spectra of binary troponin complexes. MTSL spin label attached to TnI residues: **(A)** TnI5-MTSL in the unphosphorylated state (WT) and **(B)** phosphorylated state ($TnI5_{S22/23D}$); **(C)** TnI28-MTSL in the unphosphorylated state (WT) and **(D)** the phosphorylated state ($TnI28_{S22/23D}$); **(E)** TnI39-MTSL in the unphosphorylated state (WT) and **(F)** phosphorylated state ($TnI39_{S22/23D}$). All spectra were acquired in the presence of saturating Ca^{2+}.

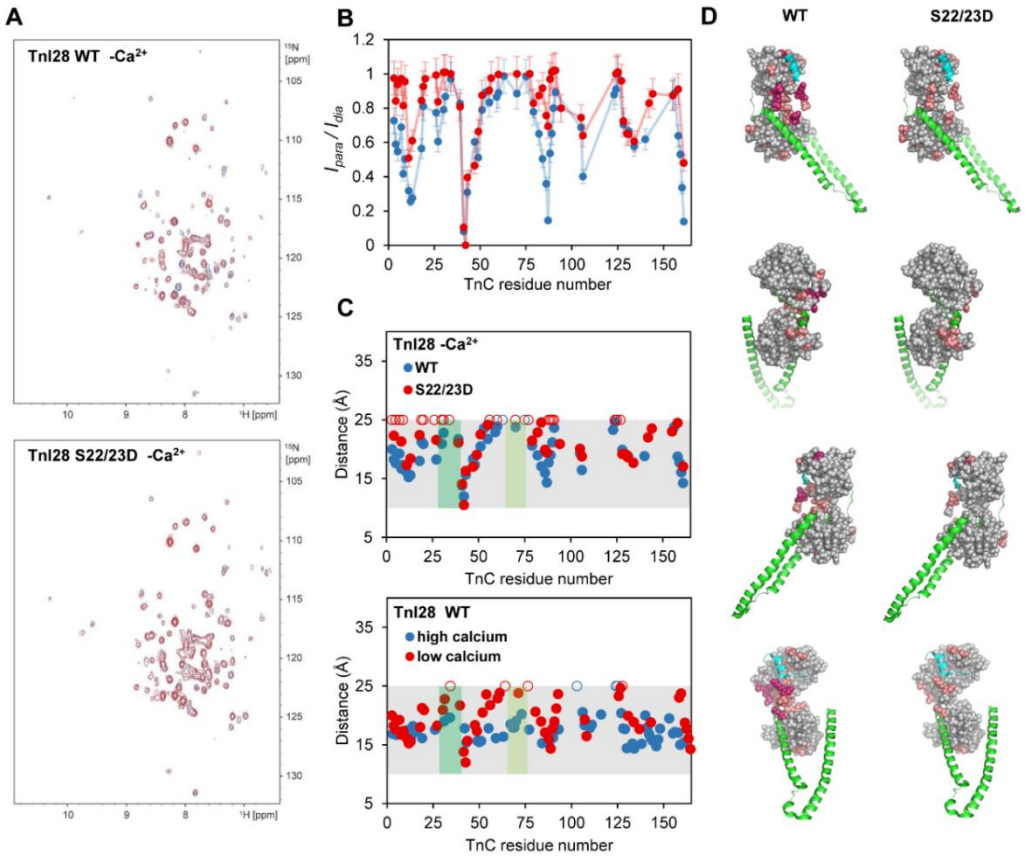

Figure S2 PRE-NMR experiment for MTSL spin attached to residue TnI28 in the Ca^{2+}-free state. **(A)** Two dimensional ^{1}H-^{15}N-TROSY spectra of the binary troponin complexes for TnI28 WT (*top*) and phosphorylated $TnI28_{S22/23D}$ (*bottom*) state. **(B)** The ratio of peak intensities in the paramagnetic and diamagnetic spectra (I_{para}/I_{dia}) for all assigned TnC residues in the WT (*blue*) and S22/23D constructs (*red*). Due to the background noise in the TROSY spectra, a 10% uncertainty in the peak intensity ratios was assumed, indicated with error bars. **(C)** Comparison of calculated distances derived from PRE intensity ratios (*filled circles*) for TnI28 WT (*blue*) and $TnI28_{S22/23D}$ (*red*) TnI28 in Ca^{2+}-free state (*top*); and between TnI28 WT in $+Ca^{2+}$ (*blue*) and Ca^{2+}-free (*red*) states (bottom). The intensity ratio of $I_{para}/I_{dia} > 0.98$ are plotted as 25 Å (open circles). The PRE distance range of sensitivity is shadowed in grey in panel C. The region of Site I and Site II are also represented by dark and bright green boxes, respectively. **(D)** Mapping of PRE derived distances onto the binary constructs of Tn28 WT (*left*) and phosphorylated $TnI28_{S22/23D}$ construct (*right*). Each construct has been represented in views with 90° rotation (*top to bottom*). TnC and TnI are in grey and green respectively. Distances of 16 Å or less are dark pink on TnC, and between 16- 20 Å are salmon. The switch peptide regulatory region of TnI is represented in cyan.

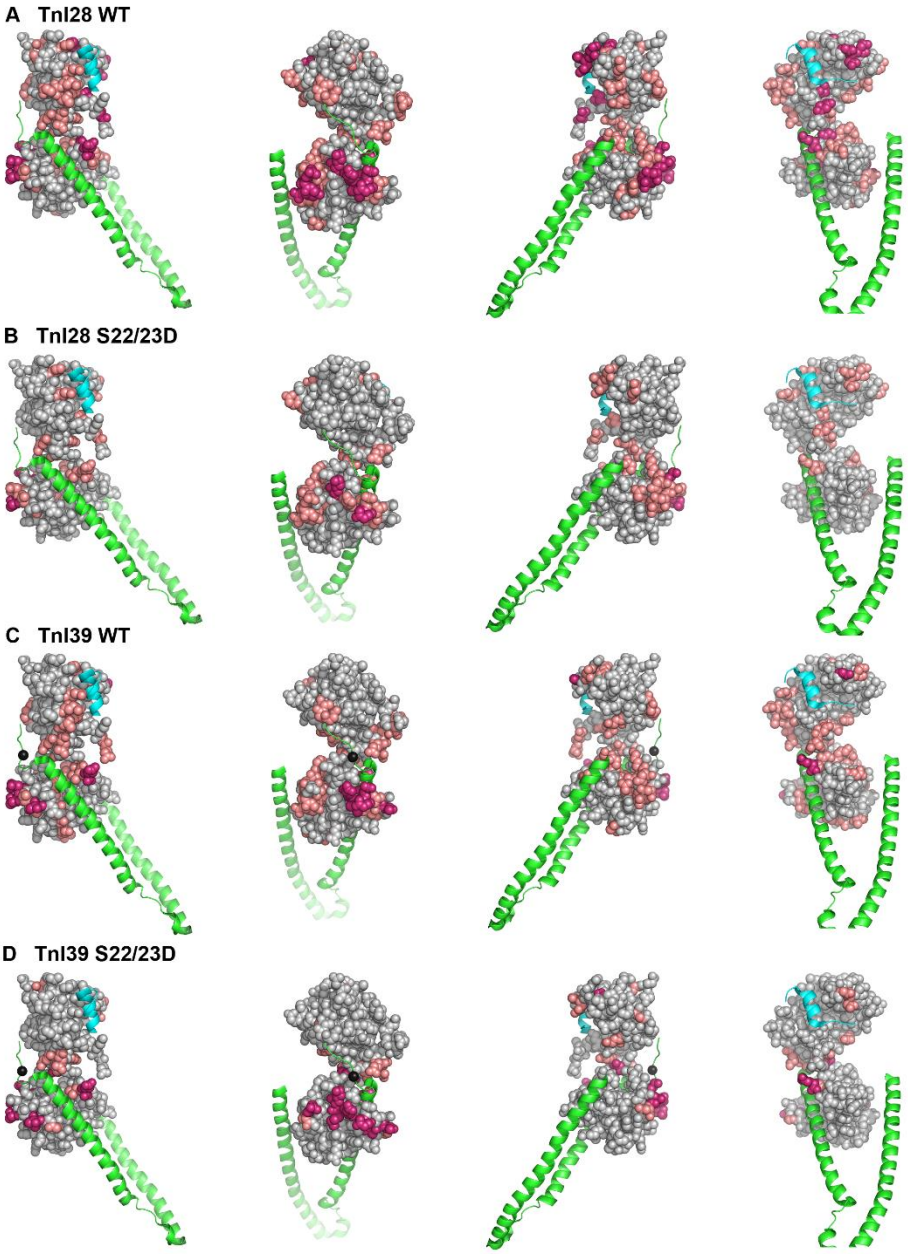

Figure S3 Four orientations of PRE distances obtained under conditions of saturating Ca^{2+}, as mapped onto the cardiac core Tn complex (1J1D [14]) for spin labeled constructs **(A)** TnI28 WT , **(B)** $TnI28_{S22/23D}$, **(C)** TnI39 WT, and **(D)** $TnI39_{S22/23D}$. Cardiac TnC is colored grey, TnI is in green and the TnI regulatory switch peptide is highlighted in cyan. The TnI39 spin label position is indicated in panels C and D (*black sphere*). PRE distances of <16 Å are shaded dark pink, and distances between 16-20 Å are shaded light pink. Each construct has been represented in views with 90° rotation (*left to right*). TnI5 mapping is not included due to limited PRE constraints for this construct.

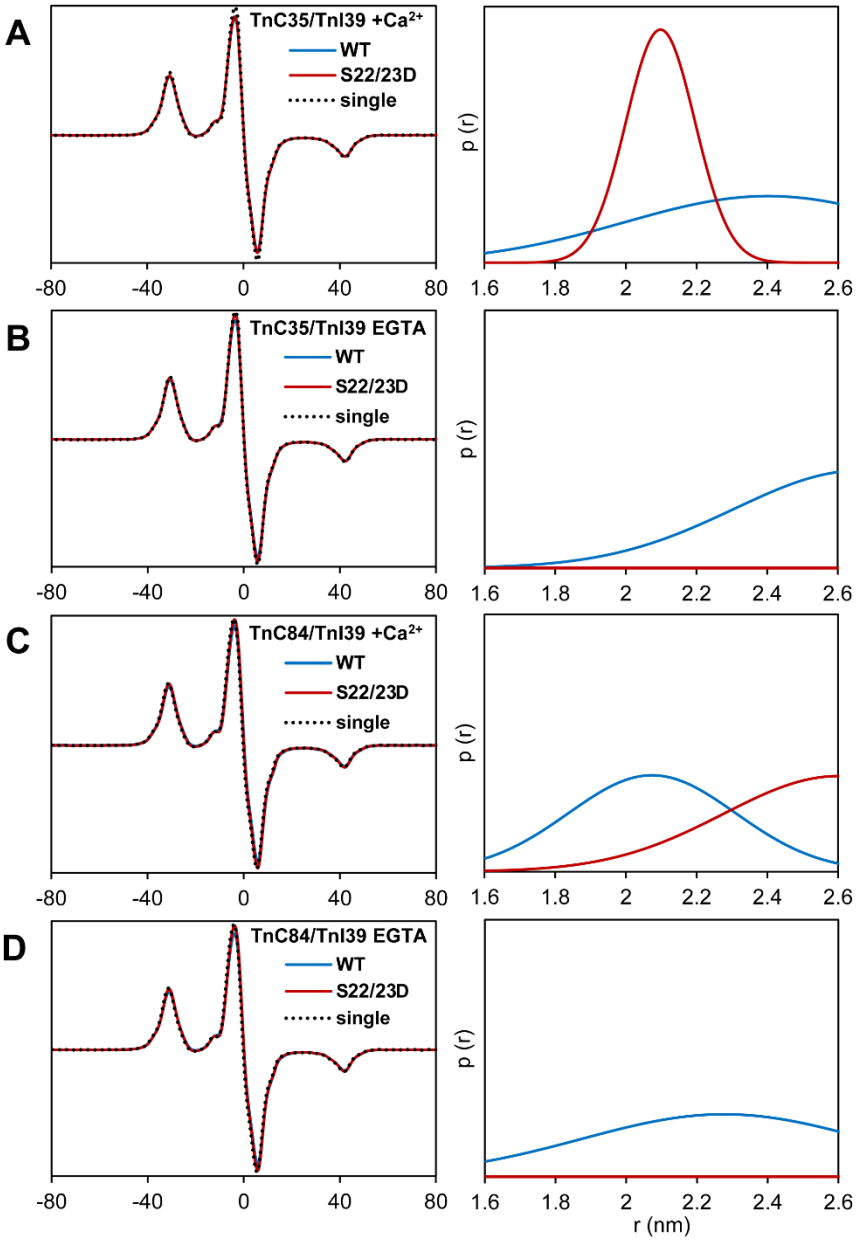

Figure S4 CW-EPR spectra for the positioning of the NH_2-TnI region with respect to TnC. CW spectra (*left column*) for the double labeled Tn samples compared with CW signal of a single spin construct for: **(A)** TnC35/TnI39 +Ca^{2+}; **(B)** TnC35/TnI39 Ca^{2+}-free; **(C)** TnC84/TnI39 +Ca^{2+}; and **(D)** TnC84/TnI39 Ca^{2+}-free. Right panels are the corresponding distance distribution (1 Gaussian). Blue line is the unphosphorylated state (WT) and red line is phosphorylated states ($TnI_{S22/23D}$). Dashed lines represent the spectrum of the single labeled Tn construct.

5. Paper 2 – Phosphorylation effect on the interaction of the TnI switch region with TnC.

5.1 Introduction

As presented in **Chapter 1, section 1.2,** muscle contraction at the molecular level occurs as a result of the sliding of myosin on actin filaments in response to Ca^{2+} influx into cardiomyocytes. Central to this mechanism is the TnI 'switch peptide' region which, with the N-domain of TnC, is responsible for transferring the Ca^{2+} - binding signal through the thin filament, leading to acto-myosin interaction. The binding of the switch peptide to the hydrophobic pocket of the N-domain of Troponin C, under high Ca^{2+} conditions, is observed in the crystal structure of cardiac core Troponin [1]. However, since there is no x-ray structure for a Ca^{2+}-free state in the cardiac isoform, the release of the switch peptide from Troponin C is still ambiguous.

Over the past 7 years, the group of A/Prof Brown have developed paramagnetic relaxation enhancement (PRE)-NMR methods to examine the structure and dynamics of the Tn complex. A previous student (Dr Cordina) was first to publish a study using the PRE-NMR approach on the binary complex of Tn. Dr Coridna's study provided a description of the Ca^{2+}-free state of cardiac Tn using PRE-NMR by describing the movement of key regions of the troponin I subunit upon the release of Ca^{2+} from Troponin C [2]. Our group have also used CW and DEER EPR to measure distances between TnI and TnC. Another previous student (Dr Potluri) used these EPR distance methods to track the Ca^{2+} induced movement of the TnI regulatory switch' region. Together, these two NMR and EPR studies targeting the TnI switch region showed, that in the $+Ca^{2+}$ state, the switch region is bound tightly to the N-domain lobe of TnC. Whereas, under conditions of low Ca^{2+}, the TnI switch region becomes partly released but remains in close proximity to TnC at all times. It was suggested that the close 'possessive' nature of TnC for its switch region may increase the frequency of collisions between the N-lobe of TnC and the regulatory switch region, counterbalancing the reduction in the collision probability that results from the incomplete opening of the N-lobe of TnC (which is unique to the cardiac isoform). However, it is important to note that, in both these studies, the Tn constructs were in the wild type (WT) or unphosphorylated state.

As described in **Sections 1.6**, phosphorylation increases the relaxation rate in cardiomyocytes which may be attributed to a higher rate of release of the switch peptide from TnC. At the commencement of this project, and still to date, there is no high-resolution structural evidence which shows the enhanced release of the switch peptide in response to phosphorylation in intact Troponin. In the manuscript presented here, distance constraints between the TnI switch peptide and TnC were again obtained using the same two similar, but different, structural lenses - PRE-NMR and EPR. The experimental design was similar to the previous approaches of Cordina and Potluri, as reported in references [2, 3]. However, in this study, additional spin label sites were also examined. These sites included TnC35/TnI159 and TnC84/TnI159 spin pairs. The results of this study provided us with striking detail of the switch release mechanism and the role of phosphorylation. We have now refined our Tn model and this is called the 'Seat-belt' model.

Notably, this research was performed in parallel with my visit to Dr. Gunnar Jeschke's group in ETH, Zurich, and Dr, Enrica Bordignon's group in Ruhr Univeristy, Bochum. During my visit, I received many further helpful advices for DEER measurement setup and collection of data for higher frequency Q-band spectroscopy. I also received advice on EPR sample preparation which has allowed for successful Q-band measurement (**sections 3.2.4.3 & 3.2.5.1**). All the DEER measurements in this manuscript were then performed using the Q-band frequency. This was the first time Dr Brown's group had performed Q-band measurements. In addition, I also learned how to model spin label rotamers using the MMM software program (as described in **Chapter 3, section 3.2.5.2**).

5.2 Authors' contributions

The design of these experiments and manuscript preparation were performed under the supervision of A/Prof. Louise Brown. During the data collection for the EPR experiments, the pulsed EPR spectrometer at UNSW required extensive repairs. In light of the delay, Dr Brown organised for the DEER measurements in Q-band frequency as a collaboration with A/Prof. Jeffrey Harmer at the Centre of Advanced Imaging at the University of Queensland. All the NMR and EPR Troponin sample preparations were performed by me. NMR spectra were

collected with the assistance of Dr. Nicole Cordina who is the NMR facility manager at Macquarie University. The EPR spectra were collected with assistance from A/Prof Harmer. The analysis and interpretation of all experimental data was performed by myself. The manuscript was written by myself under the guidance of Dr Brown. We aim to submit this manuscript following the acceptance of paper 1, as presented in the preceding Chapter.

References

1. Takeda, S., et al., Structure of the core domain of human cardiac troponin in the Ca^{2+}-saturated form. Nature, 2003. 424(6944): p. 35-41.
2. Cordina, N.M., et al., Ca^{2+}-induced PRE-NMR changes in the troponin complex reveal the possessive nature of the cardiac isoform for its regulatory switch. PLoS One, 2014. 9(11): p. e112976.
3. Potluri, P.R., et al., The concerted movement of the switch region of Troponin I in cardiac muscle thin filaments as tracked by conventional and pulsed (DEER) EPR. J Struct Biol, 2017. 200(3): p. 376-387.

The release of the cardiac Troponin switch region is coupled to both Ca^{2+} binding and phosphorylation

Ehsan Kachooei[1], Nicole M. Cordina[1], Jeffrey R. Harmer[2] and Louise J. Brown[1]

[1]Department of Molecular Sciences, Macquarie University, Sydney, NSW, 2109, Australia

[2]Centre for Advanced Imaging, University of Queensland, Brisbane, QLD 4072, Australia

KEYWORDS: Cardiac Troponin, phosphorylation, spin labeling, paramagnetic NMR spectroscopy, pulsed EPR

Abstract

Troponin (Tn) is the molecular switch which regulates striated muscle contraction in response to Ca^{2+} influx. β-adrenergic stimuli is effective in increasing the rate of relaxation in heart muscle by upregulating protein kinase A through phosphorylation of the cardiac specific N-terminal extension region of Troponin I. Our understanding of how phosphorylation regulates conformational changes within troponin to enhance the relaxation rate is hindered by the absence of crystal structures of relevant states. Here we use site directed spin labeling (SDSL) approach, in combination with NMR and EPR, to track the movement of the TnI regulatory 'switch' peptide regions within the whole Tn complex. The interspin distances by pulsed EPR show a 'locked-in' position of the switch peptide in the hydrophobic binding pocket in the N-domain of TnC under saturating Ca^{2+} condition. Distances obtained from Paramagnetic Relaxation Enhancement (PRE)-NMR showed that this interaction is destabilised by phosphorylation. More dramatically, phosphorylation enhances the release of the switch peptide upon the removal of Ca^{2+}. From these findings, we propose a 'seat-belt' model describing the phosphorylation associated regulation of the switch region from TnC to enhance muscle relaxation.

Introduction

The Troponin (Tn) protein complex is the Ca^{2+} -dependant switch located on the muscle thin filament and responsible for the regulation of the contraction-relaxation process in striated muscle. Tn is a heterotrimeric protein comprised of a Ca^{2+} binding regulatory subunit (TnC), an inhibitory subunit (TnI), and a tropomyosin anchoring subunit (TnT). Located at distinct intervals along the actin thin filament, Tn's role in contraction is to transfer the Ca^{2+} binding force to the other components on the thin filament. This then results in the interaction between the thick and thin filaments via Tn's interaction with Tropomyosin (Tm) - a cable-like helical protein positioned on the surface of thin filament. According to current models of muscle regulation, during the relaxation state (or under conditions of low Ca^{2+}), the interaction between myosin and actin is limited by Tm. Whereas, during activation, when the concentration of Ca^{2+} is high, the Tn induced translocation of Tm leads to the exposure of the myosin binding sites on the actin filament [1, 2]. While the Ca^{2+} dependent movement of Tm to enable muscle contraction is relatively well established, the subtle interplay between the Tn subunits for transferring the Ca^{2+} signal through to the thin filament is less well-understood. Further, phosphorylation is known to play a key role in the cardiac isoform for regulating muscle contraction but how the structure and dynamics of Tn is modified by this post-translational state are still to be clearly defined.

To date, our best molecular level understanding of troponin has come from the partial X-ray structures of the core domain of cardiac Tn in the Ca^{2+} saturated state; and also the X-ray structures of the skeletal core of Tn under both high and low Ca^{2+} states [3, 4]. From these studies, and a plethora of other NMR studies on isolated subunits and fragments of Tn (as reviewed in [5]), it was shown that saturation of the TnC regulatory Ca^{2+} binding site/s (Site I and II in the skeletal isoform, or Site II in the cardiac isoform) results in conformational alterations within the TnC N-lobe to expose a hydrophobic patch. This patch then interacts with the 'switch peptide' region on TnI (cardiac residues 150-159). This Ca^{2+} triggered binding of the TnI switch peptide to N-TnC then leads to the release of two other regions of TnI, the inhibitory region (cardiac residues 130-148) and the mobile domain region (cardiac residues 170-210) from their inhibitory positioning on the actin filament. Finally, the position

of Tm is then altered on the thin filament allowing for the actin-myosin interaction to occur [6].

While Ca^{2+} binding to the regulatory N-lobe of TnC promotes the binding of the TnI switch region to its hydrophobic pocket in both the skeletal and cardiac isoforms, there are several stark differences between the two isoforms for how the binding interaction is achieved, and how the release of the switch peptide region from TnC under conditions of low Ca^{2+} is regulated [3, 4, 7]. In the skeletal Tn isoform, Ca^{2+} binding results in a distinct shift from a closed-to-open state for the N-domain of TnC. Upon release, the switch region is observed to move away from TnC and fluctuate over a wide range of distance (from 20 to 80 Å) [8]. In contrast, in the cardiac isoform, a dynamic closed-to-open structural equilibrium exists for the TnC N-domain, and Ca^{2+} binding shifts this balance towards a population with a higher proportion of the open state [7]. This can be described as Ca^{2+} binding 'priming' TnC for its interaction with the switch peptide [7]. When Ca^{2+} is removed, only a modest movement (~10 Å) of the switch region away from the N-domain pocket is observed; and complete release is never achieved [9, 10]. It has been suggested that the close proximity of the switch peptide to TnC N-lobe in the cardiac isoform may be favourable for increasing the frequency of interaction between two regulatory regions; and thereby counteract the reduced probability of collisions due to the incomplete opening of the N-lobe of TnC in the cardiac isoform [9]. Thereby, different conformational cascades are presumably in play to contribute additional control over cardiac Tn regulation. This likely includes phosphorylation effects.

In the heart, unique regulation mechanisms are responsible for allowing the cardiac muscle to respond to situations of high stress or increased physical activity. These mechanisms allow the heart to address the need for the increased oxygen demand in such situations. In response to β-adrenergic stimulation, protein kinase A (PKA) is activated in the body and this enzyme then phosphorylates several sarcomeric proteins including the TnI subunit of Tn. PKA modifies two serine residues (22 and 23) which are located in a unique sequence of 32 residues at the N-terminal region of cardiac TnI termed the N-extension region or NH_2-TnI region. Phosphorylation of the NH_2-TnI results in a decrease in Ca^{2+} sensitivity and a reduction in the actomyosin ATPase activity [11, 12]. This results in an increase in

crossbridge cycling and the muscle relaxation rate [13, 14]. Although the physiological implications of TnI phosphorylation are well known, the underlying structural mechanism have remained somewhat elusive but has been the focus of several recent NMR studies and computational modelling efforts. While phosphorylation appears to have little effect on the conformation of the N-lobe of TnC, its effects on Ca^{2+} sensitivity suggest it must be involved in the switch-release mechanism.

Evidence for phosphorylation involvement in the switch-release mechanism were first observed by an NMR study of partial fragments of Tn [15]. In this study, the authors reported that the switch peptide of TnI binds to TnC in the same region in both the unphosphorylated state (or wildtype 'WT' state, as will be referred to herein) and the phosphorylated state. However, the strength of the interaction was observed to depend on the inclusion of the NH_2-TnI region in the experiments, as well as its phosphorylated state. Several other studies have also proposed phosphorylation dependent effects on the switch binding mechanism [16, 17]. This includes our own recent NMR and EPR study (**Chapter 4, Paper 1**), which revealed the phosphorylation associated positioning of the NH_2-TnI region on TnC. In our study, we proposed an allosteric model where phosphorylation triggered cooperative changes in both the interaction of the NH_2-TnI region with TnC, and the re-orientation of the TnC interdomain positioning. Together, both structural changes facilitate the release of the TnI switch from TnC. Interestingly, a molecular dynamics (MD) simulation study also demonstrated that phosphorylation can increase disorder in the Tn complex, including the TnI switch peptide; leading to a reduction in the interactions between the TnC and TnI subunits [18]. However, another MD study could not replicate the reported effects from this earlier study and reported that the changes in the contact map between the TnI switch peptide and the N-lobe of TnC were only minor [19].

With the availability of only one crystal structure of the core domain of cardiac Tn complex (52 kDa) in the presence of Ca^{2+}, and the lack of a high-resolution structure in the Ca^{2+} free state, other approaches for examining Ca^{2+} binding and phosphorylation associated effects should be sought. A detailed structural understanding of the phosphorylation regulation mechanism for the release of the switch region from TnC can be achieved through a

combined effort of site directed spin labeling (SDSL) used in combination with Paramagnetic Relaxation Enhancement (PRE)-NMR and Electron Paramagnetic Resonance spectroscopy (EPR). Here we have used this approach to examine the influence of phosphorylation on the positioning of the TnI switch peptide region with respect to TnC in whole Tn. Nitroxide spin labels were first positioned onto either end of the TnI switch peptide (TnI151 or TnI159), and long-range distances obtained to map the interaction of the switch region with TnC by (PRE)-NMR (Fig. 1A). Interspin distances were also measured between TnC (TnC35, TnC84) and the TnI switch (TnI151, TnI159) in the whole Tn ternary complex by both pulsed DEER (Double Electron-Electron Resonance) and Continuous Wave (CW) EPR (Fig. 1B). Together, these complementary spin-labeling approaches provide a detailed analysis of both the position and dynamics of the switch region within the Tn complex in response to phosphorylation and Ca^{2+} binding. The phosphorylation and Ca^{2+} associated changes in the PRE mapping profiles and interspin EPR distances support a model where phosphorylation of the NH_2-TnI region is essential to achieve the complete release of the TnI switch region from the N-lobe of TnC in the low Ca^{2+} state.

Materials and Methods

Cardiac Tn Constructs

The expression of cysteine-less constructs of either rat cardiac TnC (cTnC) or TnI (cTnI) was carried out in pET-3d expression vector (Novagen) [20]. As previously described, full length rat cardiac TnT was expressed in the pET-28a expression vector (Novagen) and purified via an N-terminal 6-histidine tag, followed by cleavage of the full-length TnT protein via thrombin cleavage [10]. Two mono-cysteine constructs of both TnI (151 and 159) and two mono-cysteine constructs of TnC (35 and 84) were expressed and purified as previously described [9, 10]. TnI151 and TnI159 are located at the two ends of the helical switch peptide region of TnI. The TnI constructs were also prepared in both unphosphorylated state (WT) and phosphorylated states. The phosphorylated state was achieved by introduction of aspartic acid residues to replace serine residues 22 and 23 ($TnI_{S22/23D}$). This 'pseudo'-phosphorylated construct has previously been shown to change the contractile properties of myofibrils in a manner consistent with PKA treatment of cardiac Tn [21-25]. The two phosphorylated monocysteine constructs used in this study are herein referred to as

$TnI151_{S23/24D}$ and $TnI159_{S23/24D}$. After verification by DNA sequencing, all constructs were transformed into Escherichia coli BL21 (DE3) cells for protein expression.

^{15}N labeling of cysteine-less cardiac TnC construct was achieved by expressing in M9 minimal media, and using IPTG induction, as previously described [7, 9]. All other single cysteine cardiac TnI and TnC constructs were expressed in terrific broth media and purified according to the previous protocols. In brief, purification of TnC and TnI involved hydrophobic chromatography (Phenyl Sepharose 6B column) and cation exchange chromatography (carboxymethyl (CM) Sepharose column), respectively [9, 10]. TnT purification was done using Ni-NTA column followed by weak anion exchange chromatography (Sephadex DEAE 25 column) to remove nucleic acid contaminations [10].

Paramagnetic labeling of TnC & TnI constructs

Paramagnetic labeling of single cysteine mutants was performed by the covalent attachment of MTSL (1-oxyl-2,2,5,5-tetra-methylpyrroline-3-methyl-16 methanethiosulfonate) (Toronto Research Chemicals), as the paramagnetic nitroxide moiety, via the cysteine sulfhydryl group. Protein samples were initially reduced with 20 mM dithiothreitol (DTT) for 2–3 h at 4 °C in labeling buffer (6 M urea, 50 mM MOPS, 1 mM EDTA and 100 mM KCl, pH 7.8). Prior to labeling, DTT was removed by application of the protein onto a HiTrap Desalting column (5 mL, GE Healthcare). A 2.5 molar excess of MTSL was added and protein samples incubated for 16 h at 4°C. Unconjugated spin label was removed by exhaustive dialysis against reconstitution buffer (6 M urea, 50 mM MOPS, 1 mM EDTA, 0.5 M KCl, 2 mM $CaCl_2$ and mM $MgCl_2$, pH 7.2).

The efficiency of spin labeling was calculated from the double integration of the EPR spectrum of the labeled proteins. A Bruker EMX X-Band (9.6 GHz) EPR spectrometer with a standard rectangular TE102 cavity was used to collect continuous wave (CW) spectra at room temperature with a microwave power of 5.0 mW, modulation amplitude of 1.0 G and sweep width of 140 G.

Reconstitution of binary Tn samples for PRE-NMR (^{15}N-TnC/MTSL-TnI)

For NMR spectroscopy, binary complexes of ^{15}N-TnC/MTSL-TnI constructs in the phosphorylated state were reconstituted by combining ^{15}N-TnC with the MTSL-labeled (^{14}N)-TnI constructs in a 4:5 molar ratio (TnC:TnI). The samples were then dialysed in reconstitution buffer with 2 M urea and 0.5 M KCl. Formation of the binary Tn complex was achieved by the gradual removal of urea, followed by the lowering of the concentration of KCl to 0.1 M [9]. Uncomplexed TnI was removed by centrifugation. The binary Tn complexes in the +Ca^{2+} state were then prepared for NMR by exhaustive dialysis into NMR buffer (200 mM KCl, 20 mM imidazole, pH 6.9) in the presence of 3 mM $CaCl_2$. To prepare Ca^{2+}-free samples (-Ca^{2+}), Ca^{2+} was removed by dialysis against 0.1 M EGTA for 2 h at 4°C. The -Ca^{2+} sample was then further dialysed against decalcified NMR buffer (treated with Chelex-100 resin, Bio-Rad) and stabilised in the presence of 5 mM $MgCl_2$ [7]. The positions of the spin-labeled TnI residues for the NMR reconstituted binary samples are shown in Figure 1A.

Reconstitution of ternary Tn samples for EPR (TnC-MTSL/TnI-MTSL)

For CW and pulsed (DEER) EPR interspin distance measurements, the ternary Tn complexes were assembled by reconstitution of the TnC MTSL labeled constructs (TnC35, TnC84) with TnI MTSL labeled constructs (TnI151, TnI159) in both unphosphorylated and phosphorylated states. The Tn subunits were combined at a molar ratio of 1.0:1.2:1.2 (TnC:TnI:TnT) in 6 M urea and 0.5 M KCl. Similar to binary complex formation, the ternary complex was achieved by the gradual removal of urea and lowering of the [KCl] to 0.10 M via a series of dialysis steps into reconstitution buffer (1 mM EDTA, 2 mM $CaCl_2$, 3 mM $MgCl_2$, 50 mM MOPS, pH7.2). The excess precipitated TnI-MTSL and TnT was removed by centrifugation before the ternary Tn complexes were stabilised in 0.2 M KCl. The high and low Ca^{2+} ternary complexes were achieved by the addition of 5 mM $CaCl_2$ and 8 mM EGTA, respectively, in EPR reconstitution buffer [26]. Similarly, a single spin ternary construct was prepared with the phosphorylated TnI151-MTSL construct and reconstituted with TnC-cysless. The positions of the spin-labeled TnI residues for the EPR ternary samples are shown in Figure 1B.

PRE-NMR spectroscopy of binary complex (^{15}N-TnC/MTSL-TnI)

NMR data were collected on a Bruker Avance 600 MHz spectrometer equipped with a cryoprobe. All experiments were performed at 303 K and spectra processed using Topspin 1.3 (Bruker, Inc). All binary complex (TnC-TnI) samples were 550 µL and concentrations ranged from 150 to 250 mM. For each paramagnetic spin-labeled binary ^{15}N-TnC/MTSL-TnI sample, a ^{1}H-^{15}N-TROSY spectra was first collected - the 'paramagnetic' spectrum. The nitroxyl radical of the MTSL label was then reduced to its hydroxylamine equivalent by the addition of ~1/250 volume of a 5-fold molar excess of ascorbic acid (from a 0.5 M stock). After 1 h incubation at room temperature, complete reduction of the spin label was achieved [9]. The ^{1}H-^{15}N-TROSY spectrum was then collected for the reduced 'diamagnetic' sample. The small volume of ascorbic acid did not significantly dilute the sample, thus enabling the direct comparison of peak intensities between paramagnetic and diamagnetic spectra for calculation of the relaxation enhancement. Spectral assignment and analysis was performed with the program Sparky [27]. Peak assignments in the diamagnetic and paramagnetic spectra of each TnC construct were made using the assignments reported for the cardiac binary complex (TnC-TnI) [25, 28], and using the chemical shifts of isolated TnC in the Ca^{2+}-free [7].

PRE NMR - distance analysis

The PRE from the presence of the MTSL spin label (Γ_2) was calculated from the ratio of the amide peak intensities obtained in the paramagnetic (I_{para}) and diamagnetic states (I_{dia}) assigned in the ^{1}H-^{15}N-TROSY spectra according to Eqn. 1. Peak heights were used as measures of peak intensities, and the intrinsic transverse relaxation rate (R_2) was estimated from the peak width at half-height ($R_2=\pi\Delta\nu_{1/2}$) [29, 30]. All spectra were recorded with the single evolution time point (t) of 10 ms.

$$\frac{I_{para}}{I_{dia}} = \frac{R_2 exp(-\Gamma_2 t)}{R_2+\Gamma_2} \qquad \text{Eqn. 1}$$

The calculated PRE rates (Γ_2) were converted to distances (r) using a modified form of the Solomon-Bloembergen equation [29-31];

$$\Gamma_2 = \frac{K}{r^6}\left[4\tau_c + \frac{3\tau_c}{1+\omega_H^2\tau_c^2}\right] \qquad \text{Eqn. 2}$$

where ω_H is the Larmor frequency of the proton; *K* is a constant (1.23 x 10^{-32} cm^6 s^{-2}) which describes the spin properties of the nitroxide spin label [30]; and τ_c is the correlation time of the electron-proton interaction $\tau_c = (\tau_r^{-1} + \tau_s^{-1})^{-1}$. Due to the long electronic relaxation time of the nitroxide spin label (τ_s) compared to the protein rotational correlation time (τ_r), the value of τ_c is effectively equal to the overall correlation time of the protein [32] and was taken as 16 ns, as estimated from linewidths as previously described [9]. It should be noted that, in order to convert experimental Γ_2 values to distances using Eqn. 2, it was assumed that the observed PRE effects arise from a single conformational state.

DEER and CW-EPR Spectral Acquisition

Tn samples were prepared in 40% v/v D8-glycerol with a final concentration of 45-90 μM. Samples were transferred into 4mm outer diameter quartz tubes and flash frozen in liquid nitrogen before collecting double electron-electron resonance (DEER) and continuous wave (CW) EPR experiments. The four-pulse DEER experiment was performed at 60 K using an ELEXSYS E580 spectrometer (Bruker) with a Q-band (32 GHz) resonator and a 200 W microwave amplifier. The pump pulse was applied at the maximum of the echo-detected field swept spectrum, with an offset of 80-100 MHz higher than the detection frequency. Detection pulses were set to 16 ns (π/2) and 32 ns (π) to set up the Hahn-echo, and pump pulse was set to 16 ns. The first pulse delay time, τ_1, was set to 160 ns, whereas τ_2 was adapted according to the expected mean distances. Nuclear modulations were averaged by increasing the first inter-pulse delay by 16 ns. Shot repetition time for all the measurements were set to 3 ms. The background of the normalized DEER primary data (V(t)/V(0)) was corrected and the resulting normalized secondary data (F(t)/F(0)) were converted by Monte-Carlo/Simplex Gaussian convolution method to distance distribution using DeFit software [33]. Gaussian populations used to describe the experimental data are in terms of distance(s) (*r*) and distance distribution(s) (*Δr*) based on a statistical F-test. The simulation of the possible spin label rotamers at the selected labeling site in the protein was performed using the Matlab program package MMM2015.1 [34].

CW-EPR experiments were carried out at 165K temperature on an ELEXSYS E500 spectrometer (Bruker) with a 9.4 GHz (X-band) resonator, 0.05 mW microwave power (36 dB power attenuation), 20 mT sweep width and 0.2 mT modulation. The analysis of spectral broadening for double labeled Tn samples was performed using a Monte-Carlo/Simplex Gaussian convolution CWdipFit software [33].

Results

The aim of this study was to track the movement of the regulatory switch region of TnI in response to phosphorylation, with respect to TnC. To achieve this, PRE-NMR measurements were performed on the TnC-TnI binary complex of cardiac Tn in solution. Two sites (TnI 151 and I159), each on either end of the switch peptide, were selected for labeling with the paramagnetic spin species (MTSL) (**Figure 1A**). The effect of phosphorylation was mimicked by the introduction of two aspartic acids in place of serines at residues 22 and 23 within the cardiac specific TnI N-terminal extension region. NMR samples for each phosphorylated construct ($TnI151_{S22/23D}$ $TnI159_{S22/23D}$) were prepared under conditions of low Ca^{2+} ($-Ca^{2+}$) and high Ca^{2+} ($+Ca^{2+}$). A ^{1}H-^{15}N-TROSY spectrum for each sample was collected first in with the paramagnetic spin label; and again, following reduction of the spin label to its diamagnetic equivalent (**Figure S1**). The PRE results of the phosphorylated binary constructs were compared to previously reported NMR spectra of the equivalent non-phosphorylated constructs [9].

Assignment of the ^{1}H-^{15}N-TROSY spectra of the phosphorylated binary complexes obtained in both the $+Ca^{2+}$ and $–Ca^{2+}$ state was achieved by comparison with available chemical shifts values of TnC, as described before [9]. Between 32 to 50% of TnC resonance peaks from the ^{1}H-^{15}N-TROSY spectra could be assigned with confidence. This assignment was adequate to provide good overall coverage of both N- (residues 1-85) and C-domains (residues 94-161) of cTnC; as well as the connecting central linker region (residues 86–93).

PRE effects ($I_{para}/I_{dia} < 1$) were observed as a reduction in peak intensity due to peak broadening in the paramagnetic state compared to diamagnetic equivalent state. As the PRE-broadening is dependent on the distance between the nitroxide group of the spin label

and the proton, distances (*r*) between the amide residue and spin label could then be extracted using Eqn. 2. The range of quantifiable PRE effects was however limited to ~12 to 25 Å due to the noise level in ^{1}H-^{15}N-TROSY spectra of the relatively large TnC-TnI complex (42.6 kDa) [9].

Due to the upper limit of the PRE approach, interspin distance measurements > 25 Å, were also characterised by pulsed DEER measurements. DEER is suitable for reporting on the large scale release of the switch peptide from TnC upon removal of Ca^{2+} [8, 10]; and can be performed on the whole 78 kDa ternary Tn complex. Again, the two TnI residues (151 and 159) at either end of the switch region were spin labeled and interspin distances measured to the native cysteines residues (35 and 84) on the N-domain of TnC (**Figure 1A**). TnC35 is located near the inactive Ca^{2+} binding Site I; and TnC84 is on the C-terminus of helix D which is near the switch peptide binding pocket on of TnC. In total, 12 interspin distance measurements were performed of the double-labeled ternary constructs in the presence and absence of Ca^{2+}. In the WT unphosphorylated state, distances were obtained for TnI159/TnC35 and TnI159/TnC84. In the phosphorylated state, distances were also obtained for TnI159/TnC35, TnI159/TnC84, TnI151/TnC35 and TnI151/TnC84 in both the WT and phosphorylated states. Comparison of the distances from the TnI151/TnC35 and TnI151/TnC84 phosphorylated constructs was made with previous measurements for the same unphosphorylated (WT) constructs [10]. CW spectra were also obtained, and broadening effects provided details of short range interspin distances (8-20 Å), where present.

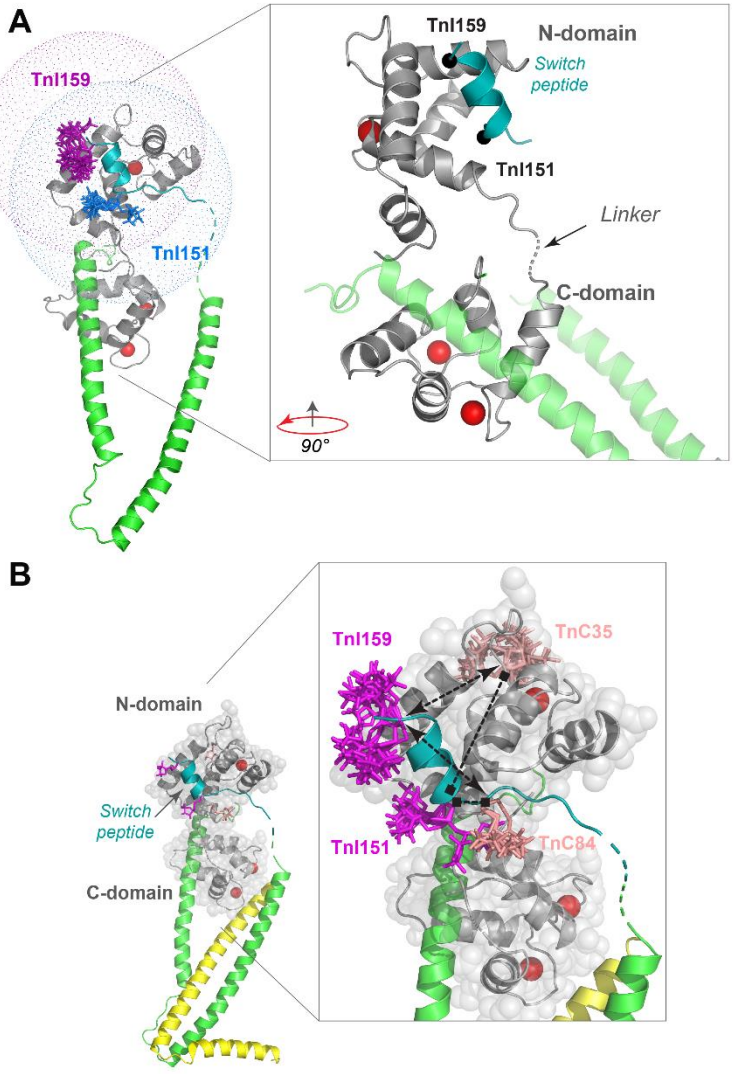

Figure 1 Positioning the TnI switch peptide with respect to TnC using MTSL-labeled Tn constructs. **(A)** Location of single TnI cysteine mutants (TnI151 and TnI159) used for PRE-NMR measurements in the Tn binary complex. Dotted spheres indicate a 20 A° radius around each spin label site where PRE distances can most accurately be measured. TnI regions missing from the X-ray structure are shown as dashed lines. Red spheres represent bound Ca^{2+}. **(B)** Spin labeled sites for EPR distance measurements are shown on the X-ray structure of cardiac Tn (PDB: 1J1D) [3]. TnC- grey, TnI- green, TnT- yellow. The TnI switch peptide is coloured in teal. Dashed lines represent the four interspin pairs measured by DEER and CW-EPR in the WT and unphosphorylated state ($TnIS_{22/23D}$) of the ternary Tn complex. Stick representation of rotamers for each of the attached spin labels, as calculated with MMM [34].

PRE effects in ^{15}N-TROSY spectra of the phosphorylated cTnC-cTnI binary complex in response to Ca^{2+} binding

NMR samples of the two spin-labeled binary TnC-TnI phosphorylated constructs were prepared in both the absence (-Ca^{2+}) and presence of Ca^{2+} (+Ca^{2+}). A ^{1}H-^{15}N-TROSY spectrum was first acquired for each sample in the presence of the paramagnetic spin label (Figure S1). A second spectrum was then acquired following the reduction of the nitroxide group of the spin label to its diamagnetic equivalent. In each case, peak broadening effects (or the disappearance of some peaks), which were observed in the paramagnetic spectrum, were alleviated in the diamagnetic spectrum.

Overall, the pattern of paramagnetic peak broadening for all four phosphorylated binary complex samples was unique. The peak broadening effects, as a result of the spin label inclusion on the switch peptide, were strongest, and greatest in number in the +Ca^{2+} state. While weaker, there were still several peak broadening effects observed for both samples in the –Ca^{2+} state. As done previously [18], assignment of the ^{1}H-^{15}N-TROSY spectra obtained in the +Ca^{2+} phosphorylated state was made by comparison with available chemical shift values of cardiac TnC bound to cardiac TnI(1–211) [28] and TnI(1–80) [25]. The chemical shifts of isolated cTnC N-domain resonances in the Ca^{2+} -free state aided in peak assignment of the –Ca^{2+} phosphorylated samples. In total, 56 to 76 residues were able to be assigned with confidence. Notably, assignment of the phosphorylated construct was not affected due to any significant change in chemical shift values.

Peak intensity ratios (I_{para}/I_{dia}) were measured for each assigned TnC resonance in the phosphorylated constructs (+/-Ca^{2+}) (**Figure 2A**). Comparison of the I_{para}/I_{dia} for TnI151 and I159 in +Ca^{2+} state showed that the mean peak intensity ratios values for TnI159 were smaller compare to TnI51 across the entire TnC molecule. The opposite was observed in the –Ca^{2+} state where, on average, the peak intensity ratios were smallest for the TnI151 construct. Many residues across the N-domain of TnC, particularly for the +Ca^{2+} construct, were broadened beyond detection. These PRE effects, and changes observed due to Ca^{2+} binding, indicate that the positioning of the switch peptide region, with respect to TnC, is within the PRE range of sensitivity (< 25 Å). The PRE-effects measured here, and the accompanying changes upon Ca^{2+} binding, are also most prominent across N-domain

residues as is expected from the binding of the switch peptide to the hydrophobic pocket in the N-domain.

Changes in PRE-derived distances in response to phosphorylation and Ca^{2+} binding

Peak intensity ratios (I_{para}/I_{dia}) were used to calculate the PRE rates (Γ_2) (Eqn. 1) for the phosphorylated constructs of TnI151 and I159 (Table S1 & Table S2). The PRE rates are then proportional to $1/r^6$ (Eqn. 2), where r is the distance between the proton and the nitroxide group of the spin label. All PRE-derived distances measured from the switch region (I151 and I159) to cTnC residues that were able to be assigned are listed in Table S1 and Table S2, respectively. Using these PRE-derived distances measured from the either termini of switch peptide (TnI151 & TnI159) to TnC, the influence of phosphorylation of the TnI NH_2-TnI region on the positioning of switch peptide with respect to TnC subunit can be observed (**Figure 2B**). PRE-derived distances were also compared to modelled distances measured from the same sites on the switch region to TnC for both the X-ray crystal structure [3] and two available computational models of Tn which include the NH_2-TnI region of TnI [19, 35] (**Figure 2B**). Lastly, the PRE measured distances from the spin labels to the residues in TnC were mapped onto the core crystal structure of Tn (1J1D) to visualize the relative positioning of switch peptide with respect to TnC (**Figure 2C**). The purple and salmon colours represent distances < 16 Å and between 16-20 Å, respectively. The mapping effects are in the order of events which represent the release of the switch peptide from the hydrophobic pocket in the N-domain of TnC upon the removal of Ca^{2+}; and the effect of phosphorylation on both the $+Ca^{2+}$ and $-Ca^{2+}$ states (Figure 2C).

Comparison of the distances for the unphosphorylated (WT) and phosphorylated constructs measured in the $+Ca^{2+}$ state for both the TnI159 and TnI151 revealed discrete and well-defined patches of strong PRE effects that primarily mapped to the hydrophobic pocket on the regulatory N-lobe to which the switch peptide can bind. These effects were strongest in the WT construct with phosphorylation causing only small changes in the PRE-distance profiles (Figure 2B, top panels). While PRE interactions were weakened in the phosphorylated construct (and a corresponding increase in PRE-derived distances), the

changes were not substantial enough to suggest the complete release of the switch region from the N-domain pocket had occurred. On average, the distance from the switch region to TnC decreased upon phosphorylation by approximately 3.5 Å for the TnI159 construct and increased by approximately 1.6 Å for the TnI151 construct. The changes in the mapping profiles of the PRE-derived distances are shown in Figure 2C.

Some of the largest phosphorylation induced increases in the PRE-distances of the $+Ca^{2+}$ TnI159 labeled construct occurred across helices A, B and D with residues located in, or in close vicinity, to the hydrophobic switch-binding pocket. For example, distances from Glu15, Gln50, and Asp88 increased by approximately 4, 1, and 2 Å, respectively. For the TnI151 construct, the increase in distance from phosphorylation were most notable for residues across the TnC N-domain and included Asp25, Glu59, Glu63, Gly68, and Glu76 which were mapped at greater than 25 Å in the phosphorylated construct. Interestingly, Asp25 is an important switch binding residue, located on helix A of the hydrophobic pocket. Similar to TnI159, other residues in the vicinity of the switch binding pocket (Asn18, Met45, Gln50, and Asp88) all showed a distance increase of approximately 3 Å upon phosphorylation. Agreement of the measured distances from the two spin label sites with the corresponding distances in the crystal structure of cardiac Tn in high Ca^{2+} state (1J1D) confirmed a 'locked-in' positioning of the switch peptide with the hydrophobic pocket of N-domain [9]. Overall, phosphorylation of the $+Ca^{2+}$ construct caused a modest destabilisation of the switch peptide interaction with TnC but did not result in the release of the switch from its hydrophobic pocket within the TnC N-domain.

Consistent with earlier studies [9], the PRE effects upon removal of Ca^{2+} showed the release of the switch region but the magnitude of movement in the WT state was only modest. The average distance change measured between the switch peptide and cTnC was only up to ~10 Å [9].

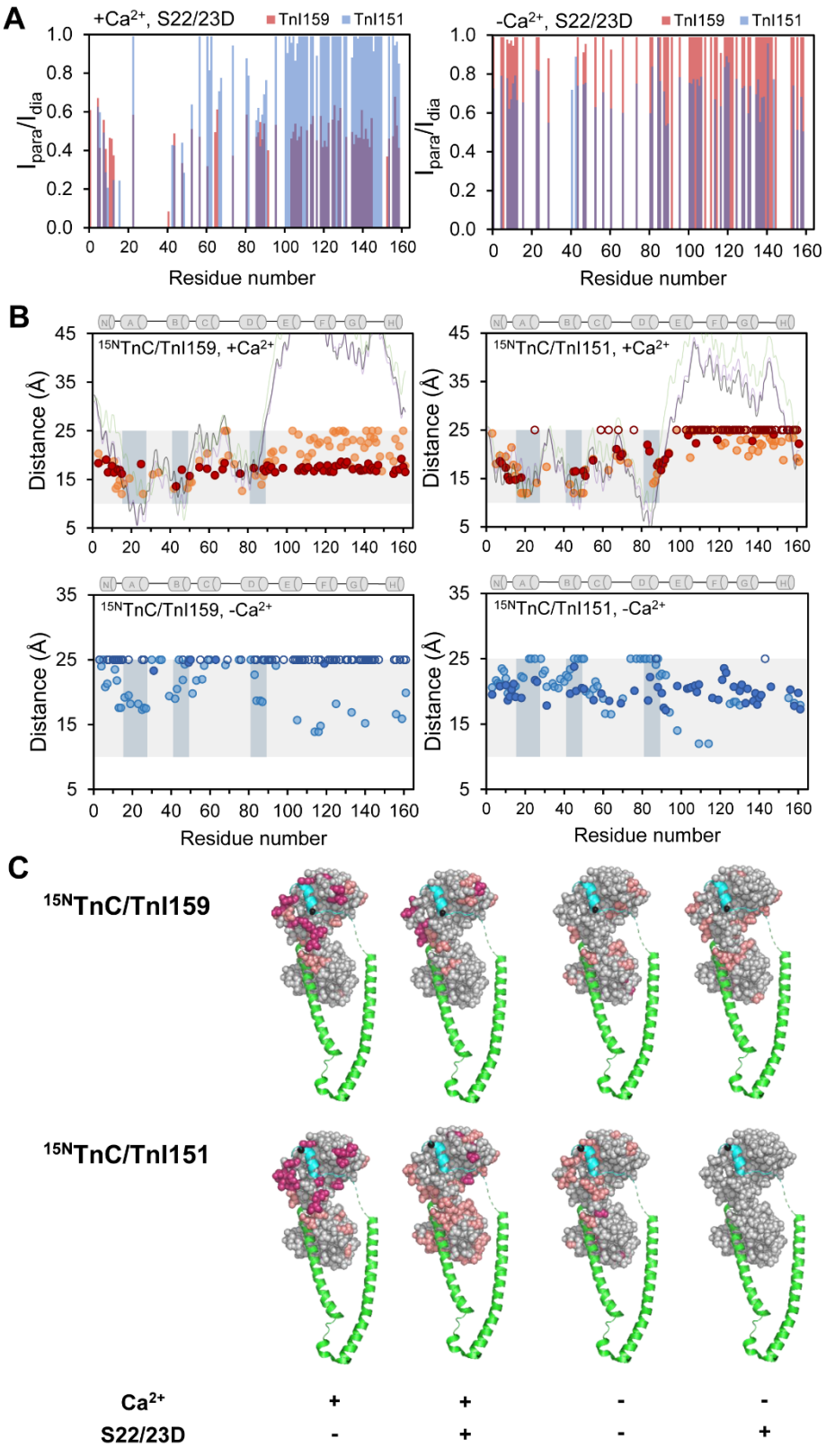
A
+Ca2+, S22/23D
TnI159
TnI151
-Ca2+, S22/23D
Ipara/Idia
Residue number
B
15NTnC/TnI159, +Ca2+
15NTnC/TnI151, +Ca2+
15NTnC/TnI159, -Ca2+
15NTnC/TnI151, -Ca2+
Distance (Å)
Residue number
C
15NTnC/TnI159
15NTnC/TnI151
Ca2+
S22/23D

Figure 2 PRE-NMR measurement for assigned peaks of WT and phosphorylated TnC from spin labels positioned at TnI151 and TnI159 on the TnI switch region in the presence and absence of Ca^{2+}. **(A)** Peak intensity ratios (I_{para}/I_{dia}) for $TnI159_{S22/23D}$ (*red*) and $TnI151_{S22/23D}$ (*blue*) in $+Ca^{2+}$ (left panel) and $-Ca^{2+}$ (right panel) conditions. **(B)** Comparison of PRE-derived distance for assigned TnC residues in phosphorylated (dark colors) and WT (light colors) states for TnI159 and TnI151 in $+Ca^{2+}$ (upper panels) and $-Ca^{2+}$ (lower panels) conditions. The distances for WT constructs were from a previous study [9]. Distance plots also show distances calculated from the coordinates of the cardiac Tn core crystal structure 1J1D (black line [3]), and distances from two structural models (purple line, Model A [35]; and green line, Model B [19]) of the TnI switch peptide region in complex with TnC. Open circles indicate residues where peak intensity ratios were > 0.98 and are thus plotted at 25 Å. The grey shading band on the distance plots represents the distance range of sensitivity of the PRE approach (10 - 25 Å). Longitudinal dark grey shaded boxes indicate TnC residues within the hydrophobic switch-binding pocket region (helices A, B, and D). **(C)** Comparison of mapping of PRE derived distances for the two spin labeled TnI constructs across the four different states of phosphorylation and Ca^{2+}binding. The Tn binary constructs for TnI159 (*up*) and TnI151 (*bottom*). TnC and TnI are in grey and green, respectively. Distances ≤ 16 Å are coloured in purple, and distances in range of 16-20 Å are coloured salmon. The TnI switch peptide is coloured in cyan. Further views of these PRE-derived distance mapping profiles are shown in Supplementary Figure S2.

The changes in the PRE-distances (**Figure 2B** bottom panel), and corresponding mapping effects, observed in the absence of Ca^{2+} state for the WT and phosphorylated states (**Figure 2C**) suggested that phosphorylation of the NH_2-TnI region of TnI has a significant influence on the release of the switch peptide region from TnC. When comparing the mapping profiles of the spin-labeled TnI constructs, the results suggest that the removal of Ca^{2+} and phosphorylation of the construct are both required to achieve the complete release of the switch region. This was particularly true for the TnI159 construct where the effect of phosphorylation can be clearly seen to result in the removal of any interaction of this spin labeled site with TnC in the $–Ca^{2+}$ state. In the $-Ca^{2+}$ state for the TnI159 labeled construct, phosphorylation is observed to shift almost all assignable TnC residues to distances at, or longer than, the 25 Å upper limit of the PRE technique. The mean increase in overall PRE-distances for residues across the N- and C-domain for this construct increased by approximately 3 and 8 Å, respectively. There was also a 6 Å increase in the average PRE distance from the TnI159 spin label with residues lining the hydrophobic switch-binding

pocket. For the TnI151 construct, the average distance changes were overall smaller in magnitude for the phosphorylated construct in the $-Ca^{2+}$ state when compared to the $+Ca^{2+}$ state. However, the magnitude of the distance changes for several residues which were assigned in both $+/-Ca^{2+}$ phosphorylation states (Glu15, Asn18, Asp25, Lys43, Met45, Gln50, and Ser84) were as large (up to approximately 6 Å) as many of the distances observed for the TnI159 construct. Interestingly, many distances, particularly across residues in the N-domain, were observed to decrease in magnitude for the phosphorylated state when Ca^{2+} was removed. It was observed that the mean distances from TnI151 to the N-domain TnC residues increased in magnitude by approximately 2 Å but decreased by 3 Å for TnC residues across the C-domain. Together, both the size of the distance changes and direction of distance changes suggest that the movement of the two ends of the switch peptide region are opposite in direction with respect to TnC N-lobe, although the switch peptide movement is always further away from C-lobe regardless of the phosphorylated state. It was observed that the mean distances from TnI151 to the N-domain TnC residues increased in magnitude by approximately 2Å but decreased by 3 Å for TnC residues across the C-domain.

Lastly, our PRE-distances measured for the $+Ca^{2+}$ WT and phosphorylated constructs showed some agreement with the distances from current available models (Model A, [35] and Model B [19]). Our PRE distances and the modelled distances show the close and tight binding of the switch region with the TnC N-domain, and this is in agreement with the X-ray crystal structure. Neither of the computational models predicted significant changes in the measured distances from the switch peptide to hydrophobic pocket region in N-lobe in phosphorylation state. This contrasts with our PRE-distances where increases in distances were observed which suggested the weakening of the interaction of the TnI switch region with TnC in the phosphorylated state. The PRE distances from the switch peptide to TnC C-domain residues, in either the WT or phosphorylated states, were not in agreement with either computational models or the X-ray structure. This was not unexpected due to the flexibility of the central linker of TnC linker [36] and therefore the bias of PRE distances for collapsed conformations of TnC.

EPR interspin distance: phosphorylation destabilises the switch position and enhances its release in low Ca^{2+} conditions

To further characterise the effects of phosphorylation on the Ca^{2+} induced interaction of the TnI switch peptide with to TnC, we also performed CW-EPR and pulsed DEER experiments using whole Tn complex. DEER experiments are valuable as they can report on interspin distances from 20 to as large as ~60 Å [37]. Whereas, CW is most sensitive to short interspin distances of ≤ 25 Å. The TnC and TnI subunits were individually labeled to create the four cysteine pairs of TnI159/TnC35, TnI159/TnC84, TnI151/TnC35, and TnI151/TnC84 before reconstitution with full-length TnT, to assemble the intact Tn ternary complex as shown in Figure 1.

A four-pulse DEER experiment was used to measure the interspin separations for 12 combinations (±Ca^{2+} or ±phosphorylation) for the TnI159/TnC35, TnI159/TnC84, TnI151/TnC35, and TnI151/TnC84 ternary samples Figure 3 shows the raw Q-band DEER data traces. Interspin distances were then obtained from the background corrected spectra, as shown in Figure 3 for TnI159 to residues 35 or 84 on TnC, and Figure 4 for TnI151 to residues 35 or 84 on TnC. DEER profiles show the decay of the spin echo intensity (*left column*), where the rate of the initial decay is proportional to the interspin distance. As such, a fast decay implies a short distance. The best model for the evolution decay is fitted to the spectral data and corresponding Gaussian distributions shown (*middle column*). A two Gaussian model was found to fit best for all interspin samples and was comprised of 'short' and 'long' distance components. The χ^2 surface from the Monte Carlo searches were represented as contour plots (*right column*). The surface asymmetry and width of the distance components on the contour plots demonstrate the validity of the distribution profiles. A summary of all DEER distances and populations are also given in **Table 1**. The broadening of CW-EPR spectra for all samples was also investigated to confirm the presence of interspin populations < 20 Å. CW-EPR broadening was obtained by comparing the double-labeled spectrum with the sum of the single non-interacting spin sample (**Figure S4**).

Effect of phosphorylation and Ca^{2+} binding on the interspin DEER distances

(i) TnI159/TnC35: Figure 3 shows the DEER distance measurements for the two interspin distances from TnI159 to TnC35 or TnC84. The DEER measurement for the TnI159/TnC35 interspin pair, under conditions of high Ca^{2+} state were similar in both the WT and phosphorylated states (**Figure 3A**). The electron spin echo modulation during evolution time for this distance pair represented similar well-defined oscillations (**Figure 3A**, *left*). The major contribution for the WT and phosphorylated states showed a short and narrow distance (*r*) of 27 ± 3 Å and 28 ± 3 Å, respectively (Figure 3A, *middle*). There was also a second 'longer' distance population for each state with a broad distance width (*Δr*) of 45 Å. However, if compared to the short distance component, this long distance was not well-defined although the contributing population was~ 30% (Figure 3A, *right*).

In the absence of Ca^{2+}, there was a notable increase in the distribution width for the TnI159/TnC35 interspin pair and significant phosphorylation dependent differences in the populations of interacting spins contributing to the short and long-distance components. In the WT state, the two distance populations were 26 ± 1 Å (*Δr* = 14 Å) and 57 ± 1 (*Δr* = 42 Å) (**Figure 3B**). Both average distances were similar in to the short and long-distance components in the $+Ca^{2+}$ state for this interspin pair. Phosphorylation of the construct in the $-Ca^{2+}$ state however resulted in a significant increase of 12-14 Å in the average distances for both the short and long components; and a dramatic increase in the disorder of the interspin pair, particular for the short distance component where the width increased from 14 to 45 Å.

(ii) TnI159/TnC84: The interspin distance to TnC84 from the same site labeled on TnI (159) also showed a similar phosphorylation and Ca^{2+} binding response to the I159/TnC35 pair (Figure 3C). Under high Ca^{2+} conditions, the majority of spins (~83%) were best represented by a short distance of 21 ± 1 Å and a narrow distribution width of Δr = 2 Å. As for the TnI159/TnC35 pair in the Ca^{2+} saturated state, most spins were at a short and well-defined distance, irrespective of the phosphorylation state of Tn (**Figure 3C**). Again, the data fits suggest a second long distance at approximately 46-47 Å for both the WT and phosphorylated states may be present. This population may represent unbound switch

peptide. Confirmation of the DEER detected close interaction between the switch region (labeled at TnI159) and TnC84can be observed by the CW-EPR measurements which showed a narrow short distance (19 ± 1 Å) (Supplementary **Figure S4 B**).

Like the TnI159/TnC35 pair, the removal of Ca^{2+} again led to an increase in both the average distance and distribution width of the short component for the TnI159/TnC84 pair. For the WT construct, the short distance pair increased by 11 Å to 32 ± 1 Å in the Ca^{2+} free state; and the distance width increased from 2 ± 1 Å to 34 ± 4 Å. The phosphorylated construct also showed a similar short distance component with an average distance of 30 ± 1 Å and *Δr* of 34 ± 3 Å. In the -Ca^{2+} state, the average distance for the second long distance component observed in the +Ca^{2+} state increased by 13 Å and 17 Å for the WT and phosphorylated states, respectively. This long distance was also more populated in the WT (23%) and phosphorylated state (32%) than compared to the +Ca^{2+} state. While phosphorylation of this interspin distance in the -Ca^{2+} was similar in both average distances and populations of the short and long component, phosphorylation effects were noted for the width of the distance distributions but for the long component only. The long distance for the phosphorylated construct was significantly more disordered (*Δr* of 7 ± 9 Å than the WT distance in the -Ca^{2+} state (*Δr* of 20 ± 3 Å).

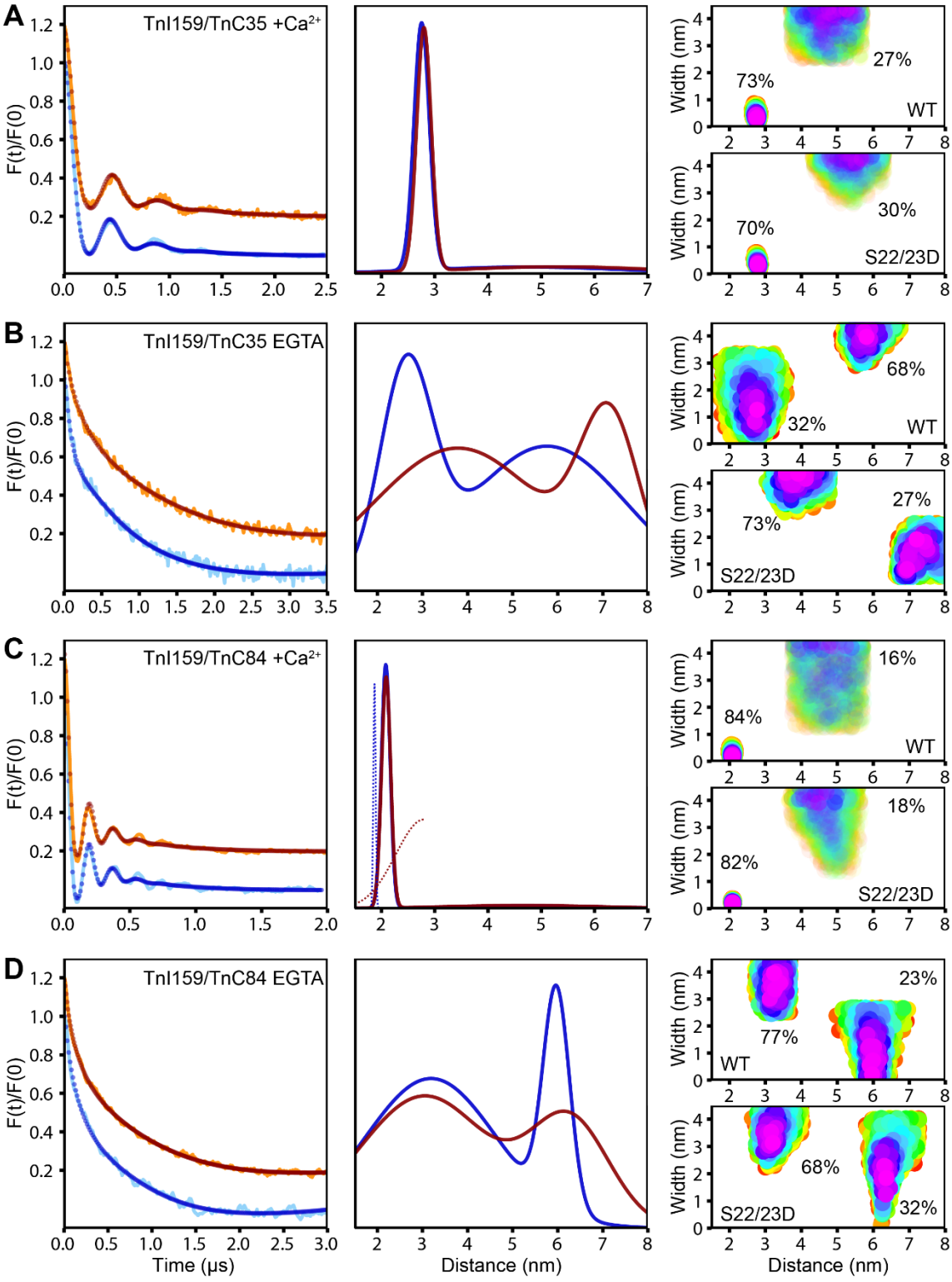

Figure 3 DEER spectra and distance analysis in soluble spin labeled ternary Tn complex to position the TnI switch peptide with respect to TnC. Interspin distances for double labeled Tn complexes in wild type (WT, blue) and phosphorylated (S22/23D, red) states for TnI159/TnC35 in **(A)** $+Ca^{2+}$ and

(B) -Ca^{2+} conditions; and for TnI159/TnC84 in **(C)** +Ca^{2+} and **(D)** -Ca^{2+} conditions. *Left panels*, DEER traces (after background correction) show the time evolution of spin echo (WT, aqua or phosphorylated, orange thin lines) and fitted modulation of the spectrum from the DeFit analysis (WT, dark blue or phosphorylated, red lines) which uses a Monte-Carlo minimization approach. *Middle panels*, two Gaussian distance-distributions representing the best fits to the experimental DEER data. In 3C, dotted lines represent the distanced obtained using CW measurement (*see* Supplementary **Figure S4**). *Right panels*, contour error surface plots representing χ^2 for the main Gaussian populations shown in in the middle panel (WT, upper plot or phosphorylated, lower plot). The percentages for each short and long-distance populations are indicated adjacent to contours. Faded surfaces indicate likely unreal populations arising from the fitting procedure.

TnI151/TnC35 and TnI151/TnC84: In an earlier study, we reported the Ca^{2+} binding effects on the interspin distances of TnI151 to TnC35 and TnI151 to TnC84 in the ternary soluble Tn construct using CW and DEER methods [10]. For completion, we now report here on the effects of phosphorylation on both these interspin distances. The DEER spectra obtained in this study for the phosphorylated constructs are shown in Figure 4. The Gaussian distance distribution profiles from our earlier study on the WT construct are also included so to allow comparison with experimental fits obtained in this present study. The CW spectra of the WT and phosphorylated constructs under both +Ca^{2+} and -Ca^{2+} conditions are available in supplementary Figure S4. A full summary of all EPR distance data for these constructs is also presented in **Table 1**.

In the presence of Ca^{2+}, phosphorylation did not significantly change the average distance or distribution width of the short distance component (28 ± 1 Å, Δr = 8Å) reported in our earlier study. There was however a small decrease in the population of the short component (by ~17%) upon phosphorylation which indicated a partial disordering of this interspin distance pair (**Figure 4A**).

In the absence of Ca^{2+}, the TnI151/TnC35 interspin pair in the WT construct previously revealed a single broad population centred at 36 ± 5 (Δr = 37Å) [10] (**Figure 4B**). In the phosphorylated construct, two distance components were observed; a narrow shorter (31 ± 3Å, Δr = 9Å) and a broad longer (61 ± 3Å, Δr = 40Å). Interestingly, the long and broad distance component showed a higher population (75%) of interacting spins suggesting that

phosphorylation increased both the interspin distance for this labeled pair, as well as the interspin disorder.

For the TnI151/TnC84 interspin pair, our earlier study of the WT construct reported the presence of only a single broad distance which was similar in both the presence and absence of Ca^{2+}. Under phosphorylation conditions, very different effects were observed. In the presence of Ca^{2+}, the fits revealed two interspin distance components (**Figure 4C**). The long component (46 ± 7Å) was very broad with a width of Δr = 29Å and a population of 40%. However, this component was not well defined. The short distance (18 ± 1 Å) which comprised 60% of the spins was narrow (Δr = 8 Å) and well-defined although it was at the lower limit of DEER sensitivity. CW measurement verified the presence of this short distance close to the upper limit of the CW-technique (19 ± 1 Å, Δr = 11 Å). CW from our earlier study on the WT state also revealed a very short distance (10 ± 1 Å) to be present [10]. Similar to the other interspin constructs, phosphorylation again increased the disorder of interspin distances but did not significantly change the average interspin distances, particularly for the short distance component, where present.

Lastly, for the TnI151/TnC84 construct, under-Ca^{2+} conditions, CW and DEER measurement revealed short interspin distances of 9 ± 2 Å (Δr = 4 Å) and 26 ± 1 Å (Δr = 10 Å), respectively for the WT construct [10] (**Figure 4D**). Fits to the DEER experimental data of the phosphorylated construct revealed two distances populations which were significantly longer; a short and broad distance (35 ± 4 Å, Δr = 45Å) and a long and narrow distance (64 ± 4 Å, Δr = 8 Å). The population of the short distance by DEER was 76%, and, in comparison to the long distance, the short distance distribution was well-defined. Thus, overall, phosphorylation again increased the average interspin distance in the Ca^{2+}-free state (by 25 Å), and also the distribution width (by 35 Å).

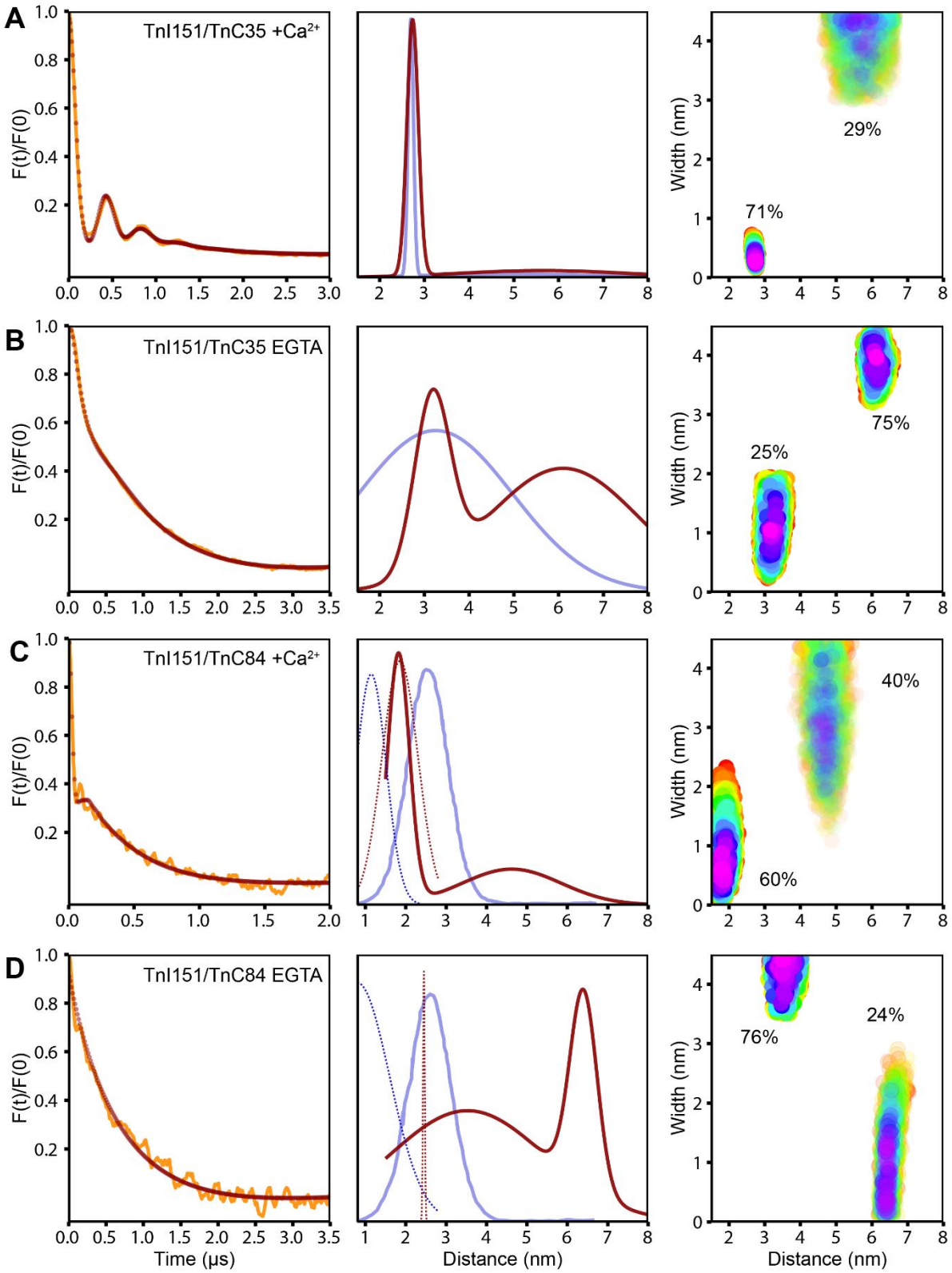

Figure 4 DEER spectra and distance analysis in soluble spin labeled ternary Tn complex to position the TnI switch peptide with respect to TnC. Interspin distances for double labeled Tn complexes in phosphorylated (S22/23D, red) states for TnI151/TnC35 in **(A)** + Ca^{2+} and **(B)** -Ca^{2+} condition, and for TnI151/TnC84 in **(C)** +Ca^{2+} and **(D)** -Ca^{2+} condition. *Left panels*, DEER traces (after background

correction) show the time evolution of spin echo (orange thin lines) and fitted modulation of the spectrum from the DeFit analysis (red lines) which uses a Monte-Carlo minimization approach. *Middle panels*, two Gaussian distance-distributions representing the best fits to the experimental DEER data (WT, aqua or phosphorylated, red lines). Distances-distributions for WT are from [10]. In 3C & D, dotted lines represent the distanced obtained using CW measurement (*see* Supplementary **Figure S4**). *Right panels*, contour error surface plots representing χ^2 for the main Gaussian populations in phosphorylated state shown in in the middle panel. The percentages for each short and long-distance populations are indicated adjacent to contours. Faded surfaces indicate likely unreal populations arising from the fitting procedure

In summary, effects from phosphorylation of the TnI NH_2-TnI region on the interaction of a label on the TnI switch region with TnC were highly dependent on the Ca^{2+}-bound condition (**Figure 5**). Under high Ca^{2+} conditions, phosphorylation resulted in little to no change to interspin distances; whereas, in Ca^{2+}-free conditions, the observed changes in both the average distance and distance distribution width were significantly greater. That is, phosphorylation is a key factor for driving partial disorder, especially in the region of Cys84 (helix D) where the switch peptide of TnI interacts with the TnC N-lobe. Phosphorylation of the NH_2-TnI region that has a direct result on the mechanism for release of the switch peptide from TnC once Ca^{2+} is no longer bound.

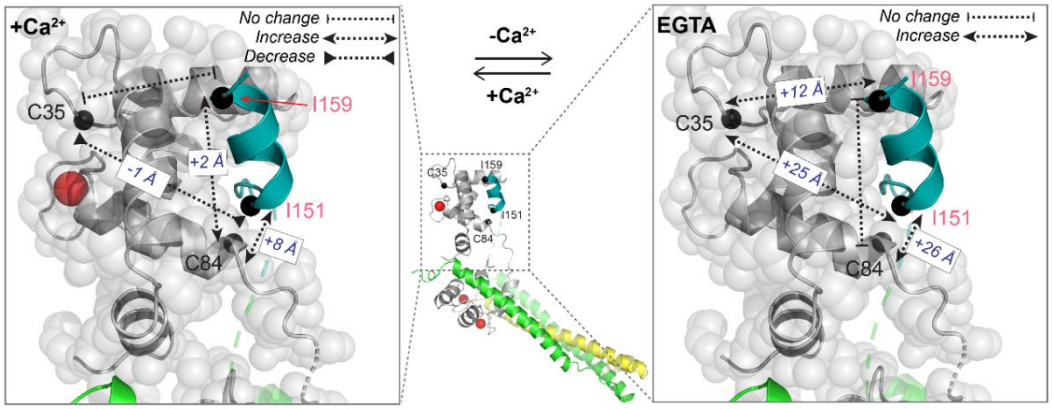

Figure 5 Phosphorylation associated changes in the interspin distances measured between the TnI switch region (TnI151, TnI159) and TnC (TnC35, TnC84) in the ternary Tn complex in the presence (*left*) and absence (*right*) of Ca^{2+}. The direction of the arrowheads represents the direction of the change of the interspin distances. Black spheres indicate the four labeling sites and Ca^{2+} bound to Site II is indicated by the red sphere. The TnI switch peptide region is in teal.

Discussion

The geometrical positioning and structural mechanisms describing the movement of the TnI switch peptide with respect to TnC, that accompanies activation, has been the focus of many studies over the past few decades [3, 4, 8-10, 15, 38]. What is clear from these earlier studies is that the switch release mechanism differs significantly for the cardiac and skeletal isoforms. In the skeletal isoform, the switch release is absolute, and upon release a large-scale movement of ~40 Å occurs between the switch region and the N-lobe in the absence of Ca^{2+}. In contrast, a higher degree of structural heterogeneity exists in the cardiac isoform which results in an ensemble of conformations of the switch region with respect to TnC under both conditions of high and low Ca^{2+} [10]. Further, a smaller size magnitude (~10 Å) in the change of the distance between the switch region and TnC occurs in the cardiac isoform [9, 10, 39, 40]. While it is well established that phosphorylation of the cardiac isoform, via serine residues 22 and 23 on the N-terminal extension region, is intimately linked to the contraction-relaxation cycle in the heart, it is less clear as to the exact nature of the structural changes that lead to the reported phosphorylation triggered decrease in the

affinity of TnC for Ca^{2+}, or also the structural changes in the interactions between TnC and TnI that lead to a higher rate of Ca^{2+} dissociation [41-43].

Here, the conformational changes in the interaction of the TnI switch region with TnC associated with Ca^{2+} binding in both the unphosphorylated (WT) and phosphorylated states of the Tn complex were determined by measuring interspin distances by NMR and EPR. Indirectly, these experiments reveal the influence that the cardiac specific N-terminal extension region has on the switch release mechanism. Overall, the experiments show that phosphorylation leads to destabilisation of the tight binding interaction of the switch region within its N-lobe hydrophobic pocket in the Ca^{2+} saturated state. While the PRE-NMR experiments in the -Ca^{2+} state suggest a complete release of the switch region upon phosphorylation, the EPR experiments further indicated that the movement of the switch away from the N-lobe is only significant in magnitude for the phosphorylated state (Figure 5).

To date, the structural models that have been proposed to explain the effect of phosphorylation on the dynamics of Tn complex have mostly focused on the mobility and positioning of the NH_2-TnI region in the Ca^{2+} saturated state, and not the switch peptide release mechanism. The positioning of the NH_2-TnI region and its interaction with other key elements within Tn has also differed in these models with experimental evidence lacking in support. Under conditions of saturating Ca^{2+}, our PRE-NMR derived distance measurements compared well with corresponding distances from the cardiac X-ray crystal structure of Tn, as also established before [9], as well as two computational models of Tn in the unphosphorylated state, a docking [35] and a molecular dynamics model [19]. This agreement confirms that, in the Ca^{2+}-bound state, the switch region of interacts with a small, well-defined small region of cTnC, consistent with tight binding of this region to the N-lobe of cTnC. The agreement with residues to the C-domain was poor but this suggests the presence of significant interdomain contacts between the two lobes of TnC due to the dynamic nature of the flexible central linker in solution which brings the two domains close to each other in a collapsed state. Oddly, there are no structural models which show Ca^{2+} associated changes in the interaction of the switch region with TnC upon phosphorylation.

Both our NMR and EPR experiments indicate that the impact from phosphorylation on this interaction is most dominant in the -Ca^{2+} state, while under high Ca^{2+} conditions, the effect from phosphorylation, while present, was minor.

In the high Ca^{2+} state, the changes in the PRE distance mapping upon phosphorylation were small which indicate a slight destabilisation of the switch peptide binding within the hydrophobic TnC pocket. Interestingly, the phosphorylation induced movement, or destabilisation, of the switch peptide in the pocket when Ca^{2+} is bound was not the same at both termini. That is, the spin-label on the C-terminal end (TnI159) appeared to be more constrained and mapped to a well-defined area on TnC; whereas, the label on the N-terminal end of the switch (TnI151) was more disordered as apparent from a disperse mapping profile. This behaviour of the switch peptide upon phosphorylation was also supported by the EPR measurements where little to no change in the interspin distances from the two spin labeled residues on TnC to TnI159 were observed, compared to the interspin distances to TnI151 where the distance changes were as much as 8 Å for the TnC84/TnI151 interspin pair (Figure 5). The narrow interspin distance distributions in the high Ca^{2+} state also support a model where the switch is 'locked-in' tight with its binding site on TnC. TnC 84 is located at the C-termini of helix D which is connected to regulatory metal binding Site II from N-termini. The change in TnC84/TnI151 interspin distance upon phosphorylation in the +Ca^{2+} state may be due to the movement of either the switch peptide itself but could also be attributed to the movement of helix D on TnC due to phosphorylation associated changes in the stability of the Ca^{2+} binding site II. According to our findings here, phosphorylation in the Ca^{2+}-bound state did not result in the release of switch peptide, but only minor destabilisation of the strength of the binding interaction, possibly due to changes in the on TnC close to site II. This phosphorylation state may be necessary to prime the switch peptide for its rapid release once Ca^{2+} is lost from site II.

Demonstrated for the first time are significant phosphorylation associated changes in the interaction of the switch region with TnC in a -Ca^{2+} state. Mapping of both the PRE-NMR distances (Figure 2C) and the changes in interspin distances by EPR (Figure 5) visibly demonstrate the enhancement in the release of the switch region, as labeled at both termini. The release is most noticeable for the spin label on TnI151 where the complete

abolishment of all PRE interactions is observed upon phosphorylation; and the magnitude of the interspin EPR distances increases by 25-26 Å. Increases in interspin distances were accompanied by a higher degree of disorder in the switch peptide.

We recently showed that the NH_2-TnI region interacts with a broad surface area on the TnC N-domain which includes the Ca^{2+} regulatory Site II and the TnI switch binding site (**Chapter 4, Paper 2**). Phosphorylation of the NH_2-TnI region both then weakens and shifts the NH_2-TnI region to an adjacent site on TnC. From this structural model of the phosphorylation controlled interaction of the NH_2-TnI region with TnC, we proposed that, in its unphosphorylated state, the NH_2-TnI region acts as a physical block to sterically prevent the release of the TnI switch peptide from its hydrophobic pocket on the N-domain. Alternatively, the NH_2-TnI region in the unphosphorylated state, through its interactions with Site II, may also stabilise the Ca^{2+} bound open form of the N-domain, priming it for an optimal and thus sustained interaction with the TnI switch region. The slow relaxation state observed physiologically supports such a model. The phosphorylation promoted release of the switch region we observed here now supports our earlier suggestions for how the cardiac isoform achieves a fast relaxation state.

The dual regulatory action of both Ca^{2+} and phosphorylation can be summarised in a 'seat-belt'-like model, as shown in Figure 6. In our model, the TnI NH_2-TnI region interacts with the TnC N-domain, like a vehicle safety seat-belt, and directly blocks the release of the switch region from its hydrophobic pocket when Ca^{2+} is bound (Figure 6, *left*). Phosphorylation of Ser 22 & 23 introduces two negative charge onto the TnI NH_2-TnI region which then disrupts and destabilises its interaction with TnC; and increasing disorder within Tn (Figure 6, *middle*). The elimination of the interaction of the NH_2-TnI region with TnC, and the switch binding pocket, then promotes the full release of the switch binding region. The switch is released and can move further away from TnC than achieved in the unphosphorylated state; akin to the shoulder-strap on a three point seat-belt 'slipping off' the shoulder (Figure 6, *right*). Other cooperative phosphorylation induced movements are also likely in play and include the rotation or twisting movement of the TnC molecule arounds its central linker to orient itself for favourable interactions with the switch peptide.

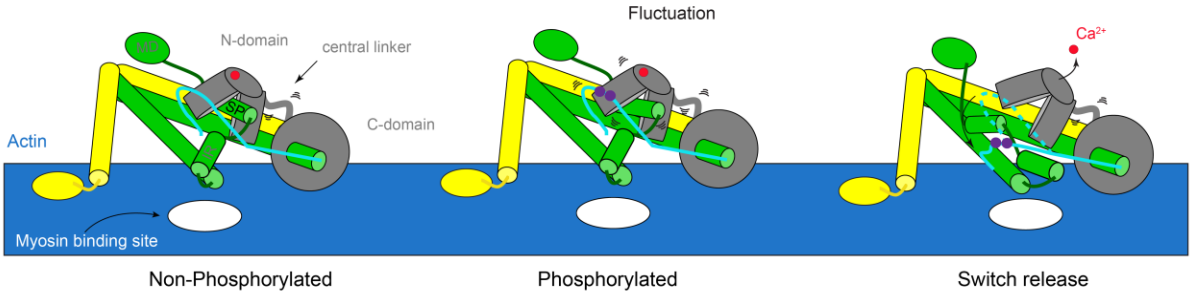

Figure 6 The NH_2-extension region of TnI 'seat-belt' model. The TnI NH_2-TnI region (cyan) blocks the switch region and restricts the release of switch peptide. Phosphorylation at Ser22/23 (as represented by purple spheres) increases the disorder of Tn, and fluctuations of the switch peptide within the TnC hydrophobic pocket occur. Ca^{2+} release, and release of the interaction of the TnI NH_2-TnI region with TnC, allows for complete release of the TnI switch region.

In conclusion, despite the considerable interest and efforts in understanding the regulation of the cardiac isoform of Tn, the mechanism by which phosphorylation, and Ca^{2+} binding, modify the relaxation-contractile cycle is not understood in detail. The wealth of past structural details from both NMR studies on peptide fragments or other truncated subfragments of Tn, as well as molecular dynamics studies, cannot be rationalised into a working model without examining experimental systems that include the whole intact Tn complex, and as measured under physiologically relevant conditions. As employed here, a site directed spin labeling approach, in combination with PRE-NMR and EPR, has been well suited for building three dimensional models of whole troponin and providing a complete description of the dynamics of the intact complex in the complex environment of a muscle fibre [44]. In conclusion, the role of phosphorylation in the cardiac isoform is a critical contributor for regulating the switch release mechanism. This more detailed understanding of cardiac muscle regulation and its dynamic regulation by phosphorylation opens the way for improving targeted intervention strategies such as inotropic compounds which are employed for diseases associated with impaired Ca^{2+} handling.

References

1. Marques, M.A., et al., *The missing links within troponin.* Arch Biochem Biophys, 2019. **663**: p. 95-100.
2. Milligan, R.A. and P.F. Flicker, *Structural relationships of actin, myosin, and tropomyosin revealed by cryo-electron microscopy.* J Cell Biol, 1987. **105**(1): p. 29-39.
3. Takeda, S., et al., *Structure of the core domain of human cardiac troponin in the Ca(2+)-saturated form.* Nature, 2003. **424**(6944): p. 35-41.
4. Vinogradova, M.V., et al., *Ca^{2+}-regulated structural changes in troponin.* Proc Natl Acad Sci U S A, 2005. **102**(14): p. 5038-43.
5. Gagne, S.M., et al., *The NMR angle on troponin C.* Biochem Cell Biol, 1998. **76**(2-3): p. 302-12.
6. Farah, C.S. and F.C. Reinach, *The troponin complex and regulation of muscle contraction.* FASEB J, 1995. **9**(9): p. 755-67.
7. Cordina, N.M., et al., *Effects of calcium binding and the hypertrophic cardiomyopathy A8V mutation on the dynamic equilibrium between closed and open conformations of the regulatory N-domain of isolated cardiac troponin C.* Biochemistry, 2013. **52**(11): p. 1950-62.
8. Aihara, T., et al., *Switch action of troponin on muscle thin filament as revealed by spin labeling and pulsed EPR.* J Biol Chem, 2010. **285**(14): p. 10671-7.
9. Cordina, N.M., et al., *Ca^{2+}-induced PRE-NMR changes in the troponin complex reveal the possessive nature of the cardiac isoform for its regulatory switch.* PLoS One, 2014. **9**(11): p. e112976.
10. Potluri, P.R., et al., *The concerted movement of the switch region of Troponin I in cardiac muscle thin filaments as tracked by conventional and pulsed (DEER) EPR.* J Struct Biol, 2017. **200**(3): p. 376-387.
11. Holroyde, M.J., et al., *Isolation of cardiac myofibrils and myosin light chains with in vivo levels of light chain phosphorylation.* Biochim Biophys Acta, 1979. **587**(4): p. 628-37.
12. Ray, K.P. and P.J. England, *Phosphorylation of the inhibitory subunit of troponin and its effect on the calcium dependence of cardiac myofibril adenosine triphosphatase.* FEBS Lett, 1976. **70**(1): p. 11-6.
13. Herron, T.J., F.S. Korte, and K.S. McDonald, *Power output is increased after phosphorylation of myofibrillar proteins in rat skinned cardiac myocytes.* Circ Res, 2001. **89**(12): p. 1184-90.
14. Kentish, J.C., et al., *Phosphorylation of troponin I by protein kinase A accelerates relaxation and crossbridge cycle kinetics in mouse ventricular muscle.* Circ Res, 2001. **88**(10): p. 1059-65.
15. Baryshnikova, O.K., M.X. Li, and B.D. Sykes, *Modulation of cardiac troponin C function by the cardiac-specific N-terminus of troponin I: influence of PKA phosphorylation and involvement in cardiomyopathies.* J Mol Biol, 2008. **375**(3): p. 735-51.
16. Colson, B.A., et al., *Myosin binding protein-C phosphorylation is the principal mediator of protein kinase A effects on thick filament structure in myocardium.* J Mol Cell Cardiol, 2012. **53**(5): p. 609-16.
17. Hwang, P.M., et al., *The cardiac-specific N-terminal region of troponin I positions the regulatory domain of troponin C.* Proc Natl Acad Sci U S A, 2014. **111**(40): p. 14412-7.
18. Cheng, Y., et al., *Computational studies of the effect of the S23D/S24D troponin I mutation on cardiac troponin structural dynamics.* Biophys J, 2014. **107**(7): p. 1675-85.
19. Zamora, J.E., et al., *Troponin structure: its modulation by Ca^{2+} and phosphorylation studied by molecular dynamics simulations.* Phys Chem Chem Phys, 2016. **18**(30): p. 20691-20707.

20. Brown, L.J., et al., *Structure of the inhibitory region of troponin by site directed spin labeling electron paramagnetic resonance.* Proc Natl Acad Sci U S A, 2002. **99**(20): p. 12765-70.
21. Hanft, L.M., B.J. Biesiadecki, and K.S. McDonald, *Length dependence of striated muscle force generation is controlled by phosphorylation of cTnI at serines 23/24.* J Physiol, 2013. **591**(18): p. 4535-47.
22. Wijnker, P.J., et al., *Impact of site-specific phosphorylation of protein kinase A sites Ser23 and Ser24 of cardiac troponin I in human cardiomyocytes.* Am J Physiol Heart Circ Physiol, 2013. **304**(2): p. H260-8.
23. Rao, V.S., et al., *N-terminal phosphorylation of cardiac troponin-I reduces length-dependent calcium sensitivity of contraction in cardiac muscle.* J Physiol, 2013. **591**(2): p. 475-90.
24. Sakthivel, S., et al., *In vivo and in vitro analysis of cardiac troponin I phosphorylation.* J Biol Chem, 2005. **280**(1): p. 703-14.
25. Finley, N., et al., *NMR analysis of cardiac troponin C-troponin I complexes: effects of phosphorylation.* FEBS Lett, 1999. **453**(1-2): p. 107-12.
26. Dong, W.J., et al., *Conformation of the N-terminal segment of a monocysteine mutant of troponin I from cardiac muscle.* Biochemistry, 1997. **36**(22): p. 6745-53.
27. Goddard, T.D. and D.G. Kneller, *SPARKY 3*. 2008, University of California: San Francisco.
28. Abbott, M.B., et al., *Regulatory domain conformational exchange and linker region flexibility in cardiac troponin C bound to cardiac troponin I.* J Biol Chem, 2000. **275**(27): p. 20610-7.
29. Volkov, A.N., et al., *Solution structure and dynamics of the complex between cytochrome c and cytochrome c peroxidase determined by paramagnetic NMR.* Proc Natl Acad Sci U S A, 2006. **103**(50): p. 18945-50.
30. Battiste, J.L. and G. Wagner, *Utilization of site-directed spin labeling and high-resolution heteronuclear nuclear magnetic resonance for global fold determination of large proteins with limited nuclear overhauser effect data.* Biochemistry, 2000. **39**(18): p. 5355-65.
31. Liang, B., J.H. Bushweller, and L.K. Tamm, *Site-directed parallel spin-labeling and paramagnetic relaxation enhancement in structure determination of membrane proteins by solution NMR spectroscopy.* J Am Chem Soc, 2006. **128**(13): p. 4389-97.
32. Iwahara, J., C.D. Schwieters, and G.M. Clore, *Ensemble approach for NMR structure refinement against (1)H paramagnetic relaxation enhancement data arising from a flexible paramagnetic group attached to a macromolecule.* J Am Chem Soc, 2004. **126**(18): p. 5879-96.
33. Fajer, P.G., L. Brown, and L. Song, *Practical Pulsed Dipolar ESR (DEER)*, in *ESR Spectroscopy in Membrane Biophysics*. 2007, Springer US: Boston, MA. p. 95-128.
34. Polyhach, Y., E. Bordignon, and G. Jeschke, *Rotamer libraries of spin labelled cysteines for protein studies.* Phys Chem Chem Phys, 2011. **13**(6): p. 2356-66.
35. Howarth, J.W., et al., *Phosphorylation-dependent conformational transition of the cardiac specific N-extension of troponin I in cardiac troponin.* J Mol Biol, 2007. **373**(3): p. 706-22.
36. Cordina, N.M., et al., *Interdomain orientation of cardiac troponin C characterized by paramagnetic relaxation enhancement NMR reveals a compact state.* Protein Sci, 2012. **21**(9): p. 1376-87.
37. Fajer, P.G., L. Brown, and L. Song, *Practical pulsed dipolar ESR (DEER)*, in *ESR spectroscopy in membrane biophysics, Biological magnetic resonance*, M.A. Hemminga and L.J. Berliner, Editors. 2007, Springer: New York. p. 95–128
38. Li, M.X., et al., *Phosphorylation and mutation of human cardiac troponin I deferentially destabilize the interaction of the functional regions of troponin I with troponin C.* Biochemistry, 2003. **42**(49): p. 14460-8.
39. Dong, W.J., et al., *Ca^{2+}-induced conformational transition in the inhibitory and regulatory regions of cardiac troponin I.* J Biol Chem, 2003. **278**(10): p. 8686-92.

40. Dong, W.J., et al., *Kinetics of conformational transitions in cardiac troponin induced by Ca^{2+} dissociation determined by Forster resonance energy transfer.* J Biol Chem, 2003. **278**(43): p. 42394-402.
41. Robertson, S.P., et al., *The effect of troponin I phosphorylation on the Ca^{2+}-binding properties of the Ca^{2+}-regulatory site of bovine cardiac troponin.* J Biol Chem, 1982. **257**(1): p. 260-3.
42. Solaro, R.J., A.J. Moir, and S.V. Perry, *Phosphorylation of troponin I and the inotropic effect of adrenaline in the perfused rabbit heart.* Nature, 1976. **262**(5569): p. 615-7.
43. Dong, W.J., et al., *Effects of PKA phosphorylation of cardiac troponin I and strong crossbridge on conformational transitions of the N-domain of cardiac troponin C in regulated thin filaments.* Biochemistry, 2007. **46**(34): p. 9752-61.
44. Kachooei, E., N.M. Cordina, and L.J. Brown, *Constructing a structural model of troponin using site-directed spin labeling: EPR and PRE-NMR.* Biophys Rev, 2019. **11**(4): p. 621-639.

Table 1 Summary of all interspin distances in ternary Tn by DEER. Distances were extracted using the DeFit program, whereas F-test was performed for up to 3 Gaussian. *r* is the central distance, *Δr* is the width of the distance distribution. The error is calculated from the χ^2 surface of the Monte Carlo search. The percentage contribution was determined with 10% accuracy. $\chi^2_{1\to2}$ is the ratio of χ^2 values for the 1 Gaussians model to the 2 Gaussian model fit. PP = Pseudo-phosphorylated, where TnI construct has S23/24D mutation.

Interspin	Status		DEER					CW		Cα- Cα Distance (Å)		
			r (Å)	Δr (Å)	%	Mod Amp. (%)	$\chi^2_{2\to1}$	r (Å)	Δr (Å)	Crystal Structure	Current Models	
											A	B
TnI159/TnC35	+Ca²⁺	WT	27 ± 1	3 ± 1	73	28	45.6	> 25	-	17	15	-
			47 ± 2	45 ± 5	27							
		PP	28 ± 1	3 ± 1	70	29	18.2	> 25	-	-	15	18
			53 ± 1	45 ± 2	30							
	EGTA	WT	26 ± 1	14 ± 4	32	23	2.3	> 25	-	-	-	-
			57 ± 1	42 ± 5	68							
		PP	38 ± 1	45 ± 3	73	27	3.4	> 25	-	-	-	-
			71 ± 1	15 ± 3	27							
TnI159/TnC84	+Ca²⁺	WT	21 ± 1	2 ± 1	84	17	13.5	19 ± 1	1 ± 1	17	15	-
			47 ± 4	32 ± 5	16							
		PP	21 ± 1	2 ± 1	82	22	17.0	> 25	-	-	15	17
			46 ± 5	34 ± 7	18							
	EGTA	WT	32 ± 1	34 ± 4	77	27	1.8	> 25	-	-	-	-
			60 ± 4	7 ± 9	23							
		PP	30 ± 1	34 ± 3	68	31	4.4	> 25	-	-	-	-
			63 ± 1	20 ± 3	32							
TnI151/TnC35	+Ca²⁺	WT*	28±1	8 ± 2	88	15	3.9	> 25	-	19	22	-
		PP	27 ± 1	3 ± 1	71	29	33.6	> 25	-	-	22	20
			56 ± 1	45 ± 7	29							
	EGTA	WT*	36 ± 5	37 ± 10	100	13	1.3	> 25	-	-	-	-
		PP	31 ± 3	9 ± 10	25	12	10.5	> 25	-	-	-	-
			61 ± 3	40 ± 9	75							
TnI151/TnC84	+Ca²⁺	WT*	25 ± 1	10 ± 3	73	26	3.2	10 ± 3	8 ± 6	5	6	-
		PP	18 ± 1	8 ± 8	60	13	5.2	19 ± 1	11 ± 1	-	6	9
			46 ± 7	29 ± 8	40							
	EGTA	WT*	26 ± 1	10 ± 5	77	26	3.9	9 ± 2 §	4 ± 5	-	-	-
		PP	35 ± 4	45 ± 1	76	14	1.5	> 25	-	-	-	-
			64 ± 4	8 ± 2	24							

* Distances are from Potluri *et al*. [10]; § shifting from 1 to 2 Gaussian was significant (r_1 = 11 ± 1, Δr_1 = 3 ± 5, % = 63; r_2 = 19 ± 3, Δr_2 = 1 ± 5, % = 37)

Supplementary information

Table S1 PRE-NMR parameters extracted from electron-proton relaxation between spin labels on the TnI switch (TnI159 & TnI151) and ^{15}N-TnC in phosphorylated and high Ca^{2+} conditions. Res. indicates residue number. PRE is in s^{-1}. Distances are in Å. Δ is distance change between residues for which assignment was done is both phosphorylated and dephosphorylated states (Δ = [S22/23D] – [WT]); WT distances were obtained from [9]. A 'Δ' preceded by either > or < means that, in one of the states, the distance was at the PRE detection limit (25 Å).

Location	TnC Res.	TnI159, +Ca^{2+}, S22/23D				TnI151, +Ca^{2+}, S22/23D			
		I_{para}/I_{dia}	PRE	Distance	Δ	I_{para}/I_{dia}	PRE	Distance	Δ
	1	-	-	-	-	-	-	-	-
	2	-	-	-	-	-	-	-	-
Helix N	3	0.61	27.8	18.3	-2.0	-	-	-	-
	4	-	-	-	-	-	-	-	-
	5	-	-	-	-	-	-	-	-
	6	-	-	-	-	-	-	-	-
	7	0.67	22.1	19.1	-	0.63	25.9	18.6	-1.1
	8	0.41	53.4	16.5	-	0.60	30.0	18.1	-
	9	-	-	-	-	-	-	-	-
	10	0.56	33.9	17.7	0.3	0.49	40.4	17.2	-2.3
	11	0.41	54.3	16.4	-2.3	0.29	80.8	15.4	-
	12	-	-	-	-	0.21	104.9	14.7	0.0
	13	0.46	44.2	17.0	3.3	-	-	-	-
Helix A	14	0.46	45.2	16.9	2.1	-	-	-	-
	15	0.37	59.6	16.2	4.2	0.25	103.1	14.7	-0.9
	16	-	-	-	-	-	-	-	-
	17	-	-	-	-	-	-	-	-
	18	-	-	-	-	0.24	86.1	15.2	3.2
	19	-	-	-	-	-	-	-	-
	20	-	-	-	-	-	-	-	-
	21	-	-	-	-	-	-	-	-
	22	-	-	-	-	-	-	-	-
	23	-	-	-	-	-	-	-	-
	24	-	-	-	-	-	-	-	-
	25	0.58	29.6	18.2	-	0.99	0.6	25.0	-
	26	-	-	-	-	-	-	-	-
	27	-	-	-	-	-	-	-	-
Site I	28	-	-	-	-	-	-	-	-
	29	-	-	-	-	-	-	-	-
	30	-	-	-	-	-	-	-	-
	31	-	-	-	-	-	-	-	-
	32	-	-	-	-	-	-	-	-
	33	-	-	-	-	-	-	-	-
	34	-	-	-	-	-	-	-	-
	35	-	-	-	-	-	-	-	-
	36	-	-	-	-	-	-	-	-
	37	-	-	-	-	-	-	-	-

Helix B	38	-	-	-	-	-	-	-	-
	39	-	-	-	-	-	-	-	-
	40	-	-	-	-	-	-	-	-
	41	-	-	-	-	-	-	-	-
	42	-	-	-	-	-	-	-	-
	43	0.09	169.8	13.6	-	-	-	-	-
	44	-	-	-	-	-	-	-	-
	45	-	-	-	-	0.43	54.4	16.4	4.4
	46	0.49	44.2	17.0	-	0.43	53.1	16.5	-
	47	-	-	-	-	-	-	-	-
	48	-	-	-	-	-	-	-	-
	49	-	-	-	-	-	-	-	-
	50	0.33	70.7	15.7	1.3	0.44	52.7	16.5	4.5
	51	-	-	-	-	0.28	75.7	15.5	-1.3
	52	-	-	-	-	-	-	-	-
	53	-	-	-	-	-	-	-	-
Helix C	54	-	-	-	-	-	-	-	-
	55	0.51	36.8	17.5	-1.3	0.64	24.5	18.7	-
	56	-	-	-	-	-	-	-	-
	57	-	-	-	-	-	-	-	-
	58	-	-	-	-	-	-	-	-
	59	0.47	41.1	17.2	-3.1	0.99	0.5	25.0	-
	60	-	-	-	-	-	-	-	-
	61	-	-	-	-	-	-	-	-
	62	-	-	-	-	-	-	-	-
	63	0.32	66.5	15.9	0.1	0.99	0.6	25.0	> 8.3
	64	-	-	-	-	0.81	12.1	21.1	-
Site II	65	-	-	-	-	0.99	0.6	25.0	-
	66	-	-	-	-	-	-	-	-
	67	0.49	42.6	17.1	-1.5	-	-	-	1.4
	68	0.61	27.7	18.4	< -6.6	-	-	-	-
	69	-	-	-	-	0.71	18.9	19.6	0.8
	70	-	-	-	-	0.78	16.5	20.0	-0.3
	71	-	-	-	-	-	-	-	-
	72	-	-	-	-	-	-	-	-
	73	-	-	-	-	-	-	-	-
Helix D	74	-	-	-	-	-	-	-	-
	75	-	-	-	-	-	-	-	-
	76	0.37	59.3	16.2	-	0.94	3.6	25.8	-
	77	-	-	-	-	-	-	-	-
	78	-	-	-	-	-	-	-	-
	79	-	-	-	-	-	-	-	-
	80	-	-	-	-	-	-	-	-
	81	-	-	-	-	-	-	-	-
	82	-	-	-	-	-	-	-	-
	83	0.59	38.9	17.3	-	0.88	9.5	22.0	-
	84	-	-	-	-	0.79	13.8	20.6	-
	85	-	-	-	-	-	-	-	-
	86	-	-	-	-	-	-	-	-
	87	-	-	-	-	-	-	-	-
	88	0.47	42.2	17.1	1.4	0.56	34.9	17.7	1.8
	89	0.49	49.6	16.7	-0.1	0.62	29.0	18.2	-0.2
	90	0.55	32.9	17.8	-0.7	0.42	48.7	16.7	-0.6
	91	0.46	43.6	17.0	-1.6	0.59	30.2	18.1	0.3

	92	0.54	36.5	17.5	-2.9	0.69	23.4	18.9	0.0
	93	-	-	-	-	0.76	16.0	20.1	-
	94	0.40	53.1	16.5	-2.4	-	-	-	-0.2
	95	-	-	-	-	-	-	-	-
	96	-	-	-	-	-	-	-	-
	97	-	-	-	-	-	-	-	-
	98	0.53	38.9	17.3	-3.8	0.99	0.6	25.0	-
Helix E	99	-	-	-	-	-	-	-	-
	100	-	-	-	-	-	-	-	-
	101	-	-	-	-	-	-	-	-
	102	-	-	-	-	-	-	-	-
	103	-	-	-	-	0.99	0.6	25.0	-
	104	-	-	-	-	0.90	5.6	24.0	-0.8
	105	-	-	-	-	0.99	0.6	25.0	> 5.7
	106	0.46	47.0	16.8	-7.4	0.96	2.5	27.5	-
	107	0.50	40.8	17.2	-3.0	0.99	0.6	25.0	0.2
	108	0.54	37.4	17.5	-	0.86	8.7	22.3	< -2.7
Site III	109	0.45	48.0	16.7	-	0.95	2.8	27.0	-
	110	0.47	39.6	17.3	-1.1	0.99	0.6	25.0	-
	111	0.52	37.3	17.5	-2.1	0.99	0.6	25.0	-
	112	-	-	-	-	0.99	0.6	25.0	-
	113	-	-	-	-	0.99	0.5	25.0	-
	114	0.50	48.9	16.7	-6.8	0.99	0.7	25.0	-
	115	-	-	-	-	-	-	-	-
	116	0.54	37.3	17.5	-4.7	0.99	0.6	25.0	-
	117	0.58	33.6	17.8	-4.8	0.99	0.6	25.0	-
	118	-	-	-	-	-	-	-	-
Helix F	119	0.45	47.8	16.8	-	0.89	7.2	23.0	< -2.0
	120	-	-	-	-	-	-	-	-
	121	0.58	32.7	17.9	-5.1	0.99	0.6	25.0	3.2
	122	0.42	50.5	16.6	-5.2	0.99	0.6	25.0	-
	123	0.45	48.0	16.7	-	0.99	0.6	25.0	2.7
	124	0.42	51.5	16.6	-8.3	0.99	0.5	25.0	-
	125	0.54	34.2	17.7	-6.9	0.99	0.6	25.0	0.4
	126	-	-	-	-	-	-	-	-
	127	0.56	31.6	18.0	< -7.0	0.99	0.6	25.0	0.1
	128	0.63	25.4	18.6	-3.0	0.99	0.6	25.0	-
	129	-	-	-	-	0.99	0.6	25.0	4.2
	130	0.55	31.1	18.0	-6.7	0.99	0.5	25.0	-
	131	0.62	25.9	18.6	-4.1	0.99	0.5	25.0	2.1
	132	-	-	-	-	-	-	-	-
	133	-	-	-	-	0.99	0.6	25.0	-
	134	0.47	42.4	17.1	-6.0	0.99	0.5	25.0	1.9
Helix G	135	-	-	-	-	-	-	-	-
	136	-	-	-	-	-	-	-	-
	137	0.50	38.7	17.4	-	0.88	7.7	22.7	1.8
	138	0.43	47.4	16.8	-6.1	0.99	0.6	25.0	-
	139	0.48	45.4	16.9	-	0.99	0.6	25.0	0.8
	140	0.47	45.1	16.9	-4.6	0.98	1.2	25.0	4.4
	141	0.47	43.0	17.1	< -7.9	0.99	0.6	25.0	2.8
Site IV	142	0.61	29.0	18.2	-4.3	0.99	0.6	25.0	3.1
	143	0.46	45.2	16.9	-6.9	0.99	0.5	25.0	-

	144	0.51	38.0	17.4	< -7.6	0.99	0.6	25.0	0.6
	145	0.46	44.5	17.0	-6.4	0.99	0.6	25.0	-
	146	0.42	48.6	16.7	-5.9	0.99	0.5	25.0	1.7
	147	0.57	32.0	17.9	< -7.1	0.99	0.6	25.0	2.2
	148	-	-	-	-	0.91	5.4	24.1	2.3
	149	-	-	-	-	0.99	0.5	25.0	2.3
	150	-	-	-	-	0.99	0.5	25.0	-
	151	-	-	-	-	0.99	0.6	25.0	-
	152	-	-	-	-	0.99	0.6	25.0	2.4
	153	-	-	-	-	-	-	-	6.2
Helix H	154	-	-	-	-	-	-	-	-
	155	0.37	59.4	16.2	-2.5	-	-	-	-
	156	0.46	45.2	16.9	-6.4	0.99	0.6	25.0	> 1.6
	157	-	-	-	-	-	-	-	-
	158	0.47	43.3	17.0	-4.8	0.99	0.4	25.0	> 1.6
	159	0.68	21.0	19.2	2.2	0.94	3.4	25.0	-
	160	0.53	35.9	17.6	< -7.4	0.96	2.1	25	> 5.8
	161	0.41	52.0	16.5	-1.3	0.85	8.9	22.2	3.7

Table S2 PRE-NMR parameters extracted from electron-proton relaxation between spin labels on the TnI switch (TnI159 & TnI151) and ^{15}N-TnC in phosphorylated and Ca^{2+}-free conditions. Res. indicates residue number. Distances are in Å. Δ is distance change between residues for which assignment was done is both phosphorylated and dephosphorylated states (Δ = [S22/23D] – [WT]); WT distances were obtained from [9]. A 'Δ' preceded by either > or < means that, in one of the states, the distance was at the PRE detection limit (25 Å).

Location	TnC Res.	TnI159, -Ca^{2+}, S22/23D				TnI151, -Ca^{2+}, S22/23D			
		I_{para}/I_{dia}	PRE	Distance	Δ	I_{para}/I_{dia}	PRE	Distance	Δ
	1	-	-	-	-	-	-	-	-
	2	-	-	-	-	-	-	-	-
Helix N	3	0.99	0.6	25.0	-	0.73	19.2	19.5	-1.1
	4	-	-	-	-	-	-	-	-
	5	-	-	-	-	-	-	-	-
	6	-	-	-	-	-	-	-	-
	7	0.99	0.6	25.0	> 3.7	0.79	13.1	20.8	-0.3
	8	0.99	0.6	25.0	-	-	-	-	-
	9	-	-	-	-	-	-	-	-
	10	0.98	1.2	25.0	-	0.78	12.5	21.0	-1.0
	11	0.96	2.4	25.0	> 1.5	0.62	25.3	18.6	-1.1
	12	0.97	1.4	25.0	> 3.2	0.67	21.2	19.2	-
	13	0.95	3.0	25.0	> 7.4	0.75	15.2	20.3	0.2
Helix A	14	0.99	0.5	25.0	> 7.4	0.79	11.8	21.2	0.5
	15	0.99	0.5	25.0	-	0.67	21.4	19.2	-1.6
	16	-	-	-	-	-	-	-	-
	17	-	-	-	-	-	-	-	-
	18	0.99	0.5	25.0	> 5.5	0.65	22.5	19.0	-3.3
	19	-	-	-	-	-	-	-	-
	20	-	-	-	-	-	-	-	-
	21	-	-	-	-	-	-	-	-
	22	-	-	-	-	-	-	-	-
	23	-	-	-	-	-	-	-	-
	24	-	-	-	-	-	-	-	-
	25	0.99	0.5	25.0	> 7.7	0.82	10.0	21.8	-3.3
	26	0.99	0.5	25.0	> 7.4	0.81	10.8	21.5	-
	27	-	-	-	-	-	-	-	-
Site I	28	-	-	-	-	-	-	-	-
	29	-	-	-	-	-	-	-	-
	30	-	-	-	-	-	-	-	-
	31	0.88	6.6	23.3	-	0.55	32.9	17.8	-2.9
	32	-	-	-	-	-	-	-	-
	33	-	-	-	-	-	-	-	-
	34	-	-	-	-	-	-	-	-
	35	-	-	-	-	-	-	-	-
	36	-	-	-	-	-	-	-	-
	37	-	-	-	-	-	-	-	-
Helix B	38	-	-	-	-	-	-	-	-
	39	-	-	-	-	-	-	-	-
	40	-	-	-	-	-	-	-	-
	41	-	-	-	-	-	-	-	-
	42	-	-	-	-	-	-	-	-

	43	-	-	-	-	0.72	18.4	19.7	-3.8
	44	-	-	-	-	-	-	-	-
	45	-	-	-	-	0.89	5.8	23.8	-1.2
	46	0.99	0.6	25.0	> 3.1	0.74	16.2	20.1	-
	47	-	-	-	-	-	-	-	-
	48	-	-	-	-	-	-	-	-
	49	0.91	4.8	24.6	< -0.4	0.75	14.2	20.5	-4.5
	50	0.95	2.5	25.0	-	0.75	14.8	20.4	-4.6
	51	-	-	-	-	-	-	-	-
	52	-	-	-	-	-	-	-	-
	53	-	-	-	-	-	-	-	-
	54	-	-	-	-	-	-	-	-
	55	0.99	0.6	25.0	-	0.63	25.0	18.7	-
	56	-	-	-	-	-	-	-	-
	57	-	-	-	-	-	-	-	-
	58	-	-	-	-	-	-	-	-
Helix C	59	0.99	0.5	25.0	-	0.71	18.3	19.7	-
	60	-	-	-	-	-	-	-	-
	61	-	-	-	-	-	-	-	-
	62	-	-	-	-	-	-	-	-
	63	0.93	4.3	25.0	-	0.62	26.0	18.6	-
	64	-	-	-	-	-	-	-	-
	65	-	-	-	-	-	-	-	-
	66	-	-	-	-	-	-	-	-
	67	-	-	-	-	-	-	-	-
	68	-	-	-	-	-	-	-	-
Site II	69	0.99	0.5	25.0	-	0.60	29.2	18.2	-
	70	-	-	-	-	-	-	-	-
	71	-	-	-	-	-	-	-	-
	72	-	-	-	-	-	-	-	-
	73	-	-	-	-	-	-	-	-
	74	-	-	-	-	-	-	-	-
	75	-	-	-	-	-	-	-	-
	76	0.99	0.6	25.0	-	0.75	16.0	20.1	-
	77	-	-	-	-	-	-	-	-
	78	-	-	-	-	-	-	-	-
Helix D	79	-	-	-	-	-	-	-	-
	80	-	-	-	-	-	-	-	-
	81	-	-	-	-	-	-	-	-
	82	-	-	-	-	-	-	-	-
	83	0.99	0.5	25.0	< 2.3	0.60	25.5	18.6	-
	84	0.99	0.5	25.0	< 6.3	0.84	8.8	22.2	-2.8
	85	-	-	-	-	-	-	-	-
	86	-	-	-	-	-	-	-	-
	87	0.99	0.5	25.0	< 6.5	0.99	0.7	25.0	> 0.9
	88	0.99	0.5	25.0	< 0.1	0.76	13.6	20.7	< -4.3
	89	-	-	-	-	-	-	-	-
	90	0.99	0.5	25.0	-	0.71	17.9	19.7	-3.0
	91	0.99	0.5	25.0	-	0.53	37.0	17.5	-
	92	0.99	0.6	25.0	-	0.55	42.0	17.1	-5.4
	93	-	-	-	-	-	-	-	-
	94	0.99	0.6	25.0	< 0.9	-	-	-	-
Helix E	95	-	-	-	-	-	-	-	-
	96	-	-	-	-	-	-	-	-

	97	-	-	-	-	-	-	-	-
	98	0.99	0.5	25.0	-	0.78	13.0	20.8	6.8
	99	-	-	-	-	-	-	-	-
	100	-	-	-	-	-	-	-	-
	101	-	-	-	-	-	-	-	-
	102	-	-	-	-	-	-	-	-
	103	0.99	0.5	25.0	-	0.75	14.6	20.4	-
	104	0.99	0.5	25.0	-	0.75	14.2	20.5	-
	105	0.99	0.5	25.0	< 9.3	0.77	13.8	20.6	-
	106	0.99	0.6	25.0	-	-	-	-	-
	107	0.99	0.5	25.0	-	0.77	12.8	20.9	-
	108	0.99	0.6	25.0	-	0.74	17.1	19.9	-
Site III	109	0.99	0.6	25.0	-	0.79	12.2	21.1	9.1
	110	-	-	-	-	-	-	-	-
	111	0.99	0.5	25.0	-	-	-	-	-
	112	-	-	-	-	-	-	-	-
	113	-	-	-	-	-	-	-	-
	114	0.99	0.7	25.0	< 11.1	-	-	-	-
	115	-	-	-	-	-	-	-	-
	116	0.99	0.6	25.0	< 11.1	0.67	22.5	19.0	-
	117	0.99	0.6	25.0	< 10.2	-	-	-	-
	118	-	-	-	-	-	-	-	-
Helix F	119	0.91	5.0	24.4	-	0.63	24.5	18.7	-
	120	-	-	-	-	-	-	-	-
	121	0.99	0.6	25.0	-	0.84	9.9	21.8	-
	122	0.99	0.5	25.0	-	0.89	6.2	23.6	-
	123	0.99	0.5	25.0	-	0.86	7.4	22.9	-
	124	0.99	0.5	25.0	-	-	-	-	-
	125	0.99	0.5	25.0	< 6.8	-	-	-	-
	126	-	-	-	-	-	-	-	-
	127	0.99	0.6	25.0	-	0.77	13.4	20.7	2.3
	128	-	-	-	-	-	-	-	-
	129	-	-	-	-	-	-	-	-
	130	0.99	0.5	25.0	-	0.73	16.2	20.1	2.2
	131	0.99	0.6	25.0	-	0.74	12.3	21.0	-
	132	-	-	-	-	-	-	-	-
	133	0.99	0.6	25.0	< 8.1	0.60	29.1	18.2	-
	134	0.99	0.6	25.0	-	0.74	14.6	20.4	-
Helix G	135	-	-	-	-	-	-	-	-
	136	-	-	-	-	-	-	-	-
	137	0.99	0.6	25.0	-	0.70	26.1	18.5	-
	138	0.99	0.5	25.0	-	0.77	18.0	19.7	-
	139	0.99	0.5	25.0	-	0.55	31.2	18.0	-
	140	0.99	0.5	25.0	< 9.8	0.68	22.5	19.0	-
	141	0.99	0.5	25.0	-	0.68	19.6	19.4	-
	142	0.99	0.5	25.0	-	-	-	-	-
	143	0.99	0.5	25.0	-	0.96	2.1	25	-
	144	0.99	0.5	25.0	-	-	-	-	-
Site IV	145	0.99	0.5	25.0	-	-	-	-	-
	146	-	-	-	-	0.77	13.4	20.7	-
	147	0.99	0.5	25.0	-	-	-	-	-
	148	-	-	-	-	-	-	-	-

	149	-	-	-	-	-	-	-	-
	150	-	-	-	-	-	-	-	-
Helix H	151	-	-	-	-	-	-	-	-
	152	-	-	-	-	-	-	-	-
	153	-	-	-	-	-	-	-	-
	154	-	-	-	-	-	-	-	-
	155	0.99	0.5	25.0	-	-	-	-	-
	156	0.99	0.5	25.0	< 8.4	0.74	15.3	20.3	-
	157	-	-	-	-	-	-	-	-
	158	0.99	0.5	25.0	-	0.51	33.5	17.8	-0.4
	159	-	-	-	-	-	-	-	-
	160	0.99	0.5	25.0	-	0.68	17.8	19.8	-
	161	0.99	0.5	25.0	5.1	0.50	39.8	17.3	-0.6

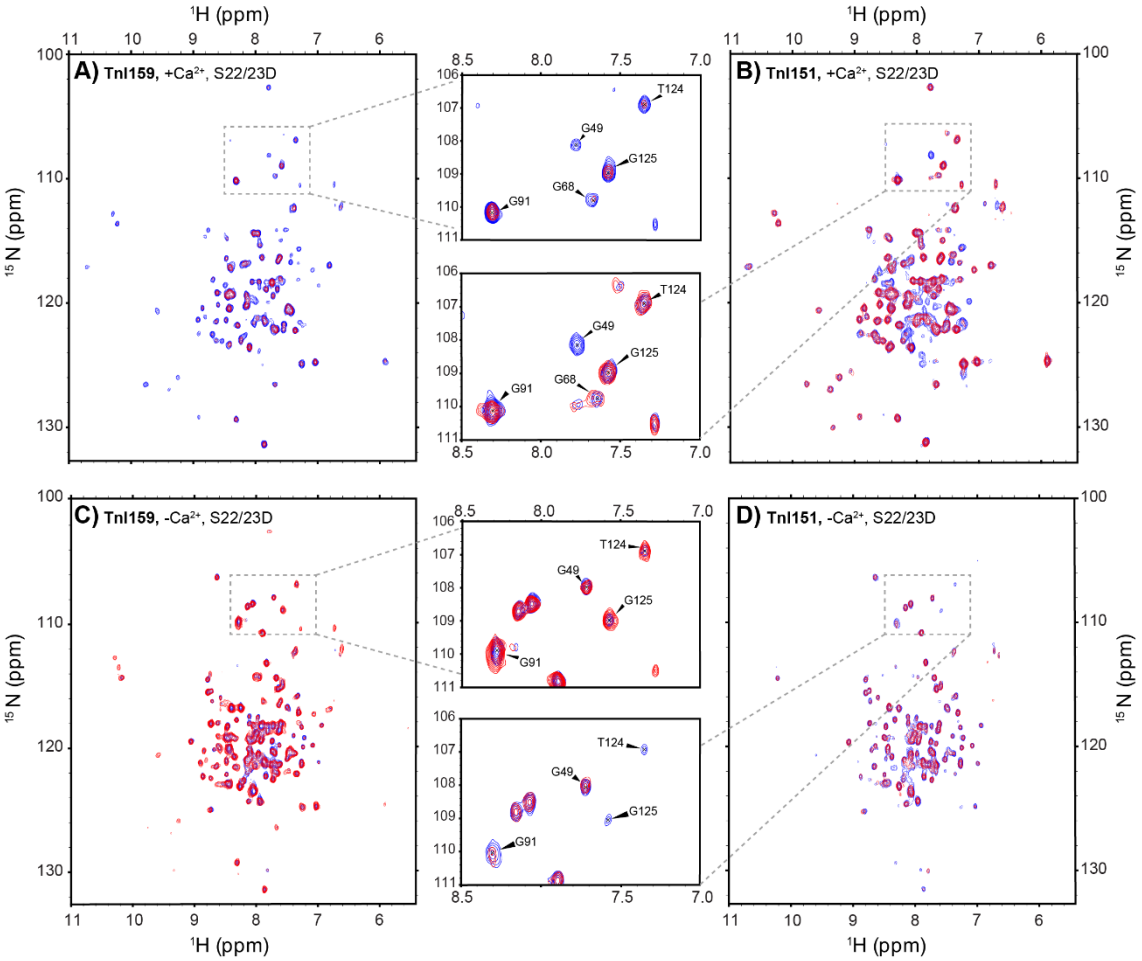

Figure S1 Two dimensional ^{1}H-^{15}N-TROSY spectra of phosphorylated binary troponin complexes show strong peak broadening effects for spin labeled TnI constructs. MTSL spin label was attached to TnI switch peptide residues TnI159 or TnI151. TnI159S22/23D-MTSL in the (A) $+Ca^{2+}$ and (C) $-Ca^{2+}$ state; and TnI151S22/23D-MTSL in the (B) $+Ca^{2+}$ and (D) $-Ca^{2+}$ state. The boxed insets represent the same magnified area of the spectrum and show peaks assignments. Blue and red peaks represent diamagnetic and paramagnetic states, respectively.

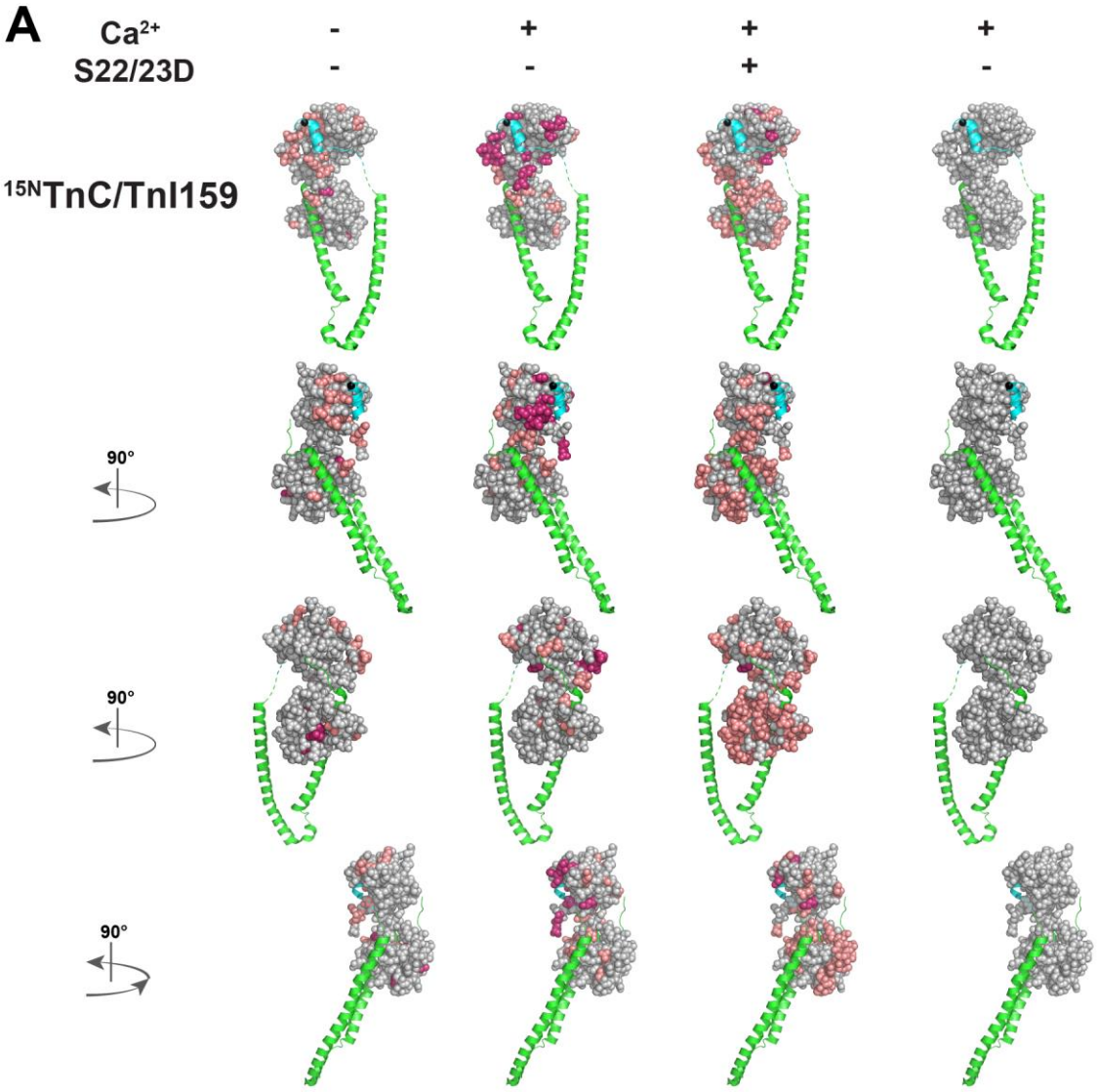
A
Ca2+
S22/23D
- + + +
- - + -
15NTnC/TnI159
90°
90°
90°

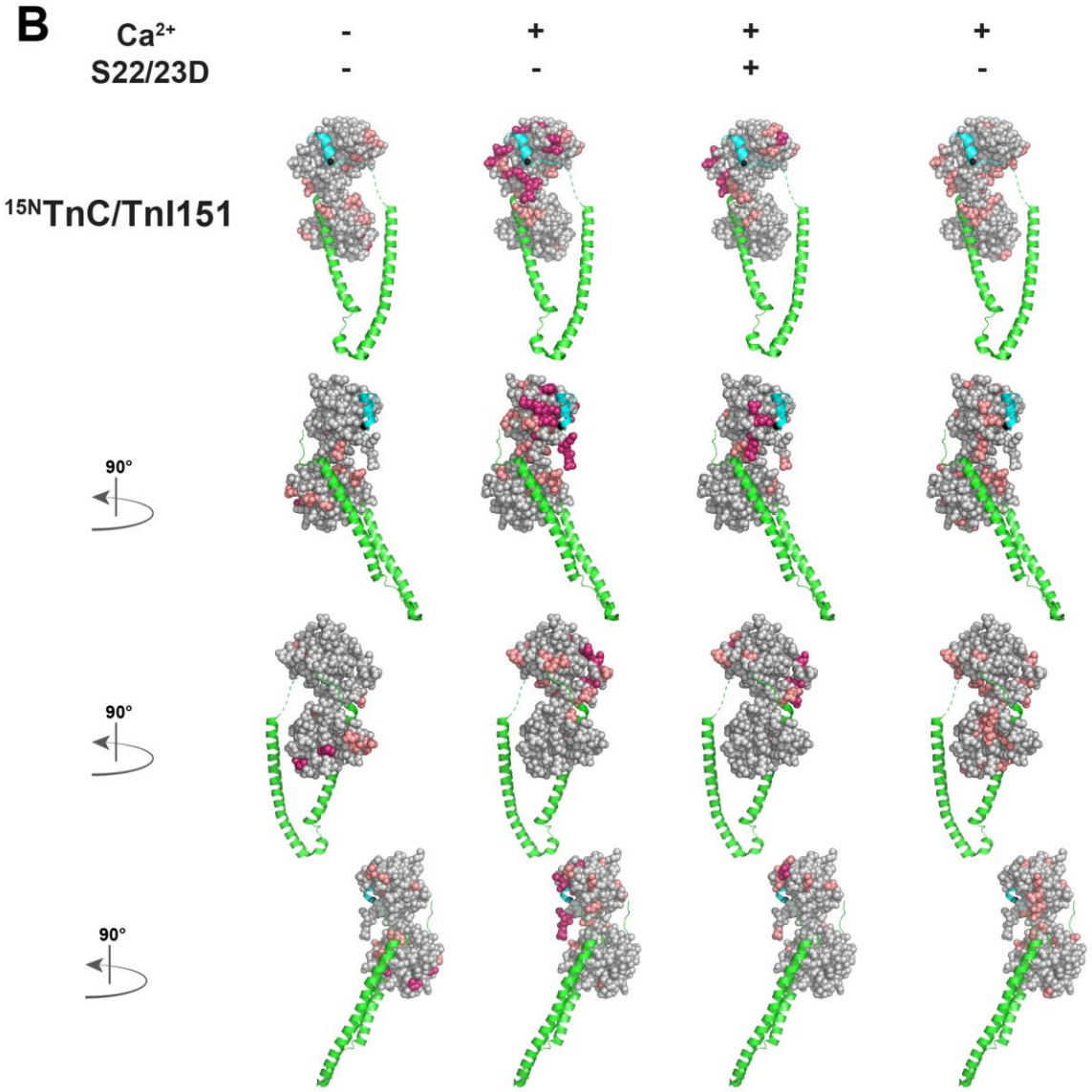

Figure S2 Mapping of PRE distances onto the X-ray crystal structure of the cardiac core Tn complex (1J1D [3]) for spin labeled binary Tn constructs **(A)** TnI159 and **(B)** TnI151. The combination of four different states of phosphorylation and Ca^{2+} binding are visualized for each construct. Each state is represented in four views with a 90° rotation (top to bottom). The TnC subunit is in grey and TnI is in green. Distances ≤ 16 Å are coloured in purple; and distances in the range of 16- 20 Å are coloured salmon. The 'switch peptide' sequence region is highlighted in cyan. The position of the spin label is represented by a black sphere.

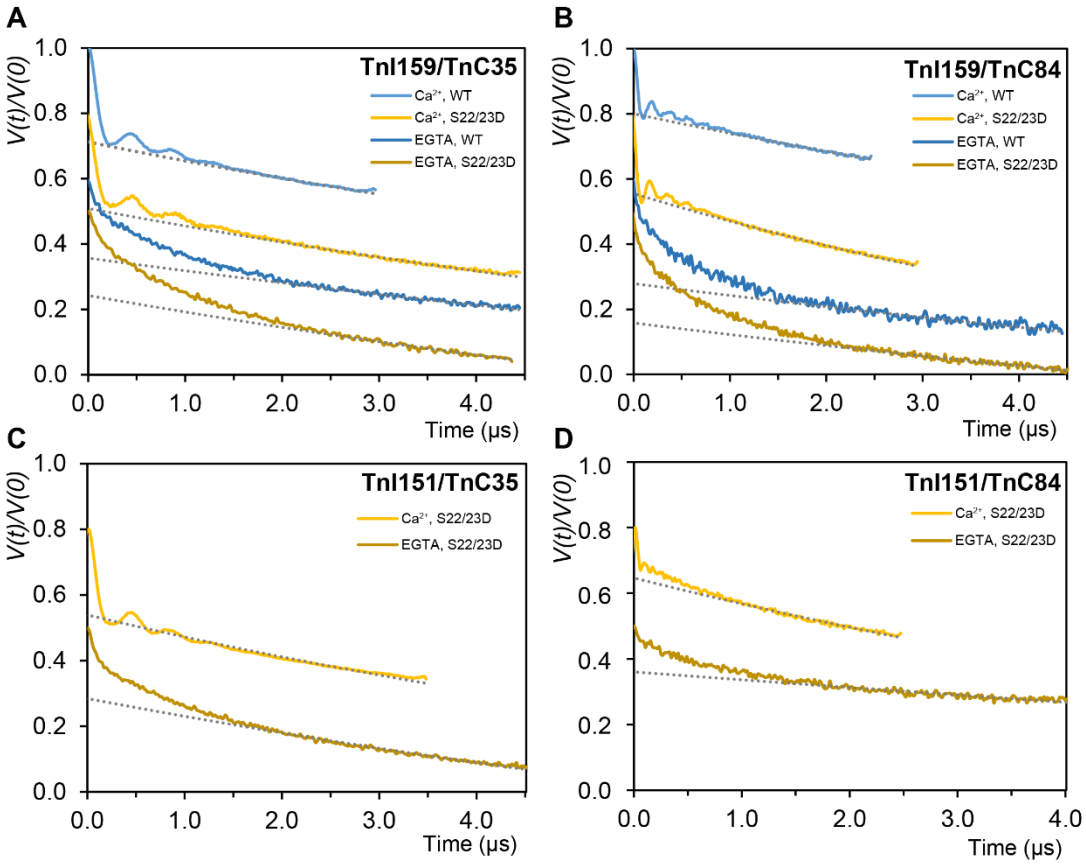

Figure S3 Experimental Q-band DEER primary data V(t)/V(0) for double spin labeled complexes of: **(A)** TnI159/TnC35, **(B)** TnI159/TnC84, **(C)** TnI151/TnC35, and **(D)** TnI151/TnC84. Coloured lines: light blue - Ca^{2+} WT; yellow - Ca^{2+} S22/23D; dark blue - EGTA WT; dark gold - EGTA S22/23D. Dotted lines represent simulated background functions. Note, WT spectra for TnI151/TnC35 and TnI151/TnC84 are available in a previous study [10].

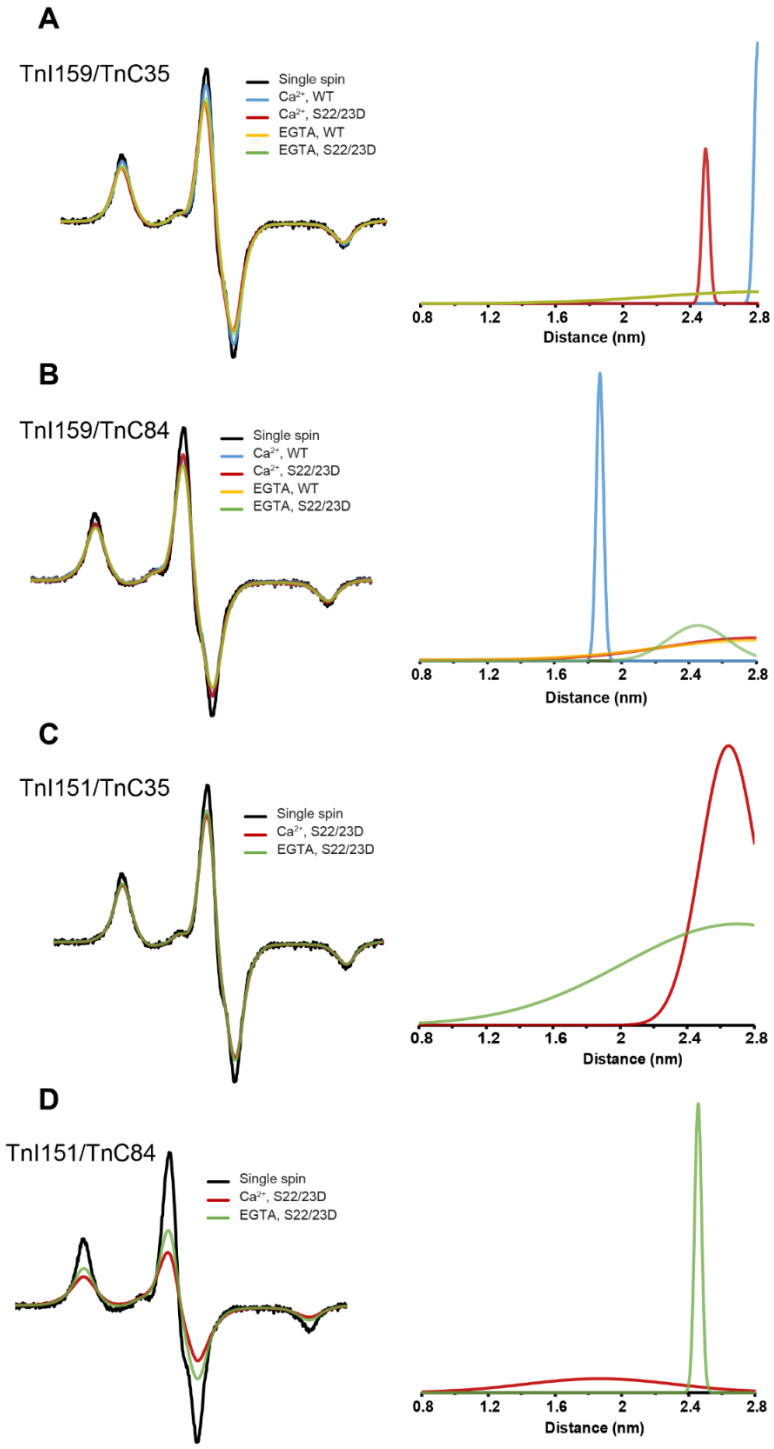

Figure S4 Measurement of short range interspin distances by CW. CW-EPR analysis of Tn complexes: **(A)** TnI159/TnC35, **(B)** TnI159/TnC84, **(C)** TnI151/TnC35, and **(D)** TnI151/TnC84. *Left panel*, comparison of the CW spectra for the double spin with sum of the single spin complex. *Coloured lines*: black, single spin complex; blue, Ca^{2+} WT; red, Ca^{2+} S22/23D; gold, EGTA WT; green, EGTA S22/23D. *Right*, single Gaussian distance distributions for each complex.

6. Conclusion

Contraction of striated muscle in the actin thin filament is regulated via acto-myosin interactions controlled by the two actin binding proteins, tropomyosin and troponin, in response to the effector molecule Ca^{2+}. Binding of Ca^{2+} to TnC is responsible for triggering a cascade of conformational changes within TnI that are passed through to Tm, and finally switch 'on' the thin filament to a state of muscle contraction. However, in the cardiac isoform, muscle contraction is controlled by another level of regulation. As the heart is beating involuntary, it is presumed that, besides the differences in chemical regulations such as the Ca^{2+} influx rate, contraction of cardiac muscle is also influenced by different structural components such as Troponin. In the present Thesis, the structural and dynamic features of cardiac Tn in response to Ca^{2+}-binding were reviewed and a regulatory mechanism was proposed - **Chapter 1**. Our understanding of the second additional level of regulation in the cardiac isoform, where contraction-relaxation is controlled via the phosphorylation of the cardiac specific N-terminal extension region, was also discussed. Despite several valuable studies on the structure and regulation process of Tn on muscle contraction, there are still many questions yet to be answered regarding the interplay between these protein subunits and the role of phosphorylation. In this Thesis, the position and dynamics of the TnI N-extension region (NH_2-region) and the TnI switch peptide region, two important functional regions in TnI, were studied in response to phosphorylation (**Chapters 4 & 5**).

To date, the current model of the molecular mechanism of thin filament regulation by Tn predominantly has relied on the x-ray crystallographic structures of the core region of the Tn complex. This model has been further refined by NMR studies of partial protein complex and peptide fragments, as well as findings that include FRET and computational studies. Recently, the developments in cryo-electron microscopy have also provided novel information of larger assemblies of thin filament. Together, each of these structural methods have their own advantages and disadvantages. For example, Tn structures resolved by x-ray crystallography are only a snapshot of a highly dynamic system and many other conformations are missed. NMR methods are limited to the size. FRET also has challenges with achieving the placement of different fluorophores on desired targeted regions. In fact, structural approaches and the different pieces of structural findings need to be integrated to

complete the pieces of a larger puzzle. The aims of this Thesis were to therefore apply an integrative structural biology approach, with a focus on paramagnetic spin labeling in combination with NMR and EPR methods. This approach allows for the study of both the structure and the dynamics of the Tn complex in as close to an intact system as the experimental technique would allow. Each approach again has its own advantages and disadvantages, but together, EPR and NMR have provided additional information on several functionally important regions that has eluded other structural approaches. The aim of this final Chapter is to briefly summarise the data presented in this Thesis and to comment on how these findings further build on and refine our current model of muscle regulation.

6.1 Developing a model for the cardiac Tn regulatory mechanism

In the review and paper presented in Chapter 1, it was demonstrated that the development of the Site Directed Spin Labeling (SDSL) methodology extended our understanding of the large and dynamic Troponin muscle protein system. The focus of the SDSL approach has mostly been on EPR measurements. The mobility of the functional region, solvent accessibility, and interspin distances can all be obtained to assess the ternary and quaternary structure, and the intra- and inter-subunit interactions. We further extended our discussion of SDSL to also include recent NMR work on cardiac Tn from our group, namely Paramagnetic Relaxation Enhancement – PRE. PRE-NMR is a further exemplar that highlights the advantages of spin labeling for obtaining both structural and dynamic information, in solution, and using large multi-protein systems. We concluded our review by presenting a model of molecular movie of the Troponin complex as built from the complementary EPR and NMR studies described in this review. In this model, the switch region is shown to be in the proximity of TnC N-domain at all times, and the flexible linker of TnC is important for resulting in a high mobility for the regulatory N-domain of TnC. Together, the frequency of collisions between the switch region and the N-domain of TnC is higher in the cardiac Tn isoform (**Figure 6.1**). Lastly, in this review, it was also suggested that the SDSL approach in combination with EPR and NMR can be applied to other multi-protein systems when high-resolution structural information is lacking.

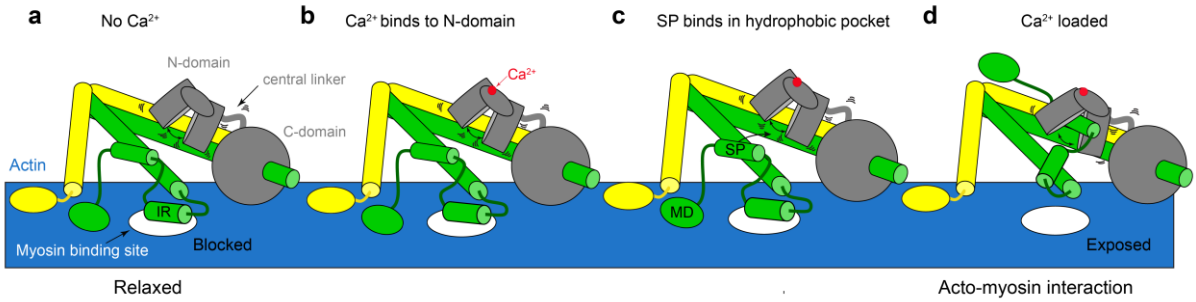

Figure 6.1 The "molecular movie" of cardiac Tn. Image taken from [1]. Note, the role of phosphorylation was not proposed in this initial model.

6.2 Movement of the cardiac specific TnI N-extension region upon phosphorylation

In Chapter 4, the dynamics and position of the cardiac specific N-extension region (NH_2-TnI) of TnI, with respect to TnC, was investigated upon phosphorylation. Three residues (Ser5, Ala28, Ser39) on the N-extension region were spin labeled to assess the inter-subunit dynamics using PRE-NMR. In addition, interspin distances of TnC35/TnI39 and TnC84/TnI39 were measured using EPR techniques to monitor inter-subunit positions. As a result of phosphorylation, three prominent inter-subunit movements were observed in the Tn complex. These were:

1) the abolition of the interaction between the N-extension region of TnI and Ca^{2+} binding Site II;
2) the disruption of the interaction between the N-extension region and residues in the vicinity of the hydrophobic pocket on the N-domain of TnC;
3) the rotation of the regulatory N-domain of TnC.

Notably, the major effect of phosphorylation was observed in the saturated Ca^{2+} state. It was concluded that phosphorylation induces an allosteric dynamic state in the Tn complex through the introduction of two negative charges. A small structural perturbation and re-orientation of the N-domain of TnC triggers the enhanced dissociation of Ca^{2+} from binding

Site II; and release of the switch region then occurs. As a result, relaxation rate is enhanced. The phosphorylation modulated release of the switch region was the hypothesis then tested in Chapter 5.

6.3 Enhancement in the release of switch peptide region upon phosphorylation

As previously described (Section 1.9, Review paper), the release of the TnI switch peptide is a key event of muscle relaxation. In Chapter 5, the release of the TnI switch region from the N-domain of TnC was investigated in response to phosphorylation (Section 1.9, Review paper). For this purpose, both ends of the switch peptide (residues 151 and 159) were spin labeled in order to measure mid-range distances to TnC (12-25 Å) using PRE-NMR. Additionally, sixteen long-range interspin distances of the combinations of TnC35,84 with TnI151,159 were obtained using EPR measurements. From this study, the prominent findings were:

1) Under Ca^{2+} saturated conditions, phosphorylation induced structural changes were minor. Phosphorylation was observed to destabilise the position of the TnI switch peptide within the hydrophobic pocket but not result in the release of the switch region, i.e. phosphorylation likely 'primes' TnC for the release of switch peptide.
2) Under Ca^{2+}-free conditions, the major effect of phosphorylation was observed. The release of the switch peptide is enhanced upon phosphorylation, compared to the WT (unphosphorylated) state.

Here, the major effect of phosphorylation was observed in the Ca^{2+}-free state. Together with the findings in Chapter 4, a model was proposed to describe the release of the switch region from the N-domain of TnC upon phosphorylation (Figure **6.2**). In this model, called the 'Seat-belt model', the interaction of the N-extension region of TnI with the N-domain of TnC is like a seat-belt which limits the release of the switch peptide. When phosphorylation occurs, the interaction between the N-extension region and the TnC is abolished which result in a further release for switch peptide region. That is, the shoulder strap of the seat-belt falls of the N-domain of TnC, and the switch is then released. In conclusion, phosphorylation induces subtle structural alterations in the Tn complex which allosterically result in the re-orientation of the N-domain of TnC, the shifting of the interaction of the N-extension region

from Site II and the switch binding pocket, the release of Ca^{2+}, and finally the release of the switch region. As a result of phosphorylation modulation, the relaxation rate is enhanced.

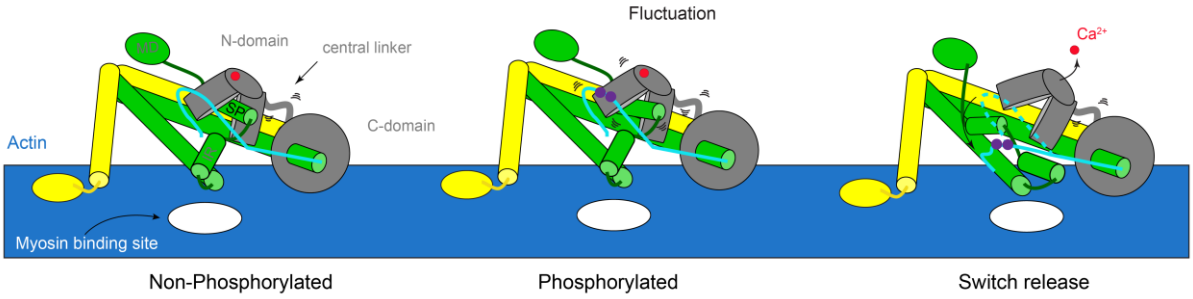

Figure 6.2 Seat-belt model. TnI N-extension (cyan) blocks the switch region and restricts the release of the switch peptide. Phosphorylation (purple spheres) increases disorders/fluctuations of the switch peptide in the hydrophobic pocket of TnC. Upon Ca^{2+} release, the TnI N-extension 'falls-off' from TnC N-domain and results in a greater movement of the switch peptide after its release.

6.4 Additional Comments

6.4.1 Pushing the limits of spin labeling

In this Thesis, double electron electron resonance (DEER) provided long interspin distances. The DEER approach was performed using two difference frequencies; X- and Q-band. I started this research project using X-band DEER but during my PhD journey I found the confidence to continue with Q-band measurements. Technically, in X-band frequency, one expects to observe the same distances as in Q-band frequency. However the advantages discussed in Section 3.2.4.3.2 were attractive enough to pursue the remainder of the DEER measurements by Q-band (as done in Chapter 5). Measuring interspin distances by Q-band also allowed the preparation of samples in deuterated buffer which could then provide a longer electron transverse relaxation time (and DEER evolution time) to more accurately analyse even longer distances [2].

The analysis of the DEER distances was performed using Gaussian distribution and DeFit program (Section 3.2.5.3). Interestingly, analysis of distances using Tikhonov regularization

and DeerAnalysis program yielded very similar results upon phosphorylation (**Figure 6.3**); no change in saturated Ca^{2+} and a shift to longer distances in the Ca^{2+}-free condition. However, the number of distances, especially in the Ca^{2+}-free state, were higher than the $+Ca^{2+}$ state, which can be attributed to the probability of a higher number of distance populations for

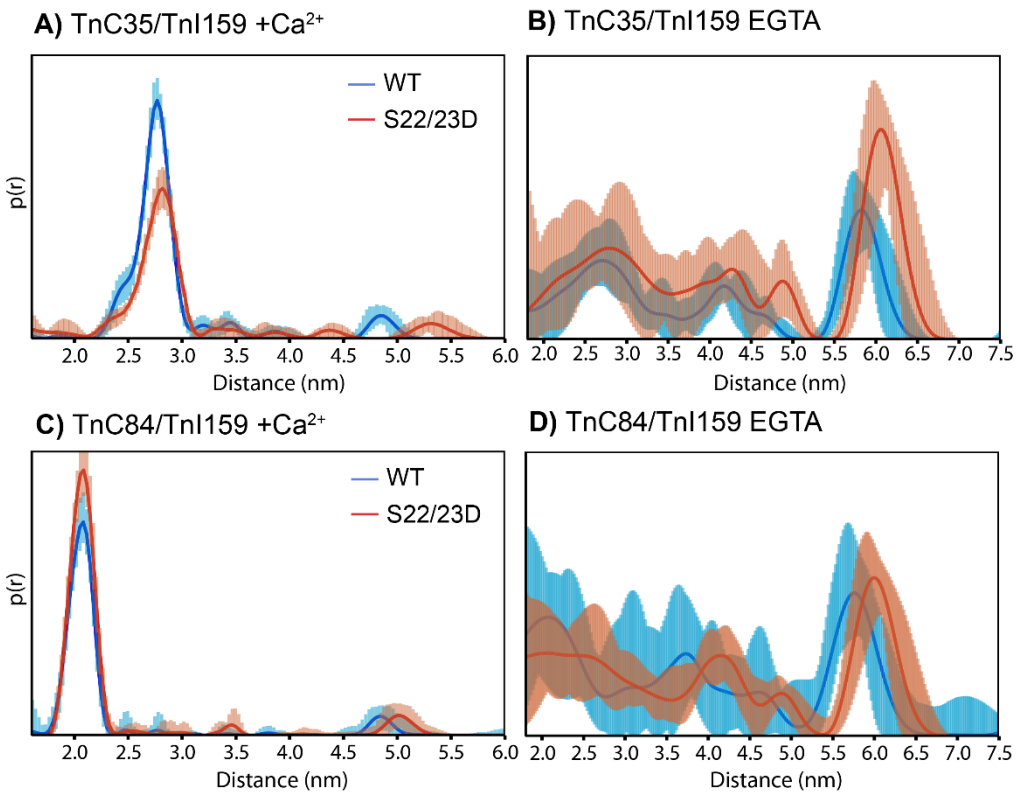

Figure 6.3 DEER Distance analysis in the soluble spin labeled ternary Tn complex to position the TnI switch peptide with respect to TnC. Distances were derived from the DEER echo amplitude decay with (i) the DeerAnalysis program and (ii) using Tikhonov regularization. Interspin distances for double labeled Tn complexes in wild type (WT, blue) and phosphorylated (S22/23D, red) states for TnI159/TnC35 in **(A)** $+Ca^{2+}$ and **(B)** Ca^{2+}- free condition, and for TnI159/TnC84 in **(C)** $+Ca^{2+}$ and **(D)** Ca^{2+}-free condition. The error bar of distances for WT and phosphorylated are represented with light blue and orange, respectively.

disordered interspin states. Notably, the larger errors in the Ca^{2+}-free state are also an indication of the disorder of the interspin distance which is represented by the width of distributions in Gaussian analysis. It seems that distance analysis with Tikhonov method is more suitable for static interspin distances, whereas Gaussian analysis is better for disordered interspin distances.

6.4.2 From Tn structure to muscle contraction

One of the challenges during my PhD was to link the structural results of phosphorylation to the physiology observed for the cardiac muscle contraction-relaxation cycle. Although the physiology of muscle contraction is beyond the scope of this Thesis, visualising the order of the structural alterations according to the observed physiology would better illustrate the beauty of these findings. Under events of stress, PKA is upregulated to phosphorylate a substrate protein/peptide - the N-extension region of TnI. However, upregulation of PKA is a signal for upregulation of phosphatase to dephosphorylate a substrate protein/peptide. Therefore, during the period of stress, there is a fine balance between kinase and phosphatase, i.e. phosphorylation and dephosphorylation are frequently happening until the stress condition ends. As a result, phosphorylation and dephosphorylation are modulating a physiological regulatory system in a cycle. In the case of Tn complex, the main regulation is binding of the switch region to the hydrophobic pocket in response to Ca^{2+} binding and vice versa. Phosphorylation facilitates the release of the switch peptide, or muscle relaxation. Phosphorylated TnI is then a substrate for phosphatase, so dephosphorylation turns Tn to initial condition for another binding (**Figure 6.4**).

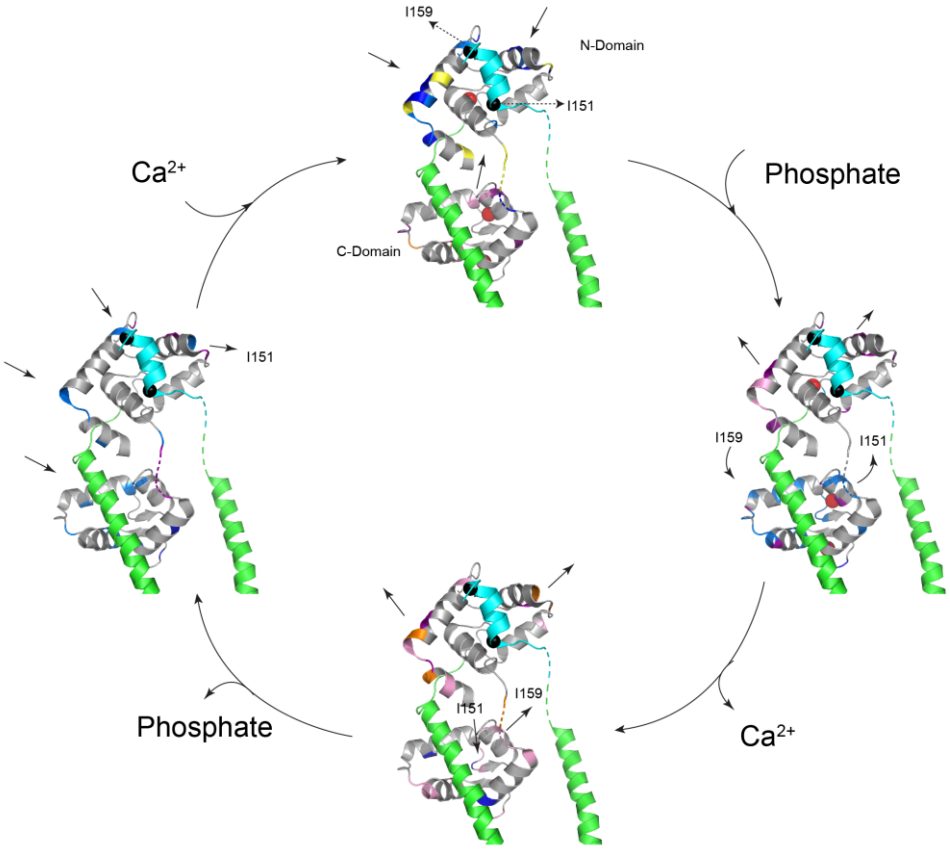

Figure 6.4 Schematic representation of the frequency of Tn structural alterations in stress condition. Grey and green cartoons represent TnC and TnI subunits. Switch peptide is in cyan. Blue colour represents the negative distance changes (moving toward); orange and pink represent positive distances changes (moving away). Arrows indicate the direction of switch peptide's movement.

6.5 Future direction

6.5.1 Completing the model: movement of the N-domain of TnC

In Chapter 4, one of the key observed movements upon phosphorylation was the rotation of the regulatory N-domain of TnC. This rotation can be attributed to the flexible linker connecting the N- and C-domains of cardiac TnC. However, in this study, the rotation of the N-domain with respect to the IT arm was assumed to occur with no direct evidence supporting this. To validate the rotation of the N-domain of TnC upon phosphorylation, the

position or orientation of the N-domain can be investigated with respect to C-domain of TnC. For this purpose, natural cysteine residues 35 & 84 can still be considered as informative labeling sites. However, the selection of the labeling site in the C-domain would need to be done with care. Inter-domain distance constraints in the whole Tn complex may be able to confirm the N-domain rotational movement; as well as provide insights of the direction and angels of such a movement.

6.5.2 Completing the model: intra-subunit interactions

In this Thesis, I attempted to understand the impact of phosphorylation on both the dynamics and positioning of both the N-extension and switch region of TnI with respect to TnC. In other words, the phosphorylation effect was investigated through the *inter-subunit* contacts. As discussed in **Section1.6**, Howarth *et al*. [3] proposed a phosphorylation induced *intra-subunit* interaction between the N-extension region and the inhibitory region of TnI. Also, Cheng *et al*. [4] confirmed this intra-subunit interaction in their reported recent molecular dynamic simulation. Thus, intra-subunit contacts, especially between the N-extension and the TnI inhibitory region, should be pursued to complete the proposed model for cardiac Tn regulation by phosphorylation. Intra-subunit contact will extend the current picture of phosphorylation regulation in the cardiac Tn complex.

However, there are challenges which need to be considered carefully. Both the N-extension and inhibitory regions are missing from the cardiac core Tn crystal structure because they are disordered and highly mobile regions [5]. As a result of intrinsic mobility of these regions, and the mobility of MTSL spin labels, the interspin distances derived by EPR method are expected to be broad and difficult to analyse. To minimize the mobility of the spin label to the backbone of the protein, the employment of bifunctional spin labels such as 'HO-1944' may be helpful. HO-1944 can be covalently attached to the protein backbone via pairs of cysteine residues such as at *i* and *(i + 3)* or at *i* and *(i + 4)* in an α-helix; or at *i* and *(i + 1)* or at *i* and *(i + 2)* in a β-strand [6].

6.5.3 Cardiomyopathy and phosphorylation regulatory mechanism

As discussed in Section 1.6, phosphorylation enhances the rate of cardiac muscle relaxation, and therefore the rate of cardiac muscle contraction, to increase blood circulation during

stress condition. However, in cardiac diseases, such as cardiomyopathies (Section 1.7), the heart muscle is not able to meet the oxygen requirement of the body. Cardiomyopathies are linked with mutations in all three subunits of Tn. Therefore, understanding the cardiac Tn structural modulations as a result of mutations is required to encounter diseases. Mutations in TnC, such as L29Q, are shown to abolish the phosphorylation effects. In this Thesis, substantial interactions and dynamics in normal Tn complex was investigated upon phosphorylation. However, comparing the dynamics of cardiomyopathic Tn (L29Q) can address the important interactions though which phosphorylation signal is transferred in Tn complex. I was also involved in a study looking at the effects of L29Q on the structure and dynamics of TnC and this is included in the Appendix of this Thesis.

References

1. Kachooei, E., N.M. Cordina, and L.J. Brown, *Constructing a structural model of troponin using site-directed spin labeling: EPR and PRE-NMR.* Biophys Rev, 2019. **11**(4): p. 621-639.
2. Jeschke, G., *DEER distance measurements on proteins.* Annu Rev Phys Chem, 2012. **63**: p. 419-46.
3. Howarth, J.W., et al., *Phosphorylation-dependent conformational transition of the cardiac specific N-extension of troponin I in cardiac troponin.* J Mol Biol, 2007. **373**(3): p. 706-22.
4. Cheng, Y., et al., *Computational studies of the effect of the S23D/S24D troponin I mutation on cardiac troponin structural dynamics.* Biophys J, 2014. **107**(7): p. 1675-85.
5. Takeda, S., et al., *Structure of the core domain of human cardiac troponin in the Ca^{2+}-saturated form.* Nature, 2003. **424**(6944): p. 35-41.
6. Fleissner, M.R., et al., *Structure and dynamics of a conformationally constrained nitroxide side chain and applications in EPR spectroscopy.* Proc Natl Acad Sci U S A, 2011. **108**(39): p. 16241-6.

Appendix 1. The structural effects of hypertrophic cardiomyopathy mutation-L29Q

A.1.1 Introduction

As discussed in Chapter 1, hypertrophic cardiomyopathy (HCM) is one of the major causes for cardiac diseases resulting in morbidity and sometimes sudden death. The focus of the manuscript presented in this Chapter is to examine the structural consequences of the hypertrophic cardiomyopathy mutation L29Q. This mutation was the first HCM mutation identified in Troponin C. In this manuscript, the suitability of the SDSL and PRE-NMR methods for rapidly assessing conformational changes arising from single point mutations linked to disease states is demonstrated.

A.1.2 Authors' Contributions

All sample preparation were performed by Dr. Phani Potluri under supervision of A/Prof. Louise Brown. The design of the experiments was done by Dr. Brown provided and Dr. Potluri. The manuscript was primarily written by Dr. Potluri, under the guidance of Dr. Brown. NMR spectra were collection with the assistance of Dr. Nicole Cordina. I contributed in data analysis and interpretation.

Biochemistry

Article

Cite This: Biochemistry 2019, 58, 908−917

pubs.acs.org/biochemistry

Characterization of the L29Q Hypertrophic Cardiomyopathy Mutation in Cardiac Troponin C by Paramagnetic Relaxation Enhancement Nuclear Magnetic Resonance

Phani R. Potluri, Nicole M. Cordina, Ehsan Kachooei, and Louise J. Brown*

Department of Molecular Sciences, Macquarie University, Sydney, NSW 2109, Australia

Supporting Information

ABSTRACT: The key events in regulating muscle contraction involve the troponin (Tn) heterotrimeric protein complex in which the binding to and release of Ca^{2+} from the highly conserved troponin C (TnC) subunit trigger a series of structural changes within Tn, and the other thin filament proteins, to result in contraction. In the heart, the control of contraction and relaxation events can be altered by many single-point mutations that may result in cardiomyopathy and sometimes sudden cardiac death. Here we have examined the structural effects of one hypertrophic cardiomyopathy mutation, L29Q, on Ca^{2+}-induced structural transitions within whole TnC. This mutation is of particular interest as several physiological and structural studies have indicated that the response of TnC to Ca^{2+} binding is altered in the presence of the L29Q mutation, but the structural nature of these changes continues to be debated. In addition, little is known about the effect of this mutation in the Ca^{2+} free state. Here we have used paramagnetic relaxation enhancement nuclear magnetic resonance (PRE-NMR) to assess the structural effects arising from the L29Q mutation. PRE-NMR distances obtained from a nitroxide spin-label at Cys84 showed that the L29Q mutation perturbs the structure of the TnC N-domain in the presence and absence of Ca^{2+}, with a more "open" TnC N-domain observed in the apo form. In addition, binding of Ca^{2+} to the TnC-L29Q construct triggers a change in the orientation between the two domains of TnC. Together, these structural perturbations, revealed by PRE-NMR, provide insight into the pathogenesis of this mutation.

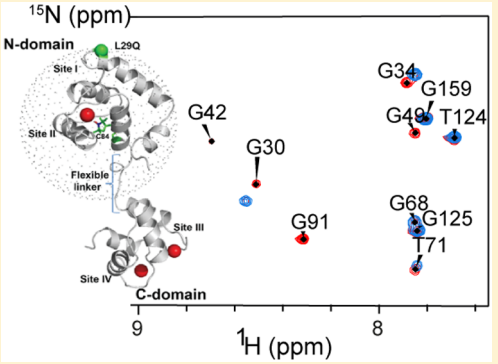

Contraction of striated muscle is regulated by troponin (Tn), a ∼70 kDa heterotrimeric calcium binding (Ca^{2+}) protein. The Tn complex consists of a Ca^{2+} binding subunit, troponin C (TnC); an inhibitory subunit, troponin I (TnI); and a tropomyosin anchoring subunit, troponin T (TnT).[1] The TnC subunit has a dumbbell shape with two EF-hand metal binding globular domains, herein known as the N- and C-domains (Figure 1). These two domains are connected by a rigid central helix in the skeletal isoform, but in the cardiac isoform, this linker region is unstructured and highly flexible.

In the skeletal isoform, muscle contraction is initiated by the binding of Ca^{2+} to the two metal binding sites (site I and site II) on the regulatory N-terminal domain of TnC. However, for the cardiac isoform (cTnC), site I on the N-domain is nonfunctional.[1,2] Metal binding to sites III and IV on the C-terminal domain primarily serves a structural role only, with Mg^{2+} typically bound to both sites under physiological conditions. When Ca^{2+} binds to N-domain site II in the cardiac isoform, a conformational change occurs within the cTnC N-domain, which in turn relieves the inhibitory influence of the TnI subunit through the interaction of the switch region of TnI (cTnI 150−159) with the cTnC N-domain. This interaction is accompanied by the movement of a further secondary actin binding region of TnI, the mobile domain (cTnI 160−211), away from the thin filament, resulting in the exposure of the myosin binding sites through the relocation in the positioning of tropomyosin on the muscle thin filament. This cascade of events triggered by Ca^{2+} binding to cTnC, which promotes the formation of the actomyosin cross-bridge, is further reviewed elsewhere.[3,4]

As Tn plays a key role in the regulation of cardiac contraction, any structural perturbations to this complex can lead to the inefficient regulation of muscle contraction and subsequently result in systolic or diastolic dysfunction. One of the most common forms of cardiac disease, in which many genetic mutations in Tn have been identified, is hypertrophic cardiomyopathy (HCM).[5] HCM mutations can result in a broad clinical spectrum but typically result in the thickening of the wall of the left ventricle of the heart, leading to complications such as progressive heart failure, atrial fibrillation with embolic stroke, and sudden death.[6] While HCM mutations are found across a wide range of proteins, more than half are found in proteins of the sarcomere, with more than 100 mutations identified in the Tn complex.[7] Several of the most severe of these HCM mutations are observed to be clustered in the proximity of metal binding site

Received: October 27, 2018
Revised: December 21, 2018
Published: January 8, 2019

DOI: 10.1021/acs.biochem.8b01140
Biochemistry 2019, 58, 908−917

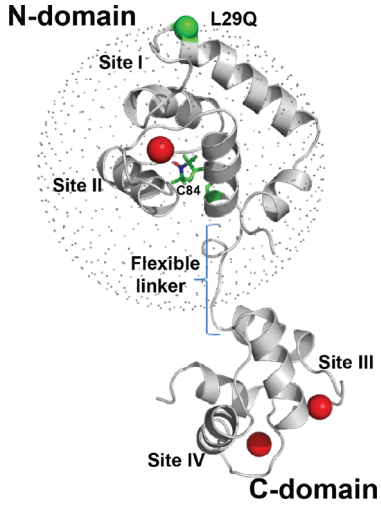

Figure 1. Ribbon representation of cTnC in the Ca^{2+}-bound state (PDB entry 1AJ4[24]). The two Ca^{2+} binding EF-hand domains (N- and C-domains) are connected by a flexible linker. The location of the L29Q HCM mutation (green) is shown in the N-domain and is near the defunct metal binding site I. Bound Ca^{2+} ions are colored red. The monocysteine construct "C84" was spin labeled with MTSL (C84-L29Q). The range over which PRE distances can most accurately be measured is indicated by a sphere with a 20 Å radius centered on the MTSL label.

II of the N-domain of cTnC (N-cTnC) and also near the defunct site I.[8] Naturally, many of these N-cTnC mutations have been found to lead to impaired Ca^{2+} handling, so shedding light on the structural nature of the effects is important for understanding the disease process.

Here we have focused on a single-point mutation, L29Q, the first mutation found in TnC to be associated with HCM.[9] The L29Q HCM mutation was first identified in a 60-year-old male who presented with significant hypertrophy of the left ventricle as a nucleotide change of T-A at position 86 of exon 3.[9] Special interest arises with L29Q because of its position in the N-domain near the junction of the defunct site I of TnC and helix A (Figure 1). The replacement of leucine, a nonpolar residue, with the polar glutamine residue has been suggested to be capable of potentially changing the Ca^{2+} affinity by reviving the defunct site I.[10,11] Calcium binding may then shift the structural equilibrium of the N-domain toward a fully "open" state, as observed for the skeletal isoform.[12] This may be significant, as an open conformation of the N-domain lobe of TnC is optimal for the interaction of the TnI switch peptide with TnC.[13] However, there are several conflicting reports with respect to the effects of this mutation on the function of Tn with some reporting that the presence of the L29Q mutation can either increase[10] or decrease[11] the myofilament Ca^{2+} sensitivity or not change it at all.[14,15]

Despite the availability of a vast amount of structural data for Tn, characterizing the conformational changes in the presence of a disease-causing mutation, or triggered by the binding of Ca^{2+}, remains an experimental challenge. This is especially true for the cardiac isoform of TnC in which the flexible nature of its central linker results in a dynamic ensemble of interdomain orientations,[16] and the binding of Ca^{2+} controls the dynamic equilibrium between the "closed" and "open" structural forms of the N-domain of cTnC.[13] In addition, most reported structural studies of TnC have been performed using only the isolated N- or C-domains. Relevant to this study, as an example, is the available nuclear magnetic resonance (NMR) structure of cTnC with the L29Q HCM mutation [Protein Data Bank (PDB) entry 2N79]. This structure was determined using the isolated N-domain fragment of TnC, and only under conditions of saturating Ca^{2+}.[17] In this study, the authors reported that the global fold of the N-domain of TnC was unperturbed by the mutation with only subtle structural changes observed in the region close to the L29Q mutation. Whether this mutation modifies the structure or dynamics of TnC in response to Ca^{2+} binding to the N-domain requires examination of the L29Q mutation in the Ca^{2+} free state.

Effectively describing the structure and dynamics of the cardiac isoform of whole TnC, including global conformational changes induced by Ca^{2+} binding, requires long-range distance measurements.[16] Conventional NMR approaches, which mostly rely on semiquantitative distance measurements derived from interproton nuclear Overhauser effects (NOEs), typically have an upper distance limit of ∼5 Å. If a paramagnetic species, such as a nitroxide spin-label, can be incorporated into cTnC, then long-range distances of up to ∼25 Å can be obtained by NMR through the paramagnetic relaxation enhancement, or "PRE"-NMR approach.[18−20] These long-range PRE-NMR distances can then be used to more reliably describe protein folds or monitor for structural changes. Here, we describe the incorporation of a paramagnetic nitroxide spin-label (at cysteine residue 84) into full length cardiac TnC and the measurement of PRE-NMR-derived distances across the range of 10−25 Å (Figure 1). The PRE-NMR experiments enabled the Ca^{2+}-induced conformational changes within cTnC, due to the presence of the L29Q HCM mutation, to be revealed. The long-range PRE-derived distances showed that the L29Q mutation perturbed the structure of the N-domain in the presence of Ca^{2+} as well as the orientation between the N- and C-domains of TnC.

MATERIALS AND METHODS

Preparation of [^{15}N]cTnC Constructs. The cardiac isoform of rat TnC (cTnC) was expressed in a pET-3d expression vector (Novagen), as described previously.[22] This construct is termed cTnC-WT. The Quik-change II site-directed mutagenesis kit (Stratagene) was used to create a single-cysteine mutant by replacing the native cysteine 35 residue with a serine (C35S) leaving the second native cysteine at residue 84 available for spin labeling. This construct is herein termed C84. This residue is appropriate for monitoring backbone movement in full length cardiac TnC by PRE-NMR.[13] Mutagenesis was also used to introduce the L29Q HCM mutation onto both the cTnC-WT and C84 constructs, which were termed cTnC-L29Q and C84-L29Q, respectively. DNA sequencing was used to verify all construct sequences prior to transformation into *Escherichia coli* BL21 (DE3) cells for expression.

All four TnC constructs (cTnC-WT, cTnC-L29Q, C84, and C84-L29Q) were expressed at 37 °C in M9 minimal medium (2.5 g L^{-1} glucose and 1 g L^{-1} $^{15}NH_4Cl$).[23] Cells were induced with 1 mM isopropyl β-D-1-thiogalactopyranoside (IPTG) at an optical density (OD_{600}) of 0.7. After being expressed for ∼3 h, cells were collected by centrifugation and resuspended in buffer A [0.2 M NaCl, 1 mM DTT, 5 mM $CaCl_2$, and 50 mM Tris (pH 7.5)]. The resuspended cells were sonicated for 6 min with an amplitude setting of 40% and a pulse rate of 10 s. The insoluble cellular debris was removed by centrifugation (30966*g*, 20 min, 4 °C) before further dialysis against buffer A.

DOI: 10.1021/acs.biochem.8b01140
Biochemistry 2019, 58, 908−917

The soluble fraction was applied to a Phenyl Sepharose 6 Fast Flow column (GE Healthcare) equilibrated in buffer A. The hydrophobic interaction of cTnC with the column was disrupted by the addition of 10 mM EDTA in buffer A. The purity of eluted fractions was checked by sodium dodecyl sulfate−polyacrylamide gel electrophoresis before concentration to 5 mg mL^{-1} using a centrifugal filtration device (Amicon Ultra-15). Ultraviolet−visible spectroscopy and a BCA assay kit (Pierce) were used to determine the protein concentrations.

Spin Labeling of C84 and C84-L29Q Constructs. For the site-specific labeling of the C84 and C84-L29Q TnC constructs, the paramagnetic nitroxide moiety MTSL (1-oxyl-2,2,5,5-tetramethylpyrroline-3-methyl-16-methanethiosulfonate) (Toronto Research Chemicals) was covalently attached to the cysteine side chain at residue 84. To ensure optimal labeling, the constructs were first dialyzed against labeling buffer [100 mM KCl and 20 mM K_2HPO_4/KH_2PO_4 (pH 8)]. The protein was then incubated at room temperature for 2 h with 20 mM DTT to reduce the Cys84 side chain. A 5 mL HiTrap desalting column (GE Healthcare) was then used to remove the DTT before a 10-fold molar excess of MTSL (0.1 M stock in dimethylformamide) was added. Labeled samples were incubated at room temperature overnight. Unreacted MTSL was removed by exhaustive dialysis (36−48 h) against NMR buffer [50 mM KCl and 20 mM K_2HPO_4/KH_2PO_4 (pH 6.7)].

X-Band Electron Paramagnetic Resonance (EPR) Spectroscopy. The continuous wave EPR spectra of the nitroxide spin-labeled C84 and C84-L29Q constructs were collected using a Bruker EMX X-band (9.5 GHz) EPR spectrometer with a standard rectangular TE cavity. The EPR absorption spectra (first derivative) were collected with a microwave power of 5.0 mW, a modulation amplitude of 1.0 G, and a sweep width of 140 G at room temperature. A LabView package (National Instruments) of EPR spectral analysis programs was used to analyze the EPR spectra. Spin labeling yields of the labeled protein were determined from the double integration of the EPR spectrum and compared to a generated standard curve constructed from MTSL standards. Near complete modification of Cys84 was achieved (>95%) for both the C84 and C84-L29Q samples.

NMR Spectroscopy of cTnC-L29Q and C84-L29Q in the Presence and Absence of Ca^{2+}. Prior to NMR, both the cTnC-L29Q and the MTSL-labeled C84-L29Q samples were dialyzed against 0.2 M EDTA in NMR buffer at 4 °C for 2 h to chelate all metal ions. Samples were then thoroughly dialyzed into NMR buffer that was first pretreated by being passed through Chelex 100 resin (Bio-Rad). Glassware and plasticware were also acid washed with 10% nitric acid and rinsed extensively with decalcified Milli-Q water. Dialyzed NMR samples were then supplemented with either 1 mM $CaCl_2$ to obtain the Ca^{2+}-bound state ($+Ca^{2+}$) or 3 mM $MgCl_2$ for the Ca^{2+} free state ($-Ca^{2+}$). NMR samples (550 μL) were prepared at concentrations ranging from 150 to 200 μM. This was necessary to prevent intermolecular PRE effects.[20] Before collection of the NMR data, 10% D_2O and 0.02 mM 2,2-dimethyl-2-silapentane-5-sulfonate (DSS) were added to all samples.

A Bruker Avance 600 MHz spectrometer, equipped with a cryoprobe, was used to collect all NMR data. All experiments were performed at 30 °C. Spectra were processed using Topspin 3.0 (Bruker Inc.). Sparky was used for assignment and analysis of the spectra.[24] For paramagnetic spin-labeled samples, ^{15}N HSQC spectra were first acquired for the C84 and C84-L29Q samples in the $+Ca^{2+}$ and $-Ca^{2+}$ states. Once spectra were obtained for the paramagnetic state, the MTSL spin-label was then reduced to its hydroxylamine equivalent by the addition of a 5-fold molar excess of ascorbic acid (using a 0.5 M stock). This was added directly to the NMR sample. The spectra of each diamagnetic sample were then obtained following a 1 h incubation in the spectrometer at 30 °C. As confirmed by EPR, 1 h at room temperature was adequate for the reduction reaction to go to completion.

Peak assignments of the diamagnetic and paramagnetic spectra for C84 ($+Ca^{2+}$ and $-Ca^{2+}$ states) and C84-L29Q ($+Ca^{2+}$ state) were made using the sequentially assigned ^{15}N HSQC spectrum of cTnC-WT.[13,16] To allow assignment of the C84-L29Q spectra in the absence of Ca^{2+} ($-Ca^{2+}$), a calcium titration experiment was performed with L29Q (180 μM). Following acquisition of the ^{15}N HSQC spectrum for the apo L29Q sample, small aliquots (0.5−2.5 μL) of 12.5 mM $CaCl_2$ were then added to the NMR sample in increments of 0.1 mM up to 1.0 mM $CaCl_2$.

PRE Data Analysis and Distance Determinations. For each amide peak assigned, the ratios of the peak heights measured in the paramagnetic state (I_{para}) and the diamagnetic state (I_{dia}), following the reduction of the spin-label, were used for calculating the PRE (Γ_2) effect caused by the MTSL spin-label (eq 1). The ^1H peak width at half-height was used to obtain the intrinsic transverse relaxation rate R_2 ($R_2 = \pi\Delta\nu_{1/2}$).[19,25] All spectra were recorded with the single evolution time point (t) of 10 ms.

$$\frac{I_{para}}{I_{dia}} = \frac{R_2 \exp(-\Gamma_2 t)}{R_2 + \Gamma_2} \quad (1)$$

The calculated PRE rates (Γ_2) were converted to distances (r) using a modified form of the Solomon−Bloembergen equation:[19,25,26]

$$\Gamma_2 = \frac{K}{r^6}\left[4\tau_c + \frac{3\tau_c}{1 + \omega_H{}^2\tau_c{}^2}\right] \quad (2)$$

where ω_H is the Larmor frequency of the proton, the spin properties of the nitroxide spin-label are described by the constant K (1.23×10^{-32} cm^6 s^{-2}),[19] and τ_c is the correlation time of the electron−proton interaction ($\tau_c = \tau_r^{-1} + \tau_s^{-1}$). The electronic relaxation time of the nitroxide spin-label (τ_s) is relatively slow compared with the protein rotational correlation time (τ_r), so the value of τ_c is effectively equal to the overall protein correlation time.[27] The value used here was 5 ns for intact cTnC, similar to the NMR-derived value of 5 ns for the individual N-domain of cTnC at 30 °C,[28,29] and the cTnC N-domain with the L29Q mutation present.[17] Distances calculated from the PRE effects assume a static structure and provide an apparent distance between the paramagnetic center and a nucleus of interest.

The population and orientation of the spin-label (MTSL) rotamers on C84 were calculated using the MMM (Multiscale Modeling of Macromolecules) Matlab-based open-source modeling toolbox program.[30] Rotamers were calculated for MTSL attached to residue C84 using full length wild-type cTnC (PDB entry 1AJ4)[21] and a L29Q structure of the isolated N-domain of cTnC (PDB entry 2N79).[17] MMM modeling takes into account probe conformation and tether length and increases the accuracy of back-calculated distances (Figure S1).

DOI: 10.1021/acs.biochem.8b01140
Biochemistry 2019, 58, 908−917

RESULTS

Calcium Titration of the L29Q cTnC Construct. To describe the conformational changes in whole cTnC upon Ca^{2+} binding by PRE-NMR, the assignments of both the fully loaded Ca^{2+} state and the state without Ca^{2+} bound to site I are required. The assignments of the C84 and L29Q Ca^{2+}-loaded states were first done using the backbone assignments of cTnC-WT.[16] For assignment of the Ca^{2+} free state of L29Q, Ca^{2+} was titrated into the apo form of this construct. The exchange between all Ca^{2+}-bound and free forms of cTnC was fast on the chemical shift time scale, which allowed peak assignment to be made by tracking changes in the chemical shifts during the course of the titration (Figure 2).

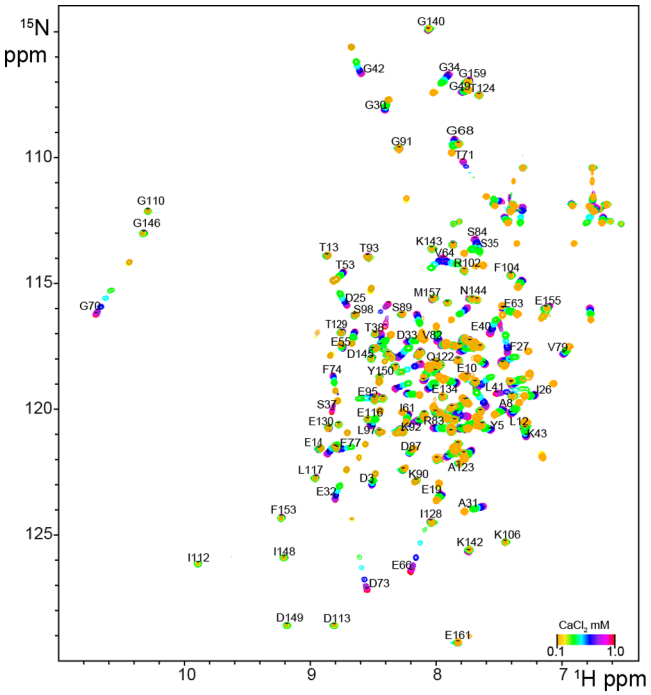

Figure 2. ^{15}N HSQC NMR spectra from the Ca^{2+} titration (0.1 to 1.0 mM) of the apo state of the L29Q cTnC construct (0.18 mM). Peak assignments are shown for the saturated titration end point achieved at 1.0 mM $CaCl_2$. Peak intensity changes were observed with each addition of $CaCl_2$ up to 0.4 mM.

Similar to our previous observations of wild-type cTnC (cTnC-WT),[13] the majority of peaks for residues in the N- and C-domain in the apo state of the L29Q sample were well dispersed (Figure 2). There were approximately 40 poorly dispersed and broadened peaks with HN chemical shifts of 7.5−8.2 ppm observed in the L29Q apo state. These broadened peaks were assigned to C-domain residues in the proximity of Ca^{2+} binding sites III and IV. The intensity of these peaks was observed to increase upon the initial additions of $CaCl_2$, from 0.1 to ~0.4 mM Ca^{2+}. No further changes were then observed beyond the addition of 2 molar equivalents of Ca^{2+}. This suggests that the metal sites in the C-domain are partially disordered in the Ca^{2+} free state and that the exchange of Mg^{2+} with Ca^{2+} for these two sites occurs on a slow time scale, as previously reported.[13,31]

Following saturation of the C-domain sites of the L29Q construct, further additions of Ca^{2+} caused chemical shift changes for the majority of N-domain resonances, in particular for residues in the vicinity of site II (Figure 2). Full occupancy of all cTnC metal binding sites was observed at 3 molar equivalents of $CaCl_2$. Taken together, our titration results are consistent with the significantly higher affinity of Ca^{2+} for the two C-domain metal sites III and IV, compared to that for the single N-domain site II.[14,32]

The assignments of the C84 construct in the $+Ca^{2+}$ and $-Ca^{2+}$ states were used for assigning residues in the C84-L29Q construct that was required for PRE-NMR. The ^{15}N HSQC spectra of the C84-L29Q construct, in the $+Ca^{2+}$ and $-Ca^{2+}$ states, are shown in Figure S2.

The L29Q Mutation Alters the Global Conformation of the Apo Form of cTnC. The effect of the L29Q mutation on the structure of cTnC was observed by comparing the chemical shifts of the C84-L29Q construct of cTnC with the C84 "wild-type" construct. The chemical shift changes ($\Delta\delta$) caused by inclusion of the L29Q mutation in the $+Ca^{2+}$ and $-Ca^{2+}$ states are shown in Figure 3. In the presence of

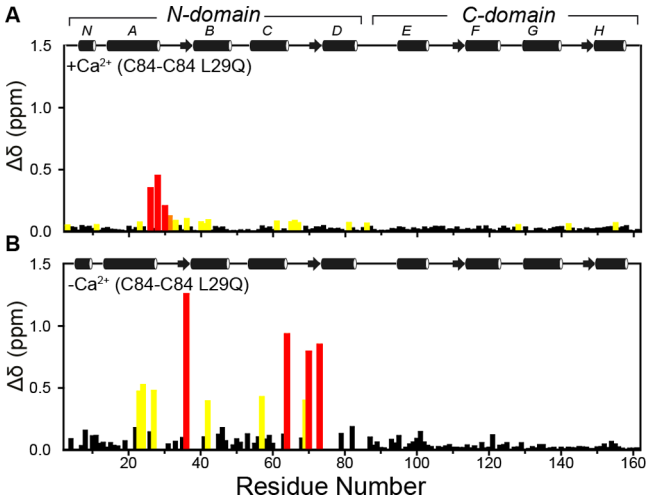

Figure 3. Combined ^1H and ^{15}N chemical shift differences ($\Delta\delta$) between C84 (wild type) and C84-L29Q constructs of cTnC under (A) $+Ca^{2+}$ (holo) and (B) $-Ca^{2+}$ (apo) conditions. Chemical shift differences were calculated via the equation $\Delta\delta = (\Delta\delta_{HN}^2 + 0.17\Delta\delta_N^2)^{1/2}$, where $\Delta\delta_{HN}$ and $\Delta\delta_N$ are the chemical shift changes for amide protons and nitrogens, respectively, in parts per million. Significant chemical shift differences ($\Delta\delta > 1\sigma$, 2σ, and 3σ) are shown as yellow, orange, and red bars, respectively.

saturating Ca^{2+}, the L29Q mutation can be seen to perturb the chemical shifts of residues within the vicinity of residue 29 [from residue 20 to 40, located at the C-terminal end of the A-helix and across the A−B linker region (Figure 3A)]. These residues map to the defunct Ca^{2+} site I. The small localization of these chemical shift perturbations suggests that the L29Q mutation does not have a significant effect on the global fold of the N-domain. In addition, the L29Q mutation did not significantly perturb the chemical shifts of any resonance peaks from the C-domain (residues 94−161). The chemical shift differences we have reported here for the $+Ca^{2+}$ state are similar in distribution and magnitude (<0.5 ppm) to those previously reported for an isolated N-domain construct of cTnC containing the L29Q mutation (and also obtained under saturating Ca^{2+}).[17]

However, upon comparison of the effect of L29Q on whole cTnC in the absence of Ca^{2+}, larger chemical shift perturbations were observed, contrasting with the results

DOI: 10.1021/acs.biochem.8b01140
Biochemistry 2019, 58, 908−917

observed in the presence of Ca^{2+}. In this Ca^{2+} free state, the L29Q mutation was observed to induce significant chemical shift changes across the entire N-domain region (Figure 3B). Residues near the defunct site I and Ca^{2+} binding site II (helices A−C) were most affected. These changes suggest perturbation in the coupling between sites I and II and possible alterations in the positioning of helices in the N-domain. Some minor structural perturbation was also observed for residues across the linker region of cTnC (residues 83−93). An alternate view comparing the chemical shift differences, but instead between the $+Ca^{2+}$ and $-Ca^{2+}$ states for the wild-type and L29Q constructs individually, is presented in Figure S3. However, this supplementary figure should be interpreted with caution as the changes we observed in the apo state due to the presence of L29Q (Figure 3B) are masked by this different comparative view of the data, so any observed chemical shift changes may possibly be attributed to Ca^{2+} binding and not the presence of the mutation.

Increased Mobility of C84-MTSL in the Presence of the L29Q Mutation. The EPR spectra from a nitroxide spin-label attached to the C84 single-cysteine mutant of cTnC were used to help report on any local Ca^{2+}-induced changes within cTnC due to the presence of the L29Q mutation. The C84 residue was selected as it is a native cysteine residue of cTnC and is favorably located in the proximity of the nonfunctional metal binding loop of site I. We have previously shown by PRE-NMR that attachment of a spin-label at C84 is optimal for detecting the Ca^{2+}-induced movement of helices within the N-domain, particularly the A- and B-helices.[13] The continuous wave (CW) EPR spectra, in the presence and absence of the L29Q mutation, and in response to Ca^{2+} binding, are shown in Figure 4. All spectra are normalized to the same number of spins.

The EPR spectra for the C84 and C84-L29Q mutant constructs both showed immobile and mobile components. Similar to findings from others, we observed a higher mobility for the spin-label in the presence of Ca^{2+} for the wild-type construct that can be attributed to a decrease in the level of tertiary interactions in the N-domain, likely due to movement of the B- and C-helices.[33] However, in the presence of the L29Q mutation, the spectra showed that the spin-label at C84 was more mobile than that in the corresponding spectrum observed for the wild-type C84 construct (Figure 4A). This was true in the Ca^{2+}-bound and free states, with both spectra for the HCM mutation appearing to be similar to each other.

PRE Effects in $+Ca^{2+}$ and $-Ca^{2+}$ NMR Spectra of C84-L29Q. The ^{15}N HSQC spectra of the paramagnetic and diamagnetic samples for the Ca^{2+}-bound and free states of the C84-L29Q spin-labeled cTnC construct are shown in Figure S2. As before, assignments were made using previously available chemical shift values for cTnC[13,16] and aided by the Ca^{2+} titration experiments (Figure 2). Representative sections from the superimposed paramagnetic and diamagnetic spectra for the $+Ca^{2+}$ and $-Ca^{2+}$ states of C84-L29Q are also shown in Figure 5A. To ensure both C-domain metal binding sites (sites III and IV) were occupied, 3 mM $MgCl_2$ was included in the Ca^{2+} free NMR buffer. The complete binding of Ca^{2+} to site II in the N-domain was then achieved by the addition of 5 mM $CaCl_2$. For the $+Ca^{2+}$ and $-Ca^{2+}$ samples, at least 85% of the N-domain resonances could be assigned in the PRE-NMR spectra.

Incorporation of the MTSL paramagnetic species at C84 resulted in distance-dependent line broadening effects on

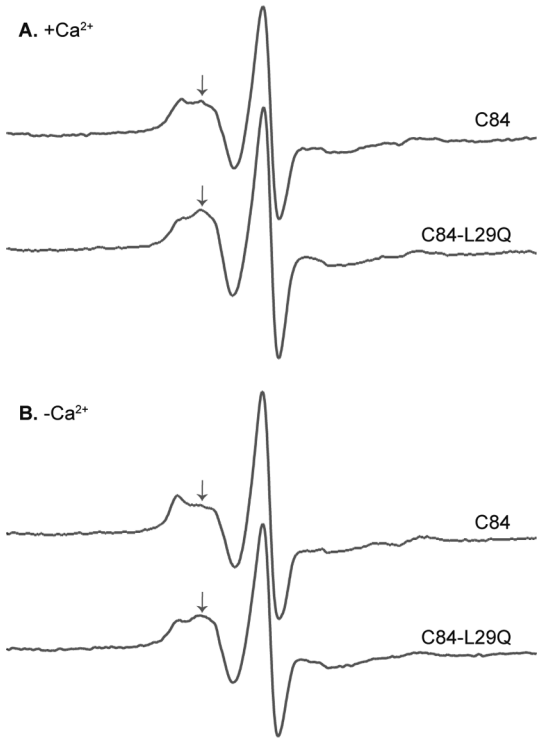

Figure 4. CW-EPR spectra of the spin-labeled wild-type C84 and C84-L29Q constructs of cTnC obtained at 25 °C in 30% (w/v) sucrose in the (A) holo (5 mM $CaCl_2$) and (B) apo (3 mM $MgCl_2$) states. The arrow indicates the mobile component. An increase in mobility of the MTSL spin-label at C84 is observed for both $+Ca^{2+}$ and Mg^{2+} states in the presence of the L29Q mutation. The scan width is 140 G.

nearby resonances (Figure 5A). The magnitude of the relaxation enhancement (Γ_2) effect, due to the presence of MTSL, was then obtained from the ratio of the paramagnetic and diamagnetic peak intensities for all detected resonances. A comparison of all assigned peak intensity ratios for the C84 "wild-type" (dark blue) and C84-L29Q (light blue) constructs is shown for the $+Ca^{2+}$ (Figure 5B) and $-Ca^{2+}$ (Figure 5C) states. For residues close in space to the spin-label (<10 Å), the strong PRE effect resulted in the broadening of peaks beyond detection in the paramagnetic spectrum. To allow differentiation from unassigned peaks, residues broadened beyond detection are represented in the intensity ratio plots with values of 0.05 as Γ_2 values could not be accurately calculated for these assignments.

Mapping of peak intensity ratios onto the cTnC structure (PDB entry 1AJ4[21]) revealed the effects of Ca^{2+} binding in the presence of the L29Q mutation (Figure 5B,C, right panels). The strongest PRE broadening effects ($I_{para}/I_{dia} \ll 0.1$, colored red) are found clustered in regions close to the spin-label and across the B- and C-helices in the N-domain for both Ca^{2+} states. Residues that were not affected by the spin-label ($I_{para}/I_{dia} \sim 1$, colored dark blue) represented distances from the spin-label of >25 Å. Although the intensity mapping due to the presence of the spin-label at C84 is mostly confined to the N-domain of TnC, as expected, some broadening of residues in the C-domain was also detected for both states. This implies significant interdomain flexibility for the cardiac isoform, as previously observed.[16]

While the mapped PRE effects appear to be quite similar for the C84 and C84-L29Q constructs in the presence of Ca^{2+}

DOI: 10.1021/acs.biochem.8b01140
Biochemistry 2019, 58, 908−917

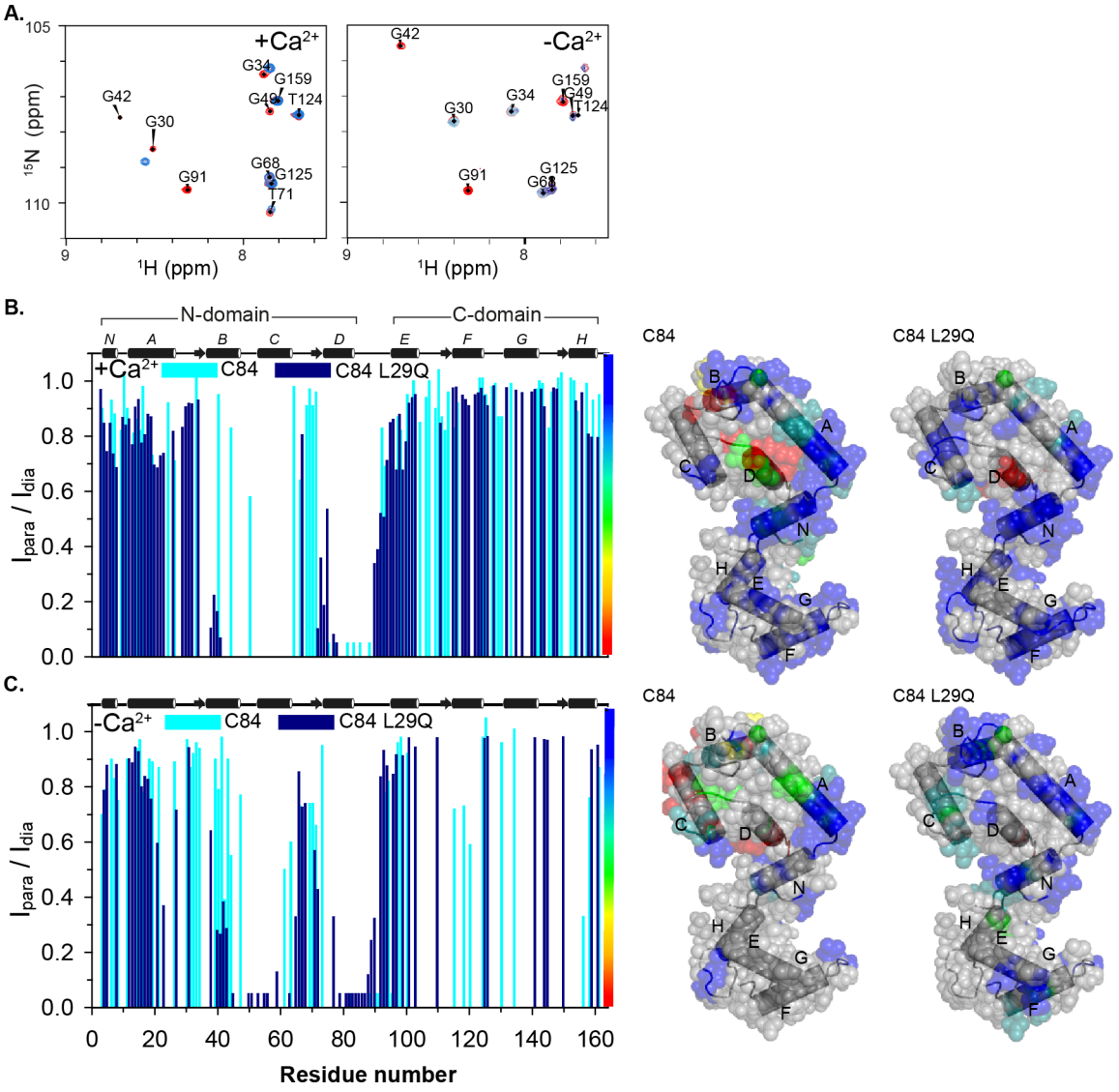

Figure 5. (A) Representative sections of the ^{15}N HSQC paramagnetic (red) spectrum superimposed onto the diamagnetic (blue) spectrum of the C84-L29Q cTnC constructs in the presence (left) and absence (right) of Ca^{2+}. Peak intensity ratios (I_{para}/I_{dia}) are shown as bars for all assigned data for the C84 "wild-type" (dark blue) and C84-L29Q (light blue) cTnC constructs in the (B) presence and (C) absence of Ca^{2+}. Peaks that are broadened beyond detection in the paramagnetic state are shown as 0.05. Peaks where residues could not be assigned with confidence are not included. The peak intensity ratios are further mapped onto the structure of cTnC (PDB entry 1AJ4,[21] right) according to the color scale bar.

(Figure 5B), there are a few notable differences. Helix A in the N-domain is largely more affected by the spin-label in the presence of the L29Q mutation, with red shading observed across this helix. Some dampening of PRE effects across the C- and D-helices is also seen in the presence of the L29Q mutation. PRE effects in the C-domain are, however, similar across the wild-type and HCM constructs.

In the absence of Ca^{2+}, the presence of the L29Q mutation increases the magnitude of the PRE effects for residues across the N- and D-helices of the N-domain. These mapped PRE effects suggest a movement of these two helices toward C84 in the presence of L29Q. To further describe the magnitude of the Ca^{2+}-induced changes observed due to the presence of the HCM mutation, the peak intensity ratios from Figure 5 were then used to calculate the distances between assignable residues and the C84 spin-label.

The L29Q Mutation "Opens" the Regulatory Domain of cTnC. As revealed through the mapping of the para-magnetic broadening effects, the placement of the spin-label at C84 in the N-domain provides a unique viewpoint for analyzing the Ca^{2+}-induced conformational changes due to the presence of the L29Q mutation. The magnitudes of these conformational changes for the $+Ca^{2+}$ and $-Ca^{2+}$ states were calculated from the PRE rates (Γ_2), as shown in Figure S4 and listed in Tables S1 and S2. The PRE distance profiles for the wild-type and L29Q cTnC constructs labeled at C84 are compared in the $+Ca^{2+}$ (Figure 6A) and $-Ca^{2+}$ states (Figure 6B). Only residues that could be assigned in the C84 and C84-L29Q constructs can be used to describe, with confidence, structural differences arising from the L29Q mutation. The paired measurements from the distance plots are further mapped onto cTnC (Figure 6C). Paired measurements, where the distance (r) is longer in the presence of the L29Q mutation than in the wild-type construct ($r_{C84\text{-}L29Q} > r_{C84}$), are colored red. For paired measurements where the distance is shorter ($r_{C84\text{-}L29Q} < r_{C84}$), these residues are colored blue.

DOI: 10.1021/acs.biochem.8b01140
Biochemistry 2019, 58, 908−917

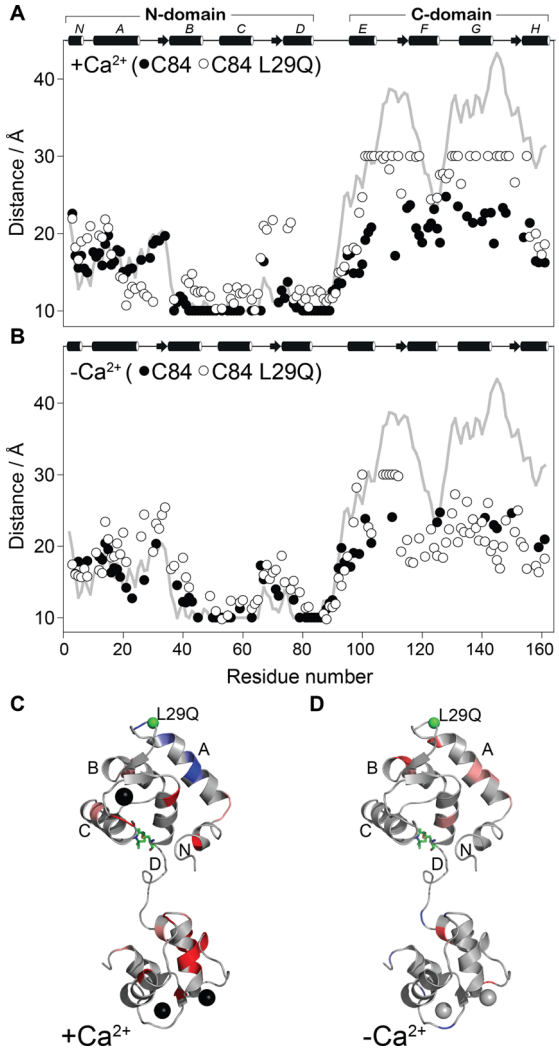

Figure 6. Comparison of PRE distances measured between cTnC residues and MTSL positioned on C84 for wild-type cTnC[13] (●) and cTnC-L29Q (○) in the (A) presence and (B) absence of Ca^{2+}. Measured PRE distances are compared with distances obtained from the coordinates of the cTnC structure 1AJ4[21] (gray lines). Residues broadened beyond detection in the paramagnetic spectrum, and all calculated distances of <10 Å, are plotted at 10 Å. The direction and the magnitude of the movement of structural elements of cTnC, suggested by the change in distances due to the presence of the L29Q mutation in the (C) presence and (D) absence of Ca^{2+}, are color mapped onto the structure of TnC (1AJ4). Dark blue and red indicate substantial movement (>4 Å) toward and away from the C84-MTSL site, respectively. Smaller changes in distance (3−4 Å) are colored light blue and pink. The distance changes are consistent with an opening of the N-domain and a change in dynamics of the central linker that alters the relative positioning between the two domains of cTnC. Bound Ca^{2+} is represented by black spheres, and Mg^{2+} by gray spheres. The location of the L29Q mutation is indicated by the green sphere.

In the $+Ca^{2+}$ state, the measured PRE distances in the presence of L29Q did not correlate as well as those of the wild-type C84 construct with the distances obtained from the coordinates of the cTnC structure 1AJ4 (gray lines, Figure 6A). From the mapping of these PRE-NMR distances onto the structure of cTnC (Figure 6C), the presence of the L29Q mutation caused a small movement of helix N away from the spin-label at C84 and a tilting of helix A at the C-terminus toward C84. Additionally, metal binding site I moved toward the spin-label in the presence of the L29Q mutation. The C-terminal end of helix B was also displaced farther from the spin-label as well as Ca^{2+} binding site II. Together, an overall "opening" of the N-domain can be described from these movements.

Interestingly, the distance profiles and mapping also indicated a significant movement of the C-domain away from the N-domain in the presence of the L29Q mutation. These interdomain PRE effects suggest that in the presence of Ca^{2+}, the L29Q mutation results in a change in the dynamics within the central linker region and thus the orientations between the two domains of TnC. A more complete description of the change in the interdomain orientation would require the placement of additional probe sites on cTnC, such as at residue C12 or C35.[16]

For the Ca^{2+} free state, an opposite shift of helix A away from the spin-label was detected in the presence of the L29Q mutation. There was also a slight movement of residues near metal binding site I and the N-terminal end of helix B farther from the spin-label. Additionally, helix D and residues near site II also appeared to move farther from the spin-label in the presence of the L29Q mutation. However, as many residues across this region were within the 10 Å radius of the unpaired electron, and thus broadened beyond detection, another paramagnetic label site is required to better view and quantitate the magnitude of movement of residues in the D-helix. Lastly, and in contrast to the $+Ca^{2+}$ state, residues in the C-domain were not significantly affected by the presence of the L29Q mutation, suggesting that the relative positioning of the N- and C-domains is not as noticeably affected by the L29Q mutation in the absence of Ca^{2+}. Overall, our observed changes in PRE-NMR distances show that the L29Q construct results in a shift in the structure of the N-domain of TnC toward a more "open" conformation compared to the C84 "wild-type" protein. This is observed in the absence and presence of Ca^{2+}.

DISCUSSION

The cardiac isoform of TnC is a primary target for the design and development of "calcium-sensitizer" drugs that can be used to treat heart failure and other cardiac disorders. Several drugs, including bepridil, anapoe, levosimendan, and trifluoperazine, have all been shown to alter the "closed-to-open" equilibrium of the regulatory N-domain of cTnC.[34] The potential application of such drugs, as well as further rational drug design and development of new drugs to treat heart disease where Ca^{2+} handling by TnC is impaired, requires a better understanding of the structural mechanism that is compromised. We have shown previously that the PRE-NMR approach is suitable for rapidly characterizing structural perturbations in cardiac TnC arising from disease-causing mutations, such as HCM.[13] This is important as the majority of HCM mutations in TnC are associated with impaired Ca^{2+} handling. Furthermore, and as highlighted by a recent molecular dynamics study, the majority of disease-causing mutations found in TnC have a more pronounced effect on the dynamics of the protein than its local static structure.[35] Therefore, in this study, we wanted to characterize the structural effects of the L29Q mutation in whole cTnC and, in response to Ca^{2+} binding, to better understand its pathogenesis and to support future drug development strategies.

The L29Q mutation itself was also an important focus for this study as several conflicting reports currently exist in the

DOI: 10.1021/acs.biochem.8b01140
Biochemistry 2019, 58, 908−917

literature regarding the structural and functional effects arising from this HCM mutation.[10,11,14,15,17] Conventionally, NMR chemical shift perturbations are typically a first strategy that is used to identify regions in a protein that may differ structurally when a mutation is introduced or when a ligand interacts with its target. On the other hand, we have shown through this and other studies[13,16] that PRE-NMR may develop as a superior approach for assessing global structural and directional changes across protein domains and even whole proteins. The PRE approach is also especially powerful when NOE interconnectivity data are sparse, as is the case for the cardiac TnC isoform. Typically, only very small numbers of interhelical NOEs within individual domains of cTnC have been observed, and no substantial NOEs between the two domains of cardiac TnC have been reported. The rapid structural characterization of cTnC can therefore be achieved through the numerous long-range distance constraints that are possible from the strategic placement of a single spin-label.

However, in this study, we first used conventional NMR chemical shift difference analysis to reveal the presence of structural changes in the whole cTnC protein molecule in response to the presence of the L29Q HCM mutation and also Ca^{2+} binding. In agreement with an earlier study of the L29Q mutation performed on the isolated N-domain of cTnC,[17] our chemical shift analysis results showed that the overall structure of cTnC was essentially unperturbed by the presence of the L29Q HCM mutation in the $+Ca^{2+}$ state. Only small local changes close to the site of the mutation were observed.

Our study has then extended this previous work[17] on the Ca^{2+}-saturated N-domain of cTnC by characterizing the effects of Ca^{2+} binding in whole cTnC using PRE-NMR. Our PRE-NMR long-range distances showed a distinct outward movement of the N-domain helices consistent with a shift toward a more "open" conformation in the presence of the L29Q mutation. This was observed for the bound and free Ca^{2+} forms of cTnC. The increase in the mobility of the spin-label attached to C84, as detected by EPR, supported this movement where the L29Q mutation destabilizes the hydrophobic core of the N-domain. Previously reported NMR relaxation measurements also reported an increase in the local dynamics for residue 29 when the L29Q mutation was present in the backbone.[17] Our findings also agree with an earlier computational study that predicted that the L29Q mutation shifts the structure of the N-lobe of cTnC toward a more "open" state.[36] Naturally, a shift in the equilibrium toward a more "open" N-domain population could potentially prime the regulatory domain of cTnC to more efficiently bind with TnI via conformational selection. This mechanism is in agreement with the reported increase in Ca^{2+} sensitivity for this HCM mutation.[10,36]

Interestingly, the L29Q mutation has also been suggested in the literature to be capable of reviving the defunct Ca^{2+} metal binding site I and in doing so would shift the conformation of the N-domain toward an open conformation.[37] Although we detected a more open conformation for the N-domain in the presence of the mutation, we did not see evidence of binding of Ca^{2+} to site I for this mutant from the Ca^{2+} titration experiments performed in the study presented here.

There is always a caveat, in particular with regard to the use of PRE-derived distance measurements to describe conformational change, when a flexible spin-label side chain is used. However, our modeling of the spin-label orientation on residue C84,[30] and our previous work,[13] showed that the C84 site is in a restricted position in the TnC structure, so packing requirements appear to stabilize specific rotamers of the spin-label side chain. The C84 residue is therefore an ideal site for placement of a spin-label to estimate backbone movements due to the presence of a mutation, particularly across the N-domain of TnC. However, we still cannot rule out minor contributions from side chain rearrangements of the spin-label on C84 that might affect the spin-label rotamers.

In addition to the structural changes that we observed across the N-domain, our PRE-NMR results in the presence of Ca^{2+}, using the full length L29Q cTnC construct, also revealed other interesting changes in the region of the central linker. The presence of the HCM mutation appeared to modify the preferred relative orientation between the two lobes of TnC. Changes in orientation between the two lobes and the inferred increase in Ca^{2+} sensitivity with the N-domain in a more open conformation together may provide an explanation as to why the L29Q mutation can abolish the effect of force-generating cross-bridges on the Ca^{2+} sensitivity of the structural changes.[17] However, further comment on the flexibility of the central linker, or "hinge" region, should not be made from the inclusion of a paramagnetic species at only a single label site.[16]

Although examining Ca^{2+}-induced structural changes was the focus of this study, the L29 residue has also been suggested to alter the interaction of the N-domain of cardiac TnC with the N-terminal region of troponin I (TnI). In cardiac muscle, the TnI subunit has a cardiac-specific N-terminal extension region of 31 residues that possesses two PKA phosphorylation sites (serine 23 and 24).[38] This region of TnI is thought to interact with the N-domain of cTnC, and specifically residue L29, in a phosphorylation-dependent manner.[11,37,39] The angle between the A- and B-helices of the N-lobe of cTnC is proposed to be sensitive to the phosphorylated state of the cTnI N-terminal extension. Interestingly, a computational study has predicted that the presence of the L29Q mutation would render this region insensitive to phosphorylation.[36] However, a recent NMR study of the isolated cTnC N-domain did not detect any changes in the A−B or C−D interhelical angles using a pseudophosphorylated peptide mimic of the cTnI N-terminal extension in the presence of the mutation.[40] Possibly the influence of Ca^{2+}, namely through a comparison of both Ca^{2+}-bound and free states upon phosphorylation, may reveal subtle changes in the N-domain, as per this proposed interaction. Further studies are therefore warranted to better understand the mechanism of regulation of contraction of the cardiac isoform by phosphorylation and the residues involved in this interaction. Our rapid single-probe PRE-NMR screening approach could be applied in a binary troponin state using a pseudophosphorylated TnI construct to examine this hypothesis.[41]

■ ASSOCIATED CONTENT

Supporting Information

The Supporting Information is available free of charge on the ACS Publications website at DOI: 10.1021/acs.biochem.8b01140.

MMM modeling of spin-label (MTSL) rotamers (Figure S1), complete ^{15}N HSQC spectra of the C84-MTSL spin-labeled L29Q cTnC construct in the presence and absence of Ca^{2+} (Figure S2), chemical shift differences between $+Ca^{2+}$ and $-Ca^{2+}$ states for C84 and C84-

DOI: 10.1021/acs.biochem.8b01140
Biochemistry 2019, 58, 908−917

L29Q, respectively (Figure S3), experimental PRE profiles (Γ_2) are compared for C84-MTSL spin-labeled cTnC-WT and cTnC-L29Q in the presence and absence of Ca^{2+} (Figure S4), changes in PRE-NMR distances in the presence and absence of Ca^{2+} from the spin-label at C84 to residues detectable in the cTnC-WT and cTnC-L29Q constructs (Tables S1 and S2) (PDF)

AUTHOR INFORMATION

Corresponding Author

*Department of Molecular Sciences, Macquarie University, Sydney, New South Wales 2109, Australia. Telephone: 61 2 9850 8294. E-mail: Louise.Brown@mq.edu.au.

ORCID

Louise J. Brown: 0000-0001-8592-2431

Author Contributions

All the experiments were performed by P.R.P. N.M.C. and E.K. helped in analyzing the data. The paper was written by P.R.P., N.M.C., and L.J.B.

Funding

P.R.P. was supported by a Macquarie University Research Excellence Postgraduate scholarship. This study was also supported by a Macquarie University Research Development Grant to L.J.B.

Notes

The authors declare no competing financial interest.

ABBREVIATIONS

cTn, cardiac troponin; HCM, hypertrophic cardiomyopathy; DTT, dithiothreitol; SDSL, site-directed spin labeling; EPR, electron paramagnetic resonance; PRE-NMR, paramagnetic relaxation enhancement nuclear magnetic resonance; HSQC, heteronuclear single-quantum coherence.

REFERENCES

(1) Farah, C., and Reinach, F. (1995) The troponin complex and regulation of muscle contraction. *FASEB J. 9*, 755−767.

(2) Gillis, T. E., Marshall, C. R., and Tibbits, G. F. (2007) Functional and evolutionary relationships of troponin C. *Physiol. Genomics 32*, 16−27.

(3) Kobayashi, T., and Solaro, R. J. (2005) Calcium, thin filaments, and the integrative biology of cardiac contractility. *Annu. Rev. Physiol. 67*, 39−67.

(4) Gordon, A., Homsher, E., and Regnier, M. (2000) Regulation of contraction in striated muscle. *Physiol. Rev. 80*, 853−924.

(5) Willott, R. H., Gomes, A. V., Chang, A. N., Parvatiyar, M. S., Pinto, J. R., and Potter, J. D. (2010) Mutations in Troponin that cause HCM, DCM AND RCM: what can we learn about thin filament function? *J. Mol. Cell. Cardiol. 48*, 882−892.

(6) Maron, B. J. (2002) Hypertrophic cardiomyopathy: a systematic review. *JAMA, J. Am. Med. Assoc. 287*, 1308−1320.

(7) Lu, Q.-W., Wu, X.-Y., and Morimoto, S. (2013) Inherited cardiomyopathies caused by troponin mutations. *J. Geriatr. Cardiol. 10*, 91−101.

(8) Landstrom, A. P., Parvatiyar, M. S., Pinto, J. R., Marquardt, M. L., Bos, J. M., Tester, D. J., Ommen, S. R., Potter, J. D., and Ackerman, M. J. (2008) Molecular and functional characterization of novel hypertrophic cardiomyopathy susceptibility mutations in TNNC1-encoded troponin C. *J. Mol. Cell. Cardiol. 45*, 281−288.

(9) Hoffmann, B., Schmidt-Traub, H., Perrot, A., Osterziel, K. J., and Gessner, R. (2001) First mutation in cardiac troponin C, L29Q, in a patient with hypertrophic cardiomyopathy. *Hum. Mutat. 17*, 524−524.

(10) Liang, B., Chung, F., Qu, Y., Pavlov, D., Gillis, T. E., Tikunova, S. B., Davis, J. P., and Tibbits, G. F. (2008) Familial hypertrophic cardiomyopathy-related cardiac troponin C mutation L29Q affects Ca^{2+} binding and myofilament contractility. *Physiol. Genomics 33*, 257−266.

(11) Schmidtmann, A., Lindow, C., Villard, S., Heuser, A., Mügge, A., Geßner, R., Granier, C., and Jaquet, K. (2005) Cardiac troponin C-L29Q, related to hypertrophic cardiomyopathy, hinders the transduction of the protein kinase A dependent phosphorylation signal from cardiac troponin I to C. *FEBS J. 272*, 6087−6097.

(12) Genchev, G. Z., Kobayashi, T., and Lu, H. (2013) Calcium induced regulation of skeletal troponin—computational insights from molecular dynamics simulations. *PLoS One 8*, No. e58313.

(13) Cordina, N. M., Liew, C. K., Gell, D. A., Fajer, P. G., Mackay, J. P., and Brown, L. J. (2013) Effects of calcium binding and the hypertrophic cardiomyopathy A8V mutation on the dynamic equilibrium between closed and open conformations of the regulatory N-domain of isolated cardiac troponin C. *Biochemistry 52*, 1950−1962.

(14) Dweck, D., Hus, N., and Potter, J. D. (2008) Challenging current paradigms related to cardiomyopathies. Are changes in the Ca^{2+} sensitivity of myofilaments containing cardiac troponin C mutations (G159D and L29Q) good predictors of the phenotypic outcomes? *J. Biol. Chem. 283*, 33119−33128.

(15) Neulen, A., Stehle, R., and Pfitzer, G. (2009) The cardiac troponin C mutation Leu29Gln found in a patient with hypertrophic cardiomyopathy does not alter contractile parameters in skinned murine myocardium. *Basic Res. Cardiol. 104*, 751−60.

(16) Cordina, N. M., Liew, C. K., Gell, D. A., Fajer, P. G., Mackay, J. P., and Brown, L. J. (2012) Interdomain orientation of cardiac troponin C characterized by paramagnetic relaxation enhancement NMR reveals a compact state. *Protein Sci. 21*, 1376−1387.

(17) Robertson, I. M., Sevrieva, I., Li, M. X., Irving, M., Sun, Y.-B., and Sykes, B. D. (2015) The structural and functional effects of the familial hypertrophic cardiomyopathy-linked cardiac troponin C mutation, L29Q. *J. Mol. Cell. Cardiol. 87*, 257−269.

(18) Clore, G. M., and Iwahara, J. (2009) Theory, practice, and applications of paramagnetic relaxation enhancement for the characterization of transient low-population states of biological macromolecules and their complexes. *Chem. Rev. 109*, 4108−4139.

(19) Battiste, J. L., and Wagner, G. (2000) Utilization of site-directed spin labeling and high-resolution heteronuclear nuclear magnetic resonance for global fold determination of large proteins with limited nuclear overhauser effect data. *Biochemistry 39*, 5355−5365.

(20) Donaldson, L. W., Skrynnikov, N. R., Choy, W.-Y., Muhandiram, D. R., Sarkar, B., Forman-Kay, J. D., and Kay, L. E. (2001) Structural characterization of proteins with an attached ATCUN motif by paramagnetic relaxation enhancement NMR spectroscopy. *J. Am. Chem. Soc. 123*, 9843−9847.

(21) Sia, S. K., Li, M. X., Spyracopoulos, L., Gagné, S. M., Liu, W., Putkey, J. A., and Sykes, B. D. (1997) Structure of cardiac muscle troponin C unexpectedly reveals a closed regulatory domain. *J. Biol. Chem. 272*, 18216−18221.

(22) Brown, L. J., Sale, K. L., Hills, R., Rouviere, C., Song, L., Zhang, X., and Fajer, P. G. (2002) Structure of the inhibitory region of troponin by site directed spin labeling electron paramagnetic resonance. *Proc. Natl. Acad. Sci. U. S. A. 99*, 12765−12770.

(23) Sambrook, J., Fritsch, E. F., and Maniatis, T. (1989) *Molecular cloning*, Vol. 2, Cold Spring Harbor Laboratory Press, Plainview, NY.

(24) Goddard, T., and Kneller, D. (2004) *SPARKY 3*, version 15, University of California, San Francisco.

(25) Volkov, A. N., Worrall, J. A., Holtzmann, E., and Ubbink, M. (2006) Solution structure and dynamics of the complex between cytochrome c and cytochrome c peroxidase determined by paramagnetic NMR. *Proc. Natl. Acad. Sci. U. S. A. 103*, 18945−18950.

(26) Liang, B., Bushweller, J. H., and Tamm, L. K. (2006) Site-directed parallel spin-labeling and paramagnetic relaxation enhancement in structure determination of membrane proteins by solution NMR spectroscopy. *J. Am. Chem. Soc. 128*, 4389−4397.

DOI: 10.1021/acs.biochem.8b01140
Biochemistry 2019, 58, 908−917

(27) Iwahara, J., Schwieters, C. D., and Clore, G. M. (2004) Ensemble approach for NMR structure refinement against ^{1}H paramagnetic relaxation enhancement data arising from a flexible paramagnetic group attached to a macromolecule. *J. Am. Chem. Soc. 126*, 5879−5896.
(28) Spyracopoulos, L., Gagné, S. M., Li, M. X., and Sykes, B. D. (1998) Dynamics and thermodynamics of the regulatory domain of human cardiac troponin C in the apo-and calcium-saturated states. *Biochemistry 37*, 18032−18044.
(29) Spyracopoulos, L., Lavigne, P., Crump, M. P., Gagné, S. M., Kay, C. M., and Sykes, B. D. (2001) Temperature dependence of dynamics and thermodynamics of the regulatory domain of human cardiac troponin C. *Biochemistry 40*, 12541−12551.
(30) Jeschke, G. (2018) MMM: A toolbox for integrative structure modeling. *Protein Sci. 27*, 76−85.
(31) Finley, N., Dvoretsky, A., and Rosevear, P. R. (2000) Magnesium−calcium exchange in cardiac troponin C bound to cardiac troponin I. *J. Mol. Cell. Cardiol. 32*, 1439−1446.
(32) Holroyde, M., Robertson, S., Johnson, J., Solaro, R. J., and Potter, J. (1980) The calcium and magnesium binding sites on cardiac troponin and their role in the regulation of myofibrillar adenosine triphosphatase. *J. Biol. Chem. 255*, 11688−11693.
(33) Ueki, S., Nakamura, M., Komori, T., and Arata, T. (2005) Site-directed spin labeling electron paramagnetic resonance study of the calcium-induced structural transition in the N-domain of human cardiac troponin C complexed with troponin I. *Biochemistry 44*, 411−416.
(34) Li, M. X., Robertson, I. M., and Sykes, B. D. (2008) Interaction of cardiac troponin with cardiotonic drugs: a structural perspective. *Biochem. Biophys. Res. Commun. 369*, 88−99.
(35) Stevens, C. M., Rayani, K., Singh, G., Lotfalisalmasi, B., Tieleman, D. P., and Tibbits, G. F. (2017) Changes in the dynamics of the cardiac troponin C molecule explain the effects of Ca^{2+}-sensitizing mutations. *J. Biol. Chem. 292*, 11915−11926.
(36) Li, A. Y., Stevens, C. M., Liang, B., Rayani, K., Little, S., Davis, J., and Tibbits, G. F. (2013) Familial hypertrophic cardiomyopathy related cardiac troponin C L29Q mutation alters length-dependent activation and functional effects of phosphomimetic troponin I. *PLoS One 8*, No. e79363.
(37) Baryshnikova, O. K., Li, M. X., and Sykes, B. D. (2008) Modulation of cardiac troponin C function by the cardiac-specific N-terminus of troponin I: influence of PKA phosphorylation and involvement in cardiomyopathies. *J. Mol. Biol. 375*, 735−751.
(38) Solaro, R. J., and van der Velden, J. (2010) Why does troponin I have so many phosphorylation sites? Fact and fancy. *J. Mol. Cell. Cardiol. 48*, 810−816.
(39) Dong, W.-J., Xing, J., Ouyang, Y., An, J., and Cheung, H. C. (2008) Structural kinetics of cardiac troponin C mutants linked to familial hypertrophic and dilated cardiomyopathy in troponin complexes. *J. Biol. Chem. 283*, 3424−3432.
(40) Hwang, P. M., Cai, F., Pineda-Sanabria, S. E., Corson, D. C., and Sykes, B. D. (2014) The cardiac-specific N-terminal region of troponin I positions the regulatory domain of troponin C. *Proc. Natl. Acad. Sci. U. S. A. 111*, 14412−14417.
(41) Cordina, N. M., Liew, C. K., Potluri, P. R., Curmi, P. M., Fajer, P. G., Logan, T. M., Mackay, J. P., and Brown, L. J. (2014) Ca^{2+}-Induced PRE-NMR Changes in the Troponin Complex Reveal the Possessive Nature of the Cardiac Isoform for Its Regulatory Switch. *PLoS One 9*, No. e112976.

DOI: 10.1021/acs.biochem.8b01140
Biochemistry 2019, 58, 908−917

Supporting Information

Characterization of the L29Q hypertrophic cardiomyopathy mutation in cardiac Troponin C by Paramagnetic Relaxation Enhancement NMR

Phani R. Potluri[1], Nicole M. Cordina[1], Ehsan Kachooei[1] and Louise J. Brown[1]

1. Department of Molecular Sciences, Macquarie University, Sydney, NSW, 2109, Australia.

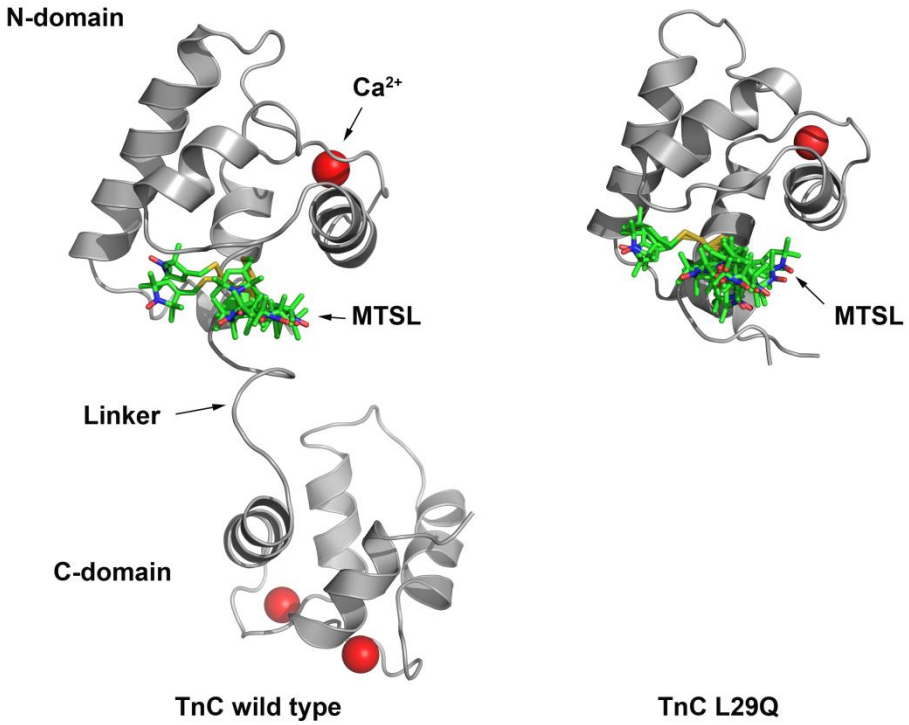

Figure S1. Population and orientation of spin label (MTSL) rotamers. Calculated rotamers for attached MTSL spin label to residue cTnC84 of Wild-type (left; PDB ID:1AJ4) and L29Q mutant (right; PDB ID:2N79) using MMM program (Jeschke, G., *MMM: A toolbox for integrative structure modeling.* Protein Sci, 2018. 27: p. 76-85.) In both structures, MTSL rotamers are populated in a similar cone and orientation with respect to the cTnC backbone.

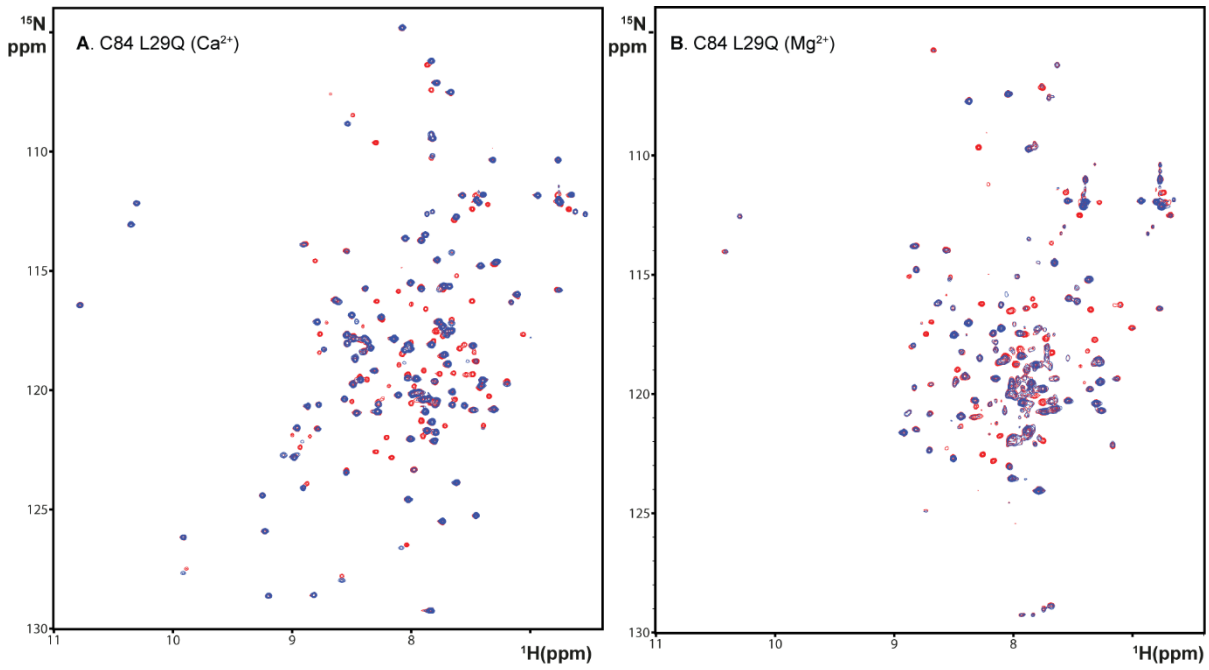

Figure S2. Complete ^{15}N-HSQC spectra of the paramagnetic (*red*) superimposed on diamagnetic (*blue*) of the C84-MTSL spin labeled L29Q cTnC construct in **(A)** the presence of Ca^{2+} and **(B)** absence of Ca^{2+}. A few peaks (<5%) showed minor shifts (<<0.5 ppm) between paramagnetic and diamagnetic states. This is observed for residues that are in conformational exchange (Ca^{2+}-binding loop residues).

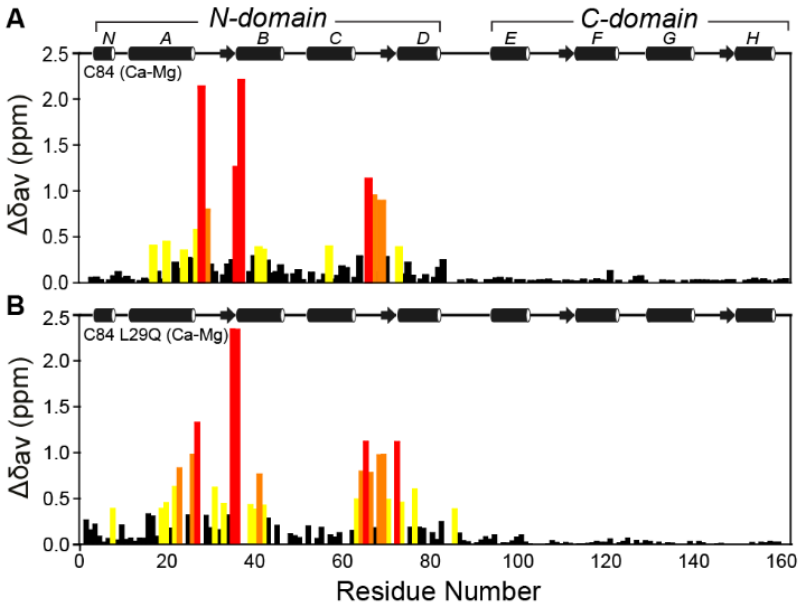

Figure S3. Chemical shift differences between $+Ca^{2+}$ and $-Ca^{2+}$ states for (A) C84 'wildtype' and (B) C84-L29Q. Chemical shift differences were calculated from [$\Delta\delta av = (\Delta\delta_{HN}^2+0.17\Delta\delta_N^2)^{1/2}$], where $\Delta\delta_{HN}$ and $\Delta\delta_N$ are the chemical shift changes for amide protons and nitrogens, respectively, in parts per million. Significant chemical shift differences ($\Delta\delta av$ > 1σ, 2σ and 3σ) are highlighted as yellow, orange and red bars, respectively.

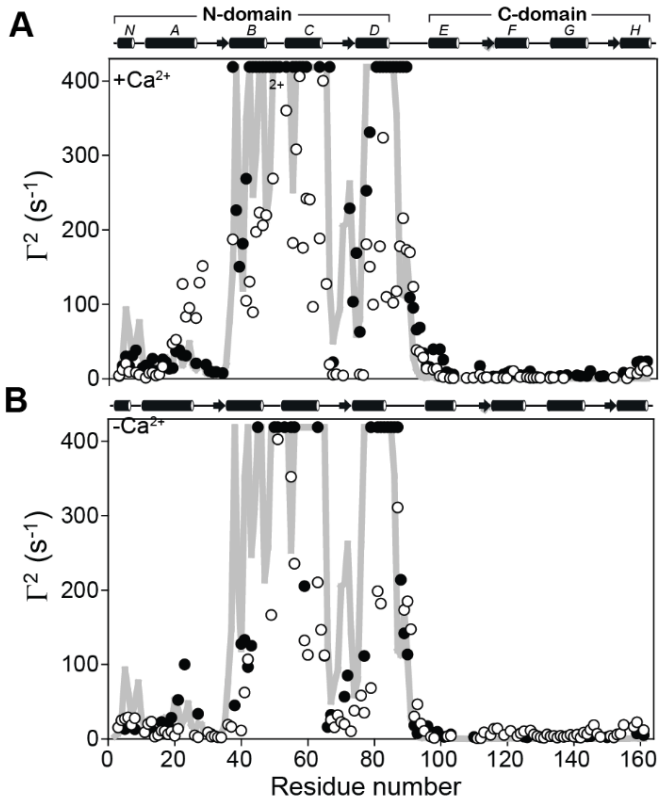

Figure S4. Experimental PRE profiles (Γ_2) are compared for C84-MTSL spin labeled (indicated by the triangle) for cTnC-WT (●) and L29Q cTnC construct (○) in (A) the presence of Ca^{2+} and (B) the absence of Ca^{2+}. For comparison, Γ_2 values were back-calculated from the coordinates of the cTnC structure PDB 1AJ4 and are shown as grey lines.

Table S1: The change (Δ) in PRE-NMR distances (Å) in the *presence* of Ca^{2+} for spin label at C84 to residues detectable in both the cTnC-WT and L29Q cTnC constructs. Distances that were broadened beyond detection are assigned as 10.0 Å.

Residue	cTnC-WT	L29Q	Distance Δ	Location
3	22.56	21.91	0.65	N-helix
4	17.09	18.17	-1.08	N-helix
5	15.54	16.59	-1.04	N-helix
6	17.10	18.95	-1.85	N-helix
8	14.93	19.37	-4.44	N-helix
12	17.44	19.73	-2.29	N-helix
13	15.84	19.47	-3.63	A-helix
14	18.61	21.81	-3.19	A-helix
15	19.73	20.71	-0.98	A-helix
16	15.93	17.25	-1.32	A-helix
19	17.62	14.41	3.22	A-helix
20	15.02	14.16	0.87	A-helix
21	14.92	10.67	4.25	A-helix
22	15.37	12.20	3.17	A-helix
23	15.47	13.10	2.37	A-helix
26	16.57	13.14	3.42	A-helix
30	18.67	11.14	7.53	A-helix
37	10.00	11.44	-1.44	B-helix
41	10.77	14.02	-3.26	B-helix
42	10.00	13.56	-3.56	B-helix
43	10.00	14.77	-4.77	B-helix
44	10.00	12.61	-2.61	B-helix
45	10.00	12.36	-2.36	B-helix
46	10.00	12.50	-2.50	B-helix
47	10.00	12.47	-2.47	B-helix
49	10.00	11.83	-1.83	B-C linker
51	10.00	10.22	-0.22	B-C linker
53	10.00	10.25	-0.25	B-C linker
55	10.00	12.90	-2.90	C-helix
56	10.00	11.55	-1.55	C-helix
57	10.00	10.93	-0.93	C-helix
58	10.00	13.02	-3.02	C-helix
59	10.00	12.22	-2.22	C-helix
63	10.00	11.43	-1.43	C-helix
66	10.00	16.79	-6.79	C-D linker (site II)
67	16.37	20.98	-4.61	C-D linker (site II)
75	13.73	20.65	-6.92	C-D linker (site II)
77	10.88	11.51	-0.63	D-helix
78	10.40	11.86	-1.46	D-helix
81	10.00	11.54	-1.54	D-helix
82	10.00	10.44	-0.44	D-helix
83	10.00	12.50	-2.50	D-helix

85	10.00	12.66	-2.66	Central linker
86	10.00	12.36	-2.36	Central linker
87	10.00	11.54	-1.54	Central linker
88	10.00	11.17	-1.17	Central linker
89	10.00	11.59	-1.59	Central linker
90	12.52	11.63	0.90	Central linker
91	12.81	12.26	0.55	Central linker
92	13.62	14.91	-1.29	Central linker
93	13.52	15.10	-1.58	Central linker
94	15.19	15.69	-0.50	E-helix
95	17.15	17.81	-0.66	E-helix
97	14.85	18.14	-3.29	E-helix
98	17.85	17.87	-0.02	E-helix
99	14.85	22.66	-7.81	E-helix
100	15.99	24.68	-8.68	E-helix
101	19.14	30.00	-10.86	E-helix
102	20.13	30.00	-9.87	E-helix
103	20.79	30.00	-9.21	E-helix
116	23.66	30.00	-6.34	E-F linker (site III)
118	20.68	29.88	-9.20	E-F linker (site III)
119	19.75	30.00	-10.25	E-F linker (site III)
123	21.31	24.38	-3.07	F-helix
125	20.60	24.60	-4.00	F-helix
126	18.79	27.58	-8.79	F-helix
128	24.75	27.11	-2.36	F-helix
132	23.48	30.00	-6.52	F-helix
148	22.64	30.00	-7.36	G-H linker (site IV)
156	21.35	19.55	1.80	H-helix
158	16.41	19.95	-3.54	H-helix
159	16.24	18.22	-1.98	H-helix
161	16.22	18.57	-2.35	H-helix

Table S2: The change (Δ) in PRE-NMR distances (Å) in the *absence* of Ca^{2+} for spin label at C84 to residues detectable in both the cTnC-WT and L29Q constructs. Distances that were broadened beyond detection are assigned as 10.0 Å.

Residue	cTnC-WT	L29Q	Distance Δ	Location
4	16.12	16.01	0.11	N-helix
5	17.82	15.81	2.02	N-helix
8	17.90	15.74	2.16	N-helix
12	18.52	16.62	1.90	N-helix
13	18.07	16.23	1.83	N-helix
14	20.39	23.38	-3.00	A-helix
15	19.52	20.96	-1.45	A-helix
16	16.29	18.40	-2.10	A-helix
17	16.94	18.54	-1.60	A-helix
18	16.74	20.37	-3.63	A-helix
19	15.69	18.85	-3.16	A-helix
21	14.16	17.78	-3.62	A-helix
27	15.24	24.40	-9.17	A-helix
31	20.31	23.12	-2.81	A-B linker (site I)
40	12.19	18.36	-6.17	A-B linker (site I)
41	12.11	15.61	-3.50	A-B linker (site I)
42	12.78	14.21	-1.43	B-helix
53	10.00	9.76	0.24	C-helix
55	10.00	10.29	-0.29	C-helix
56	10.00	12.35	-2.35	C-helix
59	11.26	12.12	-0.86	C-helix
63	10.00	11.22	-1.22	C-helix
65	12.47	12.45	0.02	C-D linker (site II)
67	15.35	15.96	-0.62	C-D linker (site II)
68	15.50	17.35	-1.86	C-D linker (site II)
71	13.97	16.66	-2.70	C-D linker (site II)
77	12.47	15.14	-2.67	D-helix
79	10.00	13.54	-3.54	D-helix
81	10.00	11.33	-1.33	D-helix
82	10.00	11.49	-1.49	D-helix
87	10.00	10.51	-0.51	Central linker
88	11.19	9.76	1.43	Central linker
89	11.98	11.59	0.39	Central linker
90	12.44	11.46	0.97	Central linker
92	16.91	15.53	1.38	Central linker
93	19.74	14.45	5.30	Central linker
94	17.77	16.58	1.19	E-helix
97	19.03	23.32	-4.29	E-helix
103	20.42	21.77	-1.35	E-helix
110	24.05	30.00	-5.95	E-F linker (Site III)

125	23.33	18.63	4.70	F-helix
141	23.94	20.63	3.31	G-H linker (Site IV)
144	22.93	20.15	2.79	G-H linker (Site IV)
145	22.48	18.02	4.46	G-H linker (Site IV)
159	19.83	16.34	3.49	H-helix
161	20.92	18.24	2.68	H-helix

Appendix 2. Clone Information

A.2.1 Troponin C

Clone: rat cardiac troponin C (cysteine-less)

Vector: pET 3d (novagen)

Properties: native cysteines at position 35 (skeletal 32) and 84 mutated to serine.

Expression system: *E.coli* BL21 DE3, carbenicillin resistance

Theoretical pI/Mw: 4.05 / 18398.44

```
1                                                                   54
ATG GAT GAC ATC TAT AAG GCG GCG GTT GAG CAG TTG ACA GAA GAA CAA AAA AAT
TAC CTA CTG TAG ATA TTC CGC CGC CAA CTC GTC AAC TGT CTT CTT GTT TTT TTA
Met Asp Asp Ile Tyr Lys Ala Ala Val Glu Gln Leu Thr Glu Glu Gln Lys Asn
1                                   10                              18
55                                                                 108
GAG TTT AAG GCT GCC TTC GAC ATC TTC GTG CTG GGG GCA GAG GAT GGC AGC ATC
CTC AAA TTC CGA CGG AAG CTG TAG AAG CAC GAC CCC CGT CTC CTA CCG TCG TAG
Glu Phe Lys Ala Ala Phe Asp Ile Phe Val Leu Gly Ala Glu Asp Gly Ser Ile
20                                      30                          36
109                                                                162
AGC ACC AAG GAG CTG GGG AAG GTG ATG AGG ATG CTG GGG CAG AAC CCC ACC CCT
TCG TGG TTC CTC GAC CCC TTC CAC TAC TCC TAC GAC CCC GTC TTG GGG TGG GGA
Ser Thr Lys Glu Leu Gly Lys Val Met Arg Met Leu Gly Gln Asn Pro Thr Pro
37          40                                  50                  54
163                                                                216
GAG GAG CTG CAG GAG ATG ATT GAT GAG GTG GAT GAG GAT GGC AGT GGC ACT GTG
CTC CTC GAC GTC CTC TAC TAA CTA CTC CAC CTA CTC CTA CCG TCA CCG TGA CAC
Glu Glu Leu Gln Glu Met Ile Asp Glu Val Asp Glu Asp Gly Ser Gly Thr Val
55                  60                                      70      72
217                                                                270
GAC TTT GAT GAG TTC CTT GTT ATG ATG GTT CGG TCT ATG AAA GAT GAC AGC AAA
CTG AAA CTA CTC AAG GAA CAA TAC TAC CAA GCC AGA TAC TTT CTA CTG TCG TTT
Asp Phe Asp Glu Phe Leu Val Met Met Val Arg Ser Met Lys Asp Asp Ser Lys
73                          80              84                      90
271                                                                324
GGA AAA ACT GAA GAG GAG CTC TCA GAT CTC TTC AGG ATG TTT GAT AAG AAT GCT
CCT TTT GCA CTT CTC CTC GAG AGT CTA GAG AAG TCC TAC AAA CTA TTC TTA CGA
Gly Lys Thr Glu Glu Glu Leu Ser Asp Leu Phe Arg Met Phe Asp Lys Asn Ala
91                                  100                             108
325                                                                378
GAT GGC TAC ATT GAT CTT GAG GAA CTG AAG ATC ATG CTA CAG GCA ACT GGA GAG
CTA CCG ATG TAA CTA GAA CTC CTT GAC TTC TAG TAC GAT GTC CGT TGA CCT CTC
Asp Gly Tyr Ile Asp Leu Glu Glu Leu Lys Ile Met Leu Gln Ala Thr Gly Glu
110                                     120                         126
379                                                                432
ACG ATC ACT GAG GAT GAC ATA GAA GAA CTG ATG AAA GAT GGG GAC AAA AAC AAT
TGC TAG TGA CTC CTA CTG TAT CTT CTT GAC TAC TTT CTA CCC CTG TTT TTG TTA
Thr Ile Thr Glu Asp Asp Ile Glu Glu Leu Met Lys Asp Gly Asp Lys Asn Asn
127         130                                     140             144
433                                                                486
GAT GGC AGG ATT GAC TAT GAC GAG TTC CTG GAG TTC ATG AAG GGA GTT GAA TAA
CTA CCG TCC TAA CTG ATA CTG CTC AAG GAC CTC AAG TAC TTC CCT CAA CTT ATT
Asp Gly Arg Ile Asp Tyr Asp Glu Phe Leu Glu Phe Met Lys Gly Val Glu End
145                 150                                     160  161
```

A.2.2 Troponin I

Clone: rat cardiac troponin I (cysteine-less)

Vector: pET 3d (novagen)

Properties: native cysteines at position 81 and 98 mutated (C81I, C98S).

Expression system: *E.coli* BL21 DE3, carbenicillin resistance

Theoretical pI/Mw: 9.69 / 24252.7

```
1                                                                   54
ATG GCT GAT GAA AGC AGC GAT GCG GCT GGG GAA CCG CAG CCT GCG CCT GCT CCT
TAC CGA CTA CTT TCG TCG CTA CGC CGA CCC CTT GGC GTC GGA CGC GGA CGA GGA
Met Ala Asp Glu Ser Ser Asp Ala Ala Gly Glu Pro Gln Pro Ala Pro Ala Pro
     1                                  10
55                                                                 108
GTC CGA CGC CGC TCC TCT GCC AAC TAC CGA GCC TAT GCC ACC GAG CCA CAC GCC
CAG GCT GCG GCG AGG AGA CGG TTG ATG GAT CGG ATA CGG TGG CTC GGT GTG CGG
Val Arg Arg Arg Ser Ser Ala Asn Tyr Arg Ala Tyr Ala Thr Glu Pro His Ala
         20                                  30
109                                                                162
AAG AAA AAG TCT AAG ATC TCC GCC TCC AGA AAA CTT CAG TTG AAG ACT CTG ATG
TTC TTT TTC AGA TTC TAG AGG CGG AGG TCT TTT GAA GTC AAC TTC TGA GAC TAC
Lys Lys Lys Ser Lys Ile Ser Ala Ser Arg Lys Leu Gln Leu Lys Thr Leu Met
                40                                  50
163                                                                216
CTG CAG ATT GCG AAG CAG GAG ATG GAA CGA GAG GCA GAA GAG CGA CGT GGA GAG
GAC GTC TAA CGC TTC GTC CTC TAC CTT GCT CTC CGT CTT CTC GCT GCA CCT CTC
Leu Gln Ile Ala Lys Gln Glu Met Glu Arg Glu Ala Glu Glu Arg Arg Gly Glu
                          60                                  70
217                                                                270
AAG GGG CGT GTT CTG AGG ACT CGT ATC CAG CCT TTG GAG TTG GAT GGG CTG GGC
TTC CCC GCA CAA GAC TCC TGA GCA TAG GTC GGA AAC CTC AAC CTA CCC GAC CCG
Lys Gly Arg Val Leu Arg Thr Arg Ile Gln Pro Leu Glu Leu Asp Gly Leu Gly
                               80
271                                                                324
TTT GAA GAG CTT CAG GAC TTA AGC CGA CAG CTT CAC GCT CGG GTG GAC AAA GTG
AAA CTT CTC GAA GTC CTG AAT TCG GCT GTC GAA GTG CGA GCC CAC CTG TTT CAC
Phe Glu Glu Leu Gln Asp Leu Ser Arg Gln Leu His Ala Arg Val Asp Lys Val
90                                  100
325                                                                378
GAT GAA GAG AGA TAT GAC GTG GAA GCA AAA GTC ACC AAG AAC ATC ACT GAG ATT
CTA CTT CTC TCT ATA CTG CAC CTT CGT TTT CAG TGG TTC TTG TAG TGA CTC TAA
Asp Glu Glu Arg Tyr Asp Val Glu Ala Lys Val Thr Lys Asn Ile Thr Glu Ile
         110                                 120
379                                                                432
GCA GAT CTG ACC CAG AAG ATC TAT GAC CTC CGT GGC AAG TTT AAG CGG CCC ACC
GCT CTA GAC TGG GTC TTC TAG ATA CTG GAC GCA CCG TTC AAA TTC GCC GGG TGG
Ala Asp Leu Thr Gln Lys Ile Tyr Asp Leu Arg Gly Lys Phe Lys Arg Pro Thr
                130                                 140
433                                                                486
CTC CGA AGA GTG AGG ATC TCT GCA GAT GCC ATG ATG CAG GCG CTG CTG GGG ACC
GAG GCT TCT CAC TCC TAG AGA CGT CTA CGG TAC TAC GTC CGC GAC GAC CCC TGG
Leu Arg Arg Val Arg Ile Ser Ala Asp Ala Met Met Gln Ala Leu Leu Gly Thr
                          150                                 160
```

A.2.3 Troponin T

Clone: rat cardiac troponin T

Vector: pET 28a (novagen) N-terminal His tagged with thrombin cleavage site (cleavage occurs after 'R')

Properties: Double rare arginine codons mutated from AGG/AGG to CGT/CGT at amino acids 167/168 and 216/217. No native cysteine residues

Expression system: *E.coli* BL21 DE3, kanamycin resistance

Theoretical pI/Mw: 5.54 / 36615.44

```
1                                                                   60
ATG GGC AGC AGC CAT CAT CAT CAT CAT CAC AGC AGC GGC CTG GTG CCG CGC GGC AGC CAT
TAC CCG TCG TCG GTA GTA GTA GTA GTA GTG TCG TCG CCG GAC CAC GGC GCG CCG TCG GTA
Met Gly Ser Ser His His His His His His Ser Ser Gly Leu Val Pro Arg Gly Ser His
61                                                                 120
ATG TCT GAC GCC GAG GAA GAG GTG GTG GAG TAC GAG GAG GAA CAG GAA GAG CAA GAG GAG
TAC AGA CTG CGG CTC CTT CTC CAC CAC CTC ATG CTC CTC CTT GTC CTT CTC GTT CTC CTC
Met Ser Asp Ala Glu Glu Glu Val Val Glu Tyr Glu Glu Glu Gln Glu Glu Gln Glu Glu
1                                                                   20
121                                                                180
GCA GTG GAG GAG GAG GAT GGT GAG GCC GAG CCT GAT CCC GAG GGT GAG GCA GAG GCA GAG
CGT CAC CTC CTC CTC CTA CCA CTC CGG CTC GGA CTA GGG CTC CCA CTC CGT CTC CGT CTC
Ala Val Glu Glu Glu Asp Gly Glu Ala Glu Pro Asp Pro Glu Gly Glu Ala Glu Ala Glu
21                                                                  40
181                                                                240
GAG GAC AAG GCA GAA GAG GTT GGT CCT GAT GAA GAA GCC AGA GAT GCT GAA GAT GGT CCA
CTC CTG TTC CGT CTT CTC CAA CCA GGA CTA CTT CTT CGG TCT CTA CGA CTT CTA CCA GGT
Glu Asp Lys Ala Glu Glu Val Gly Pro Asp Glu Glu Ala Arg Asp Ala Glu Asp Gly Pro
41                                                                  60
241                                                                300
GTA GAG GAC TCC AAA CCC AAG CCC AGC AGG CTC TTC ATG CCC AAC TTG GTG CCA CCC AAG
CAT CTC CTG AGG TTT GGG TTC GGG TCG TCC GAG AAG TAC GGG TTG AAC CAC GGT GGG TTC
Val Glu Asp Ser Lys Pro Lys Pro Ser Arg Leu Phe Met Pro Asn Leu Val Pro Pro Lys
61                                                                  80
301                                                                360
ATC CCT GAC GGA GAG AGA GTG GAC TTT GAT GAC ATC CAC AGG AAG CGC ATG GAG AAG GAC
TAG GGA CTG CCT CTC TCT CAC CTG AAA CTA CTG TAG GTG TCC TTC GCG TAC CTC TTC CTG
Ile Pro Asp Gly Glu Arg Val Asp Phe Asp Asp Ile His Arg Lys Arg Met Glu Lys Asp
81                                                                 100
361                                                                420
CTG AAC GAG CTG CAG ACT CTG ATC GAG GCT CAC TTC GAG AAC AGG AAG AAG GAG GAA GAG
GAC TTG CTC GAC GTC TGA GAC TAG CTC CGA GTG AAG CTC TTG TCC TTC TTC CTC CTT CTC
Leu Asn Glu Leu Gln Thr Leu Ile Glu Ala His Phe Glu Asn Arg Lys Lys Glu Glu Glu
101                                                                120
421                                                                480
GAG CTC ATT TCT CTC AAA GAC AGG ATC GAA AAG CGT CGG GCA GAG CGG GCT GAA CAG CAG
CTC GAG TAA AGA GAG TTT CTG TCC TAG CTT TTC GCA GCC CGT CTC GCC CGA CTT GTC GTC
Glu Leu Ile Ser Leu Lys Asp Arg Ile Glu Lys Arg Arg Ala Glu Arg Ala Glu Gln Gln
121                                                                140
481                                                                540
CGT ATT CGC AAT GAA CGA GAG AAG GAA AGG CAG AAC CGC CTG GCT GAA GAG AGG GCC CGG
GCA TAA GCG TTA CTT GCT CTC TTC CTT TCC GTC TTG GCG GAC CGA CTT CTC TCC CGG GCC
Arg Ile Arg Asn Glu Arg Glu Lys Glu Arg Gln Asn Arg Leu Ala Glu Glu Arg Ala Arg
141                                                                160
```

```
541                                                                 600
CGT GAG GAG GAG GAG AAC CGT CGT AAG GCT GAA GAT GAG GCC CGG AAG AAG AAG GCT CTG
GCA CTC CTC CTC CTC TTG GCA GCA TTC CGA CTT CTA CTC CGG GCC TTC TTC TTC CGA GAC
Arg Glu Glu Glu Glu Asn Arg Arg Lys Ala Glu Asp Glu Ala Arg Lys Lys Lys Ala Leu
161                                                                 180
601                                                                 660
TCC AAC ATG ATG CAT TTT GGA GGG TAC ATC CAG AAG GCT CAG ACA GAG CGG AAG AGT GGG
AGG TTG TAC TAC GTA AAA CCT CCC ATG TAG GTC TTC CGA GTC TGT CTC GCC TTC TCA CCC
Ser Asn Met Met His Phe Gly Gly Tyr Ile Gln Lys Ala Gln Thr Glu Arg Lys Ser Gly
181                                                                 200
661                                                                 720
AAG AGA CAG ACA GAG CGA GAG AAG AAG AAG AAG ATT CTG GCA GAG CGT CGT AAG GTG CTG
TTC TCT GTC TGT CTC GCT CTC TTC TTC TTC TTC TAA GAC CGT CTC TCC TCC TTC CAC GAC
Lys Arg Gln Thr Glu Arg Glu Lys Lys Lys Lys Ile Leu Ala Glu Arg Arg Lys Val Leu
201                                                                 220
721                                                                 780
GCC ATC GAC CAC CTG AAT GAA GAC CAG CTG AGA GAG AAG GCC AAG GAG CTA TGG CAG AGT
CGG TAG CTG GTG GAC TTA CTT CTG GTC GAC TCT CTC TTC CGG TTC CTC GAT ACC GTC TCA
Ala Ile Asp His Leu Asn Glu Asp Gln Leu Arg Glu Lys Ala Lys Glu Leu Trp Gln Ser
221                                                                 240
781                                                                 840
ATC CAC AAC CTA GAG GCC GAG AAG TTC GAC CTG CAG GAA AAG TTC AAG CAG CAG AAA TAT
TAG GTG TTG GAT CTC CGG CTC TTC AAG CTG GAC GTC CTT TTC AAG TTC GTC GTC TTT ATA
Ile His Asn Leu Glu Ala Glu Lys Phe Asp Leu Gln Glu Lys Phe Lys Gln Gln Lys Tyr
241                                                                 260
841                                                                 900
GAA ATC AAC GTT CTG CGA AAC AGG ATC AAC GAC AAC CAG AAA GTC TCC AAA ACT CGT GGG
CTT TAG TTG CAA GAC GCT TTG TCC TAG TTG CTG TTG GTC TTT CAG AGG TTT TGA GCA CCC
Glu Ile Asn Val Leu Arg Asn Arg Ile Asn Asp Asn Gln Lys Val Ser Lys Thr Arg Gly
261                                                                 280
901                                 930
AAG GCC AAA GTC ACC GGG CGT TGG AAA TAG
TTC CGG TTT CAG TGG CCC GCA ACC TTT ATC
Lys Ala Lys Val Thr Gly Arg Trp Lys -
281                               289
```